A MECHANISTIC UNDERSTANDING OF SOLVENT ADDITIVES' INFLUENCE ON POLYMER:FULLERENE PHASE SEPARATION FOR ORGANIC PHOTOVOLTAICS

A Dissertation
Presented to
The Academic Faculty

By

Jeff Hernandez

In Partial Fulfillment
of the Requirements for the Degree of
Doctor of Philosophy in the
School of Chemistry & Biochemistry
Georgia Institute of Technology

May 2017

A MECHANISTIC UNDERSTANDING OF SOLVENT ADDITIVES' INFLUENCE ON POLYMER:FULLERENE PHASE SEPARATION FOR ORGANIC PHOTOVOLTAICS

Approved by:

Dr. John R. Reynolds, Advisor
School of Chemistry and Biochemistry
School of Materials Science & Engineering
Georgia Institute of Technology

Dr. David M. Collard
School of Chemistry and Biochemistry
Georgia Institute of Technology

Dr. Elsa Reichmanis
School of Chemical and Biochemical Engineering
Georgia Institute of Technology

Dr. Steven Usselman
School of School of History and Sociology
Georgia Institute of Technology

Dr. Joseph W. Perry
School of Chemistry and Biochemistry
Georgia Institute of Technology

Date Approved: January 30, 2017

ACKNOWLEDGEMENTS

First, I would like to thank my advisors Elsa Reichmanis and John Reynolds. Elsa has been a tremendous support to my education at Georgia Tech. I have greatly enjoyed being in her group meetings and interacting with the Reichmanis research group. I would also like to thank John Reynolds for accepting me into his research group. I am grateful for his time, and patience, that he has invested in me. I greatly admire his dedication to nurturing and developing everyone around him. I will never forget the time I spent in his group or lessons he has taught me throughout graduate school.

Secondly, I would like to thank numerous people at Georgia Tech: Caroline Grand, for her guidance during my initial years as a graduate student. Chi Kin Lo, Rylan Wolfe, Marcel Said, Nabankur Deb, Brian Schmatz, Eric Shen, Erdal Uzunlar, James Ponder, Dylan Christiansen, Sandy Pittelli, Gus Lang, Ian Pelse, Nabil Kleinhenz, Josh Hollett, and Anna Österholm, for riveting scientific discussion. I would also like to thank Wes Wynens for allowing me to be part of the Leadership Development Program and Grand Challenges, and Jorge Breton for support through the Goizueta Fellowship.

I would like to thank my collaborators at NIST, Dean DeLongchamp, Jon Downing, Lee Richter, and Sebastian Engmann. Lee Richter and Sebastian Engmann have been a tremendous aid in my scientific development.

Not to go unmentioned, I would like to express my gratitude to Butch Knudsen, who in many ways steered me to graduate school.

I thank my committee Members; John Reynolds, Elsa Reichmanis, David Collard, Joseph Perry, and Steven Usselman, for their valuable input during my original proposal, six month review, and defense.

I thank my family; my mother and father, Julie and Jose Hernandez, who have supported and encouraged me throughout graduate school. My father and mother in law, Bob and Michelle Hey, who have always supported us and were instrumental in helping us find a home in Atlanta. I would like to thank my uncle and his wife, Michael and Laura Hannin, who invited me into their home during my stay at NIST. I thank my brother Jake Hernandez and brother in law Allan Hey. Their support is greatly appreciated.

Lastly, I would like to thank my wife Jackie Hernandez who has always been supportive, and encouraging, throughout this entire process. I cannot thank her enough for the countless sacrifices she has made that allowed me to pursue my goals. Without her unwavering support this would not have been possible.

TABLE OF CONTENTS

LIST OF TABLES

LIST OF FIGURES

LIST OF SYMBOLS AND ABBREVIATIONS

AFM	Atomic force microscopy
BHJ	Bulk heterojunction
CB	Chlorobenzene
CF	Chloroform
CN	1-Chloronaphthalene
CT	Charge transfer
DCB	*o*-Dichlorobenzene
DIO	1,8-Diiodooctane
DPP	Diketopyrrolopyrrole
EPBT	Energy payback time
FF	Fill factor
GIWAXS	Grazing incidence wide angle X-ray scattering
GISAXS	Grazing incidence small angle X-ray scattering
HOMO	Highest occupied molecular orbital
IPCE	Incident photon-to-current efficiency
ITO	Indium tin oxide
J_{sc}	Short-circuit current density
LCOE	Levelized cost of electricity
LUMO	Lowest unoccupied molecular orbital
ODT	1,8-Octanedithiol
OFET	Organic field-effect transistor
OPV	Organic photovoltaic
P3HT	Poly(3-hexylthiophene)
$PC_{61}BM$	[6,6]-phenyl-C61-butyric acid methyl ester fullerene
$PC_{71}BM$	[6,6]-phenyl-C71-butyric acid methyl ester fullerene
PCE	Power conversion efficiency
PDI	Polydispersity index
PEDOT:PSS	Poly(3,4-ethylenedioxythiophene):poly(styrene sulfonate)
SCLC	Space-charge limited-current
TEM	Transmission electron microscopy
V_{oc}	Open-circuit voltage

SUMMARY

Solution processable conjugated organic materials offer a route to low cost electronic devices which include transistors, LEDs, electrochromics, and photovoltaics. The ability of these materials to be solubilized allows for simple, low temperature, processing on rigid and flexible substrates. This dissertation focuses on processing of conjugated materials for photovoltaic applications. The impact that additives have on solidification, film morphology, and ultimately device performance, is studied, beginning with examination of the solution state, then processing, followed by thin film characterization and device performance. Each chapter focuses on a different conjugated polymeric material and examines the influence that additives have on the solid state film formation. Using in situ measurements, coupled with static thin film measurements, the mechanism of thin film formation is explored when processed with, and without, modifications to the starting ink solution. Chapter 3 focuses on poly(3-hexylthiophene-2,5-diyl) (P3HT) mixed with $PC_{61}BM$. Blade coating this blend from solvents of varying vapor pressures yield different drying dynamics, and solar cell performance. Chapter 4 explores morphological and performance differences of blade coated, or spin coated, poly[5-(2-hexyldecyl)-1,3-thieno[3,4-*c*]pyrrole-4,6-dione-*alt*-5,5-(2,5-bis(3-dodecylthiophen-2-yl)-thiophene)], P(T3-TPD), blended with $PC_{71}BM$, and processed with, or without, the solvent additive 1,8-diiodooctane (DIO). Results presented in this chapter show processing of aggregated solutions yields similar morphologies and solar cell performance, regardless of processing type. Further, DIO was found to increase the nucleation density, reducing domain size, and improving polymer crystallinity, leading to enhance photovoltaic performance. Chapter 5 examines the impact that co-solvent processing has on the

polymer:fullerene blend known as DT-PDPP2T-TT:$PC_{71}BM$. Blade coating this bulk-heterojunction blend from chloroform leads to liquid-liquid phase separation, whereas, when the co-solvent *ortho*-dichlorobenzene is introduced the morphology evolution is nucleation and growth dominated, leading to a reduced characteristic length scale, and improved power conversion efficiencies. Lastly, Chapter 6 focuses on the organic photovoltaic market, how organic photovoltaics compare to their Si counterpart, and areas where organic photovoltaics can improve in order for this technology to become viable to the market.

CHAPTER 1. INTRODUCTION

1.1. General Background on Organic Electronics.

1.1.1. History of Conjugated Polymers.

Conjugated polymers have been the subject of tremendous investigation over the past several decades. During the mid-20th century numerous researchers made significant strides in the field of conjugated materials giving us the foundation of organic electronics. Early work by Letheby on the oxidation of aniline, and presumed synthesis of polyaniline (**1**), Figure 1, is arguably the first reported conjugated polymer synthesis.[1] Further, work done on the conductivity of polypyrrole (**2**), Figure 1, by Dall'Olio et al.[2], iodine doping of polypyrrole by Weiss et. al.[3, 4], and conductivity of polyaniline by Buvet et al.[5] led to the discovery of metallic-like conductivity in organic polymers.

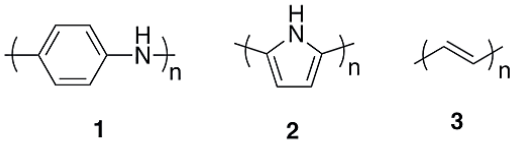

Figure 1. First reported synthesized conjugated polymers studied. (**1**) polyaniline, (**2**) polypyrrole, (**3**) polyacetylene. Adapted from Müllen et al.[6]

Groundbreaking work done by Ziegler and Giulio Natta on coordination polymerization of unsaturated molecules, which won them the Nobel Prize in 1963, provided a synthetic route to make structurally well-defined polymers.[7] Natta demonstrated high molecular weight polyacetylene (**3**), Figure 1, (CH_x) which was an insoluble powder.

Berets and Smith continued work on polyacetylene by examining vapor phase treatment of the powders with Lewis acids and bases, finding that when treated with the dopant BF_3 the conductivity of the material was enhanced by three orders of magnitude.[8] Another major milestone in conjugated materials occurred when Ito et al. demonstrated a synthetic method to yield free standing films of polyacetylene which had a metallic sheen.[9] The combined efforts of Alan Heeger, Alan MacDiarmid, and Hideki Shirakawa, who studied the conductivity of polyacetylene films treated with Cl_2, Br_2, I_2, and AsF_5, found that conductivities of 500 S/cm could be achieved, which was remarkable because at the time no disordered polymer systems had displayed conductivity values that high.[10] This work led them to receive a Nobel Prize in 2000. Since this seminal work, focus has been on developing solution processable conjugated materials. The advent of palladium catalyzed cross coupling work by Richard Heck, Ei-ichi Negishi and Akira Suzuki, which led to a Nobel Prize in 2010, allowed for a variety of conjugated materials to be synthesized, ushering in tremendous advancements in the organic electronics field.[11] For the last 30 years researchers have developed a plethora of new conjugated moieties for the backbone, and have explored side chain variation for solubility and its effects on morphology and device performance.

1.1.2. Electronic States of Conjugated Materials.

The electronic properties of π-conjugated polymers come from electrons in overlapping p_z orbitals. The electrons in the π bonds are less bound than electrons in the σ bonds which gives these molecules their electronic nature. Figure 2 demonstrates as the number of π bonds increases there are new discrete energy levels formed which are stabilized by the delocalization of the electrons.[12] Ethylene, the simplest π system

molecule, has a band gap (E_g) of 6.7 eV. As the conjugation is extended the E_g decreases, as shown in polyacetylene, which has a band gap of approximately 1.5 eV.[13] The E_g is the difference between the top of the valence band (VB) and the bottom of the conduction band (CB) also referred to as the highest occupied molecular orbital (HOMO) and the lowest unoccupied molecular orbital (LUMO) respectively.

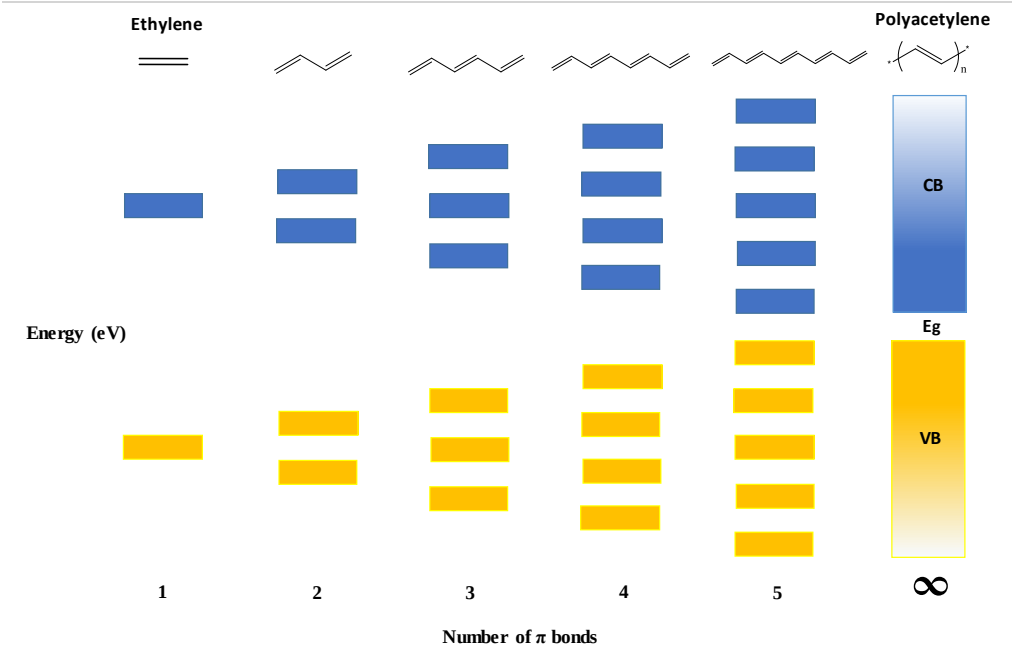

Figure 2. Schematic of the transition from discrete energy levels to energy bands as the conjugation increases from ethylene to polyacetylene. Filled HOMO levels are represented in gold while empty LUMO levels are shown in blue. Adapted from Salzner et al.[12]

If all the bond orders were equal (1.5) in polyacetylene, such as a 1D periodic lattice, the polymer would behave as a metal, having a band gap of 0 eV, due to degenerate π and π* bands. However, due to Peierl's distortion atomic positions oscillate to a lower energy state, which leads to alternating single and double bonds, thus creating a E_g and the semiconducting nature of these materials. In the context of polymer materials for organic

photovoltaics (OPV) applications, synthetic design can be used to tune the E_g of the polymer to obtain a E_g with strong light absorption in the visible spectrum. Figure 3 shows the solar spectral irradiance at AM1.5. As the band gap decreases, a greater extent of the solar spectrum is absorbed by the material. The color coding in Figure 3 highlights the area of the solar spectrum that is absorbed based on the E_g of the material. Achieving a band gap of 1.1 eV would theoretically be capable of absorbing 77% of solar irradiation whereas, a band gap of 2 eV would absorb only 30% of solar irradiation.[14] An E_g of 0.92 eV is capable of absorbing 90% of the solar spectrum.[15] This highlights the importance of tuning the band gap to achieve absorption across the visible spectrum.

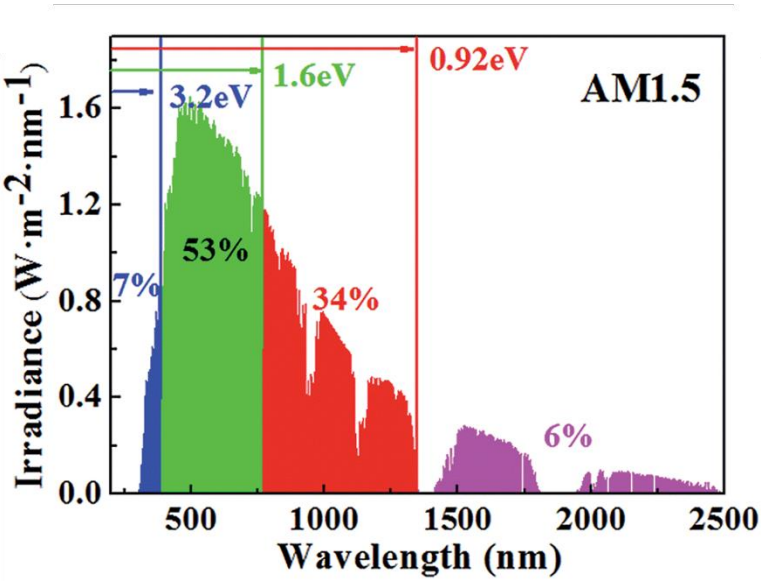

Figure 3. Solar spectral irradiance at AM1.5. The color coding indicates the area of the spectrum that can be absorbed based on the E_g of the material. Reproduced from Wu et al.[15] with permission from the Royal Society of Chemistry.

Band gap tuning is typically done by coupling an electron accepting moiety with an electron donating moiety creating D-A co-polymers with lower band gaps than the

homo-polymer due to orbital mixing. While homo-polymers, like P3HT, have been effective materials for a number of applications, the use of D-A co-polymers yield materials with reduced E_g allowing for more of the solar spectrum to be absorbed, and converted to photocurrent. Effectively, the donor determines the new HOMO level, while the acceptor determines the new LUMO level, as shown in Figure 4.[16, 17]

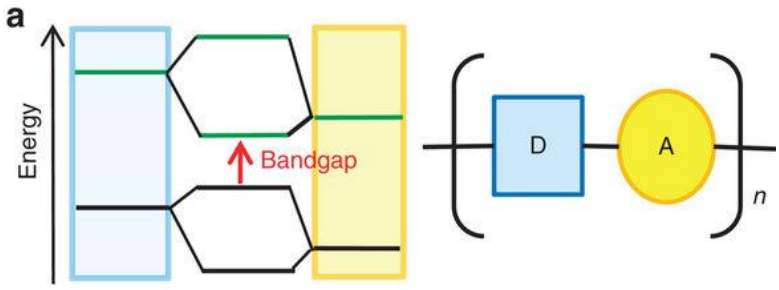

Figure 4. Schematic representation of donor-acceptor moieties coupled together to form a donor-acceptor polymer with a band gap determined by the HOMO-LUMO energy levels of the two components. Adapted from Tautz et al.[17] Copyright 2012, Nature Publishing Group.

1.2. Organic Photovoltaics (OPVs): Operating Principles.

This section details the operating principles of bulk-heterojunction solar cells, composed of a polymer-fullerene blend, and factors that influence the operation of these devices.

1.2.1. OPV Device Operating Principles.

Significant advances in understanding the operating principals of OPVs have been made over the past several years. While inorganic solar cell operation relies on a P-N junction, in which the physics are well understood, charge generation in organic solar cells

undergoes a different mechanism due to the nature of the excited state.[18] When light is absorbed by low dielectric constant organic materials, this leads to a coulombically bound electron-hole pair, with a binding energy of ca. 500 meV, known as an exciton, unlike inorganic materials in which free charge carriers are generated.[19, 20] Figure 5 demonstrates the working principals of charge carrier generation and separation upon absorption of light by organic materials. Light is absorbed by the donor, or acceptor, promoting an electron from the singlet ground state (S_0) to the first single excited state (S_1), creating an exciton, Figure 5 step (1). At the donor/acceptor interface intermolecular charge transfer leads to the electron moving into charge transfer (CT) states shown in Figure 5 step (2). CT_1 denotes the lowest charge transfer state in which recombination is likely, step (3), while CT_n denotes higher CT states. From the CT states, charges can be separated, and enter the charge separated (CS) state, step (4). The k_i terms denote varying competing relaxation and electron-transfer rates.[21] Once charges are separated they can be collected.

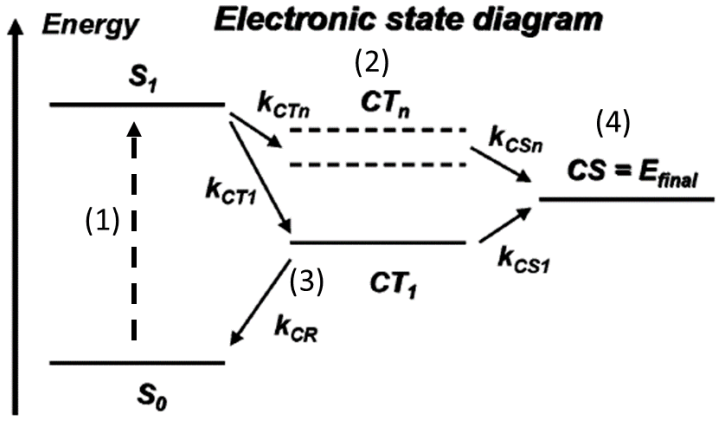

Figure 5. The electronic state diagram depicting the excitation of an electron to form an exciton, and the varying possible pathways that exciton can be split, or recombined. Adapted from Kippelen et al.[20] with permission from the Royal Society of Chemistry.

In order to characterize the performance of a solar cell three parameters are considered – the short circuit current density (J_{sc}), the open circuit voltage (V_{oc}), and the fill factor (FF), as combined in Equation 1-1. The product of these three variables divided by the incidence power gives the power conversation efficiency (PCE), equation 1-2, which is typically considered one of the most important metrics for photovoltaics. PCE is simply the efficiency in which light is converted to electricity. Figure 6 shows a J-V curve under illumination of 1 sun (100 mW/cm^2)(solid red line). At zero bias where the line crosses the y-axis is the J_{sc}. At zero current where the line crosses the x-axis is the V_{oc}. FF is a measure of how square the curve is, which is determined by the max power point (MPP). It symbolizes the difficulty of charge extraction, with a FF of 1 representing a perfect FF in which all charges generated are extracted.[22] Many variables can influence FF which include series resistance, shunt resistance, and film quality.

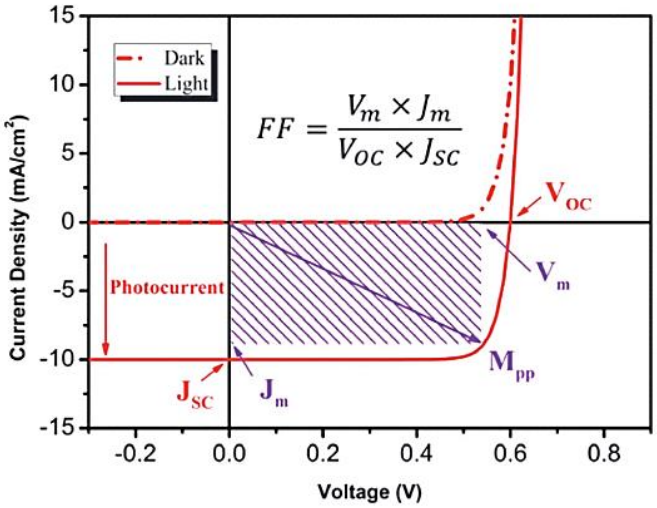

Figure 6. Example J-V curve used to extract J_{sc}, V_{oc}, FF, and PCE%. The dashed red line represents dark current, while the solid red line shows a device under illumination. Adapted from Qi et al.[22] with permission from the Royal Society of Chemistry.

FF can be determined by Equation 1-1:

$$\text{Equation 1-1: } FF = \frac{P_m}{J_{sc}V_{oc}} = \frac{J_m V_m}{J_{sc}V_{oc}}$$

Where P_m is the max power point determined by the max voltage (V_m) and max current density (J_m).

PCE can be obtained using Equation 1-2:

$$\text{Equation 1-2: PCE} = \frac{P_m}{P_{in}} = \frac{J_{sc}V_{oc}FF}{P_{in}}$$

Where P_m is the max power divided by the light power, P_{in}, incident on the device.

1.2.2. Active Layer Architectures: Bulk-Heterojunction (BHJ) vs. Bilayer.

While efficient exciton dissociation, low series resistance, and high shunt resistance, are necessary for high performance OPVs, they are often heavily influenced by the morphology of the BHJ film and the interfaces between the layers of the device. Thin film OPV's got their start with the seminal work done by Tang, who introduced a bilayer OPV architecture with the active layer composed of copper phthalocyanine (CuPc) and a perylene tetracarboxylic derivative (PV), that achieved a PCE value of ~1%.[23] The bilayer solar cell architecture is show in in Figure 7 a),[24] in which one layer is processed on top of the other. This bilayer architecture provides very little surface area between the donor and acceptor phases to separate excitons. Due to very small exciton diffusion lengths of 5 nm – 10 nm, which is determined by Equation 1-3, in which L is the diffusion length, D is the diffusion coefficient ($cm^2\ s^{-1}$), and τ is the exciton lifetime (s), a bilayer device would not achieve high efficiency because of low interfacial area between the donor and the acceptor, and high recombination rates.[25]

$$\text{Equation 1-3: } L = \sqrt{D\tau}$$

A major breakthrough occurred when Heeger et al.[26] and Friend et al.[27] built the first polymer-fullerene, and polymer-polymer, mixed phase organic solar cells. This mixed phase was termed a bulk-heterojunction (BHJ) and is made up of randomly distributed phases of donor and acceptor as shown in Figure 7 b). Extensive work has been conducted to understand the dynamics of this mixed phase system, to control the phase separation, and phase sizes. Ultimately, a bi-continuous network, Figure 7 c), of donor and acceptor with a very large surface area between the donor and acceptor would be ideal. However, due to fabrication difficulties, constructing this type of ideal film architecture has not been easily realized.

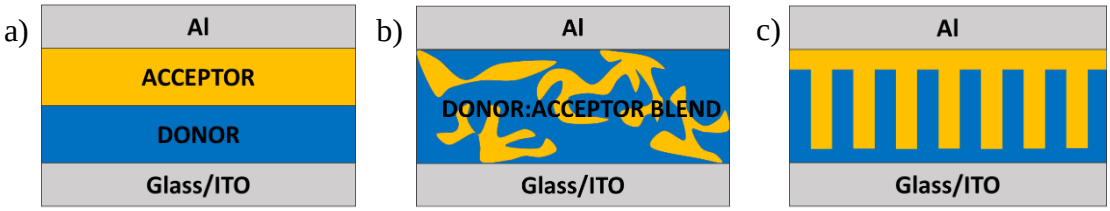

Figure 7. Evolution of organic solar cell processing from a) bilayer devices, to b) bulk-heterojunction device, to c) the ideal bi-continuous network.

1.2.3. Processability and Morphology Control: Importance of Side Chains and Polymer Molecular Weight.

A key advantage of conjugated polymers, and discrete molecules, is their ability to be solution processed at low temperatures to yield thin films, unlike their inorganic counterparts which usually require very high processing temperatures. There are many aspects that contribute to the processablitiy and morphology control of conjugated organic polymers which include, molecular weight, solubilizing side chains, polymer-solvent interactions, aggregation, solvent evaporation rates, crystallinity, ect. Here, I focus on two

aspects that have been shown to greatly influence processability and morphology, which are, 1. Molecular weight, and 2. Solubilizing side chains.

Polymer molecular weight is critical to high performance organic electronic devices. OPV's, and transistors, built with varying M_n fractions of P3HT from 2200 – 11,300 [g/mol] have been shown to yield radically different device performances. Transistors fabricated with low molecular weight P3HT demonstrate mobility values on the order of 10^{-7} cm^2/V s, while those built with high molecular weight P3HT show mobility values in the range of 10^{-3} cm^2/V s.[28] This same trend is observed for OPV's in which devices fabricated with low molecular weight P3HT yield < 0.5% PCE while devices made using high molecular weight P3HT show ~3% PCE.[29] It is important to note that higher molecular weight does not guarantee improved performance for transistors or solar cells. Work by Ballantyne et al.[30] examined six fractions of P3HT with M_n values ranging from a low of 13 kDa to a high of 121 kDa. Their work finds that, as P3HT M_n weight increases past 34 kDa there is a decrease in charge mobility, and photovoltaic performance, suggesting that there is an optimum molecular weight range between 13 kDa – 34 kDa. Polymer molecular weight dependence on device performance has been demonstrated in other systems as well. Chu et al.[31] studied the molecular weight dependence of 4,4-bis(2-ethylhexyl)-dithieno[3,2-b:2′,3′-d]silole and N-octylthieno[3,4-c] pyrrole-4,6-dione (PDTSTPD-C8), ranging from 10 kDa – 31 kDa M_n finding that higher molecular weight (31kDa) produced OPVs with improved performance. Li et al.[32] examined a polymer system, composed of a benzodithiophene (BnDT) unit coupled to a fluorinated analog of benzotriazole (FTAZ), known as PBnDT-FTAZ. Number average molecular weights of PBnDT-FTAZ ranged from 18.3 – 71.4 kg/mol. Their findings show there is an optimal

range of molecular weight, around 55 kg/mol, that produced the highest performing OPVs, while M_n weights lower, or higher, yielded decreased OPV performance.[32] This trend of improved performance based on an optimal molecular weight has been observed in many other systems,[33-35] and highlights the importance of polymer molecular weight, and its impact on device characteristics.

Like polymer molecular weight, the solubilizing side chain is equally important for obtaining an optimum morphology that leads to high performance OPVs. Extensive work by many groups have explored the influence of varying side chains on solubility, and morphology control, primarily using straight chains of varying length, or branched alkyl groups, where the branching point is moved relative to the polymer backbone.[36-39] Figure 8 demonstrates the vast breadth of side chains that have been studied.[40]

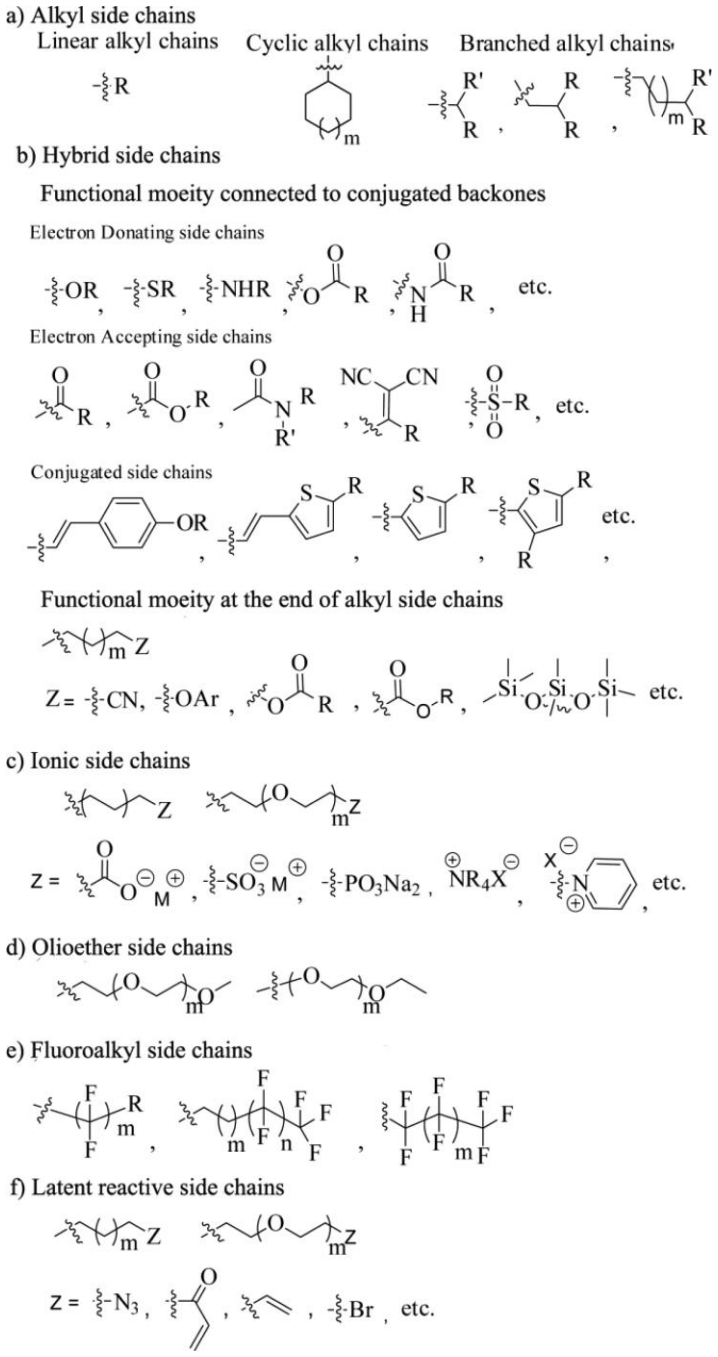

Figure 8. Side chains used in conjugated polymers. Reprinted with permission from reference [40] Copyright 2013, American Chemical Society.

To date, there is no side chain that yields optimum morphology and delivers improved devices, however, it is clear that side chain engineering plays a pivotal role in solubility and morphology control, which will impact device characteristics. Often times, there is a tradeoff between choosing a side chain which will give improved polymer solubility, or using a side chain that produces a desired solid state morphology which gives high performance devices.

1.3. Polymer:Fullerene Thin Film Processing.

While materials design for OPV polymers and small molecules has improved throughout the years, processing has afforded significant gains in achieving optimum phase separated morphologies which leads to enhanced PCEs. Here, I will discuss various processing techniques that have been demonstrated to alter the polymer:fullerene phase separated morphology and thus increase PCE.

1.3.1. Polymer Aggregation.

Conjugated materials are known to aggregate in solution. Aggregation can be used as a method for altering solidification of neat polymer, or the polymer:fullerene blend, leading to different solid state morphologies. Recently, work done by Yan & co-workers demonstrates the importance of processing aggregated solutions. Poly[(5,6-difluoro-2,1,3-benzothiadiazol-4,7-diyl)-alt-(3,3'''-di(2-octyldodecyl)2,2';5',2'';5'',2'''-quaterthiophen-5,5‴-diyl)], PffBT4T-2OD, also known by the trade name PCE-11, with the chemical structure shown in Figure 9 a), can be processed in an aggregated or non-aggregated state, which leads to different morphologies and device performances.[41] Figure 9 b) is the temperature dependent UV-vis absorbance spectra of PffBT4T-2OD in solution, and shows

the thermochromic nature of the material. At elevated temperatures the polymer is in a non-aggregated state and its absorbance spectra is blue shifted, while at lower temperatures the polymer is aggregated in solution which red shifts the λ_{max} of the absorbance spectra. Solutions of polymer and fullerene processed at high temperature (90 ºC) affords photovoltaic devices with PCEs of 9.3%, while low temperature processing (55 ºC) yields devices with PCEs of 6.2%. Films processed from an aggregated solution show many morphological differences from films processed from a non-aggregated solution which include polymer crystallinity, crystal orientation, phase purity, and domain size, all of which will greatly impact photovoltaic performance. This work demonstrates the influence polymer aggregation in solution has on device morphology and device performance.[42] It should be noted that processing of aggregated solutions for BHJ films can also lead to an enhanced morphology and PCE[33], signifying there are no definitive rules when processing conjugated polymers.

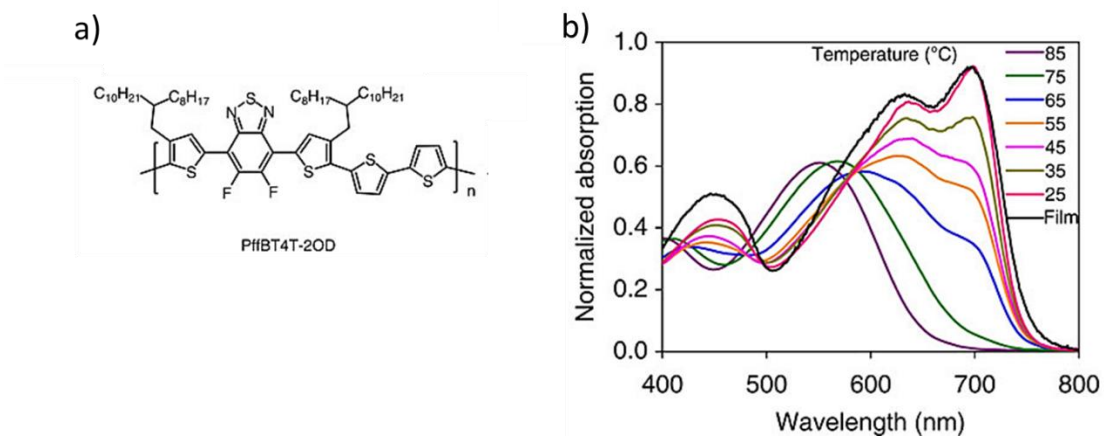

Figure 9. a) Chemical structure of PCE-11, and b) temperature dependent UV-vis absorption spectra of PCE-11 in solution. The black line shows the thin film UV-vis absorption spectra. Adapted from Ro et al. and Yan et al.[41, 42] with permission from the Royal Society of Chemistry and Nature Publishing Group.

1.3.2. Solvent Additives.

Solvent additives have a profound effect in the field of organic electronics. In the context of OPVs, there are many effects at play which will alter the phase separated BHJ morphology when using a solvent additive.[43] This section focuses on two typically highlighted parameters which are:

1. There is selective solubility of one component.
2. The solvent additive has a high boiling point/low vapor pressure compared to the host solvent.

Figure 10 shows examples of various solvent additives used to improve BHJ morphology and thus improve solar cell performance.

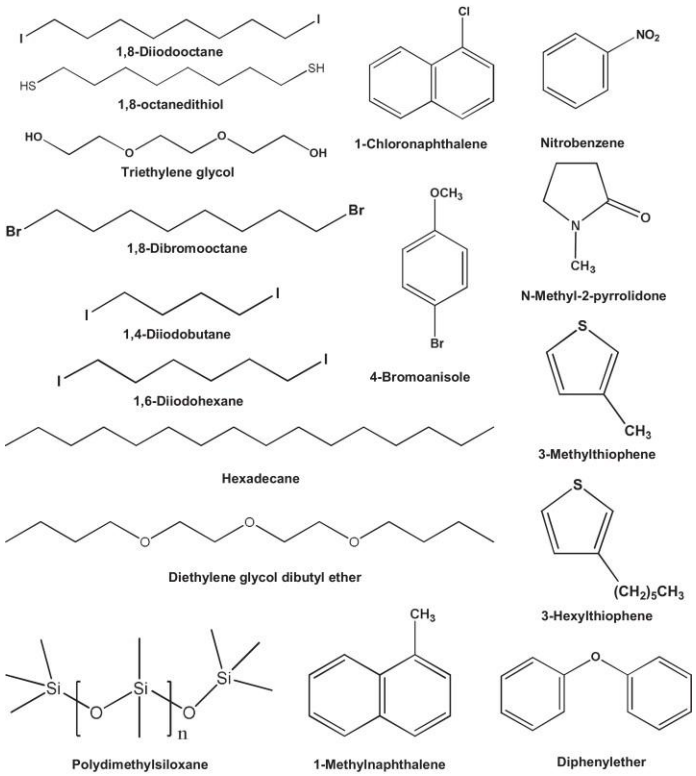

Figure 10. Various solvent additives used to alter BHJ morphology and improve device performance. Adapted from Liao et al.[44] Copyright 2013, Elsevier.

The exact mechanism in which a solvent additive alters film morphology is not universal. Research has found that solvent additives can influence polymer, or discrete conjugated molecules, aggregation, crystallinity, crystal size, lamellar stacking, π-π stacking, domain size, domain interfaces, phase separation gradation, and drying time. Through combinations of in situ UV-vis absorbance/reflection spectroscopy and X-ray scattering, and ex situ morphology measurements such as AFM and TEM, a mechanistic picture can be developed to understand how solvent additives influence phase separation. While some general similarities exist between the vast amount of solvent additives that have been used to enhance the BHJ morphology, there are no key guidelines that can be used to predict whether or not a particular additive will be beneficial to the system. Often, solvent additives influence domain purity and the nucleation density which, in turn, changes the relative degree of crystallization and domain size. The effect of adding additional solvents to the starting solution are discussed in Chapter 4 using the system P(T3-TPD):$PC_{71}BM$ with the additive being DIO, and in Chapter 5 using DT-PDPP2T-TT:$PC_{71}BM$ and the additive *ortho*-dichlorobenzene.

1.3.3. Solvent Vapor Annealing (SVA).

Solvent vapor annealing is the process of exposing the BHJ film to a saturated atmosphere of solvent vapor which then influences morphology development. Typically, this involves taking a cast film and placing it under a dish which contains a high vapor pressure solvent. SVA has been shown to improve the crystallinity of the polymer, or discrete conjugated molecule, which leads to enhanced OPV performance. The choice of solvent vapor is critical as some solvent might re-dissolve the active layer leading to large

scale phase separation, while other solvents enhance the crystallinity of the molecule without the negative large scale phase separation.[45-47]

1.3.4. Thermal Annealing

Thermal annealing is the simple application of heat to the solid film. PCEs can be improved for P3HT:PCBM based OPVs using thermal annealing due to improved polymer crystallinity leading to enhanced charge transport.[48, 49] However, there is a tradeoff when using thermal annealing. While thermal annealing improves efficiencies for some materials it can be detrimental for others. The exposure to heat can lead to large scale phase separation of the polymer and fullerene, and coarsening of the morphology. Long exposure time to heat will crystallize the polymer and fullerene leading to large phase separated domains, reduced donor:acceptor interfacial area, and reduced PCE. Ideally, the point of thermal annealing is to increase polymer crystallinity, and domain purity, while maintaining small domain sizes.

1.3.5. Non-halogenated Solvents.

As research continuously pushes to higher and higher PCE values, this increases the likelihood of one day commercializing this technology on a mass scale. However, there are some drawbacks to this technology, namely the use of toxic halogenated solvents. The vast majority of high performance organic solar cell devices are fabricated from halogenated solvents with halogenated solvent additives. In order for this technology to be commercially viable, the removal of toxic solvents will have to occur. Significant steps have been taken for processing of organic films from non-halogenated solvent.[50, 51]

1.4. Thin Film Deposition Techniques for OPV.

A key advantage of organic electronic devices is the fact they can be solution processed at low temperatures which greatly reduces manufacturing cost compared to their inorganic counterparts. There are numerous ways that thin films can be applied which is the topic of this section. Each method provides some advantages and disadvantages which will be discussed here.

1.4.1. Spin Coating.

Spin coating is the most ubiquitous coating technique used for fabrication of thin films for organic electronic applications owing to the simplicity of the technique. First, the substrate is placed on a vacuum chuck and a solution of the donor and acceptor is placed on the substrate. The substrate spins spreading the solution across the surface and forming a thin film, shown in Figure 11. Spin speeds, acceleration time, and spin time can be adjusted to yield varying film thicknesses and morphologies.[52]

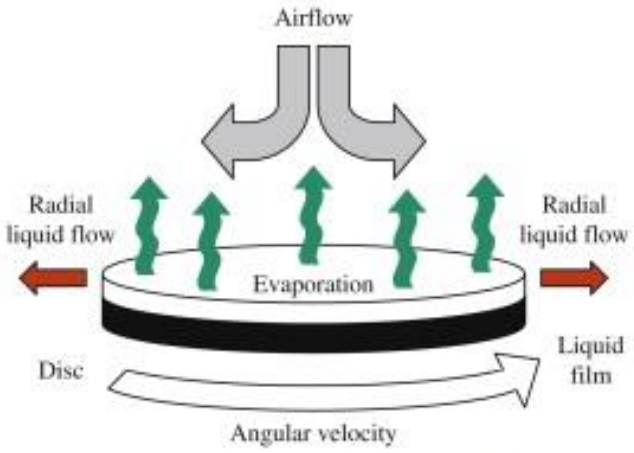

Figure 11. Schematic of spin coating process for thin film formation. Adapted from Krebs et al.[53] Copyright 2009, Elsevier.

The spin coated film thickness can be approximated by Equation 1-4:

$$\text{Equation 1-4: } d = k\omega^{\alpha}$$

Where d is the film thickness, ω is angular velocity, and k and α are constants that are dependent on the physical properties of the polymer, the solvent, substrate, materials/solvent interactions, and interface interactions.[54] Recently, the advancement of "off center" spin coating has been demonstrated to yield highly aligned polymer morphologies for OFET devices. Seminal work done by Yuan et. al. demonstrated that off-center spin coating of 2,7-dioctyl[1]benzothieno[3,2-b][1]benzothiophene (C8-BTBT) blended with polystyrene leads to OFETs with a reported hole mobility's up to 43 $cm^2V^{-1}s^{-1}$.[55] Typically, 100-150 μL of solution are needed to form a full film across a 1 in. x 1 in. substrate. A large portion of solution is lost during the coating process that is unrecoverable making this coating technology unideal for large area device fabrication. Further, while spin coating is suitable for small scale device fabrication it is not a roll-to-roll transferable method, meaning this technology is not amenable to large scale device production.

1.4.2. Blade & Slot Die Coating.

Blade coating, sometimes referred to as doctor-blading, and slot die coating are both shear coating film deposition techniques. Figure 12 shows the operational mechanism of a) blade coating and b) slot die coating. With blade coating the solution is in front of the blade and is pushed by the blade to form a thin film. In slot die coating there is a die head with a channel in which the solution is pushed through the head using a pump to form a thin film. The advantage slot die has over blade coating is the ability to coat well defined

strips with very high material usage efficiency.[56] In both cases a meniscus is formed between the substrate and coater interface in order to generate a film.

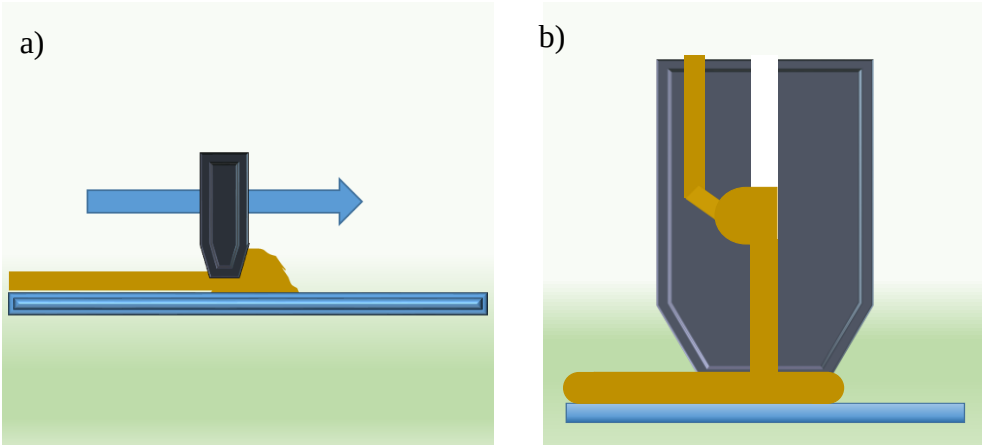

Figure 12. a) Blade coating operation and b) slot die coating operation.

For blade coating the dry film thickness can be estimated by Equation 1-5:

$$\text{Equation 1-5: } d = 0.5\left(g\ \frac{c}{\rho}\right)$$

Where d is the film thickness, g is the gap between the blade and substrate, c is the concentration, and ρ is the solid state film density.[53] It should be noted that this equation does not account for coating speed which can significantly impact film thickness. At low speed this equation accurately approximates final film thickness, however, at higher coating speeds this equation will not suffice. Coating speed can have a significant impact on the drying kinetics and polymer, or discrete molecule, alignment which will ultimately result in differing morphologies and device performances. Shaw et al.[57] studied the effect that coating speed has on film thickness, dichroic ratio, morphology and OFET

performance using the material poly[2,5-bis(2-hexyldecyl)-2,3,5,6-tetrahydro-3,6-dioxopyrrolo[3,4-c]pyrrole-1,4-diylc-alt-[2,2':5',2''-terthiophene]-5,5''-diyl] (PDPP3T). The top of Figure 13 shows film thickness as a function of coating speed. In this figure, two drying regimes are identified in which the effect of coating-speed on film thickness differs. During the evaporative regime (red line) the deposition of the solution and solidification occur on a similar time scale meaning the fluid flow has a direct influence on the film formation. As a result, as coating speed increases the film thickness decreases. In the Landau-Levich regime (purple line) the coating occurs so fast that a wet film is left behind meaning morphology is controlled by the drying rate which is influenced by solvent vapor pressure, temperature, and air flow. Thus, as blade coating speed increases film thickness also increases. The bottom of Figure 13 shows the effect that blade coating speed has on dichroic ratio of PDPP3T. The dichroic ratio, which is simply the ratio of the polarized UV-vis absorption peak intensity of a film taken at 0^{o} and 90^{o} relative to the coating direction, reaches a maximum at 0.2 mm/s indicating that there is a high degree of polymer alignment in the evaporative regime at that coating speed. For faster coatings, indicating that drying dynamics will be governed by the Landau-Levich regime, the dichroic ratio is very small which is expected because shear forces have little influence on the film formation properties in this regime. Typically, coatings for research scale organic electronic devices occur at speeds between 10 mm/s – 50 mm/s, indicating that morphology is often influenced by solvent evaporation and not shear force.

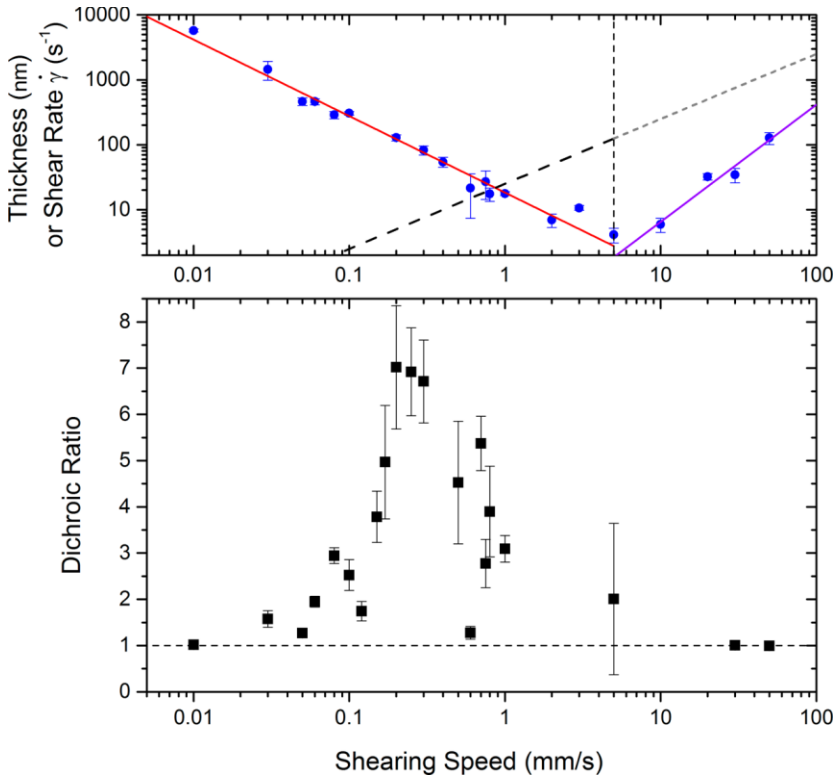

Figure 13. Top, film thickness as a function of coating speed. The red line indicates the evaporative regime, while the purple line is for the Landau-Levich regime. Bottom, the dichroic ratio of PDPP3T as a function of shearing speed. A maximum is reached at 0.2 mm/s. Adapted with permission from reference [57]. Copyright 2016, American Chemical Society.

There are two key advantages that blade, and slot die, coating have over spin coating: 1. Very efficient use of solution. While spin coating takes ca. 100 μL of solution, blade coating takes only ca. 20-50 μL of solution to coat a 1" x 1" substrate. Upon optimization there can be effectively no waste of solution using blade coating, whereas, with spin coating, a large amount of solution is lost due to centrifugal force. 2. Blade, and slot die, coating are roll-to-roll compatible, whereas spin coating is not. Large area devices

can be produced rapidly on roll-to-roll (RTR) equipment which would reduce the cost of device fabrication.

1.4.3. Spray Coating.

Spray coating is a RTR compatible technology that can be uses to fabricate thin films for organic electronic devices. The mechanism of spray coating involves a pressurized carrier gas, typically N_2 or Ar, that carries droplets of solution to a substrate. For smooth film formation, the droplets need to hit the substrate surface and coalesce. Typically, spray coating produces rough surface morphologies composed of dried droplets. Figure 14 shows an a) optical microscopy image, and b) AFM height image, of a spray coated P3HT:PCBM film. It is apparent that the film is rough which will lead to increases in resistances which decrease FF and device performance for OPVs.[58]

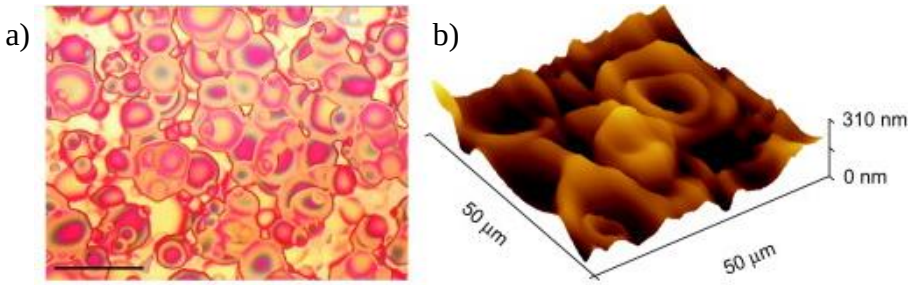

Figure 14. a) Optical microscopy image of spray coated P3HT:PCBM film. b) AFM height image of P3HT:PCBM film showing how rough surfaces are created through spray coating. Adapted from Girotto et al.[59] Copyright 2009, Elsevier.

While work in spray coating of various layers for OPV devices has been explored, it is not a common method of film deposition because of the difficulty of producing smooth, uniform, thin films.[60, 61]

1.4.4. Ink Jet Printing.

Ink jet printing allows for patterning of substrates through the ejection of individual droplets of solution from a nozzle. While reports exist on ink jet printed organic solar cells it is typically not a preferred method of deposition because it requires complex solvent mixtures using high boiling point solvents in order to minimize the 'coffee ring' effect and produce smooth films.[62, 63] Further, it is difficult to produce large scale devices using ink-jet printing because each printed dot would have to coalesce together in order to form a unified film. The complex drying dynamics of ink jet printing makes production of smooth thin films a difficult task.

1.5. Review of *In Situ* Morphology Studies.

The importance of the BHJ phase separated morphology to the organic solar cell performance cannot be overstated. Over the past several years' numerous groups have used in situ measurements to gain insight into how changing processing parameters affects the phase separated morphology. *In situ* measurements of thin film formation have shed light onto the mechanism of BHJ morphology formation, and allows us to better understand how solvent additives, thermal annealing, co-solvents, and different coating techniques, can produce varying degrees of phase separation. This section is a review of the literature concerning in situ morphology development for organic solar cell thin film active layers.

1.5.1. Review of P3HT In Situ Studies.

Naturally, P3HT morphology evolution has been extensively studied using *in situ* measurements as it is a benchmark polymer for many applications. Sanyal et al.[64] studied the effect of substrate temperature, ranging from 10 ºC to 80 ºC, on film morphology of blade coated P3HT:$PC_{61}BM$ cast from *ortho*-dichlorobenzene. Using *in situ* GIWAXS and reflection spectroscopy they showed that lower drying temperature leads to enhanced π-π stacking, a broader crystal orientation distribution, and a finer interpenetrating network, suggesting that low temperature processing of P3HT:$PC_{61}BM$ will produce an enhanced morphology for organic solar cells. Schmidt-Hansberg et al.[65] studied the morphology evolution of P3HT:$PC_{61}BM$ cast from *ortho*-dichlorobenzene and chlorobenzene (CB) with the solvent additive cyclohexanone (CHN). They show, using *in situ* GIXD and reflectometry, when P3HT:$PC_{61}BM$ is cast from dichlorobenzene the solvent evaporates increasing the solid mass fraction (x_s). Phase separation is dominated by polymer nucleation, which occurs at a x_s = 5-14%, and crystallization (x_s >14%) which is preferentially edge-on indicating a heterogeneous nucleation either at the liquid-substrate or liquid-air interface which is shown in Figure 15. Further, the effect of adding the poor solvent CHN was shown to induce polymer aggregation in solution leading to a disperse set of crystal orientations suggesting that nucleation and growth was occurring at the surface and in the bulk of the film. This indicates that CHN induces heterogeneous and homogeneous nucleation to occur during solidification.

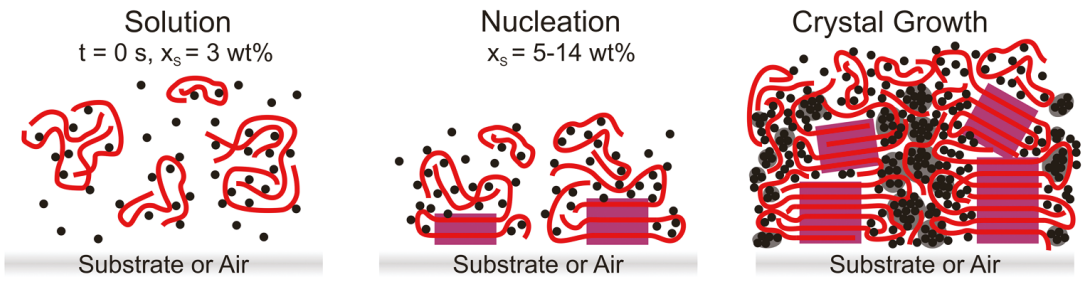

Figure 15. Morphological evolution of P3HT:$PC_{61}BM$ cast from dichlorobenzene. Adapted with permission from reference [65]. Copyright 2011, American Chemical Society.

Solvent additive effects have been studied extensively due to their ability to lead to more optimum morphologies and improved device efficiencies. Richter and co-workers have studied the effect of the solvent additives 1-chloronaphthalene (CN) and 1,8-octanedithiol (ODT), with the host solvent being chlorobenzene (CB), on the film formation of P3HT:$PC_{61}BM$ using *in situ* GIXD, absorption, reflection, and ellipsometry spectroscopy. [66, 67] Their results, summarized in Figure 16, show when P3HT:$PC_{61}BM$ is processed from CB, polymer order and domain formation occur simultaneously toward the end of CB evaporation. When the additive CN is used, local and long range order co-evolve toward the end of CB evaporation, leaving a CN wet film. The CN plasticizes the mixed amorphous P3HT and PCBM phase. As the CN slowly evaporates additional P3HT is crystallized. For the additive ODT, when CB evaporates there is an initial crystallization of P3HT leaving three phases, 1) crystalline P3HT, 2) an ODT solution of PCBM, and 3) a mixed P3HT:PCBM phase. As ODT evaporates the PCBM moves into the mixed P3HT:PCBM amorphous phase leaving a final film composed of crystalline P3HT phase and an amorphous P3HT:PCBM mixed phase.

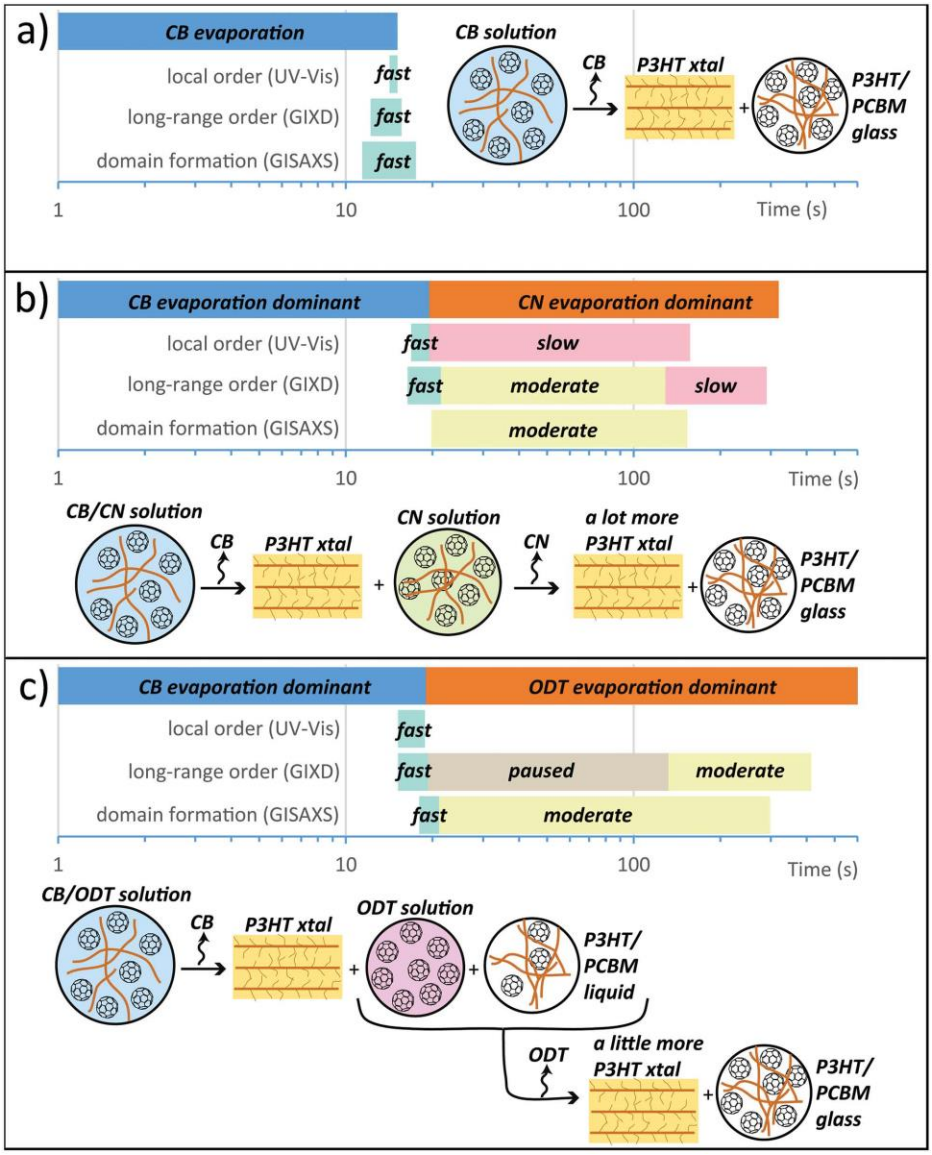

Figure 16. Diagram of the morphological evolution of P3HT:PCBM blade coated films when processed from chlorobenzene (CB), chlorobenzene with the additive 1-chloronapthalene (CN), or the additive 1,8-octanedithiol. Reproduced from Richter et al.[66] Copyright 2015, Wiley-VCH.

While these are not the only pieces of work to study morphology evolution in real time using in situ measurement techniques, they provide a glimpse into the complexity of how

phase separated morphology is developed, and how it changes with different processing conditions. In addition to the work presented here, others have studied the effect of phase separation of P3HT:PCBM cast from a single solvent [68-71], thermal annealing [72], solvent additives [73, 74], solvent mixtures[75], and phase separation of polymer blends, P3HT:N2200.[76]

1.5.2. Review of non-P3HT In Situ Studies

1.5.2.1. Discrete Conjugated Molecules.

Perez et al.[77] examined the morphological evolution of 7,7′-(4,4-bis(2-ethylhexyl)-4H-silolo[3,2-b:4,5-b′]dithiophene-2,6-diyl)bis(6-fluoro-4-(5′-hexyl-[2,2′-bithiophen]-5-yl)benzo[c][1,2,5] thiadiazole) (p-DTS(FBTTh$_2$)$_2$):PC$_{71}$BM spin coated from chlorobenzene (CB), or CB with DIO as an additive. Their in situ GIXD reveal that the morphology p-DTS(FBTTh$_2$)$_2$:PC$_{71}$BM, when cast from CB, rapidly evolves due to fast evaporation of CB, which leaves behind a kinetically trapped morphology. When DIO is present, the slow evaporation of the additive leads to a metastable state, different from the final film morphology, that allows for enhanced crystallization of the molecule with improved order. Recently, Engmann et. al.[78] has studied the morphology evolution of discrete conjugated molecule p-DTS(FBTTh$_2$)$_2$ mixed with PC$_{71}$BM cast from chlorobenzene (CB) with varying amounts of the solvent additive DIO, which has been shown to improve the PCE. Using in situ GIXD, and reflectometry, on blade coated samples it was found that increasing the DIO content decreases nucleation density leading to larger crystal size. The use of in situ, and ex-situ, morphology characterization showed that DIO acts as both a solvent and a plasticizer for p-DTS(FBTTh$_2$)$_2$ decreasing nucleation density and increasing p-DTS(FBTTh$_2$)$_2$ crystallization upon evaporation of the additive.[78]

Engmann et. al.[45] also studied the impact of the solvent used for SVA on the discrete conjugated molecule benzodithiophene terthiophene rhodanine (BTR) mixed with $PC_{71}BM$. When BTR:$PC_{71}BM$ is exposed to CF (good solvent) vapor it dissolves small crystallites present in the BHJ film. As the CF vapor is removed the remaining large crystallites act as nucleation sites for crystal growth. CF vapor ultimately reduces nucleation density leading to increases in crystallization of BTR and larger phase separated domains. Using THF (moderate solvent) vapor for SVA allows for increased mobility of BTR without dissolving small crystallites. This leads to an increase in nucleation density, BTR crystallinity, and phase separated domains on the order of 30 nm, which is why THF shows improved PCE over CF for SVA. In both cases presented here the control of nucleation density is critical to the formation of optimal domains and crystallinity. The use of solvent additives and SVA controls the nucleation density thereby leading to reduced domain sizes composed of crystalline small molecules with higher phase purity.

1.5.2.2. Non-P3HT polymers.

Other polymer:fullerene blends outside of P3HT:PCBM have been studied using in situ measurements to elucidate the influence of processing on phase separation. Polymers based on the acceptor unit diketopyrrolopyrrole (DPP) coupled to thiophenes have been studied using spin coating, drop casting, [79, 80], and slot-die coating [81], cast from CF or CF:DCB solvent mixture. van Franeker et. al.[79] examined the phase separation using in-situ absorption, reflection, and light scattering, of diketopyrrolopyrrole–quinquethiophene:$PC_{71}BM$ (PDPP5T:$PC_{71}BM$) cast using spin coating from CF or a mixture of CF:DCB. Figure 17 shows the influence of solvent type on phase separation of PDPP5T:$PC_{71}BM$ during spin coating. When the polymer:fullerene blend is cast from CF

there is a L-L phase separation that occurs prior to polymer aggregation leading to large scale phase separation of the polymer and fullerene. The polymer:fullerene blend phase separation is dominated by a L-L transition leading to a large scale (ca. 300 nm -500 nm) phase separated morphology. When PDPP5T:$PC_{71}BM$ is processed using co-solvents, polymer aggregation occurs due to evaporation of CF leading to a reduction in solvent quality. This polymer aggregation during solidification serves as nucleation sites for crystallization to occur. The addition of DCB or DIO increases the nucleation density, allowing for reduced domain sizes seen in the solid state morphology, and ultimately improved OPV device efficiencies.[79] This example demonstrates the importance of phase separation being dominated by either a L-L transition which leads to large scale phase separation, or nucleation and growth, which leads to small scale phase separated domains.

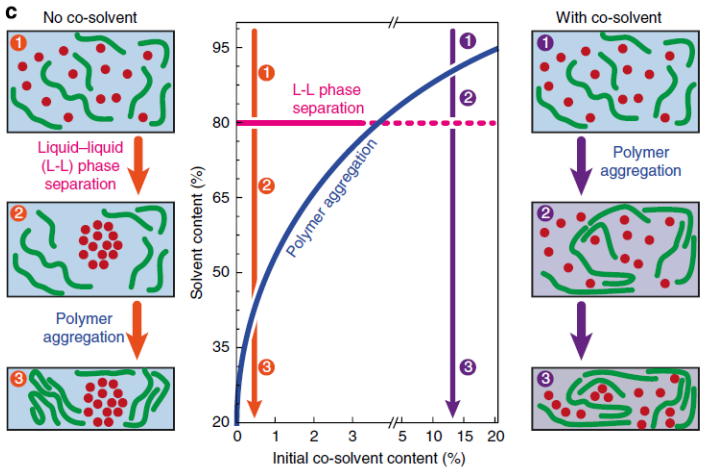

Figure 17. Phase diagram of PDPP5T:$PC_{71}BM$ processed from CF or CF:DCB showing with no co-solvent the morphology is determined by L-L phase separation, whereas, with co-solvent processing polymer aggregation occurs due to a reduction in solvent quality leading to reduced domain sizes. Reproduced from van Franeker et al.[79] Copyright 2015, Nature Publishing Group.

Buss et. al.[82] has investigated the morphology evolution of PCPDTBT:$PC_{71}BM$ cast with, and without, the solvent additive ODT, using in situ GIXD and reflectometry on blade coated films, finding that ODT prolongs polymer crystallization and delays $PC_{71}BM$ aggregation. Ro et al.[42] have studied the effect of the solvent additive DIO, and the effect of processing type (spin coating, blade coating, and slot die coating), on high performance polymer PCE-11 mixed with $PC_{71}BM$. A combination of ex-situ and in situ GIXD, absorption, and reflectometry, on blade coated films, show that processing type leads to differences in solidification and morphology, however, yield similar device performance for OPVs. Interestingly, Ro et al.[42] found that processing method (spin, blade, or slot die coating) yield different crystal orientations and characteristic phase separated length scales, yet their devices show similar performance, implying multiple morphologies can produce high performance OPVs. Further, Kassar et. al.[83] studied the intercalation of varying types of fullerenes using pBTTT. A combination of in situ GIWAXS, and GISAXS, on blade coated films revealed fullerene intercalation into the polymer crystal is dependent on the fullerene size.

The combination of in situ studies on multiple polymer systems, and discrete conjugated molecules, using blade coating, spin coating, and slot die coating, have provide a wealth of information as to the nature of the role that solvent additives, thermal annealing, SVA, and co-solvent processing, play on influencing BHJ phase separation that ultimately leads to improved OPV performance. In many cases the addition of an additive/SVA/thermal annealing, and co-solvents, alters the nucleation density and phase purity, leading one to speculate that what's important is not the additive or process, rather, control of nucleation sites and phase purity.

1.6. Thesis of this Dissertation

The information contained in this dissertation focuses on the influence of processing polymer:fullerene blends from single solvents, solvent systems with additives, and co-solvents, on the thin film phase separated morphology, and how this final morphology relates to photovoltaic performance. Through a combination of solution characterization, ex-situ, and in situ, thin film morphology characterization, I seek to understand the dynamics of phase separation. Chapter 1 details background information concerning polymer based photovoltaics, their operating principles, morphology, coating processes, and a brief review of the field of real time structural evolution studies on conjugated systems. The information found in Chapter 2 serves as an experimental guide of the techniques used for this work. Chapter 3 focuses on the polymer:fullerene system P3HT:PCBM and how processing from varying solvents impacts film solidification and device performance. Chapter 4 explores the similarities and differences in morphology and OPV performance of blade coated and spin coated BHJ thin films for OPVs using the polymer:fullerene system P(T3-TPD):$PC_{71}BM$. Also found in Chapter 4 is the influence the solvent additive DIO has on film morphology and polymer:fullerene phase separation. Chapter 5 explores the impact that single solvent and co-solvent processing has on the phase separation, and the OPV performance, of polymer:fullerene system DT-PDPP2T-TT:$PC_{71}BM$. Chapter 6 explores the field of OPV in context of the photovoltaics industry as a whole. The appendix examines a novel discrete conjugated molecule that showed optimum performance at low donor:acceptor ratio.

CHAPTER 2. EXPERIMENTAL METHODS AND CHARACTERIZATION TECHNIQUES

Introduction

This section, Chapter 2, deals with the experimental details, theory, and data analysis, used to conduct the work presented in this dissertation.

2.1. Construction of custom blade coater.

For construction, schematic, and parts, of the blade coating apparatus used for this work see Appendix 1. Design, parts, and construction of the coater is based off of NIST design.[84]

2.2. Polymer Solution Characterizations.

2.2.1 Solubility.

Polymer solubility is difficult to accurately measure. In order to gain insight into solubility concentrated solutions of neat polymer were dissolved in the host solvent used for device fabrication. For example, if solutions of polymer:fullerene were cast from chloroform, such as P(T3-TPD) presented in Chapter 4, then solubility of the polymer was determined in chloroform. Once a concentrated solution is made it is filtered through a glass syringe using a 0.45 μm PTFE filter. For P3HT, and P(T3-TPD), solutions were filtered at room temperature giving the room temperature solubility of the polymer. The solution was filtered into an amber glass vial, afterwards, a 100 μL aliquot of the filtered solution was placed on a pre-weighed glass slide and heated at 50 ºC for 30 minutes in an Ar filled glovebox on an aluminum top hot plate to remove the solvent. Samples containing

high boiling point solvents, such as DIO, were heated and then placed under vacuum at 10^{-5} mbar for 1 hour to ensure that the solvent is removed. The glass slides with the polymer deposited on them were weighed and the solubility was back calculated using the weight difference.

2.2.2. Solution UV-vis Absorption.

To obtain quantitative information of polymer solutions, and thin films, such as thermochromism, aggregation, and absorption spectra, a Varian Cary 5000 Scan UV-vis-NIR spectrophotometer was used. For solution spectra a quartz crystal cell with a 1 cm path length was used. The spectral range was 300 nm – 900 nm. Thermochromic UV-vis absorbance was conducted using a Cary 5E UV-vis-NIR spectrophotometer with Scan software. Solutions were placed in a sealed quartz crystal cell with a 1 cm path length. The sample was placed in a heating element attached to the spectrophotometer which was controlled by Quantum Northwest TC125 temperature controller. UV-vis absorbance measurements were taken every 5 ºC starting at 20 ºC and going up to 50 ºC. Data was later processed using Origin Pro.

2.3. Thin Film Characterization Techniques.

The use of static thin film characterization allows for a deep understanding of film morphology, and its role in device performance. The techniques discussed here probe morphology from angstroms to micrometers in length scale in order to provide a complete picture of film structure.

2.3.1. Thin film UV-vis/Polarized UV-vis.

Thin film UV-vis was performed with a Varian Cary 5000 Scan UV-vis-NIR spectrophotometer. Thin films were processed in the same manner as their application, therefore, if a conventional solar cell was to be built, then the thin film UV-vis absorbance would be conducted on glass/ITO/PEDOT:PSS with glass/ITO/PEDOT:PSS used as a blank. Likewise, if an inverted OPV device was the application of the material then thin film UV-vis would be conducted on glass/ITO/ZnO with glass/ITO/ZnO as a blank. All films were either spin coated or blade coated. For specifics on film deposition see Chapter 3 for P3HT, Chapter 4 for P(T3-TPD), Chapter 5 for DT-PDPP2T-TT, and Appendix A2 for the discrete molecules 2EH-CDT($FBTTh_2$)$_2$ and 5EN-CDT($FBTTh_2$)$_2$. The band gap is estimated from the film UV-vis absorbance using Equation 2-1:

$$\text{Equation 2-1: } E_{gap} = \frac{1240\ nm}{\lambda_{onset}}$$

Where E_{gap} is the energy gap and λ_{onset} is the onset of optical absorption.

Polarized UV-vis spectroscopy was conducted to observe if there was alignment of the polymer due to the shear force of blade coating. A polarizer was set to one position and a UV-vis absorption spectra was taken, the polarizer is then rotated 90º and another UV-vis spectra is taken. If alignment was present there would be a change in optical absorption, if the local polymer order was randomly oriented the absorption spectra would overlap. An example of polarized UV-vis is given in Figure 18 where aligned MEH-PPV shows two different absorbance's due to polymer chain alignment. Data for thin film UV-vis absorption was worked up using Origin Pro.

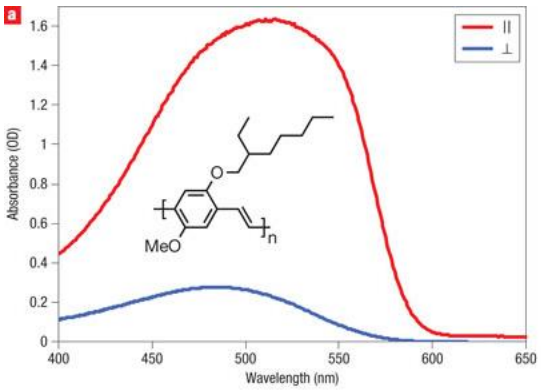

Figure 18. Aligned MEH-PPV shows two different UV-spectra under polarized light. Adapted from Martini et al.[85] Copyright 2007, Nature Publishing Group.

2.3.2. Atomic Force Microscopy (AFM).

Atomic force microscopy is a surface imaging technique that involves bringing a sharp probe in close proximity with the surface of the sample to gain qualitative and quantitative information on the topology of the system. There are two typical modes used to probe the surface which are contact mode and tapping mode. Figure 19 demonstrates the basic working principal of AFM. There is a laser focused on the top of a cantilever with a sharp tip. As the tip comes into close proximity of the sample the long range attractive forces (van der Waals) bring the tip close to the sample causing a change in the direction of the laser beam. As the tip comes very close to the sample it experiences strong short range repulsion forces due to electron-electron Coulomb interactions and the Pauli exclusion principal. These repulsion forces cause the cantilever to move away from the sample, which deflects the laser signal and is recorded. The long range attraction forces and short range repulsion forces cause a change in the tip oscillation amplitude. These amplitude oscillation changes are observed and recorded using a position sensitive photodetector, in which the signal is sent to the controller to adjust the height of the scanner

head to maintain a set oscillation amplitude. Surface topology images are generated through the changes in oscillation amplitude due the tip interactions with the sample.

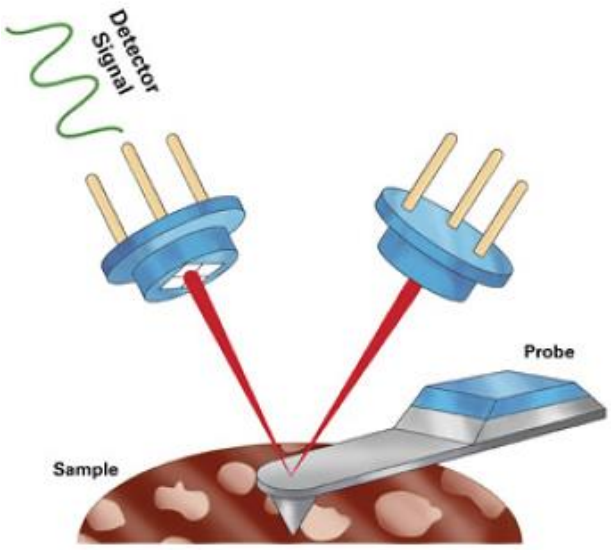

Figure 19. Illustration of the working principal of an AFM. Figure adapted from Bruker (*www.bruker.com*)

Phase imaging, a secondary imaging technique of tapping mode, allows for mapping of surfaces based on material differences such as elasticity, adhesion, and friction, which will cause a phase lag. Phase imaging examines the phase lag between the signal that drives the cantilever and the output signal of the cantilever which is dependent on the mechanical properties of the surface. The phase signal changes when the tip moves to another part of the sample with a different surface composition. The advantage of a phase image is that it can show differences in film morphology that might not be apparent in the height images, for example, Figure 20 shows the height and phase image of diblock co-polymer P3HT-b-PFO.[86] Comparing the height and phase images in Figure 20, it is clear that the phase image shows distinct phase separation in the solid state from the block co-polymer whereas the height image does not. Figure 20 demonstrates that additional

information about phase separation can be obtained from the phase image that is not clear in a height image. For the work presented here, phase images were collected simultaneously with height images using tapping mode.

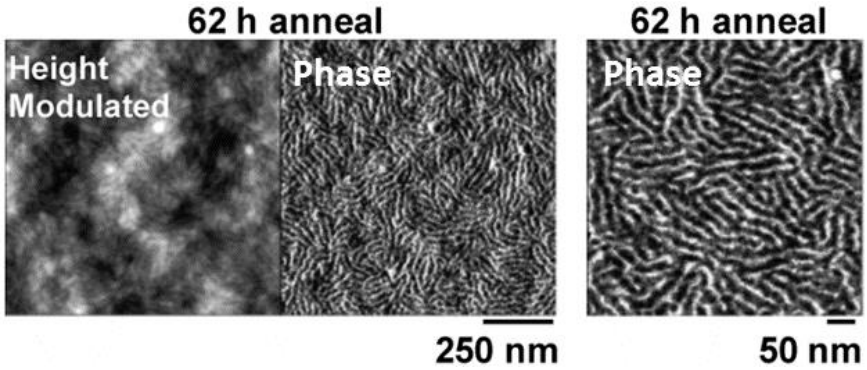

Figure 20. AFM height and phase image diblock co-polymer P3HT-b-PFO. Adapted from Verduzco et al.[86]

All AFM images were conducted at Georgia Tech using a Bruker Dimensions Icon with ScanAsyst. Height and phase images were generated using tapping mode experiment in which the cantilever oscillates at a particular frequency (150 Hz) and "taps" the surface of the sample to generate a topographical image. Bruker AFM tips, model:TAP150, (Part: MPP-12100-10) with a frequency between 150-200 kHz and a spring constant of 5 N/m were used for tapping mode experiments. Tapping mode is used instead of contact mode because it is less destructive of a measurement. Contact mode AFM has the problem of lateral forces between the cantilever tip and the sample, whereas in tapping mode the tip is briefly in contact with the surface.

2.3.3. Profilometry.

A Bruker Dektak XT profilometer was used to gain information on film thicknesses. A profilometer measures a 3D surface profile, surface roughness, and film thickness, using contact or non-contact mode. A Bruker Dektak XT contact mode profilometer was used with a 12.5 μm radius diamond tipped stylus with a 3 mg force on the sample. The height range was set to 6.5 μm to ensure the most accurate measurement of film thickness. Samples were prepared by scratching the film to be studied with a razor blade, or sharp tweezers, to create a sharp interface between the film and the substrate. The profilometer stylist moves unidirectionally over the film and substrate to creating an analog signal which is converted into a digital signal that is analyzed using the Vision 64 software. The speed of the measurement was kept constant, and distance the stylist traveled ranged from 200 μm – 800 μm. The 1D line profile of the substrate was leveled to 0 and the film thickness was measured using the Vision 64 software. For film thickness measurements 3-5 scans were taken across different areas of the film, and the film thicknesses were averaged in order to gain insight into film uniformity.

2.3.4. Grazing Incidence Wide Angle X-ray Scattering (GIWAXS).

GIWAXS is an X-ray scattering technique that probes the bulk film to gain quantitative information on crystal size, distribution, orientation, and spacing. The need for a grazing incidence geometry as oppose to a transmission measurement is due the low crystallinity of the films measured, the film thicknesses being on the order of < 500 μm, and the light elements (C, H, S) found in the sample. Figure 21 shows the experimental setup for both GIWAXS, and GISAXS which is discussed in section 2.3.5. For GIWAXS,

the area detector is placed anywhere from 150 mm to 400 mm away from the sample, whereas for GISAXS the detector distance is 3 to 4 meters, pictured in Figure 21.

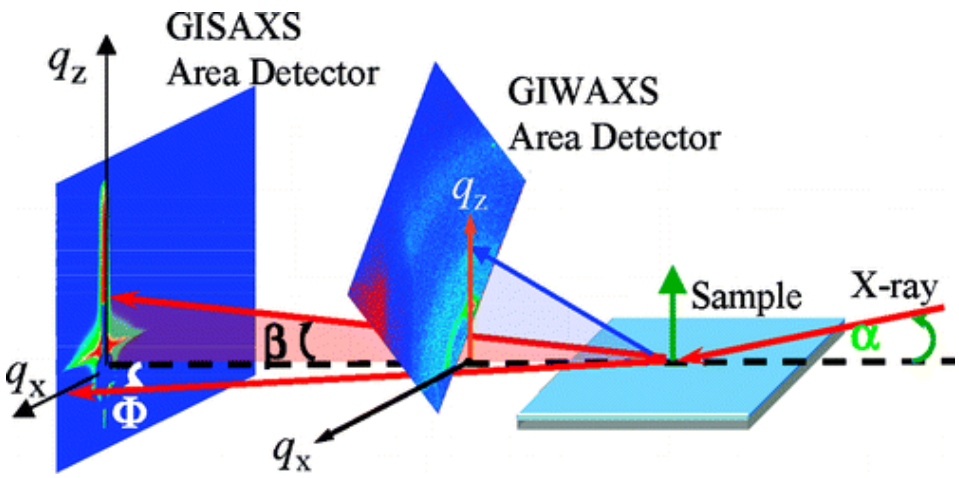

Figure 21. Experimental setup of GIWAXS and GISAXS in which a X-ray hits the sample at some angle (α) and the scattered angles β and Φ are the out of plane (q_z) and in plane (q_x) directions. Reprinted with permission from reference [87]. Copyright 2011, American Chemical Society.

The angle of incidence (α_i) of the X-ray onto the sample is important. At an α_i less than the critical angle (α_c), which is material dependent and determined by the mean refractive index, only information about the first couple of nanometers of the surface of the sample can be obtained. When the α_i is greater than the α_c of the material but less than the α_c of the substrate then quantitative information about the bulk sample can be obtained. When the α_i is greater than the α_c of the substrate then information about the material and the substrate can be obtained. Once the measurement is taken a 2D image is produced as shown in Figure 22. This missing wedge in the q_z direction shown in Figure 22 is a consequence of using a planar area detector which is intersecting the Ewald sphere of diffraction. This missing

wedge is removed during post processing of a raw 2D image. From this 2D image 1D line cuts are taken in the q_z and q_{xy} directions in order to calculate lamellar stacking distances, π-π stacking distances, the crystal coherence length, and gain insight into the orientation of crystals.

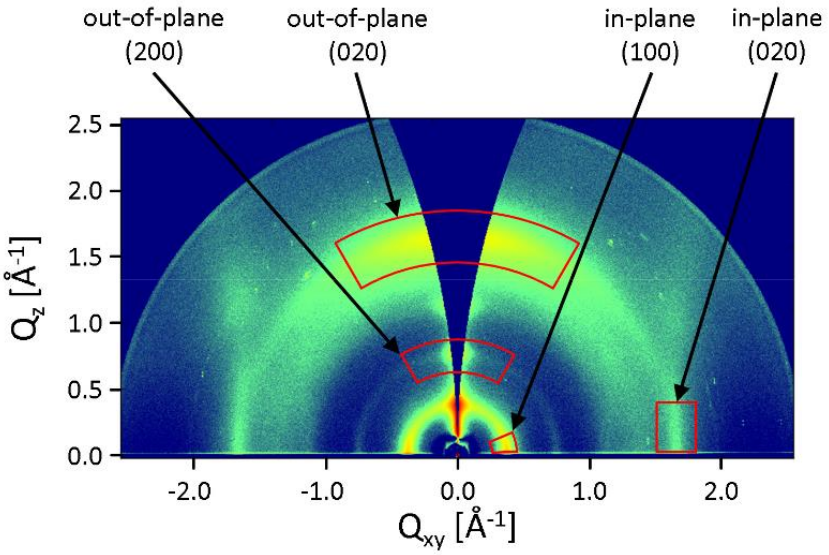

Figure 22. Two dimensional GIWAXS image of P3HT. Reprinted with permission from reference [88]. Copyright 2012, American Chemical Society.

Figure 23 demonstrates some basic qualitative information that can be obtained about the crystal structure from the 2D GIWAXS image. If there is perfect vertical lamellar stacking this will show up as points with strong intensity in the q_z direction, Figure 23 a). If there is both vertical and horizontal lamellar stacking, reflections with strong intensity in the q_z and q_{xy} directions will be present as in Figure 23 b). If there is vertical lamellar stacking that is disordered, this will show as broadened intensity in the q_z direction as seen in Figure 23 c). The last case, Figure 23 d), is if there is crystallinity but it shows no preferential order, or is isotropic. Isotropic scattering is presented as rings with similar intensity in all directions.

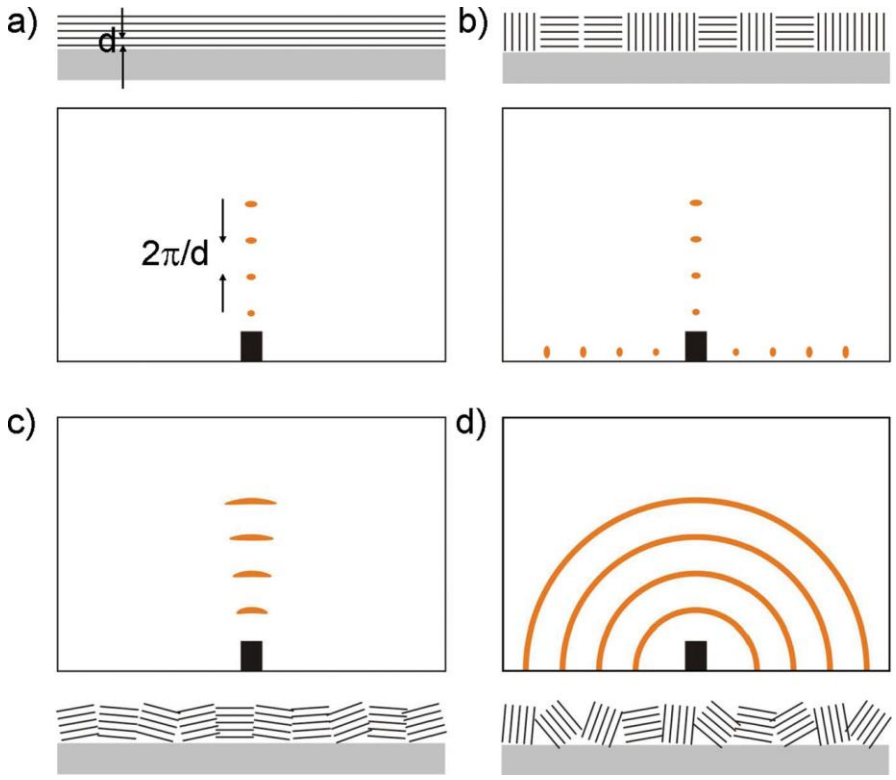

Figure 23. Example a) vertical lamellar stacking, b) vertical and horizontal lamellar stacking, c) disordered vertical lamellar stacking, and d) completely disordered crystallites. Reproduced from Müller-Buschbaum.[89] Copyright 2014, Wiley-VCH.

The 2D data can be reduced into 1D line cuts in which spacing, orientation, and relative degree of crystallinity (rDoC) can be obtained. Bragg's equation, Equation 2-2, is used to determine average spacing between particles.

$$\text{Equation 2-2: } d = \frac{2\pi}{q}$$

Where d is the average spacing between particles and $q = \frac{4\pi\sin(\theta)}{\lambda}$ with 2θ being the angle of incidence of the X-ray onto the sample and λ being the wavelength of the X-ray. The crystal coherence length (CCL) is the average size of crystal grains obtained from the first order (100) peak. Equation 2-3 is used to quantify the size of the crystal coherence length.

Equation 2-3: $L_c = \frac{2\pi K}{\Delta q}$

Where L_c is the crystal length, K is the shape factor with a value between 0.8-1 (0.9 is typically used), and Δq is the FWHM of the peak.[90]

Information of crystallite orientation and the relative degree of crystallinity (rDoC) is derived from a pole figure. A pole figure is a plot of the distributions of orientations of crystallites for a specific set of lattice planes. Figure 24 demonstrates how a 1D pole figure is obtained from a 2D GIWAXS image. Figure 24 a) shows a 2D GIWAXS image, with labeled reflections, of neat P(T3-TPD) which is integrated along chi on the (100) reflection, also referred to as a cake segment. The cake segment is converted to a polar angle (χ^o) plot, Figure 24 b), which can then be converted to a 1D pole figure, which is shown in Figure 24 c), using WxDiff [91] or IGOR Pro with Nika.[92] The pole figure shown in Figure 24 c) describes the distribution of crystallites in neat P(T3-TPD) spin coated from chloroform with respect to substrate normal. Scattering intensity centered around $\chi = 0^o$ arises from an edge on crystal orientation, while scattering intensity close to $\chi = \pm 90^o$ is due to face on crystal orientation. The scattering intensity found between $\chi = -90^o$ and $\chi = 90^o$ is due to isotropic crystal orientation, and in Figure 24 c) presents itself as an isotropic pedestal.

a)

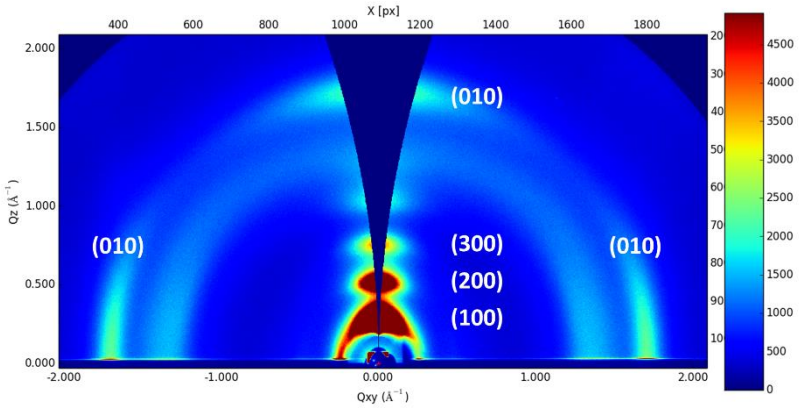

b)

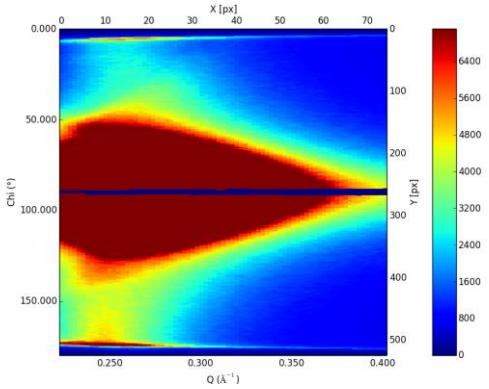

c)

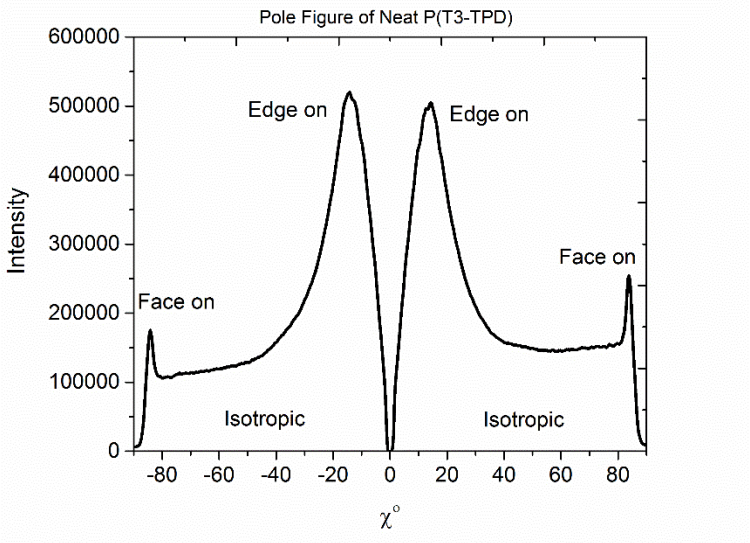

Figure 24. Demonstration of pole figure analysis. a) corrected 2D GIWAXS image of neat P(T3-TPD) cast from chloroform, with labeled reflections. b) χ^{o} vs Q image obtained from the (100) reflection. c) 1D pole figure of neat P(T3-TPD) cast from chloroform. Labels aid in identifying crystal orientation.

Once the appropriate geometric corrections have been applied to the pole figure, and the intensity has been normalized by the film thickness, or film volume, a rDoC can be obtained from the integrated 1D pole figure using Equation 2-4.[93] The integrated area must be weighted by a correction factor of sin(χ).[94]

Equation 2-4. $rDoC \propto \int_{\chi}^{\frac{\pi}{2}} \sin(\chi)\, I(\chi) d\chi$

GIWAXS experiments were conducted at SSRL on beamline 11-3 or ALS on beamline 7.3.3. Samples were prepared on p-type Si (University Wafer product ID# 1317). Films were either coated directly onto cleaned Si wafer or onto PEDOT:PSS (Al 4083)/Si. For films coated on PEDOT:PSS/Si substrates, PEDOT:PSS was prepared in the same manner as in solar cell devices, see section 2.5.1. The α_i was between 0.12º and 0.14º and the beam energy we set at 12.7 keV with a detector distance of 150mm - 250 mm. Measurement times varied between 150 seconds to 500 seconds for ex-situ samples. Data was collected using a MAR 365 detector or a MAR ccd detector. SSRL samples were run in a helium chamber, while samples run at ALS were done in ambient air. 2D data was worked up with WxDiff ver. 1.2 or IGOR Pro with Nika and Irena packages.

2.3.5. Grazing Incidence Small Angle X-ray Scattering (GISAXS).

GISAXS is an X-ray scattering technique used to probe large scale domain morphology. It is useful for understating domain sizes, domain interfaces, shape, phase purity, orientation and degree of mixing between the components on the order of approximately tens of nanometers to a couple of hundred nanometers. The experimental setup for GISAXS is similar to that of GIWAXS with the exception of the detector distance

as seen in Figure 21. Like GIWAXS if the α_i is greater than the α_c then there is high X-ray penetration depth and an average structure over the entire depth of the film can be obtained. Likewise, if α_i is less than α_c then only the first few nanometers of the surface of the film will be probed. For BHJ systems it is useful to perform a Kratky plot ($I(q)q^2$ vs q) in order to derive a characteristic length scale for the system, as well as, phase purity.[78] Figure 25 shows a Kratky plot for tightly crosslinked polystyrene nanoparticles.[95] The shape of the plot is indicative of the shape of the scattering particles present in the system. Peaks indicate particle like behavior, or mass fractal, while a plateau is for Gaussian chain, and a linear increasing plot is representative of a rigid rod. Often, for BHJ system a peak is observed, indicating particle like behavior, in which the peak maximum determines the characteristic length scale of the phase separated morphology.

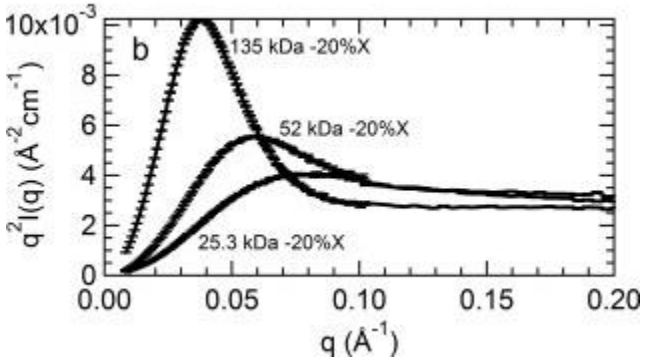

Figure 25. Example of Kratky plot ($I(q)q^2$ vs q) showing particle like and Gaussian like behavior for tightly crosslinked polystyrene nanoparticles. Reproduced from Tuteja et al.[95] Copyright 2006, Wiley-VCH.

Integration of the Kratky plot yields the total scattering invariant (TSI), which represents the relative purity in a two phase model, is found through Equation 2-5:[96]

$$\text{Equation 2-5: } TSI = \int I(q)q^2 dq$$

GISAXS was carried out at SSRL on beamline 1-5 or ALS on beam line 7.3.3. The detector was set 3 to 4 meters away from the sample. The beam energy was kept constant at 10 keV. Samples were prepared in the same way as GIWAXS samples in which p-type Si was the substrate. BHJ samples were prepared on bare p-type Si, or on PEDOT:PSS coated p-type Si in order to mimic a conventional solar cell device architecture. The X-ray incidence angle was either 0.12º or 0.13º. For GISAXS carried out at SSRL and ALS the measurement was conducted in air with an evacuated flight tube to minimize air scatter. Data was reduced using IGOR PRO with Nika and Irena packages.

2.4. In situ Monitoring Thin Film Solidification.

In situ thin film measurements that follow the evolution of a film during solidification provide a wealth of knowledge as to the mechanism that different processing techniques, and conditions, have on the final solid state morphology. Here, I will discuss the in situ measurements used to probe thin film solidification and morphological evolution of conjugated materials.

2.4.1. In situ UV-vis absorbance.

In situ UV-vis absorbance spectroscopy was conducted on the custom blade coater either in the transmission mode or at Brewster's angle (approximately 55º). An example of the experimental setup for in situ UV-vis absorbance/reflection spectroscopy, done at nominally Brewster's angle, is shown in Figure 26. An unpolarized light source is incidence onto a spot at ~55º. The light is split into two beams where the reflected beam (reflection) is S-polarized and the transmitted beam (absorbance) is partially P-polarized.

Using Brewster's angle during a coating allows for real-time reflection and absorbance data to be collected on the same sample at the same spot. Note: Measurements done at Brewster's angle were conducted on Sebastian Engmann's blade coater setup at NIST. For specifics on Brewster's angle setup see Chapter 4. Figure 27 shows the experimental setup for transmission in situ UV-vis absorbance spectroscopy on a blade coater. An Ocean Optics HL-2000 Family Tungsten Halogen Light Sources connected to a R400-7-UV-VIS-a fiber optic was setup above the sample. As the coating occurred, white light was transmitted through the sample and a hole in the stage to a mirror where the signal was bounced to an Ocean Optics Flame detector. Spectra were taken on the order of every 50 ms to 100 ms using Ocean Optics OceanView: Real-Time Acquisition and Analysis software. Data was further analyzed using IGOR Pro software. Figure 28 demonstrates a 2D absorbance image of DT-PDPP2T-TT:$PC_{71}BM$ blade coated from chloroform, in which the Z axis intensity, the X axis is wavelength (nm) and the Y axis is time (s). From this, information about polymer aggregation as a function of time can be obtained. The blade passage is set to 1 s. After blade passage a wet film is deposited, labeled polymer in solution in Figure 28. There is an increase in optical absorbance, labeled as change in local polymer order in Figure 28, as solvent evaporates and solidification occurs. When combined with in situ reflection, polymer aggregation and film thickness can be plotted which provides insight into polymer local order as the solution is drying into a film. If there is alignment present in the film then Brewster's angle will show a decrease in optical absorption as solvent evaporates and a thin film is formed, whereas if the measurement is taken normal to the substrate there will be an increase in optical absorption as the thin film is formed.

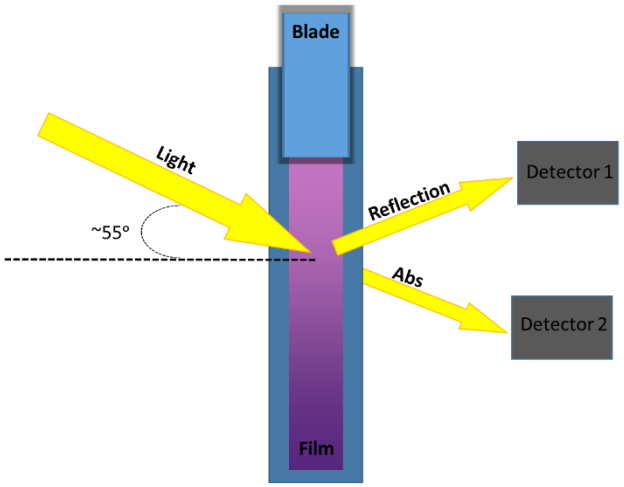

Figure 26. Brewster's angle setup for in situ UV-vis absorption and reflection spectroscopy during blade coating.

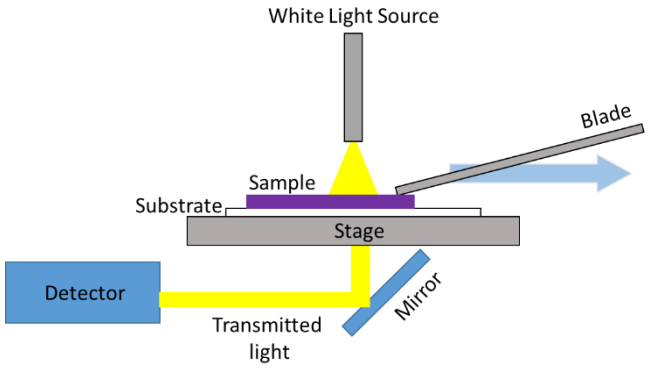

Figure 27. Transmission in situ UV-vis absorption/reflection spectroscopy setup. White light is incident onto the sample normal to the substrate. Light transmitted is bounced off a mirror into a detector while reflected light is captured in the reflection probe.

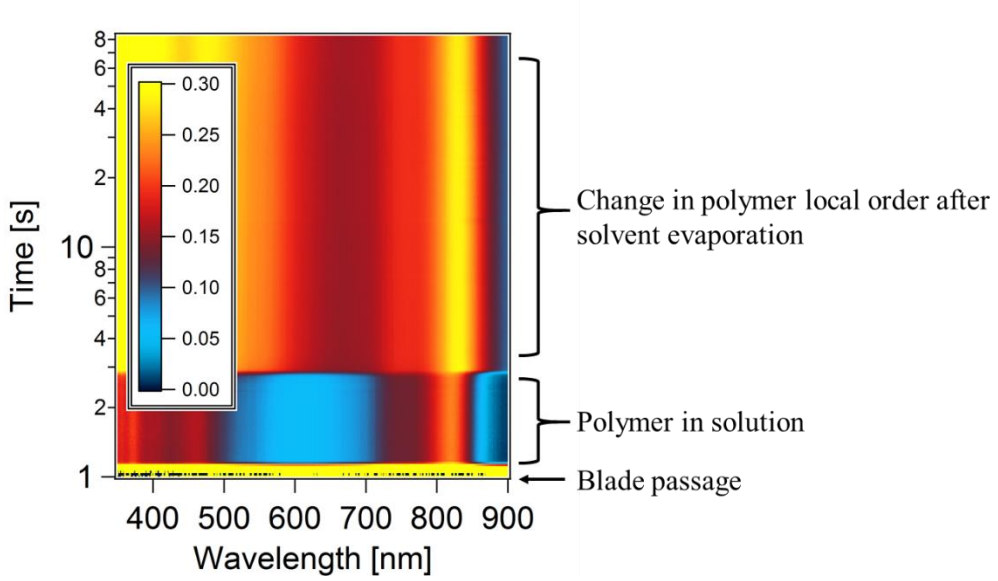

Figure 28. Two dimensional image of in situ UV-vis absorbance of DT-PDPP2T-TT:$PC_{71}BM$ blade coated from chloroform.

2.4.2. In situ reflection.

In situ reflection was performed one of two ways. The first way was using Brewster's angle in which is discussed in section 2.4.1. The reflected light is S-polarized while the transmitted light is partially P-polarized. The second way in situ reflection is collected is using a reflection probe (Ocean Optics R400-7-UV-vis) that is normal to the substrate, which is pictured in Figure 27. White light from an Ocean Optics HL-2000 Tungsten Halogen Light Source is emitted onto the substrate during the coating while reflected spectra are collected using an Ocean Optics Flame-NIR Spectrometer. Data is collected using Ocean Optics Spectra Suite software. In situ reflection data is then processed using Igor Pro to generate 2D graphs in which the z-axis is intensity, the x-axis is wavelength (nm) and the y-axis is time (s). Figure 29 demonstrates an in situ reflection measurement of DT-PDPP2T-TT:$PC_{71}BM$ blade coated from chloroform:*ortho*-

dichlorobenzene solvent mixture, in which the interference of waves, known as fringing, is clearly evident. The blade passage is set to 1 s. Two evaporated regimes are shown, in which chloroform evaporation dominates evaporative regime 1, shown in Figure 28, due to its high vapor pressure, followed by *ortho*-dichlorobenzene evaporation shown in evaporative regime 2. Note, evaporation of *ortho*-dichlorobenzene is occurring during evaporative regime 1, however, for simplicity we assign one solvent evaporation to one designated evaporative regime. Reflection spectra provide information on timing of solvent evaporation, and film thickness during solidification.

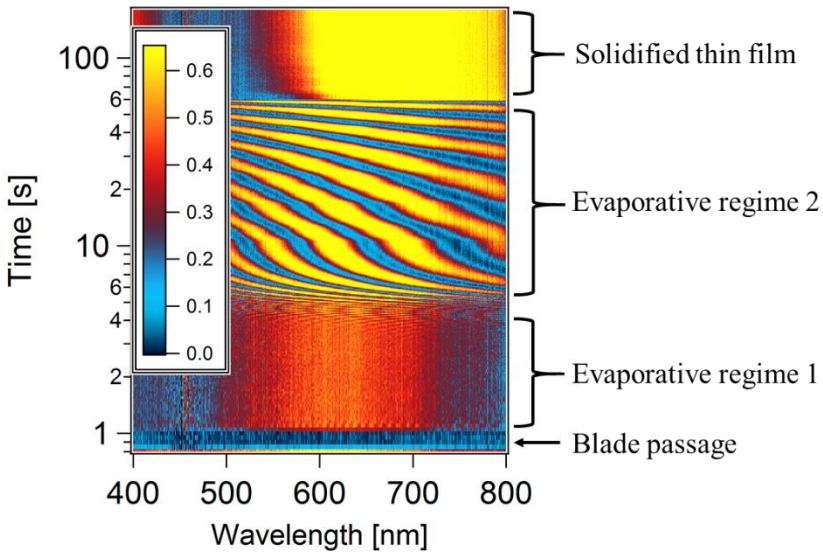

Figure 29. Two dimensional plot from in situ reflection of DT-PDPP2T-TT:$PC_{71}BM$ blade coated from chloroform:*ortho*-dichlorobenzene solvent mixture.

2.4.3. In situ GIWAXS.

In situ GIWAXS allows for the measurement of polymer crystallization, lamellar spacing, and crystal orientation as a function of time. Figure 30 shows a representation of the experimental design used for in situ GIWAXS and GISAXS data collection.[66] X-rays are incident onto the sample at an angle above the critical angle during the coating.

Multiple 2D GIWAXS, or GISAXS, images are taken during the coating, which are then converted into pole figures, and the integrated intensity from each pole figure is plotted as function of time. There is a reflectivity probe normal to the substrate to monitor solvent evaporation and film thickness during the coating. In situ GIWAXS was carried out at ALS on beamline 7.3.3. with a beam energy of 10 keV in ambient air.

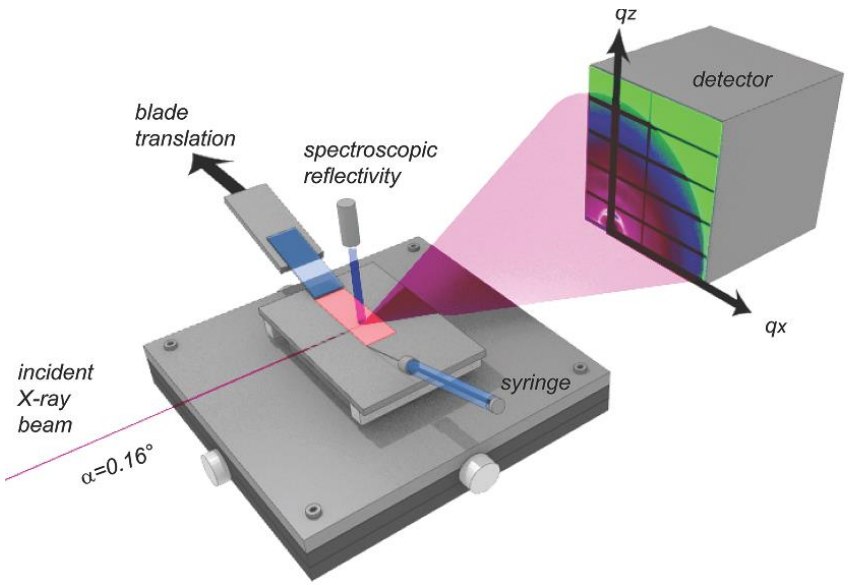

Figure 30. Schematic of in situ GIWAXS or GISAXS experimental setup. Reproduced from Richter et al.[66] Copyright 2015, Wiley-VCH.

For specifics concerning in situ GIWAXS on DT-PDPP2T-TT see Chapter 5.

2.4.4. In situ GISAXS.

In situ GISAXS allows for the measurement of domain formation, and phase purity, as a function of time. The experimental setup is the same as in situ GIWAXS pictured in Figure 30, with the exception of the detector distance. In situ GISAXS was carried at ALS on beam line 7.3.3. For specifics concerning in situ GISAXS on DT-PDPP2T-TT see Chapter 5.

2.5. Device Fabrication & Measurements.

Section 2.5. describes the types of devices built in order to study the photovoltaic properties, and charge mobility, of various polymer and discrete molecules. Details are given on the fabrication of each device, its use, relevant mathematical equations, and hardware/software, used to measure specific properties.

2.5.1 Conventional OPV Fabrication.

Conventional and inverted OPVs architecture is depicted in Figure 31 a) and b) respectively.

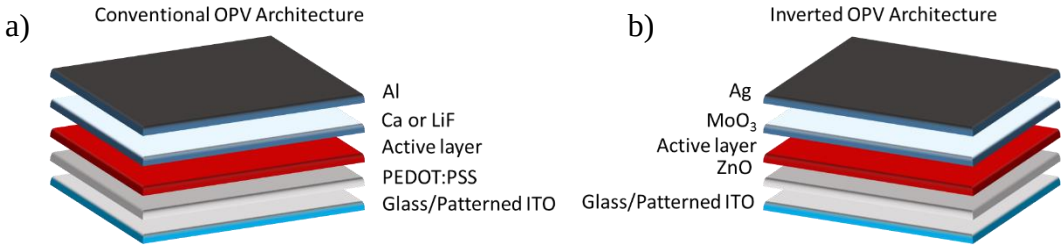

Figure 31. a) Conventional OPV architecture and b) inverted OPV architecture.

Patterned indium tin oxide (ITO) from Tinwell Technology (tinwell@incnets.com , project # TI1678D), was scrubbed with a Kimwipe dipped in a mixture of sodium dodecyl sulfate (SDS) and Millipore water. Afterword, the ITO slides were placed in a holder and submerged into the SDS/water mixture using a substrate holder and placed in a Branson 2510 sonicator. The ITO was sonicated for 5 minutes, then taken out, rinsed with Millipore water, then placed in a beaker of acetone and sonicated for 5 minutes, followed by sonication in isopropanol (IPA) for 5 minutes. The ITO was then blown dry with Ar gas and placed in a Novascan PSD Pro Series UV-ozone cleaner for 10 minutes. PEDOT:PSS (Cleavios PVP 4083) was spun coat on the clean ITO outside of the glovebox using a Laurell spin coater. (Model: WS-650MZ-23NPP). For PEDOT:PSS films a solution of

PEDOT:PSS (Clevios Al 4083) was filtered through a plastic syringe with a 0.45 μm Nylon filter onto the UV-ozone cleaned substrate. Filtered PEDOT:PSS solution was spun at 5000 r.p.m. for 50 seconds with an acceleration of 1450 r.p.m. per second. The portion of ITO that would contact the leads for electrical measurements were gently wiped with a cotton swab dipped in IPA. PEDOT:PSS films were then dried in air on a IKA C-MAG H7 hotplate set to 120 ºC for 10 minutes. Dried PEDOT:PSS films were then place in plastic boxes. The active layer solution was applied either by spin coating or by blade coating. For specific coating instructions of the active layer see the Chapter 3 for P3HT, Chapter 4 for P(T3-TPD), and Chapter 5 for DT-PDPP2T-TT. Once the active layer is coated the devices are place in a Ar filled MBraun glovebox. Devices were placed in a custom built holder for thermal evaporation of electrodes. Electrodes were evaporated at a pressure of 10^{-5} mbar. For conventional devices electrodes were either 1 nm of LiF (deposition rate 0.5Å/s) /100nm of Al (deposition rate of 2Å/s) or 10 nm Ca (deposition rate 0.5 Å/s) /100 nm Al (deposition rate of 2 Å/s). The overlapping area between the ITO and the electrode defines the active are size. Two sizes were used, either 0.07 cm^2 or 0.08 cm^2.

2.5.2. Inverted OPV Fabrication.

Inverted organic solar cell architecture is pictured in Figure 31 b). The advantage of using an inverted architecture over a conventional architecture is that the lifetime of the device in ambient air is improved due to avoiding using hygroscopic PEDOT:PSS, and using low-work function metal cathodes.[97] Patterned ITO from Tinwell Technology (tinwell@incnets.com , project # TI1678D), was scrubbed with a Kimwipe dipped in a mixture of SDS and Millipore water. Afterword, the ITO slides were placed in a holder and

submerged into the SDS/water mixture and placed in a Branson 2510 sonicator. The ITO was sonicated for 5 minutes, then taken out, rinsed with Millipore water, then placed in a beaker of acetone and sonicated for 5 minutes, followed by sonication in IPA for 5 minutes. The ITO was then blown dry with Ar gas and place in a Novascan PSD Pro Series UV-ozone cleaner for 10 minutes. ZnO sol-gel, made from 0.32 g of Zn acetate dihydrate (Sigma Aldrich) in 1920 µL of 2-methoxyethanol (Sigma Aldrich) and 80 µL of ethanolamine (Sigma Aldrich), was spin coated in air on the ITO at 800 rpm using a using a Laurell spin coater. (Model: WS-650MZ-23NPP) for 50 sec. The ZnO thin film was annealed in air at 400 ºC for 5 minutes on a hotplate. The substrates were allowed to cool before being placed in a 1" x 1" plastic case. The active layer was coated on top of the ZnO films. After the active layer was applied the devices were brought into a MBraun Ar filled glovebox and place in a thermal evaporator where 4 nm -10 nm of MoO_3 was evaporated on followed by 80 nm -100 nm of Ag. Inverted organic solar cells were tested in the same fashion as conventional solar devices.

2.5.3. SCLC Device Fabrication.

For hole mobility SCLC devices, patterned ITO from Tinwell Technology (tinwell@incnets.com , project # TI1678D) was cleaned in the same fashion as reported for solar cell fabrication. Afterwards, the ITO was UV-ozone cleaned, and PEDOT:PSS (Clevios P VP Al 4083) was spun cast onto cleaned ITO the same way as solar cell fabrication. PEDOT:PSS slides were dried in air on a hotplate at 120 ºC for 10 minutes. The substrates were then placed in 1" x 1" plastic cases (Althor Product, item #H-1). The active layer was then coated onto the PEDOT:PSS substrates either by spin coating, or by

blade coating. Following the coating, devices were transferred to a thermal evaporator in an Ar filled MBraun glovebox where 80 nm of Ag was put down as a contact at a rate of 2 Å/s at a pressure of 10^{-5} mbar. Devices were then measured, using a custom holder, under dark conditions using a Keithley SMU 2410 to scan the voltage from 0 V to +10 V.

2.5.4. OPV Device Power Conversion Efficiency.

Photovoltaic power conversion efficiency (PCE) is dependent on numerous factors which include light intensity, angle of incidence, and light source. In order to standardize PCE values there are three common solar measurements which are air mass (AM) 0, AM 1.0, and AM 1.5. Figure 32 a) demonstrates the differences between AM 0, AM 1.0 and AM 1.5.[98] AM 0 is representative of the solar spectrum prior to reaching Earth's atmosphere and is typically used for space applications, AM 1.0 is the solar spectrum normal to one earth atmosphere, and AM 1.5 is the solar spectrum that has penetrated through one Earth atmosphere at an angle of 48.2º. For solar cell measurements AM 1.5 global (AM 1.5G), the global includes direct and diffuse radiation, calibrated to 100 mW/cm^2 taken at 25 ºC is the accepted protocol for measuring PV performance unless otherwise stated. NREL solar reference spectra for AM 0, AM 1.0, and AM 1.5 can be seen in Figure 32 b).[99]

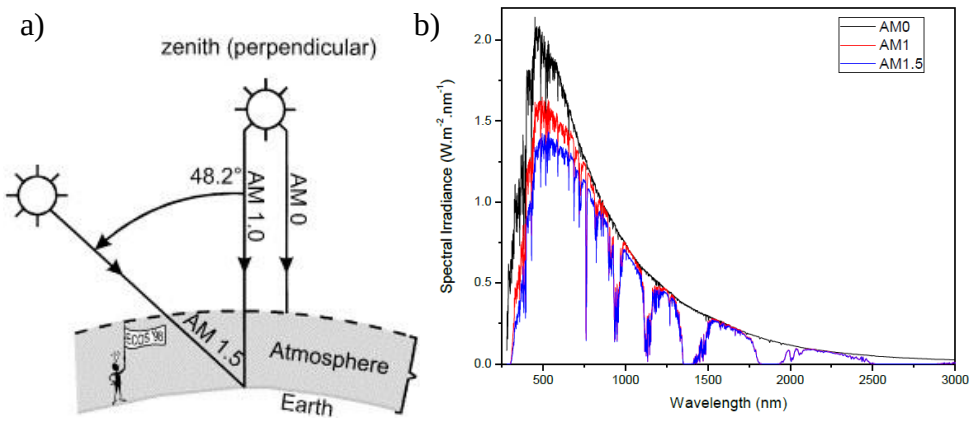

Figure 32. a) Schematic of the different AM sunlight spectra to determine PCE%. b) solar spectra for AM 0, AM 1.0, and AM 1.5. Reproduced from Emery.[99]

Devices were measured using AM 1.5G solar simulator made up of a Newport Oriel 69907 universal arc lamp power supply connected to a 150 W xenon arc lamp (Newport 6255) with collimating lenses in a Newport Oriel 94021A simulator lamp housing. A AM1.5G filter (Newport 81088A) is applied to the xenon arc lamp to correct the spectral mismatch. Corrected light passes through a quartz window into the glovebox where it is measured using a 2 x 2 cm^2 reference silicon solar cell (Newport 91150V) to calibrate the light intensity. Solar cells to be tested are placed in a custom built solar cell holder in which pins contact the ITO and electrodes simultaneously. Devices can be measured independently using a switch board to active a particular device. A voltage bias form -1 V to + 1 V is applied to the device and the current is measured under illumination using a Keithley SMU 2410. This produces a current-voltage curve which is converted to current density when the active area is known. Active areas were either 0.07 cm^2 or 0.08 cm^2 which is defined by the overlap of the electrode and the ITO. From the current density and voltage curve plot the J_{sc}, V_{oc}, FF and PCE% was calculated. Multiple devices were tested in order to gain an average and standard deviation of solar cell performance.

2.5.5. Incident Photon to Current Efficiency (IPCE).

Incident photon to current efficiency (IPCE), also referred to as external quantum efficiency (EQE), is a measure of current generation in percent as function of the wavelength of incident light. IPCE can be calculated using Equation 2-6:

$$\text{Equation 2-6: } IPCE = \frac{\#\ electrons}{\#\ incident\ photons}\ x\ 100$$

$$\#\ electrons = \frac{I}{e}$$

$$\#\ incident\ photons * s^{-1} = \frac{P\lambda}{hc}$$

Where I is the current generated from the device under short circuit conditions, e is the charge of an electron (1.602 × 10-19 C), P is power, λ is the wavelength of incident light in nm, h is Planck's constant (6.62607004 × 10^{-34} m^2 kg/s), and c is the speed of light in vacuum (299, 792, 458 m/s). The above equations can be combined to yield an equation for IPCE (%) as a function of λ in Equation 2-7.

$$\text{Equation 2-7: } IPCE\% = \frac{hcI}{eP\lambda}x100$$

An ideal IPCE would be a rectangle that reaches an IPCE(%) of 100 and stretches across the visible spectrum. This would be a device that converters every incident photon into an electron. It is important to note that IPCE does not take into account those photons that are scattered or reflected. Internal quantum efficiency (IQE) is the measure of the ratio of charges generated to the number of photons absorbed by the solar cell. IQE is always larger

than EQE because it considers that not all photons incident on the solar cell are absorbed, rather, some may scatter, reflect, or pass through the device.

A schematic of the IPCE, taken from the Newport Measurement System manual, is shown in Figure 33. A collimated 600 W Xe lamp (Newport #66485) produces light that is passed through filters to remove second harmonic radiation and a 30 Hz light chopper. The light is sent to a Cornerstone 260 1/4M monochromator which produces monochromic light. The monochrotaic light is focused on a calibrated silicon photodetector that is covered with a mask the same size as the active area of the solar cell to be tested in order to ensure that there no over illumination of the device. Photovoltaic devices are tested in the same spot as the calibrated detector. The current is measured as varying wavelengths are incident on the device using a dual channel Merlin digital lock-in radiometry system (RS-232 Newport #70104). The solar cell being tested and the detector are connected to an Oriel Merlin digital lock-in amplifier. TracQ Basic 6.0 is the software used to analyze the IPCE spectra.

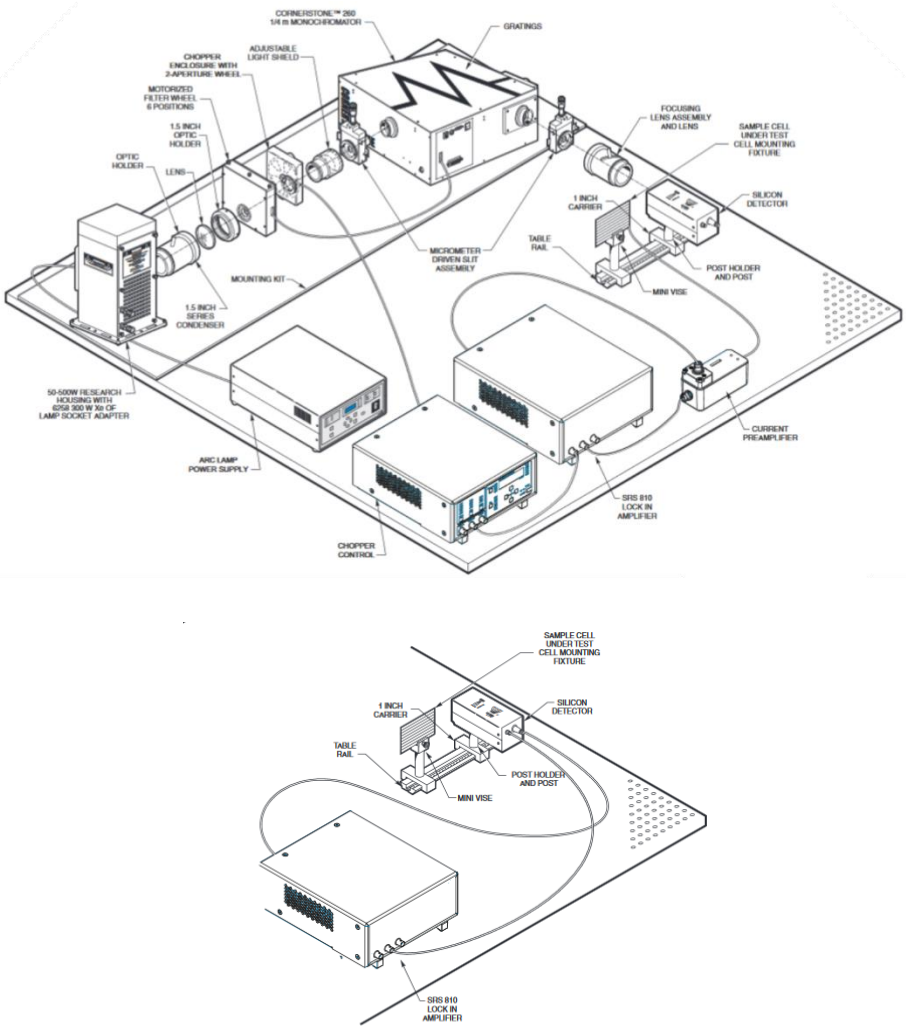

Figure 33. Schematic of IPCE equipment used. Reproduced from IPCE manual.

2.5.6. SCLC Measurements.

SCLC measurements were conducted in an Ar filled glovebox under dark conditions. Devices were scanned from 0V to +10V using a Keithley SMU, giving a current-voltage plot. Current (A) was converted to current density (A/m^2) and the built-in

voltage was subtracted from the applied voltage to give the effective voltage. The current density and effective voltage were plotted on a log-log scale. The region where a slope of approximately 2 is observed is the SCLC region where mobility can be extracted using Equation 2-8. [100]:

$$\text{Equation 2-8: } J = \frac{9}{8}\mu_0 \varepsilon_r \varepsilon_0 \exp(0.891\gamma\sqrt{E})\frac{V^2}{L^3}$$

Where μ_0 is hole mobility, ε_r is the relative permittivity of the material (about 3.0)[101], ε_0 is the permittivity of free space, γ is the field dependent parameter, E is the electric field, V is the voltage and L is the film thickness. It is necessary to make devices of three different film thicknesses to ensure that the current density follows a $1/L^3$ dependence and to gain an average and standard deviation mobility value.

CHAPTER 3. PROBING THIN FILM SOLIDIFICATION OF P3HT:PCBM

3.1. Review of literature involving blade coating P3HT.

As reported by the U.S. Energy Information Administration, world energy consumption is expected to grow 56% from 2010 to 2040. The fastest growing segments of the energy market are renewables and nuclear, which are expected to increase by 2.5% per year.[102] As the global demand for energy increases, new, innovative ways to meet those demands in a cost effective, sustainable manner are essential and imperative. Further, technologies having a low carbon footprint are desirable. One attractive, emerging renewable energy technology that offers the potential to meet all the desired attributes is broadly represented by solar, organic and hybrid photovoltaics (OPVs) in particular. OPV utilizes highly tunable materials; single junction devices based upon small molecules have achieved efficiencies approaching 9%,[103, 104] while polymeric materials have afforded cells with power conversion efficiencies (PCEs) higher than 9% .[97, 105]

Substantial efforts have been focused towards materials design and synthesis to produce novel small molecule and polymeric materials that will yield devices with optimized performance attributes, PCE in particular.[34] However, until recently, a quantitative understanding of how materials processing impacts device characteristics has lagged behind efforts to identify alternative molecular structures. While the design and synthesis of materials that afford high PCE's and demonstrate good stability is important, the ability to process those materials into integrated large-scale OPV systems, while maintaining optimum device performance, may well be the defining element to the success of OPV technology.[53]

The most readily available laboratory-based process methodology used in the fabrication of thin polymer films is spin coating, and this technique is the one most commonly used to fabricate OPV devices in a research environment. However, spin coating is not viable for either the manufacture of large-area or flexible devices. Further, and perhaps more importantly, the critical process parameters that control thin-film morphology will be substantially different for films prepared *via* spin coating *vs*. alternative methods such as spray coating,[106, 107] slot die coating,[108] ink jet printing,[109] and blade coating,[67, 110-118] which makes it critical to investigate these various large scale processing techniques. While the final morphology and its evolution during spin coated film formation has been extensively studied, investigations associated with blade coating have lagged behind, even though it is especially well-suited for ultimate comparison to roll-to-roll (RtR) manufacturing processes.[69, 119] The impact of the active layer deposition process is aptly demonstrated in a report by Brabec et al. who showed that the thin-film morphology obtained upon blade *vs*. spin coating active layer thin-films is markedly different, with blade coating affording higher open circuit voltage (V_{oc}).[111]

An additional principal consideration related to OPV device fabrication pertains to the ability to integrate the active layer thin-film deposition method with low-cost, high through-put, large-area fabrication via RtR production. While solution processed OPV's can be realized using RtR methods, to be commercially viable, a sound knowledge base regarding critical process parameters associated with RtR compatible solution processed materials for solar cell devices is imperative, as is knowledge concerning the impact and control of resultant morphology. Fundamentally then, we ask *"How do we bridge the*

processing gap?", and move away from spin coating to RtR compatible processing methods for large area high efficiency OPVs?

Here, blade coating was used to fabricate the active layer of inverted solar cells from a solution of poly(3-hexylthiophene-2,5-diyl) and [6,6]-phenyl C_{61} butyric acid methyl ester(P3HT/$PC_{60}BM$) to identify and investigate the critical process parameters associated with the fabrication of OPVs *via* blade coating of the active layer. A series of common chlorinated processing solvents, which have a difference in vapor pressure over a range of three orders of magnitude, were selected to examine solvent effects, such as evaporation rate, on ultimate morphology and device performance. Solvents such as chlorobenzene, *ortho*-dichlorobenzne and toluene are commonplace in OPV fabrication,[112-115] however, their impact on the performance of blade coated devices has not been investigated. Since the kinetic and thermodynamic phenomena associated with blade coating will differ substantially from the largely kinetically driven processes operational during spin coating, it is essential to elucidate the role of the solvent in the former approach to OPV device fabrication.[120]

Bulk-heterojunction inverted solar cells were fabricated using P3HT (>98% head to tail) and $PC_{60}BM$ in anhydrous chloroform (CF), chlorobenzene (CB), *ortho*-dichlorobenzne (DCB) and 1,2,4-trichlorobenzene (TCB) as the deposition solvent. All four systems exhibit significant vapor pressure differences of approximately one order of magnitude between each solvent at room temperature, which facilitates investigation of the effects of deposition solvent characteristics, solvent vapor pressure in particular, on active layer thin-film morphology and ultimately device performance.

3.2. Experimental.

Materials. $PC_{60}BM$ was purchased from Nano-C. Poly(3-hexylthiophene-2,5-diyl) (P3HT) Plexcore OS 2100, Mn 54,000–75,000 kDa, 99.995% trace metal basis was purchased from Sigma–Aldrich. All other materials were purchased from Sigma–Aldrich and used as is unless otherwise noted.

Solubility of P3HT. P3HT was dissolved in four solvents; chloroform, chlorobenzene, *ortho*-dichlorobenzene and 1,2,4-trichlorobenzene. Concentration of all solutions was 40 mg mL^{-1}. Solutions were placed on a hot plate set to 70 ºC and allowed to stir for 24 h. All solutions were then removed from the hotplate and allowed to cool to room temperature. After, all solutions were individually filtered through a 0.45 μm PTFE filter using a glass syringe into separate vials. Next, a known amount of the filtered solution was taken and placed into a pre-weighed vial. All vials were then placed in a vacuum oven with a temperature at 60 ºC and pressure of 10^{-1} mbar for 8 h. 1,2,4-trichlorobenzene solution was placed on a hotplate set to 300 ºC for another hour to insure all the solvent was removed. All four vials were then re-weighed and the mass difference was used to calculate solubility.

Solar cell fabrication. Patterned ITO on glass was ultra-sonicated in sodium dodecyl sulfate in water followed by acetone and then isopropanol. ITO was blown dry with Ar gas then UV ozone treated. ZnO sol–gel, made from 0.32 g of Zn acetate dihydrate in 1920 μL of 2-methoxyethanol and 80 μL of ethanolamine, was spin coated on the ITO at 800 rpm for 50 s. The ZnO thin film was annealed in air at 400 ºC for 5 min. Solutions of P3HT and $PC_{60}BM$ in a 1:0.8 wt ratio, in concentrations of 33 mg mL^{-1} in chloroform, 38 mg mL^{-1} in

chlorobenzene, 26 mg mL^{-1} in *ortho*-dichlorobenzene, 20 mg mL^{-1} in 1,2,4-trichlorobenzene, and 26 mg mL^{-1} DCB:CF were made and allowed to stir for 48 h at 70 ° C in an Ar filled glove box. All solutions were then blade coated onto the ZnO film at 5 mm s^{-1} with a 15 μm blade gap in air using a Zehntner ZAA 2300 with a ZUA 2000 blade in air. The solvent mixture was calculated to be 3 mmHg vapor pressure using Raoult's Law. The devices were left to dry for 12 h in air and then transferred to an Ar filed glovebox where they were annealed at 140 ºC for 35 min. 4 nm of molybdenum oxide and 100 nm of Ag was thermally evaporated onto the devices through a mask at 10^{-6} mbar as the top electrodes. Active area of devices is 0.07 cm^2.

SCLC hole mobility devices. ITO was cleaned the same way as described in solar cell fabrication. Following cleaning, PEDOT:PSS (Al 4083) was spun coat at 5000 rpm for 60 s and dried in air at 120 ºC for 20 min. The active layer was then blade coated on, and devices were annealed in the same fashion described for solar cell fabrication. 80 nm of Au were thermally evaporated on as the top contacts.

***Characterization*.** A Newport ABB solar simulator coupled with a Keithley SMU for measuring device efficiency under standard AM 1.5 conditions calibrated to 100 mW/cm^2 using a reference solar cell was used to collect J–V. A Newport EQE/IPCE setup with a white light source and a monochromator to allow for external quantum efficiency and incident photon-to-current efficiency measurements was used to collect IPCE. UV–vis spectra were obtained using a Varian Cary 5000 UV/VIS/NIR. Thin film characterization was performed with a Bruker stylus profilometer. AFM was gathered with a Bruker Atomic Force Microscope (Dimension icon), which can operate under standard tapping mode

(using a Bruker Tap 150 cantilever) to gather height and phase information. A Perkin Elmer Spectrum One FT-IR was used for IR measurements.

3.3. Solvent Analysis.

The physical characteristics of the four solvents (CF, CB, DCB, TCB) used in this investigation are shown in Table 1. The solvents were selected based upon wide differences in vapor pressure and boiling point: the former ranges from a high of just over 190 mmHg to a low of approximately 0.3 mmHg for CF and TCB, respectively, while boiling point spans from 61 to 214 ºC. The boiling point and vapor pressure differences will affect blade coated thin-film drying time, which in turn will impact both morphology and device characteristics, thereby facilitating correlation of device properties with process solvent attributes. It is hypothesized that an increase in drying time through the use of low vapor pressure solvent, will allow for development of an optimum nanoscale phase morphology and will correlate with high device efficiencies.

The inherent solubility characteristics of a deposition solvent may also be expected to affect the film deposition process. One measure of solubility derives from the Hansen solubility parameters (HSP), which provide insight into polymer/solvent mixing through calculated thermodynamic characteristics of the media. As seen from the data in Table 1, P3HT:$PC_{60}BM$ solubilizes well in the four chlorinated solvents under investigation.[121] While HSP analysis can be a useful tool to evaluate the solubility of specific components and impacts ink formulations, kinetic factors play a large and influential role, thereby ultimately regulating morphology and device performance.[122] Factors such as vapor pressure and/or boiling point will bear directly on the kinetics of film formation.

Table 1. Characteristics of solvents investigated for blade coating P3HT:PCBM thin films: properties that influence polymer-solvent interactions and drying kinetics in polymer solutions and films.

Solvent	**Vapor Pressure at 25°C (mmHg)**	**Boiling Point (°C)**	**Hansen Solubility Parameters***				
			δ_D[MPa$^{1/2}$]	δ_P[MPa$^{1/2}$]	δ_H[MPa$^{1/2}$]	[a)]P3HT solubility [mg/mL]	[b)]PCBM solubility [mg/mL]
Chloroform (CF)	193.5	61.2	17.8	3.1	5.7	34	28.8
Chlorobenzene (CB)	11.8	131	19	4.3	2	15	59.5
***ortho*-Dichlorobenzene** (DCB)	1.47	180.5	18.3	7.7	2.8	21	42.1
1,2,4-trichlorobenzene (TCB)	0.29	214.4	20.2	4.2	3.2	18	81.4

[a)] Solubility of P3HT determined experimentally, [b)] HSP parameters and solubility taken from reference [121].

3.4. Blade Coating P3HT:$PC_{61}BM$ Films Solar Cell Performance.

Figure 34 and Table 2 show the current density (mA/cm^2) vs. voltage (V) (J-V) characteristics of inverted solar cells fabricated via blade coating the active layer under ambient atmosphere. In this study, inverted solar cells were fabricated starting with cleaned indium tin oxide (ITO) substrates onto which ZnO sol-gel was spin coated and annealed in air to form a semi-transparent electron transporting layer. P3HT:$PC_{60}BM$ was blade coated onto the ZnO layer in air and allowed to dry. Devices were then brought into a glovebox where they were thermally annealed at 140 ºC for 35 minutes followed by thermal

evaporation of 4 nm of MoO_3, which serves as a hole-transporting layer, and 100 nm of Ag. The inverted architecture was used due to the higher air stability of inverted devices vs. conventional structures brought by the higher work function a Ag (4.73eV) electrode relative to Ca (2.9eV) and Al (4.08). Electrons are collected at the ITO interface while holes are collected at the Ag electrode. Incorporating this geometry also circumvents using poly(3,4-ethylenedioxythiophene):poly(styrenesulfonate) (PEDOT:PSS) on ITO which is reported to hinder device performance due to chemical instabilities at the interface.[123] Average solar cell characteristics were determined in order to more accurately represent the experimental data,[124] with typically 8 devices tested for each set of conditions.

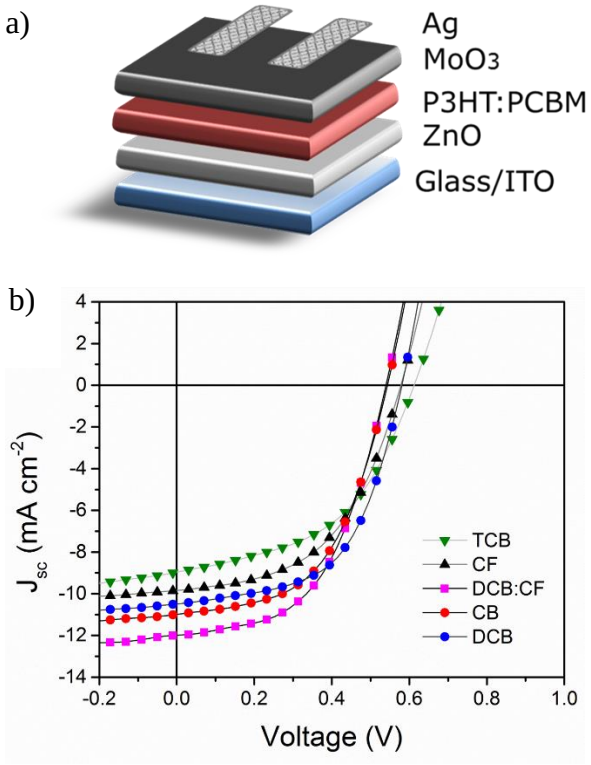

Figure 34. a) Schematic of inverted organic solar cell, b) J-V characteristics of P3HT:PCBM blade coated inverted solar cells as a function of processing solvent.

Table 2. J-V characteristics of blade coated P3HT:PCBM solar cells. The values in parentheses are for the best performing device.

SOLVENT	J_{sc}(mA/cm^2)	V_{oc}	FF%	PCE%	μ_H (cm^{2}V^{-1}s^{-1})	W(meV)
CF	9.66 ±0.24 (9.87)	0.58 (0.58)	48.38 ± 3.14 (50.52)	2.69 ± 0.18 (2.87)	2.4x10^{-6}	202
CB	11.29 ± 0.6 (11.52)	0.54 (0.54)	52.11 ± 2.47 (53.72)	3.16 ± 0.09 (3.31)	1.2x10^{-5}	169
DCB	10.52 ± 0.31 (10.44)	0.57 (0.58)	53.23 ±2.57 (57.09)	3.18 ± 0.12 (3.43)	3.0x10^{-5}	135
TCB	8.69 ± 0.43 (8.89)	0.60 (0.62)	48.72 ± 1.47 (48.56)	2.53 ± 0.09 (2.66)	4.6x10^{-5}	125
DCB:CF	11.62 ± 0.72 (12.73)	0.54 (0.54)	53.18 ± 1.88 (53.92)	3.28 ± 0.25 (3.67)	2.0x10^{-5}	102

The impact of solvent on device performance is readily apparent: J_{sc} increases with the solvent sequence CF to CB to DCB, yet a significant drop in J_{sc} is observed with TCB (~10.5 mA/cm^2 for DCB processed devices vs. ~8.7 mA/cm^2 those using TCB). Film thickness (~160 nm), as determined using profilometry (Figure 35) was similar for all devices investigated here.

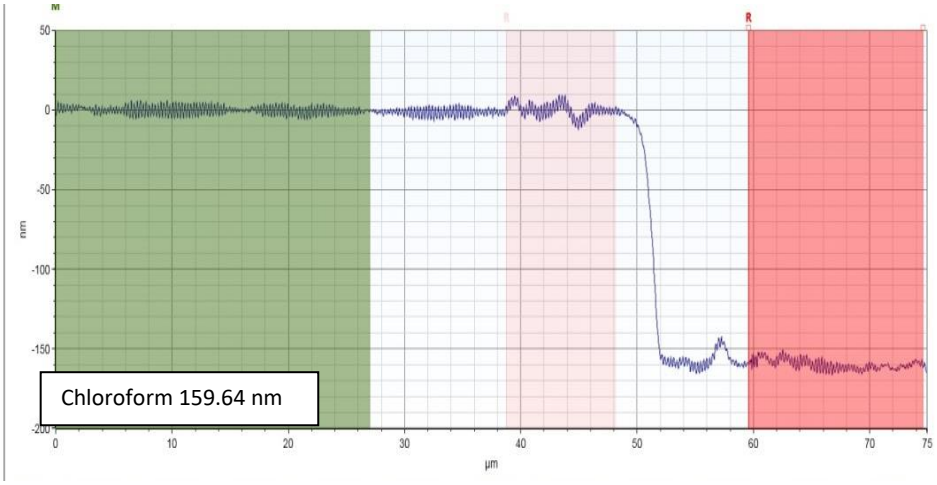
Chloroform 159.64 nm
nm
µm

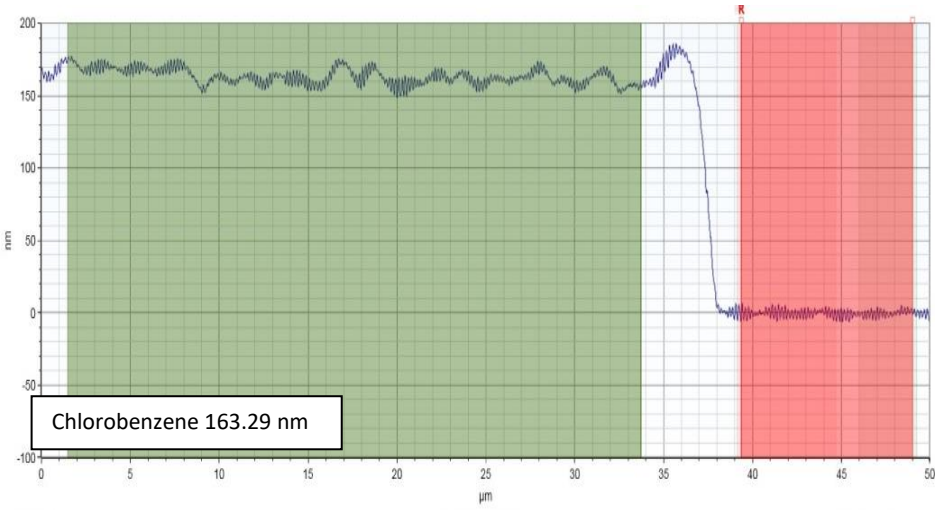
Chlorobenzene 163.29 nm
nm
µm

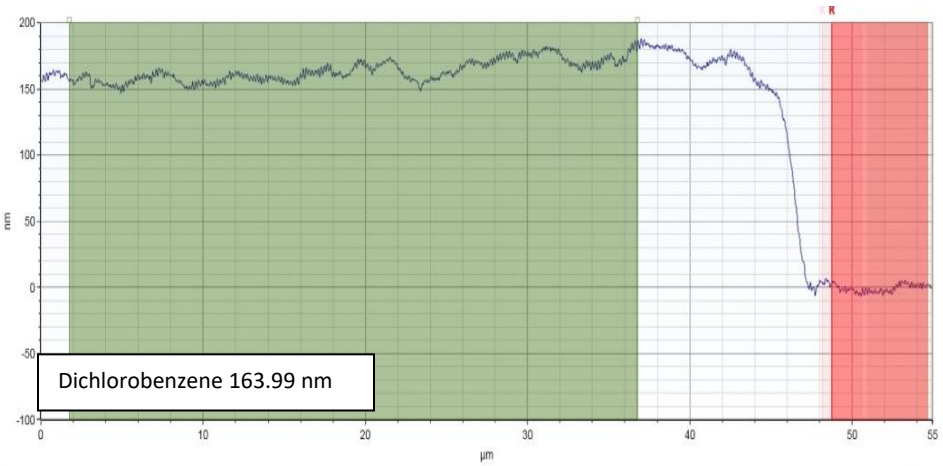
Dichlorobenzene 163.99 nm
nm
µm

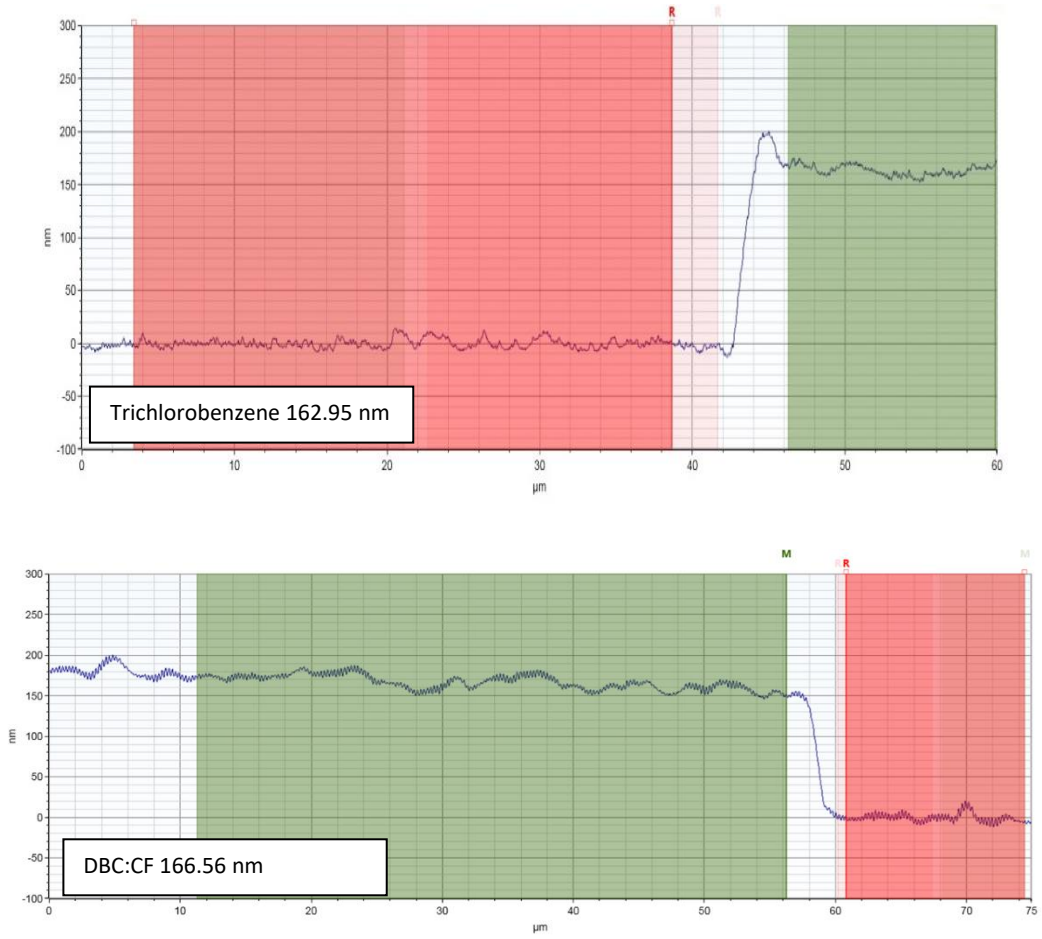

Figure 35. Profilometry of CF,CB,DCB, TCB and DCB:CF devices showing that all films are of the same thickness ~160 nm.

The absence of a C-Cl stretch at 600-800 cm^{-1} in the FT-IR spectra, shown in Figure 36, of coated films confirmed that solvent was essentially absent, and thus residual solvent is not a relevant factor. Figure 36 shows FT-IR spectra of the BHJ thin film active layer blade coated from a) CF, b) CB, c) DCB and d) TCB. The region where C-Cl shows a strong stretching peak is (600-800cm^{-1}). The absence of this peak indicates there is little to no solvent trapped in the film. Furthermore, there is an absence of a peak between 3000 cm^{-1} – 3100cm^{-1} where aromatic C-H stretches occur.

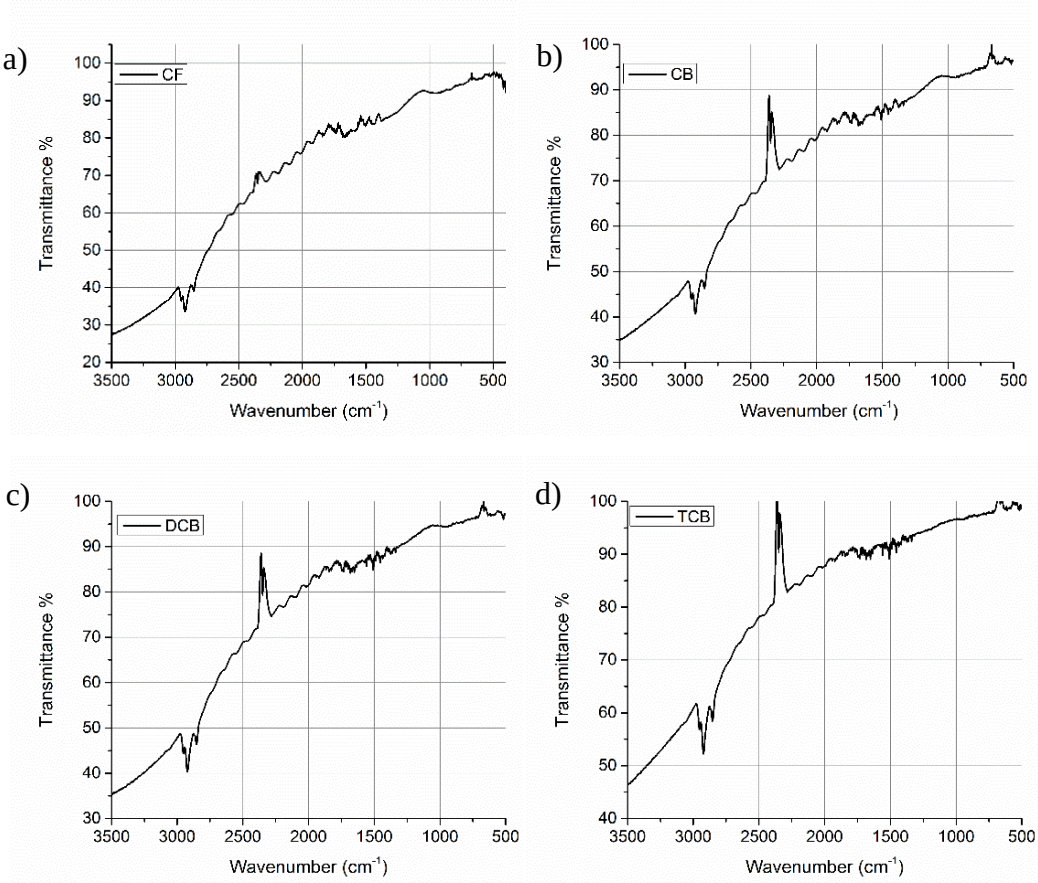

Figure 36. FT-IR spectra of BHJ films blade coated from a) CF, b) CB, c) DCB and d) TCB.

Open circuit voltage (V_{oc}) was similar for devices fabricated using CF, CB and DCB, but was slightly higher for TCB processed cells. Fill factor (FF%) and PCE(%) increased with decreasing vapor pressure, but then decreased with TCB; a similar trend to that observed for J_{sc}. Hole mobility (μ_H) and exciton bandwidth (W) will be discussed later. Notably, a plateau is apparent at a vapor pressure between those of CB and DCB.

Since it was reported that spin coated P3HT:$PC_{60}BM$ OPV active layer performance improved when mixed high/low vapor pressure solvents were used,[116, 125-127] the viability of the same approach was investigated for blade coated active materials. When

moving to a mixed solvent system, DCB:CF, with a calculated initial vapor pressure of 3mm Hg, the J_{sc}, FF, and PCE% improve to an average of 11.6 mA/cm^2, 53.2%, and 3.3% respectively, with PCE reaching a high of 3.7%. Though small, this improvement in average device efficiency using a mixed solvent system relative to a single solvent is evident in Figure 4. While the statistical variation for the mixed solvent results is a larger than that for single solvents, some of the cells exhibited higher PCEs.

The results presented in Figure 37 are in concert with earlier spin coating investigations and demonstrate that a combination of low and high vapor pressure solvents may advantageously change/adjust the active layer composition. In the mixed solvent approach, the higher vapor pressure/lower BP solvent evaporates first and, thus, the conditions associated with active layer solidification are optimized.[128] In the case of the lower vapor pressure solvents, increased drying time facilitates the degree to which self-organization within the films can change to more closely match the optimum P3HT:PC_{60}BM morphology.[129] However, longer drying times in and of themselves, do not correlate with improved morphology and device efficiency, rather, there is a finite drying time window which allows for development of an optimum nanoscale morphology leading to enhanced performance.

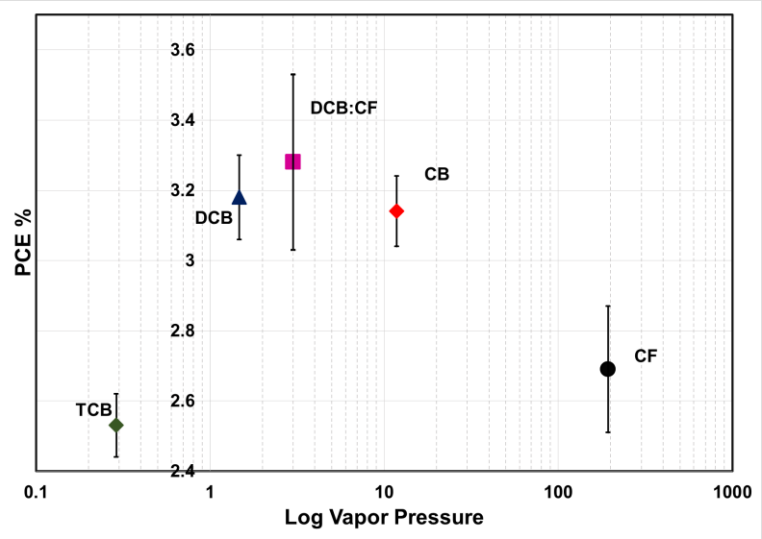

Figure 37. Influence of initial vapor pressure of P3HT:PCBM solution on blade coated solar cell device performance. The vapor pressure of the mixed solvent DCB:CF (X:Y) was calculated to be 3mm Hg (see Experimental Section) in order to investigate both mixed solvents and the vapor pressure regime between 1 and 10 mmHg.

While the magnitude of the PCE's measured in DCB, CB, and DCB:CF are shown to be statistically similar, the values observed for the mixed solvent shows a larger standard deviation. In the mixed solvent, it is hypothesized that CF rapidly evaporates from the solvent blend leaving behind DCB. The fast mass transfer process leads to evaporative cooling which will lower the temperature of the remaining solution. Evaporative cooling has been shown to induce controlled morphological features in non-conjugated polymer films.[130, 131] Given that these experiments were performed in an ambient environment, where temperature and room air flow were not tightly controlled, it is not surprising that DCB-CF which has low and high vapor pressure components exhibits a larger statistical deviation.

3.5. Monitoring Film Solidification Using In situ UV-Vis Absorption.

In order to gain fundamental insight into how single solvents, and mixed solvents, affect the dynamically developing photovoltaic properties described earlier, an *in situ* UV-vis blade coater system, built in house, was used to explore the solidification process of P3HT:PCBM as illustrated in Figure 38.

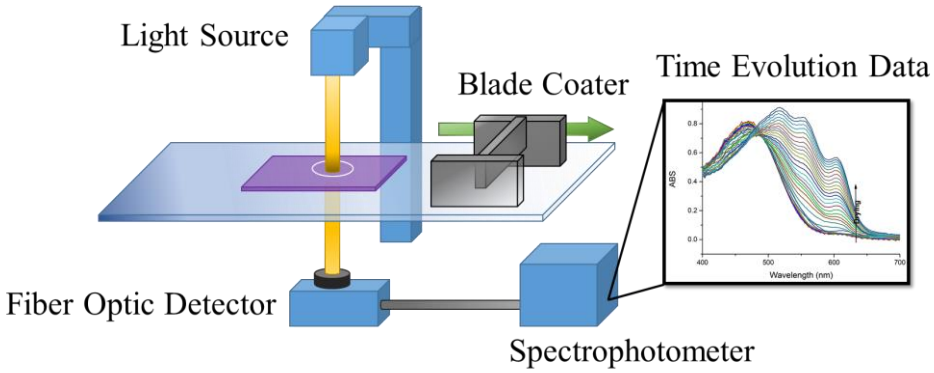

Figure 38. Measurement setup of in situ UV-vis absorption for blade coated P3HT:PCBM films. A white light source was placed above the glass/ITO substrate. Spectra were taken as the blade passed over the substrate coating the glass/ITO with P3HT:PCBM.

Figure 39 shows the results of the in situ blade coated experiment. Specific time selected spectra were chosen in order to show the morphological transition that occurs during solidification. Qualitatively, it is evident that as vapor pressure decreases, the development of the A_{0-0} and A_{0-1} peaks, at ~605 nm and ~550 nm respectively, are more pronounced as indicated by the arrows. The band at ~520 nm present in films prepared from all five solvents is due to the π-π* transition, while the bands at ~550 nm and ~605 nm are vibronic features indicative of a high degree of molecular ordering which takes place through interchain interactions.[129, 132] Films coated from CF and CB show weak shoulder features at 605 nm, while for films prepared from DCB, TCB, and DCB:CF, the

~605nm absorbance is significantly more pronounced suggesting that decreased vapor pressure facilitates an increased level of interchain interactions.[133]

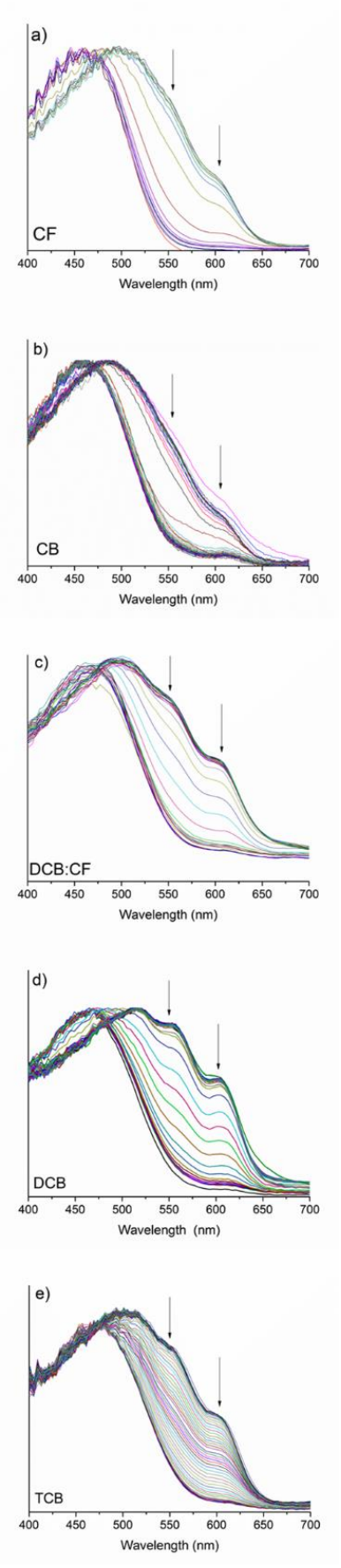

Figure 39. In situ UV-vis absorbance spectra of blade coated P3HT:PCBM films. Spectra are arranged in order of a) highest initial vapor pressure to e) lowest initial vapor pressure. The arrows at 605 nm and 550 nm demonstrate the development of the $A_{0\text{-}0}$ and $A_{0\text{-}1}$.

The drying curves, which monitor λ_{max} of the solidifying film as a function of time for each solvent employed here, are shown in Figure 40. There are three distinct regions in these curves, to the left of the sigmoidal curve onset would be solution on substrate, where the onset of the curve begins and then ends is the drying regime, and the solidified film is apparent to the right of the end of the drying regime. The slope of the sigmoidal curves represents evaporation rate. The slopes for CF, CB, DCB:CF, DCB and TCB are 0.044, 0.038, 0.025, 0.025, and 0.014 respectively, while the corresponding times are 18 s, 20 s, 20 s, 20 s, and 60 s, respectively. The trend shows that as initial vapor pressure decreases, the solidification rate slightly decreases. The evolution of peaks at 550 nm and 605 nm, corresponding to molecular order, were also plotted vs time (Figure 41), and show similar trend to that of Figure 40.

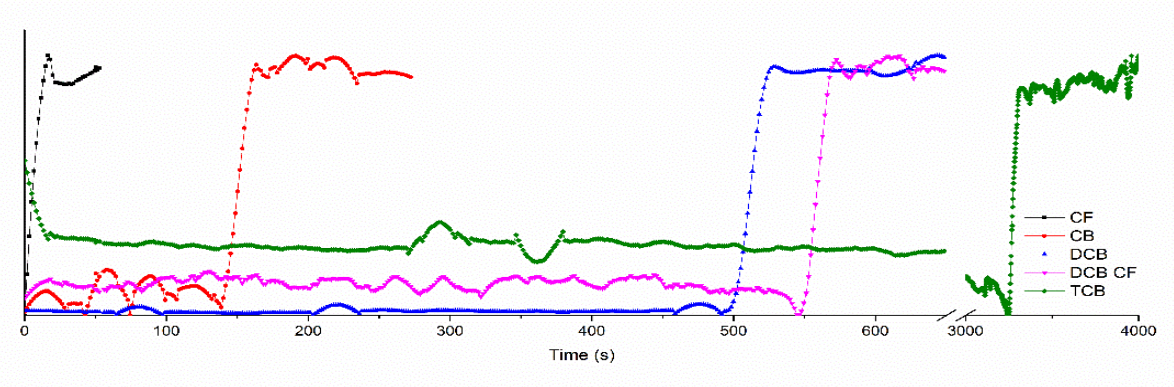

Figure 40. Solidification curves of P3HT:PCBM from various solvents monitoring λ max of the solidified film as a function of time. The sigmoid shape of each drying curve contains three regions. To the left of the onset is solution, the onset to plateau is the drying regime, and the plateau to the right is the solidified film.

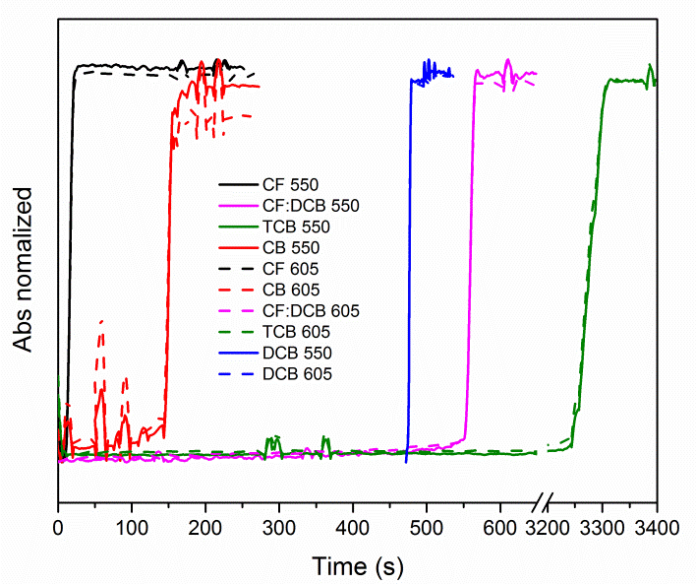

Figure 41. Evolution of 550 nm and 605 nm peaks as a function of time.

Notably, even though the solvent vapor pressures differ by orders of magnitude, the solidification rate is fairly rapid for all solvents. Interestingly, the short solidification time seen in all five solvents was also observed by others.[67, 134] Wang et al. also demonstrated similar results using in situ ellipsometry, where the extinction coefficient of the vibronic peaks at λ_{max}, 550 nm, and 605 nm of P3HT:PCBM films, cast from CB and TCB, were monitored vs time. For both solvents three distinct regions corresponding to a wet film, in which the absorption profile is similar to that of the polymer in solution, a crystallization regime, and solidified regime were also identified.[134] TCB, with an initial vapor pressure of 0.29 mmHg, exhibits the longest drying time (60 s), while all other solvent systems have drying times of ~20 seconds. The development of the P3HT absorption bands associated with aggregation is not seen until the onset of solidification. At the conclusion of the drying regime, and the solidification curve plateaus, no further morphology development is detected by UV–vis absorbance. Thus, depending on the solvent and evaporation conditions, the bulk heterojunction morphology develops in a span of seconds up to

perhaps a few minutes, in this critical regime. Since the solidification regime defines solid state film morphology, insight into this dynamic regime is vital for process optimization and control. Similar observations were presented by Schabel and co-workers, who also found that slow drying of P3HT:PCBM led to improved crystallization, improved π-π stacking and reduced series resistance.[65]

3.6. Quantitative UV-Vis Spectroscopy.

Using a modified equation developed by Neher et al, and first proposed by Spano, a quantitative picture of P3HT:PCBM films can be developed from UV-vis spectroscopic data via Equation 3-1.[135, 136] This UV-vis spectral analysis was coupled with space charge limited current (SCLC) hole mobility measurements, Figure 42, using a modified Mott-Gurney equation, Equation 3-2.[137]

Equation 3-1: $$A(E) \propto \sum_{m=0}\left(\frac{S^m}{m!}\right)\mathrm{x}\left(1-\frac{We^{-S}}{2E_p}\sum_{n\neq m}\frac{S^n}{n!n-(m)}\right)^2 \mathrm{x}\exp\left(\frac{\left(E-E_{0-0}-mE_p-0.5WS^m e^{-S}\right)^2}{2\sigma^2}\right)$$

Equation 3-2: $$J_{SCL} = \frac{9}{8}\varepsilon_0\varepsilon_r\mu\frac{V_{in}^2}{L^3}exp\left(\frac{0.89\beta}{\sqrt{L}}\sqrt{V}\right)$$

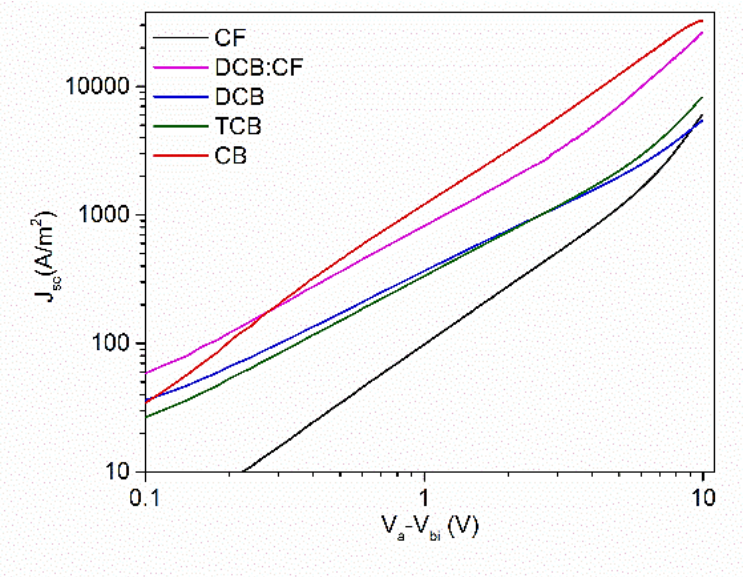

Figure 42. SCLC hole mobility of blade coated P3HT:PCBM cast from various solvents.

Using the UV-vis absorption spectra of the annealed P3HT:PCBM films coated from the different solvents, seen in Figure 44 a), the exciton bandwidth (W) was calculated from fitting of Equation 3-1. Figure 43 shows the fitting of the UV-vis absorbance spectra for each of the bulk-heterojunctions films cast from varying solvents. From these fitted spectra the exciton bandwidth (W) was calculated.

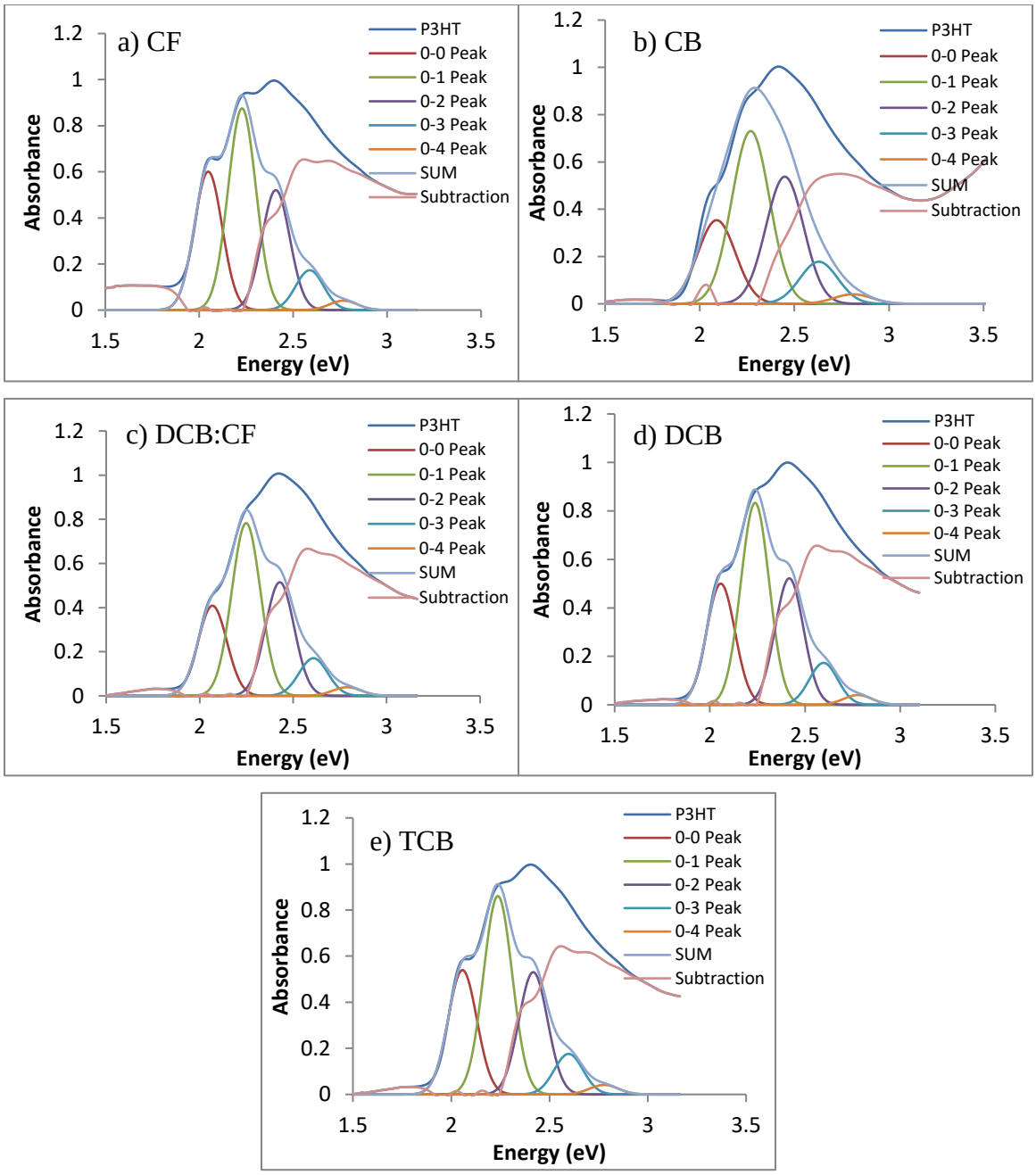

Figure 43. Fits of P3HT:PCBM thin film UV-vis absorbance spectra using Equation 3-1 in order of decreasing vapor pressure from left to right; a) CF, b) CB, c) DCB:CF, d) DCB, and e)TCB.

Previously, it was shown that W correlates with polymer backbone planarity and conjugation length: a smaller value of W signifies increased ordering within the polymer film. In turn, increased ordering has been shown to correlate with improved mobility for P3HT.[135] Figure 44 b) shows that as the solvent vapor pressure increases (lower boiling point), there is a decrease in W and simultaneously, an increase in hole mobility. CF shows the highest W (202 meV) and lowest hole mobility ($2.4x10^{-6}$ cm^2 V^{-1} s^{-1}). Interestingly, the mixed solvent, DCB:CF, exhibited the lowest W, 102 meV, suggesting that improved polymer order can be achieved using mixed solvents to tune the vapor pressure, which also impacts the overall conditions surrounding the developing film. As noted above, evaporative cooling during the film deposition process using DCB:CF is likely to occur, effecting a change in system temperature during solidification. In turn, temperature may be expected to have significant impact on the resulting BHJ morphology. For instance, the solubility of a given polymer in any given solvent is thermodynamically controlled and will be affected by temperature.[130, 131] In the present case, evaporative cooling will lower the system temperature, thereby decreasing solute solubility. The dynamic changes that take place during solvent evaporation, particularly evaporation of a mixed solvent system where the components have significantly different vapor pressures, will impact the overall morphology of the solidifying film.

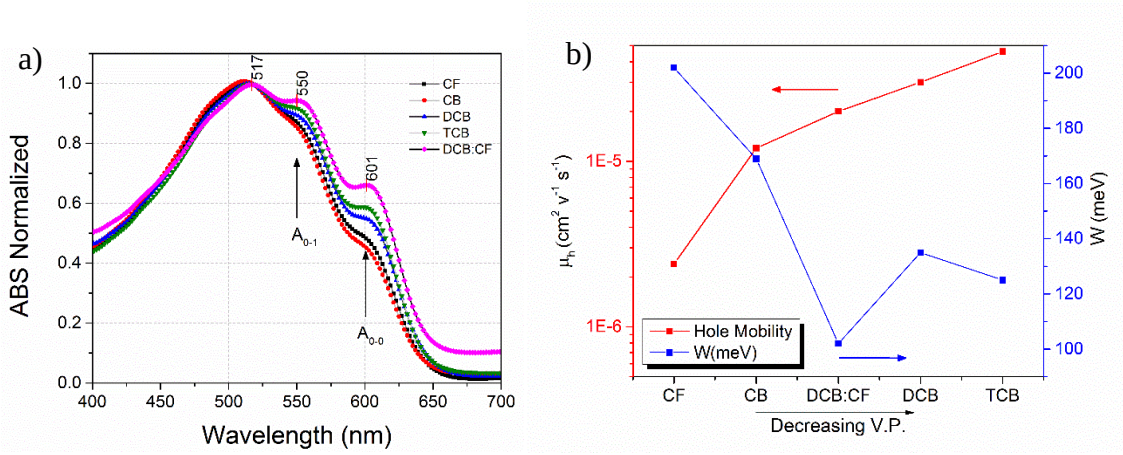

Figure 44. a) Absorbance spectra of annealed blade coated P3HT:PCBM films cast from the five solvent systems. b) SCLC hole mobility and exciton bandwidth (W) of P3HT:PCBM cast from the five solvent systems in order of decreasing vapor pressure.

3.7. Incident photon-to-current efficiency (*IPCE*).

Figure 45 depicts the measured incident photon to current efficiency (IPCE) in the range of 300 nm – 700 nm. Integration of the IPCE curves matches the experimentally determined J_{sc} values (Table 3) to within 7% difference.

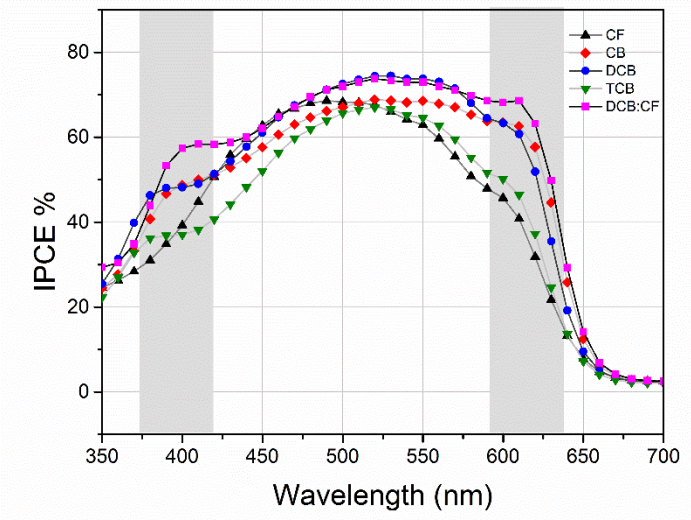

Figure 45. IPCE of devices fabricated with a blade coated P3HT:PC_{60}BM active layer.

Table 3.Calculated J_{sc} from IPCE compared to J_{sc} values determined under AM1.5G 1 sun.

IPCE/J-V	CF	CB	DCB	TCB	DCB:CF
Jsc	8.96/9.51	10.13/10.91	10.42/10.44	8.75/8.82	11.12/11.62
% Difference	5.80%	7.10%	0.20%	0.80%	4.3%

Examination of Figure 45 reveals the presence of pronounced shoulders in the range of 375 nm – 425 nm and 575 nm – 625 nm for the devices fabricated with the active layer/low vapor pressure solvent (CB, DCB and TCB) systems. These peaks are not as developed in films obtained from CF. Presumably, the lower vapor pressure solvents facilitate P3HT:PCBM phase separation into more defined domains of polymer and fullerene simply because of the time-span for solvent evaporation. While the polymer:fullerene blend is well mixed in CF, the film dries rapidly with insufficient time for an optimized interpenetrating bulk heterojunction network to develop. Furthermore, upon examination of the mixed solvent system, the shoulders at 390 nm and 600 nm are significantly more developed explaining the increased J_{sc} as compared to the single solvents systems. This result re-enforces the contention that solvent vapor pressure, and thus the rate with which the solvent evaporates from the blade coated active layer, is a key variable that must be controlled in order to achieve high efficiency devices through enhancing J_{sc}.

Furthermore, there is a difference in the λ_{max} as determined from the ICPE amongst the different P3HT:PCBM blade coated films. That obtained from CF exhibits a λ_{max} at ~490 nm, while use of CB and TCB afford films with a λ_{max} at ~520 nm, and DCB, DCB:CF lead to a broadening of the IPCE spectra in which a clear λ_{max} is not discernable.

Thus, use of high vapor pressure solvents appears to facilitate development of aggregation bands at about 610 nm, and red shift and broaden the IPCE spectrum. Notably, addition of a high vapor pressure component to DCB accentuates these effects.

3.8. Atomic Force Microscopy of P3HT:PC_{61}BM Films.

Tapping mode AFM was used to evaluate the blade coated P3HT:PC_{60}BM thin-film surface topographies. Height and phase images are presented in Figure 46.

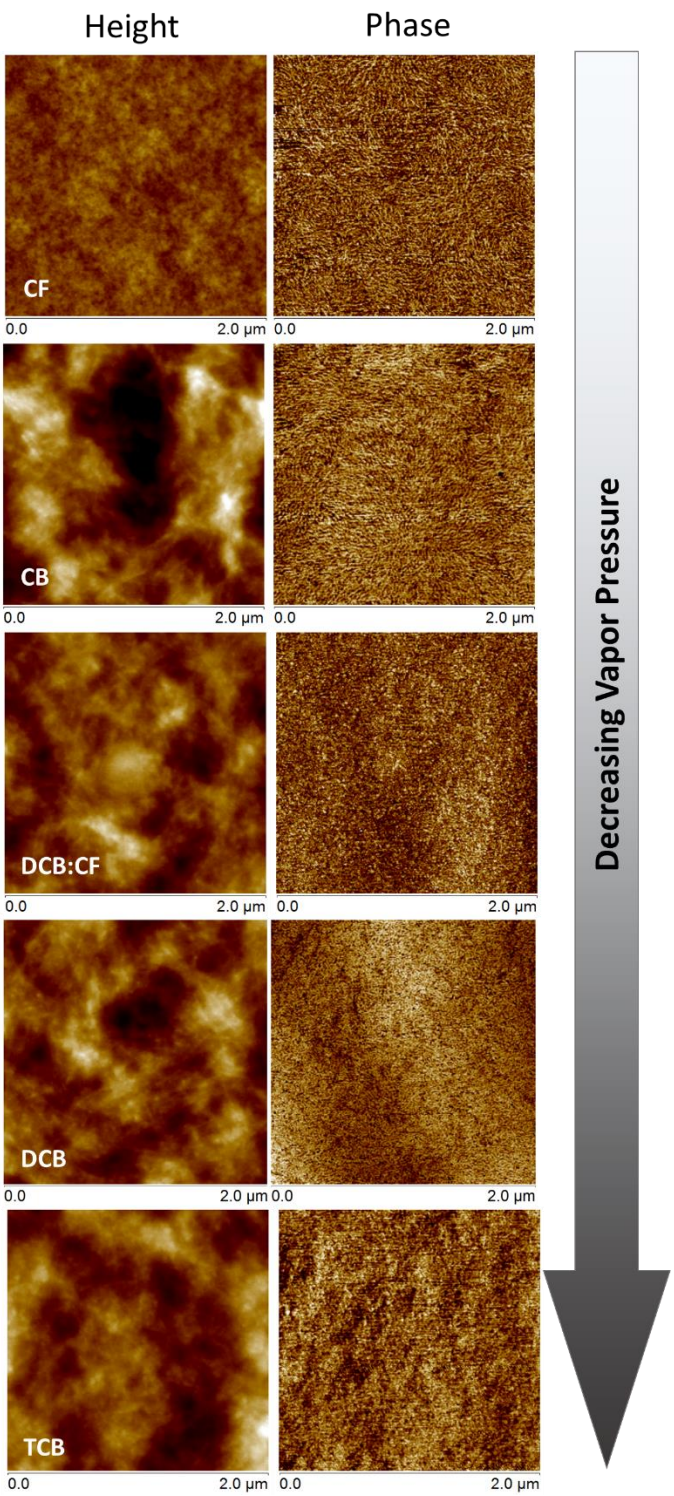

Figure 46. AFM tapping mode height (left) and phase (right) images of P3HT:$PC_{60}BM$ thin-films obtained using CF, CB, DCB:CF, DCB and TCB as the processing solvent.

From examination of Figure 46, blade coating of the active layer blend from the solvent systems investigated here has as a pounced effect on film roughness. All images are 2μm by 2 μm with a light to dark, peak to valley, height sensitivity of ±25 nm. The films coated from CF have a RMS roughness of only about 1 nm, while CB, DCB:CF, DCB and TCB films show RMS roughness values of 9.5, 5.4, 5.9, and 6.5 nm respectively. The smooth film features present in the devices fabricated from CF are attributed to the high vapor pressure of the solvent: with CF as the deposition medium, the film effectively solidifies and dries immediately upon coating. The fast drying process does not allow for sufficient time for the P3HT:$PC_{60}BM$ blend to phase separate, thus the resultant film is smoother than those prepared from lower vapor pressure solvents.[80, 138] The increased roughness apparent in films prepared from the lower vapor pressure solvents is ascribed to a higher degree of P3HT self-organization.[67, 115]

Phase images of the blade coated active layers are shown in Figure 46 on the right. The films obtained from CF and CB are quite comparable. Both present a granular-like phase structure where small fibril-like components can be discerned. These small fibrillar structures are not apparent in P3HT:$PC_{60}BM$ films prepared from either DCB or TCB. The DCB and TCB films are similar, with no clear, well defined structure. The lower vapor pressure DCB and TCB solvents evaporate more slowly from the solidifying active layer and thereby provide time for development of a much more finely grained nanoscale morphology that was not discerned. The phase image for the blend deposited from the mixed solvent shows no definitive characteristics.

3.9. Relating Solvent Characteristics to Solar Cell Performance.

The impact of chlorinated solvent characteristics, specifically the effect of vapor pressure, on the performance of inverted solar cells prepared with blade coated P3HT:$PC_{60}BM$ active layers has been investigated. From the single solvent systems examined here, DCB provides a morphology that facilitates optimum device performance. However, a mixed solvent system having a combination of high and low vapor pressure solvents formed a more advantageous composition allowing for an optimum time for solidification of the film and formation of a nanoscale morphology conducive to charge separation and transport, thereby maximizing OPV device performance. These results correspond well with other studied conjugated polymer systems. For instance, Russell and co-workers demonstrated that solvent mixing of CF and DCB proved advantageous for the low bandgap polymer pDPP and $PC_{71}BM$.[80] The evaporation of CF induces crystallization of pDPP due to the poor solvent quality interactions with the remaining solvent, DCB, while DCB aids to solubilize $PC_{71}BM$. As DCB is a poor solvent for this polymer, it aids in crystallization during solidification. At the same time, it is well known that DCB is a good solvent for PCBM, thus there for there is finer phase separation between the crystallized polymer and fullerene in the blend. While CF, CB, DCB, and TCB, are known to be good solvents for P3HT:$PC_{60}BM$, when used as solvents for blade coating the active layer films, resultant thin-film morphologies and ultimate OPV device characteristics markedly differ. OPV performance was demonstrated to improve for devices prepared with P3HT:$PC_{60}BM$ blends processed with lower vapor pressure solvents, but only up to a threshold value. After crossing that threshold, performance decreases dramatically as seen with DCB and TCB. Solvent mixing will likely be pivotal to achieve optimum device

efficiencies and could also be beneficial as a method for fine tuning surface energies to obtain uniform blade coated thin films for OPV devices. A key finding is that bulk heterojunction morphology development occurs during a short period of time in the film solidification regime. As demonstrated by in situ UV–vis spectroscopic analysis, polymer packing occurs during a short, defined point in time when solvent evaporation occurs rapidly. As ascertained from the results associated with the mixed DCB:CF solvent system, temperature and thus system thermodynamics and phase behavior are also important in defining the ultimate film morphology which plays a significant role in solar cell performance.

CHAPTER 4. SIMPLE TRANSFER FROM SPIN COATING TO BLADE COATING THROUGH PROCESSING AGGREGATED SOLUTIONS OF P(T3-TPD)

4.1 Introduction.

As conjugated polymers used in bulk heterojunction (BHJ) solar cells continue to be developed and refined, many structurally dissimilar systems now exhibit elevated AM 1.5G power conversion efficiencies (PCE) between 8% and 11%.[41, 139, 140] The material diversity presented in laboratory scale devices drives a need for developing and understanding rules for scaling to large scale coating processes. Recent attention has brought up the importance of transitioning laboratory studies away from spin coating to roll-to-roll compatible processing methods, such as blade coating, spray coating, and slot die coating, that more properly mimic practical processing approaches and yield thin films with morphologies that match those that will be obtained in large scale production.[141,142] Within the multi-component processing solutions (inks) employed for polymer:fullerene,[44] polymer:non-fullerene acceptor,[143] and polymer:polymer blends,[144] the use of processing additives to enhance performance through morphology control has become wide-spread.[44, 145, 146] However, a clear understanding of both the influence that processing type has on morphology and the mechanisms of how these additives interact with the various components to form a more optimum phase separated morphology has not emerged.

A review of non-spun coat, small area devices found that, as of 2013, in 36 trials only 4 systems demonstrated PCE greater than 4%, indicating the general complexity of using spin coating to guide scalable deposition.[141,147] Blade coating is an easily implemented prototyping tool[84] for direct comparison to continuous deposition processes

such as slot-die coating.[148] With care, similar PCE can be attained between optimized spun coat and blade coat devices.[111-113, 115, 149, 150] The transfer from spin coating to blade coating usually involves re-optimization of both the starting solution and deposition conditions, such as substrate temperature, in order to match the drying dynamics of spin coating.[151, 152] Zhao et al. found that simple transfer from spin coating to blade coating of PTB7, PTB7-Th, and PBDTTT-CT yielded decreased organic photovoltaic (OPV) performance for blade coated samples. A re-optimization was required that included tuning the solution solids content, processing at an elevated temperature and changing the additive concentration to maintain similar additive to solute volume ratio in order to mimic the drying kinetics of spin coating and achieve similar device performance and film morphology.[153] In contrast, recent work by Ro et al. showed that optimized blade coating of PffBT4T-2OD:$PC_{71}BM$, while yielding similar OPV performance to spin coating, not only required significant modification in coating conditions (substrate temperature) but produced significantly different film morphologies.[148]

In this study, we utilize the high performance, semi-crystalline polymer poly[5-(2-hexyldecyl)-1,3-thieno[3,4-c]pyrrole-4,6-dione-alt-5,5-(2,5-bis(3-dodecylthiophen-2-yl)-thiophene)], P(T3-TPD), developed by Marks and co-workers,[154-156] to explore in detail the effect that ink formulation (presence of solution additive) and processing type (spin coating or blade coating) have on dry film morphology and OPV performance. P(T3-TPD) has been demonstrated to provide high power conversion efficiencies when processed via spin coating with $PC_{71}BM$ and the processing additive 1,8-diiodooctane (DIO),[154] and in polymer:polymer blends with N2200 when processed with the solvent additive 1-chloronapthalene.[156] We find no re-optimization of solution composition is necessary when

transferring from spin coating to blade coating. We attribute this to processing from an aggregated solution that predetermines the solid state morphology regardless of the processing method which is advantageous for the scaling of OPV technology. To gain further insight into how phase separated morphology is developed with the solvent additive DIO, and without DIO (w/o DIO), we perform in situ UV-vis absorbance and reflectance on blade coated films. In situ thin film measurements, coupled with ex situ film measurements, reveal that DIO increases the nucleation density during solidification, leading to reduced domain size and enhanced polymer crystallinity in the BHJ film.

4.2. Experimental.

***Organic solar cell fabrication*.** Patterned indium tin oxide (ITO) was sonicated in a solution of sodium dodecyl sulfate and Millipore water, then rinsed with Millipore water, followed by sonication in acetone, then isopropanol for 5 minutes in each solution. The ITO was blown dry with nitrogen gas, then UV ozone cleaned for 10 minutes. ZnO sol-gel[157] was spun coat onto the ITO at 800 r.p.m. for 50 seconds and then annealed at 300 °C for 5 minutes in air resulting in a 30 nm thick film. Solutions of P(T3-TPD):$PC_{71}BM$ (1:2 weight ratio, [12 mg mL^{-1}], in chloroform, or in chloroform:DIO (98%:2% by volume), were either blade coated onto the substrates in air with a blade to substrate gap of 300 μm and a blade velocity of ≈20 mm s^{-1} or spun coat at 3000 r.p.m. for 60 s in an Ar filled glovebox. Films processed from $CHCl_3$ without DIO were immediately placed in a thermal evaporator for contact deposition, while films processed from $CHCl_3$ with 2% DIO added by volume were allowed to dry 2 hours in ambient air for blade coated films, or in an Ar filled glovebox for spin coated films, prior to electrode deposition. Devices were placed in a thermal evaporator at a pressure of < 10^{-5} mbar for 1 hour prior to sequential deposition

of 8 nm MoO_3 followed by 120 nm Ag which were used as the top electrodes. The active area of the devices, defined by the overlap of the top and bottom electrode, was 0.07 cm^2. Film thicknesses for blade coated devices were optimized to achieve the highest PCE and measured using a Bruker DetakXT profilometer. Devices were tested in an Ar filled glovebox using a Newport class ABB solar simulator coupled with a Keithley SMU 2410 for measuring device efficiency under standard AM 1.5G conditions calibrated to 95 mW cm^{-2}. A Newport EQE/IPCE setup with a Newport 66485 xenon lamp, an Oriel CS26 VIS-NIR 1/4 m monochromator, and a Merlin 70104 Digital Lock-in radiometry detector, was used.

X-ray Scattering. Grazing incidence wide angle X-ray scattering (GIWAXS) measurements were carried out on beamline 11-3 at the Stanford synchrotron radiation light source (SSRL). The beam energy was 12.7 keV. The angle of incidence was 0.12°, whereas the nominal critical angle for the films at the used energy is about 0.08°. A LaB_6 standard sample was used to calibrate the instrument and the software WxDiff[91] version 1.11 was used to reduce the 2-D scattering data into the corrected 1-D integration plots (I vs q and I vs chi). The sample to detector distance was ca. 150 mm. The crystalline correlation length (CCL) was estimated using $CCL = 2\pi/\Delta q_{FWHM}$, where Δq_{FWHM} is the full width half maximum of the (100) peak.[158] Grazing incidence small angle X-ray scattering (GISAXS) was also carried out at SSRL on beamline 1-5 with the beam energy set to 10 keV and an incidence angle of 0.12° was used. The sample to detector distance was ca.2900 mm. IGOR PRO with Nika,[92] and Irena, packages were used to reduce the GISAXS data.

Space Charge Limited Current (SCLC) Hole devices. ITO, cleaned in the same fashion as solar devices, was coated with PEDOT:PSS (Al 4083) filtered through a 0.45 μm nylon

filter, by spin coating in air at 5000 r.p.m. for 60 seconds. Films were dried in ambient air on a hot plate at 120°C for 10 minutes. A solution of P(T3-TPD):$PC_{71}BM$ (1:2 weight ratio), [12 mg mL^{-1}], was blade coated with a 500 µm gap at 30 mm s^{-1} to produce films that were 300 nm thick, measured using a Bruker DetakXT profilometer. Devices were allowed to dry, followed by evaporation of 100 nm of Au. SCLC hole mobility was determined in the same way as reference [159].

Atomic force microscopy (AFM). AFM was collected using a Bruker atomic force microscope (Dimension icon) with a Bruker Tap 150 cantilever in standard tapping mode.

In situ UV-vis measurement. In situ UV-Vis absorbance/reflection spectra were collected during deposition of films using optimized solar cell parameters. Solutions of P(T3-TPD):$PC_{71}BM$ (1:2 weight ratio [12 mg mL^{-1}] were coated on top of quartz that was cleaned with isopropanol, then UV ozone cleaned for 10 minutes. A fiber optic spectrometer based system (Dual spectrometer - Ocean Optics Inc. SD 2000) was used to simultaneously record s-polarized reflection and p-polarized transmission spectra at an incidence angle near the substrate's Brewster angle (≈ 56°). Polarizers were setup in front of the collection optics to select p-polarized light for the transmission and s-polarized light for the reflection and the incident light is non-polarized. The integration time for both the transmission and reflection channel were 50 ms, and the first available spectra was stored every 50 ms for further analysis.

4.3. Results and Discussion.

4.3.1. Solution Properties.

P(T3-TPD), having the repeat unit chemical structure shown in Figure 47 a), and a number average molar mass (M_n) of 19.7 kDa, was synthesized according to a modified literature procedure. The polymer was found to be soluble in chloroform up to ~3 mg mL^{-1} at room temperature by passing a known amount of solution through a 0.45 μm PTFE filter onto a pre-weighed glass slide and taking the mass difference and insoluble in DIO at room temperature. Figure 47 b) shows the temperature dependent UV-vis absorbance of P(T3-TPD) in chloroform indicating that it displays thermochromism in dilute solution (~ 0.1 mg mL^{-1}). At elevated temperature, the polymer is in a non-aggregated state and the solution appears orange, while at room temperature the polymer is aggregated and the solution appears purple. This observed thermochromic transition was found to be reversible with no hysteresis (Figure 48). Figure 48 also shows the thermochromic behavior of P(T3-TPD):$PC_{71}BM$ solutions b) w/o DIO and c) with DIO. When the polymer is in a non-aggregated state at 50 ºC, its λ_{max} is at 480 nm. As the solution cools to room temperature, there is a planarization of the polymer backbone, extending the conjugation length,[160] which causes the λ_{max} to shift to 580 nm, along with the development of a low energy shoulder at 635 nm. The longer wavelength absorbance is typically attributed to an increased aggregation of the polymer chains.[161] Figure 47 c) shows the UV-vis absorbance spectra of the BHJ solution (solid line) and BHJ thin film (dashed line) normalized to the $PC_{71}BM$ peak at 375 nm with DIO and w/o DIO. The addition of DIO to a dilute (0.04 mg mL^{-1}) BHJ solution, seen in the UV-vis absorbance solution spectra in Figure 47 c), shows a slight increase in absorbance intensity suggesting that DIO promotes additional

aggregation. The BHJ thin film UV-vis absorbance, normalized to the $PC_{71}BM$ peak at 375 nm, also shown in Figure 47 c), demonstrates that DIO significantly increases the polymer order in the dry film evidenced by the increase in optical absorbance of the low energy peaks, and a shift in the λ_{max} of 20 nm. It is important to note that all thin films used in this study are processed at room temperature meaning that a solution of aggregates are being coated and not a well dissolved solution.

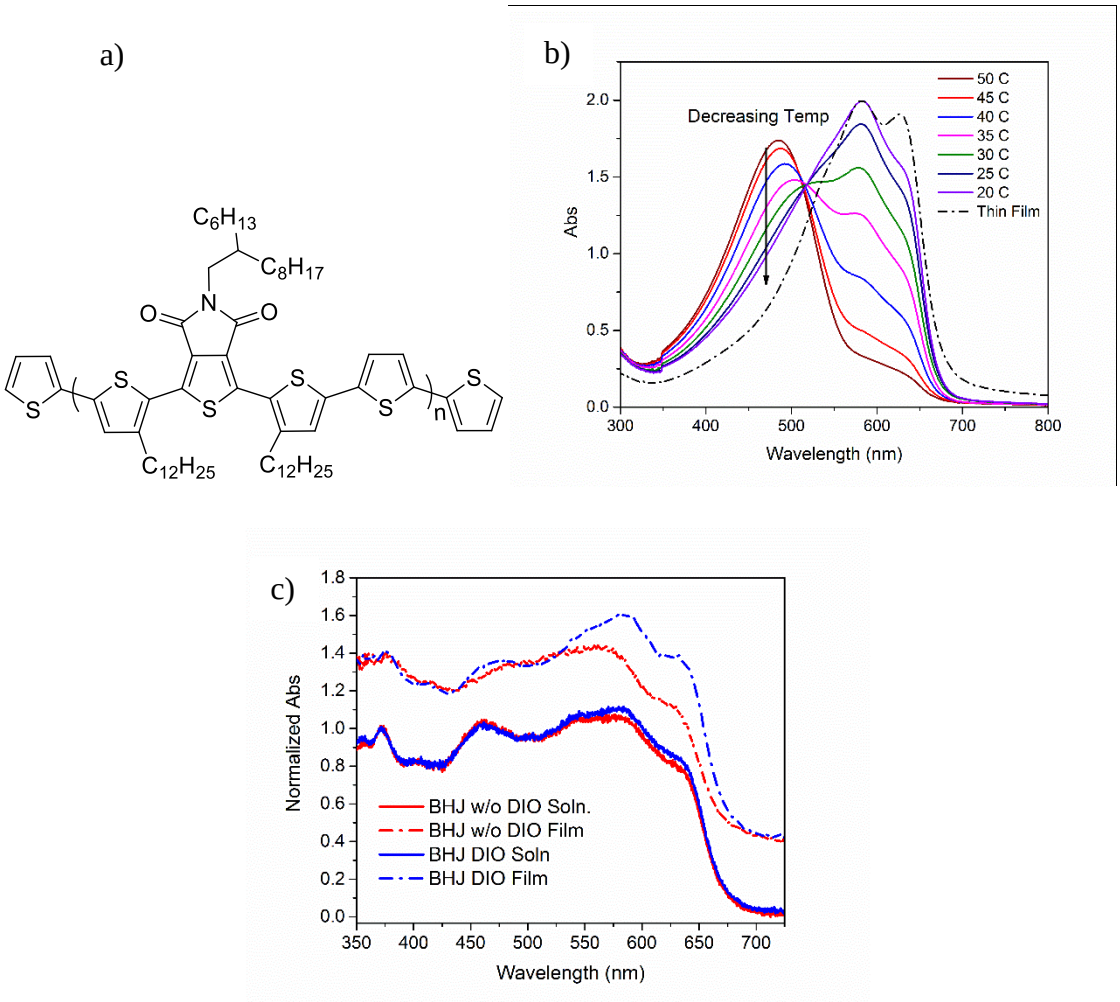

Figure 47. a) Repeat unit structure of P(T3-TPD), b) temperature dependent solution UV-vis absorbance spectra of neat P(T3-TPD) in chloroform and thin film UV-vis of neat P(T3-TPD). c) Comparison of spectra of the solution and dry film with DIO and w/o DIO. The

solid lines show P(T3-TPD):$PC_{71}BM$ in chloroform with DIO and w/o DIO at 25°C. Dashed lines correspond to the UV-vis absorbance of BHJ thin film processed with DIO and w/o DIO. For clarity the absorbance of the films with DIO and w/o DIO was offset by 0.4.

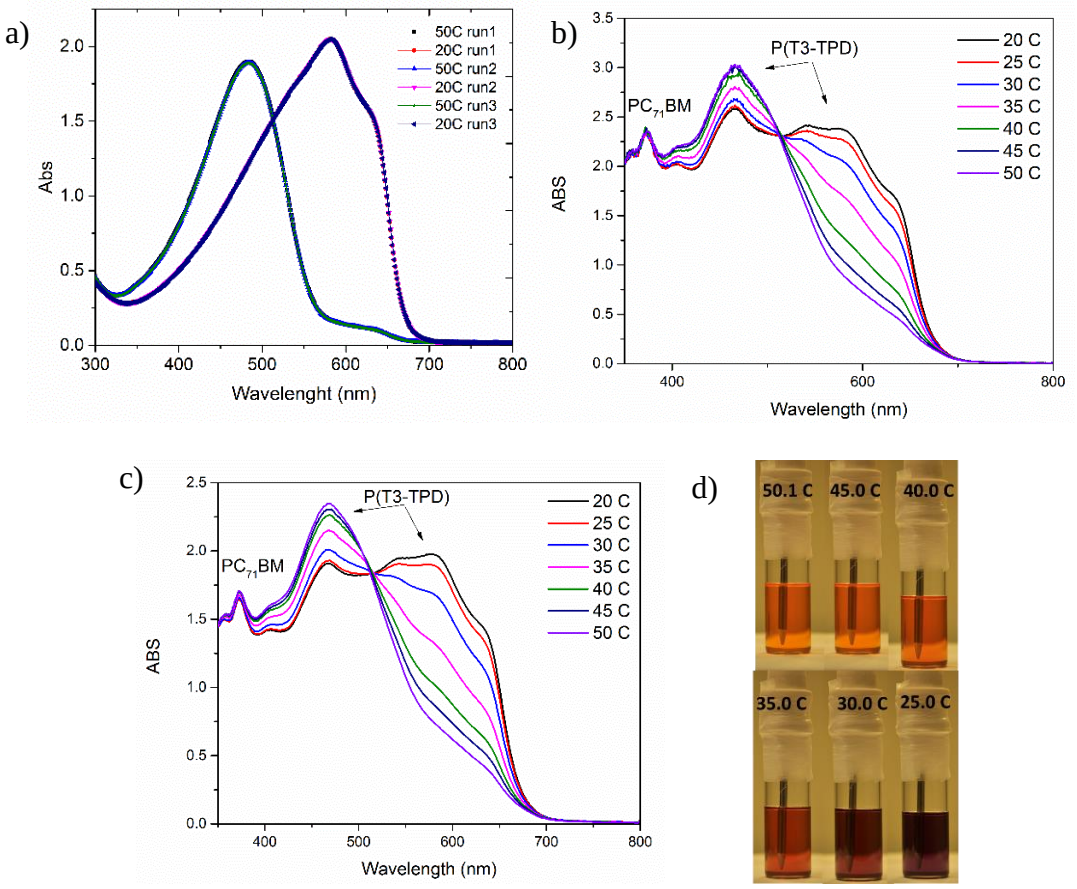

Figure 48. a) Solution UV vis absorbance of three heating and cooling cycles of P(T3-TPD) in CF at 50 ºC and 20 ºC. Overlapping spectra indicated no hysteresis effect. b) P(T3-TDP):$PC_{71}BM$ in CF [~0.12 mg/mL]. c) P(T3-TPD):$PC_{71}BM$ in CF:DIO [~0.1 mg/mL], d) pictures of neat P(T3-TPD) in CF at varying temperatures.

4.3.2. Photovoltaic Properties.

Bulk heterojunction OPV devices were processed at room temperature from chloroform, w/o DIO, or chloroform with 2% DIO added by volume, labeled as DIO, using an inverted solar cell architecture of ITO/ZnO/P(T3-TPD):$PC_{71}BM$ (1:2 weight ratio)/MoO_3/Ag. Figure 49 a) shows the current-voltage characteristics (*J-V* curves) of devices made with DIO and w/o DIO processed using spin coating or blade coating demonstrating that a small amount of DIO added has a pronounced effect on the solar cell electrical characteristics for both deposition techniques. Table 4 shows the addition of DIO afforded a fivefold increase in short circuit current density (J_{sc}) and *PCE*, along with an increase in fill factor (*FF*) from 44% to 61% for blade coated samples. The large increase in short circuit current is represented in the external quantum efficiency (*EQE*) spectrum, Figure 49 b), where the addition of DIO leads to a significant increase in photon conversion between 350 nm to 700 nm, whereas the films processed from chloroform alone show EQE values <20 % across the spectrum. Table 5 shows the integrated EQE J_{sc} values closely match the experimentally determined J_{sc}. When blade coating is compared to spin coating, the photovoltaic characteristics are similar with comparable reproducibility. While spin coated samples were processed in an Ar filled glovebox, blade coated samples were processed in ambient air, indicating that this system is not sensitive to processing type or atmosphere, which is advantageous for large scale ambient processing. The optimized film thickness for BHJ films cast from $CHCl_3$ was found to be ca. 90 nm while the optimized thickness for BHJ films cast with DIO was found to be 150 nm. The observation that films processed with the solvent additive optimize at greater thickness suggests reduced recombination and improved transport. Interestingly, no further optimization was needed

when transferring from spin coating to blade coating to produce similar OPV performance. The solution used for spin coated devices is the same solution used for blade coated devices and the processing temperature remained the same.

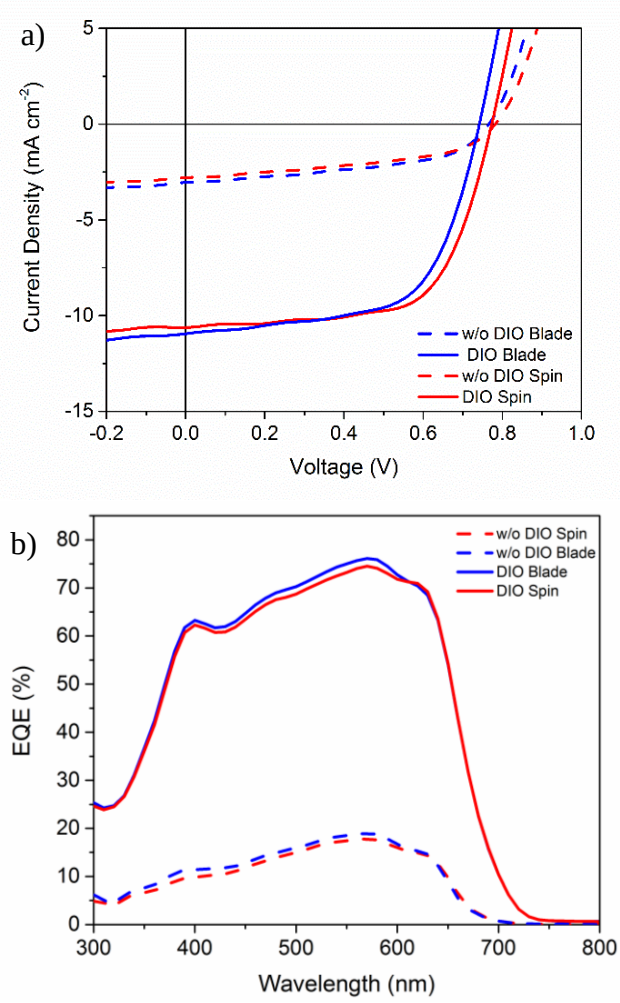

Figure 49. a) J-V characteristics of P(T3-TPD):$PC_{71}BM$ processed w/o DIO and with DIO, and processed via blade coating and spin coating. b) EQE of P(T3-TPD):$PC_{71}BM$ processed w/o DIO and with DIO via blade coating or spin coating.

Table 4. Comparison of solar cell electrical characteristics of P(T3-TPD):$PC_{71}BM$ processed w/o DIO or with DIO by blade coating or spin coating. Averaged values were obtained from 8 devices. Numbers in parenthesis represent best performing device.

Processing Condition	J_{sc} (mA/cm^2)	V_{oc} (V)	FF (%)	PCE (%)	Film Thickness (nm)
DIO (Blade)	11.5 ± 0.5 (11.8)	0.73 ± 0.01 (0.74)	61 ± 2 (61)	5.4 ± 0.1 (5.6)	150
w/o DIO (Blade)	2.7 ± 0.2 (3.0)	0.75 ± 0.02 (0.78)	44 ± 3 (48)	1.0 ± 0.1 (1.2)	90
DIO (Spin)	11.0 ± 0.5 (10.6)	0.74 ± 0.02 (0.76)	62 ± 3 (65)	5.3 ± 0.2 (5.5)	140
w/o DIO (Spin)	2.7 ± 0.2 (2.9)	0.75 ± 0.02 (0.78)	43 ± 3 (47)	0.9 ± 0.1 (1.1)	80

Table 5. Calculated J_{sc} from EQE and measured J_{sc} for P(T3-TPD):$PC_{71}BM$ solar cells.

	J_{sc} Spin w/o DIO	J_{sc} Blade w/o DIO	J_{sc} Spin DIO	J_{sc} Blade DIO
EQE	2.5	2.6	12.5	12.3
Measured	2.7	2.7	11	11.5
% difference	7.7%	3.4%	12.8%	6.7%

4.3.3. Thin Film Morphology.

To elucidate the effect DIO has on P(T3-TPD):$PC_{71}BM$ BHJ thin film solidification, and to understand how this impacts solar cell performance, the morphology of dry spin coated and blade coated films was investigated. Atomic force microscopy (AFM) was used to qualitatively probe the morphology of the BHJ system. Figure 50 depicts AFM height images of the BHJ film processed from the two solvent systems.

Height images of the BHJ films processed w/o DIO show large features for both blade coated and spin coated films. The average feature diameter seen in blade coated samples is ≈280 nm, and in spin coated films is ≈260 nm which is in agreement with TEM images reported by Guo et al.[154] Evaluation of the topographic contrast demonstrates that the effect DIO has on polymer:fullerene phase separation is striking. Two key features stand out when examining the topographical contrast seen in the height images. First is how fine the phase separation is between polymer rich and fullerene rich phases. This observed reduction in feature size suggests an increased interfacial area between the polymer and fullerene, allowing for increased charge separation that would account for the large increase in J_{sc} seen in the photovoltaic parameters. Secondly, the small fibril like structures, which are not seen in the BHJ films processed w/o DIO, indicates there is a change in polymer order at the surface. This trend is seen in both spin and blade coated films signifying that processing of aggregated P(T3-TPD):$PC_{71}BM$ solutions yields similar surface topologies.

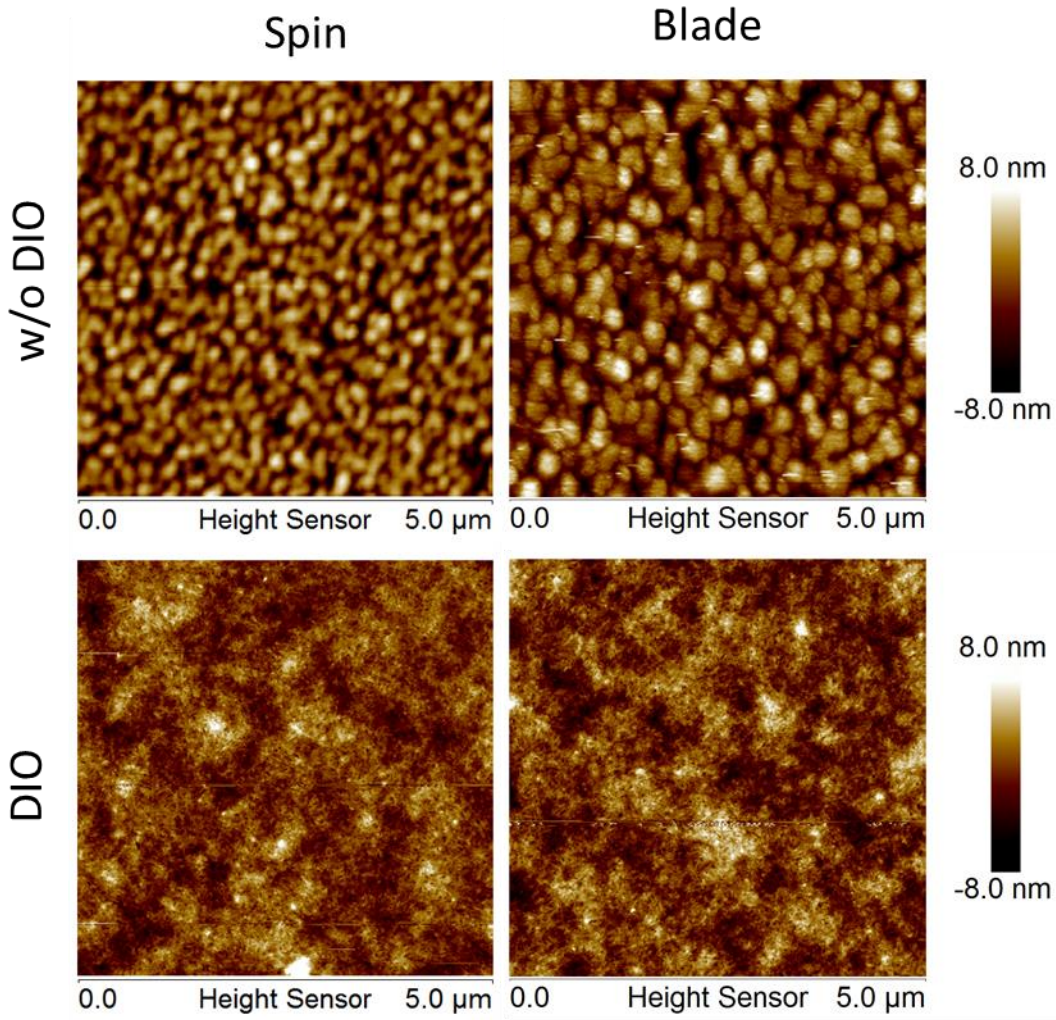

Figure 50. AFM height images of P(T3-TPD):$PC_{71}BM$ films processed by spin coating or by blade coating with DIO or w/o DIO. The image size in all cases is 5µm x 5µm.

Grazing incidence small angle X-ray scattering (GISAXS) was used to probe the bulk morphology of the BHJ films processed with DIO and w/o DIO. Figure 51 shows log-log film thickness normalized GISAXS 1D line profiles at $q_z \approx 0$ of BHJ films processed using spin coating or blade coating both with DIO and w/o DIO. Films processed with DIO show a feature at scattering vectors q_{xy} of approximately 0.017 $Å^{-1}$ which corresponds to a

domain spacing, calculated using $2\pi/q_{xy}$, of ca. 37 nm for both spin coated and blade coated films. The increase in scattering intensity seen in the films processed with DIO suggests enhanced domain purity, which is consistent with other high performance semi-crystalline polymer:fullerene systems.[41, 162] The GISAXS of films processed without the solvent additive do not show a defined 'Guinier knee'[163] in the probed range indicating that the length scale is larger than 125 nm, consistent with the AFM. Remarkably, the BHJs processed using spin coating or blade coating show near identical characteristic length scales, in contrast to high performance systems such as PffBT4T-2OD,[148] and PBDT-TSR[164], which demonstrate different characteristic length scales based on deposition method.

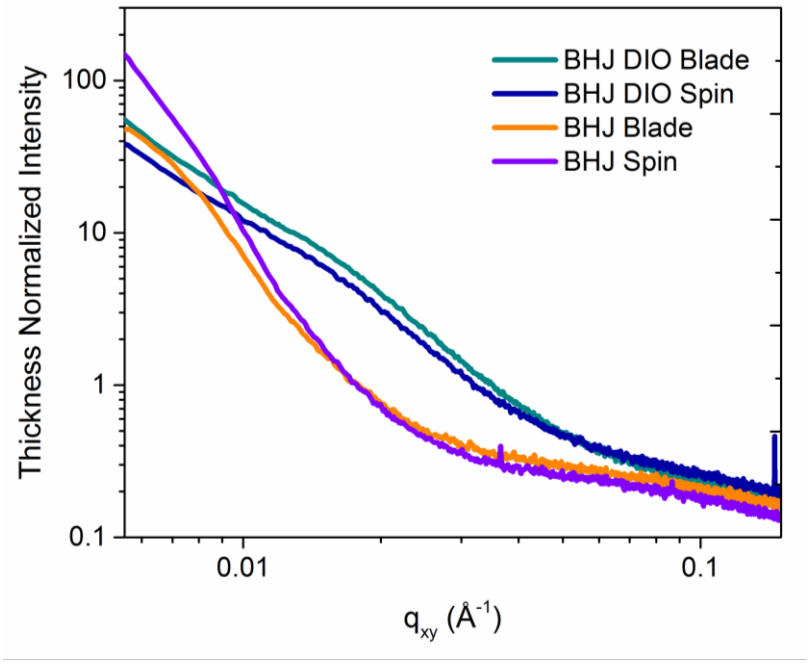

Figure 51. Thickness normalized GISAXS of BHJ films processed with DIO and w/o DIO using blade coating and spin coating.

In order to further understand the impact that processing type and additive have on polymer order, crystallinity, crystal orientation, and lamellar spacing, grazing incidence wide angle X-ray scattering (GIWAXS) was performed. Figure 52 shows the film thickness and illumination time normalized (100) pole figures for spin coated, and blade coated, P(T3-TPD) and P(T3-TPD):$PC_{71}BM$ processed with DIO and w/o DIO extracted from 2D images shown in Figures 53 - 56. Also shown in Figure 52 (insets) is the relative degree of crystallinity (rDoC), calculated using $\int_0^{\frac{\pi}{2}} I(\chi) \sin\chi \, d\chi$,[90] as a function of sample. From Figure 52 a) it can be deduced that DIO has a twofold impact. First, it changes the polymer crystallite orientation from being bimodal (significant edge on and face on components) to mostly face on when processed with DIO. This is evident from the loss of intensity centered around $\chi \approx 0$ º and increase in intensity near $\chi \approx \pm 90$ º. Secondly, DIO changes the rDoC. When the neat polymer is processed with the additive, DIO suppresses crystallinity; however, in the BHJ films DIO enhances polymer crystallinity. It is not uncommon to observe enhanced crystallinity in the BHJ films when a processing additive is used. This has been shown for multiple semi-crystalline polymer:fullerene blends. [44,66, 148] Examination of the blade coated films in Figure 52 b) shows similar characteristics to that of the spin coated films. First, DIO influences crystal orientation. Again, when processed without the additive DIO the crystal orientation is bimodal as indicated by the strong intensity near $\chi \approx 0$ º and $\chi \approx \pm 90$ º. The addition of DIO drastically reduces the edge on orientation and increases the face on crystal orientation analogous to spin coated films. Like the spin coated samples, the addition of DIO suppresses polymer crystallization in the neat sample. However, it enhances polymer crystallization in the BHJ samples. In both the spin coated and blade coated BHJ films we find that DIO enhances polymer crystallinity,

changes the crystal orientation, and reduces domain size. The reduction in feature size found in the AFM images coupled with the enhanced polymer crystallinity in the BHJ films, shown in the GIWAXS, signals that DIO serves to increase nucleation density.

Like the results observed in the AFM and GISAXS both spin coating and blade coating of the aggregated solution yield very similar GIWAXS characteristics. The lamellar stacking distance, and π-π stacking distance, calculated from the 1D line profiles found in Figures 53 - 56, were found to be similar for blade coated and spin coated films as shown in Table 6. In fact, the only observed difference between the two processing methods is the crystal coherence length (CCL), which was found to be larger for spin coated samples relative to blade coated samples. The difference in CCL found in spin and blade coated P(T3-TPD):$PC_{71}BM$ samples indicate that a range of crystal dimensions achieves similar device performance.

a)

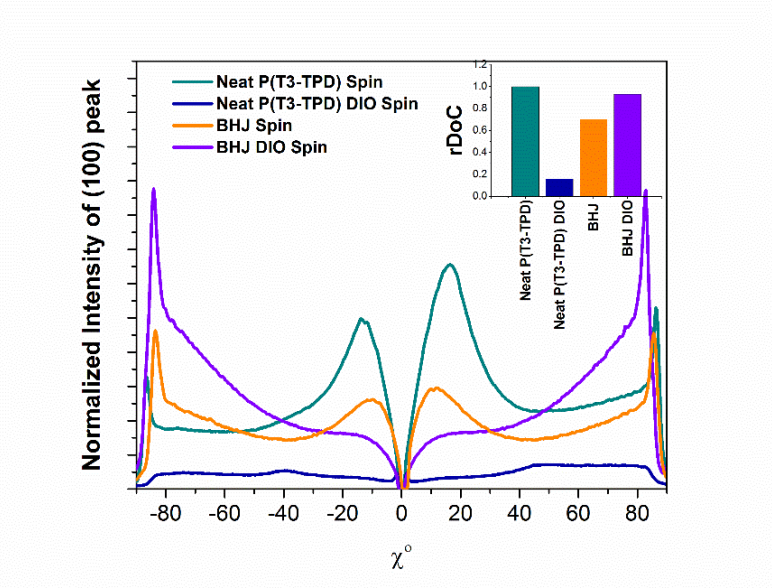

b)

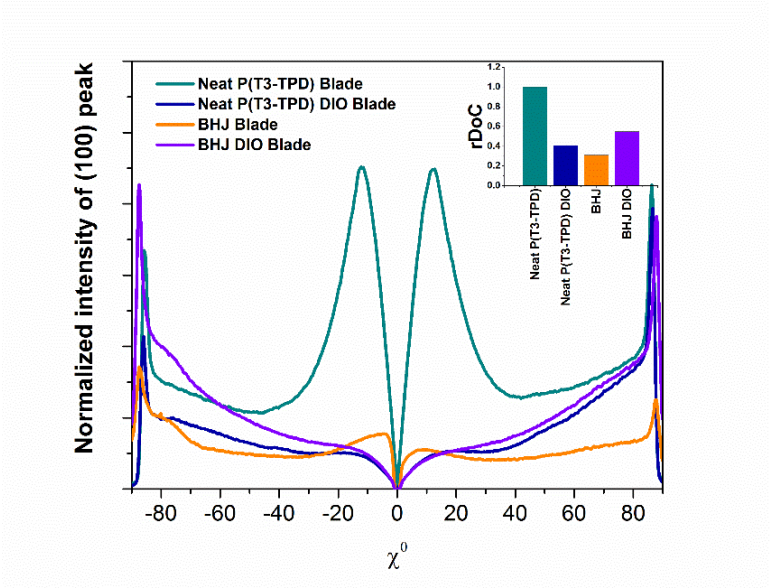

Figure 52. Thickness and illumination time normalized pole figure of a) spin coated, and b) blade coated, neat P(T3-TPD) and BHJ processed with DIO and w/o DIO. For BHJ samples the volume fraction was taken into account.

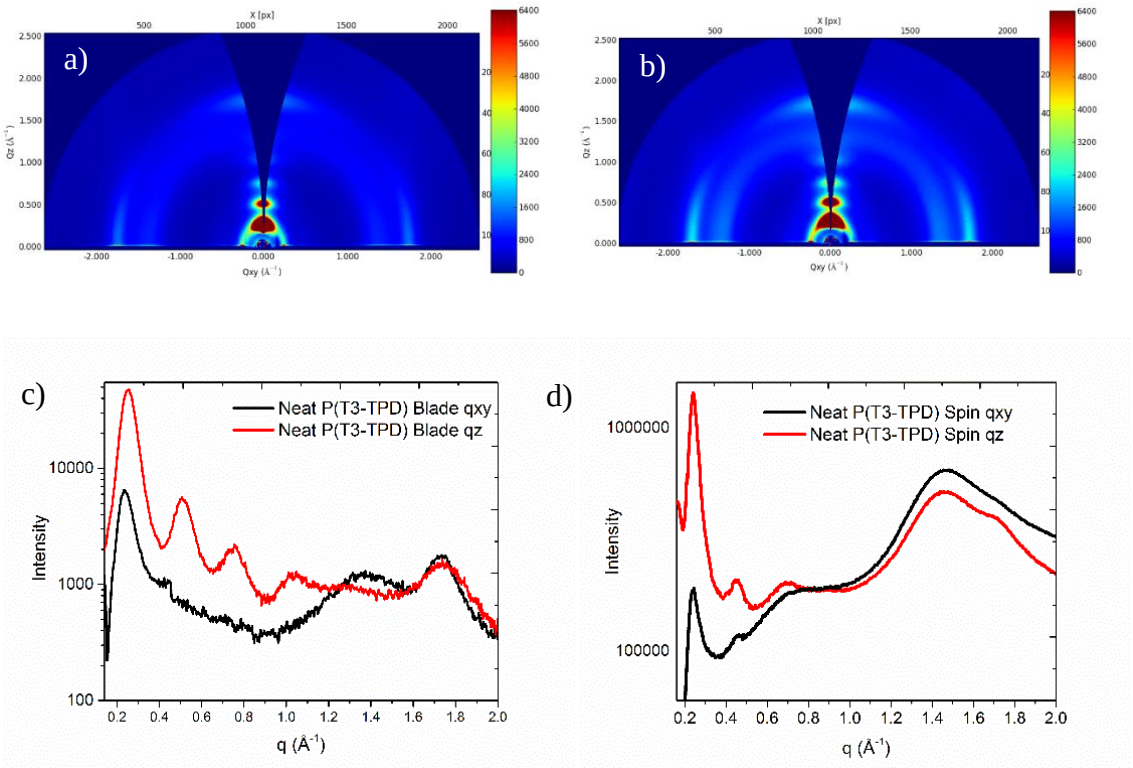

Figure 53. 2D GIWAXS image of a) neat P(T3-TPD) blade coated and b) neat P(T3-TPD) spin coated. Their corresponding c) blade coated and d) spin coated 1D line profiles in the q_{xy} and q_z direction are shown.

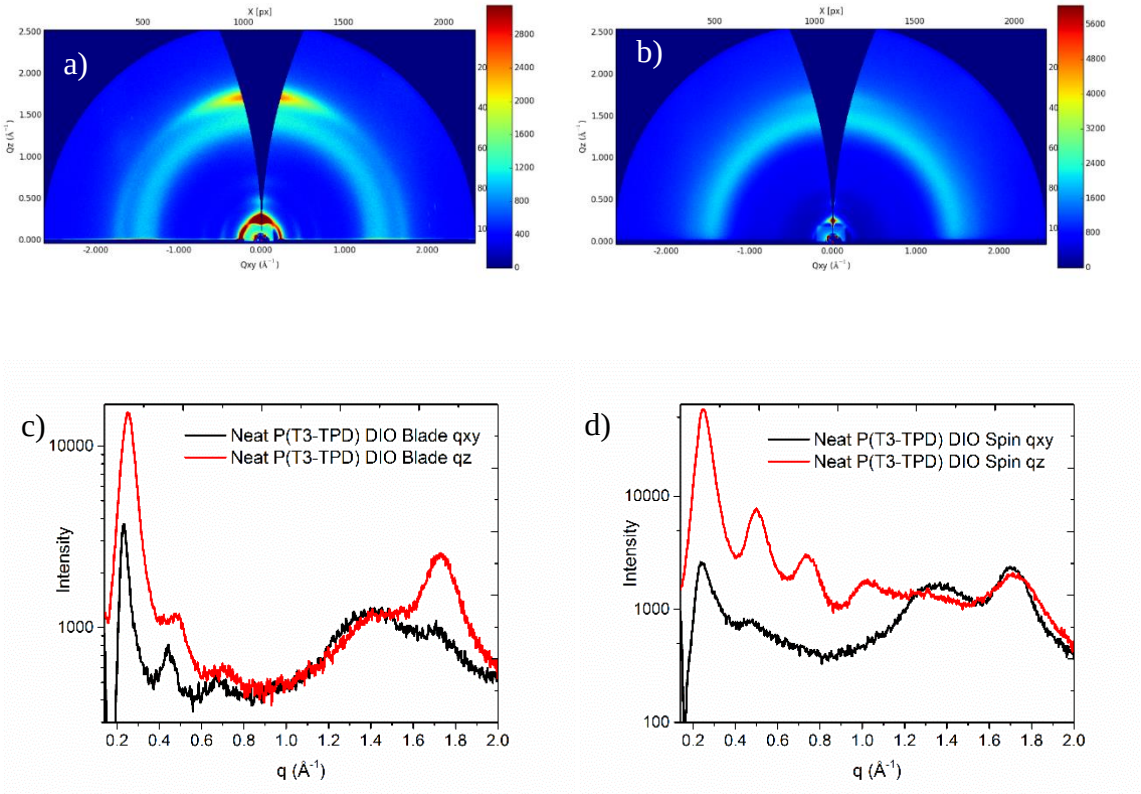

Figure 54. 2D GIWAXS image of a) neat P(T3-TPD) with DIO blade coated and b) neat P(T3-TPD) with DIO spin coated. Their corresponding c) blade coated and d) spin coated 1D line profiles in the q_{xy} and q_z direction are shown.

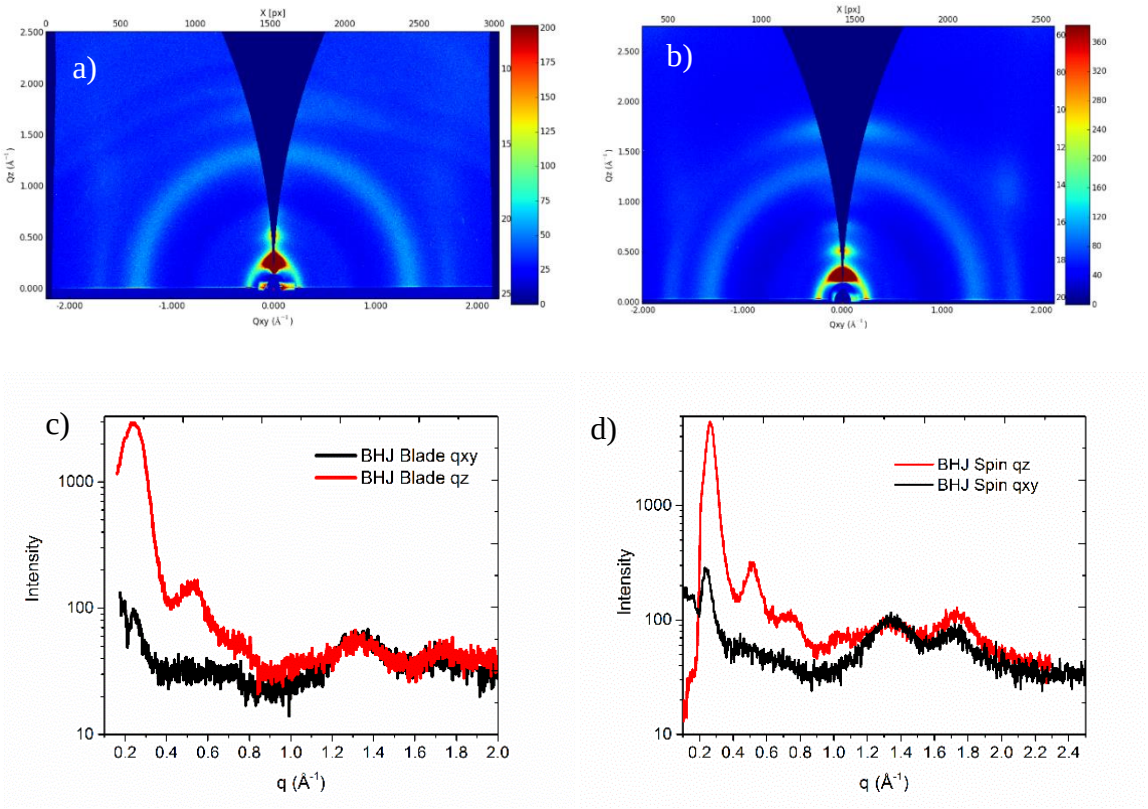

Figure 55. 2D GIWAXS image of a) P(T3-TPD):$PC_{71}BM$ w/o DIO blade coated and b) P(T3-TPD):$PC_{71}BM$ w/o DIO spin coated. Their corresponding c) blade coated and d) spin coated 1D line profiles in the q_{xy} and q_z direction are shown.

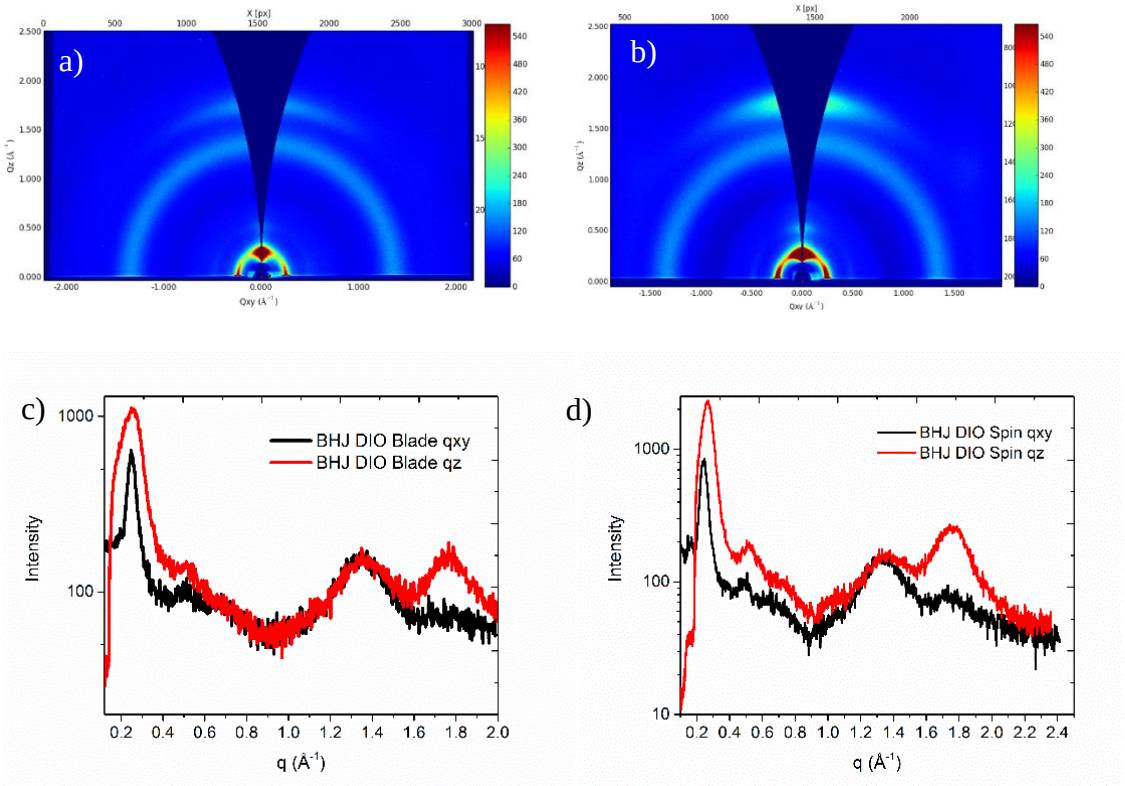

Figure 56. 2D GIWAXS image of a) P(T3-TPD):$PC_{71}BM$ with DIO blade coated and b) P(T3-TPD):$PC_{71}BM$ with DIO spin coated. Their corresponding c) blade coated and d) spin coated 1D line profiles in the q_{xy} and q_z direction are shown.

Table 6. Blade/spin coated P(T3-TPD) neat polymer, and BHJ, processed with DIO and w/o DIO lamellar stacking distance, π-π stacking distance, and crystal coherence length (CCL) values taken from 1D line cuts.

	Blade		Spin		Blade		Spin			
	(100) lamellar d spacing (Å)				(010) π-π spacing (Å)				Crystal Coherence Length (100) (Å)	
	q_z	q_{xy}	q_z	q_{xy}	q_z	q_{xy}	q_z	q_{xy}	Spin	Blade
P(T3-TPD)	25.0	27.1	26.3	26.8	3.6	3.7	3.7	3.7	107	82
P(T3-TPD) DIO	24.5	26.3	25.0	25.5	3.6	3.6	3.6	3.7	67	66
P(T3-TPD) PCBM	27.6	22.8	23.9	25.9	3.7	3.6	3.6	3.6	108	48
P(T3-TPD) PCBM DIO	24.5	25.7	23.7	25.6	3.6	3.6	3.6	3.6	77	45

4.3.4 Hole Mobility.

Space charge limited current (SCLC) measurements were performed in order to investigate whether or not the crystal orientation change from bimodal to preferentially face on contributes to increased mobility through the device, which could be the cause of the observed increase in short circuit current density. For some conjugated systems it is hypothesized that face on orientation of crystallites is beneficial for charge carrier transport to the electrodes for solar cells.[165, 166] Using a modified Mott-Gurney expression,[159] SCLC hole mobility was found to be $(1.1\pm0.4)\times10^{-4}$ cm^2 V^{-1} s^{-1} and $(2.1\pm1.2)\times10^{-4}$ cm^2 V^{-1} s^{-1} for 300 nm thick blade coated BHJ films cast w/o DIO and with DIO respectively with the deviation accounting for fit uncertainty as demonstrated in Figure 57. While the addition of DIO changes the edge-on to face-on ratio, this does not appear to have a significant

impact on charge transport. Therefore, the impact of crystal orientation with respect to the substrate seen in BHJ films processed with DIO is insufficient for explaining the large increase in J_{sc} when DIO is used as a solvent additive.

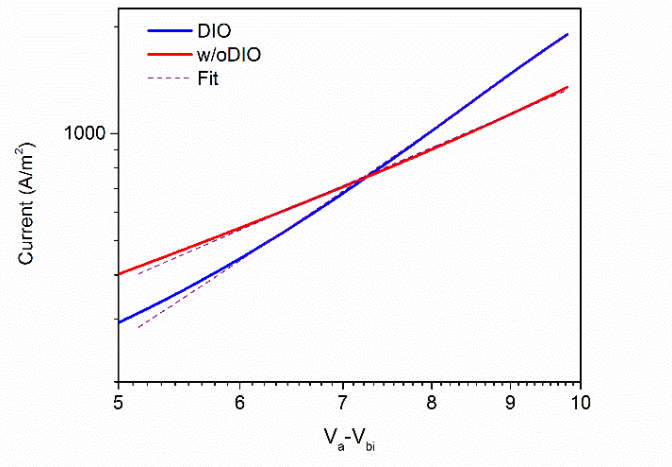

Figure 57. SCLC of P(T3-TPD):$PC_{71}BM$ processed w/o DIO and DIO. Fit was determined using $J_{SCLC} = \frac{9}{8}\varepsilon_0\varepsilon_r\mu\frac{V_{in}^2}{L^3}exp(\frac{0.89\beta}{\sqrt{L}}\sqrt{V})$, where ε_0 is the permittivity of free space, ε_r is the dielectric constant of the polymer which is assumed to be 3, μ is the mobility, β is field-activation factor, L is the active layer thickness, and V is the applied voltage (V_a) – the built in voltage (V_{bi}).

Spin coating and blade coating the same concentration solution at room temperature results in nominally identical device performance and behavior at optimal thickness w/o DIO and with DIO. This is consistent with the production of virtually identical film morphology by all measures, which is striking, given the radically different drying speeds of spin coating and blade coating.[151] We ascribe this observed similarity to the use of an aggregated solution that appears to dominate the final film morphology with respect to drying dynamics.

4.3.5 In situ UV-vis and Morphology Evolution.

In situ morphology evolution studies have proven to be a powerful method for investigating thin film solidification of polymer:fullerene blends cast from mixed solvents.[65, 74, 79-81, 157] In an attempt to gain insight into how DIO influences the BHJ film formation, in situ reflection/absorbance UV-vis spectroscopy was performed during blade coating of P(T3-TPD):$PC_{71}BM$ films cast w/o DIO and with DIO. Polarized UV-vis absorbance spectroscopy of dry films was taken, in order to investigate in-plane optical anisotropy caused by a preferential orientation of the polymer backbone with respect to the blade coating direction in P(T3-TPD):$PC_{71}BM$; however, an in-plane orientation was not observed indicating that blade coating does not induce polymer alignment with respect to the blading direction in this system as shown in Figure 58.

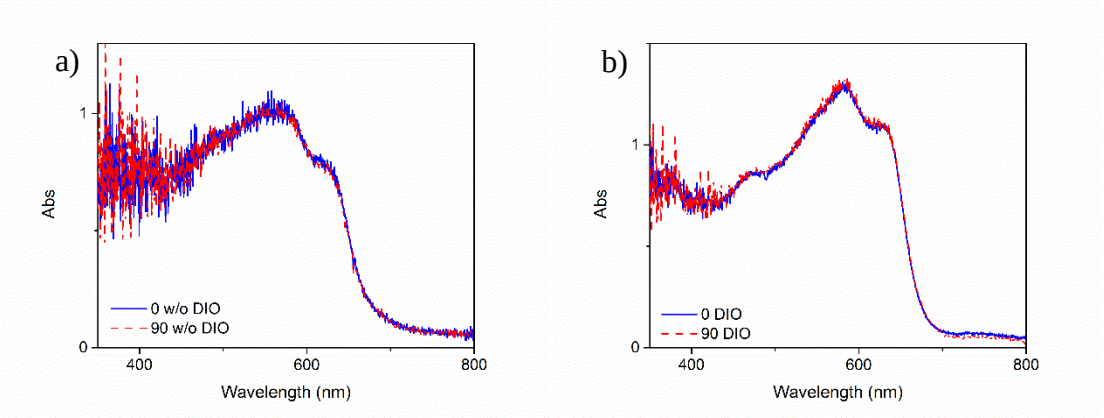

Figure 58. UV-vis spectroscopy of P(T3-TPD):$PC_{71}BM$ films with a rotating polarizer set to 0° (parallel to the coating direction) and 90° (perpendicular to the coating direction) for a) w/o DIO and b) DIO. No anisotropy was observed indicating that blade coating does not induce polymer alignment in this system.

Figure 59 shows both in situ absorbance and in situ reflection measurements taken at the same spot, at the same time, and on the same sample. 2D plots were rendered with the y-axis accounting for time (s), the x-axis for wavelength (nm), and the color represents absorbance, where a strong absorbance is yellow, and where there is little absorbance, dark blue. The passage of the blade was set to one second in order to compare time scales between films cast w/o DIO or with DIO. Films cast w/o DIO are straightforward, wherein the chloroform rapidly evaporates, and at approximately 3.5 seconds after blade passage the film is subsequently dry. The in situ UV-vis absorbance shows little formation of new aggregate peaks as seen in P3HT:PCBM film solidification;[67, 157] however, by plotting the absorbance and reflection intensity as a function of time, Figure 60, a transition can be observed at ~2.5-3 seconds which is further aggregation of the polymer as concentration sharply increases during solidification. The most significant change in the UV-Vis upon film formation is a broad increase in absorbance above 400 nm, that we attribute to scatter due to film roughness and/or the coarse morphology. Films cast with DIO exhibit a two step drying process, and significantly increased drying times. Two transitions can be observed in the reflection spectra, the first one corresponds to the end of rapid chloroform evaporation at approximately 2.5 seconds after blade passage, shown in Figure 60, and the second transition is at the end of the DIO evaporation, that is not complete until ~5500 seconds. Both transitions seen in the in situ reflectance are marked by dashed lines and labeled in Figure 59. While the chloroform evaporation rate is rapid (<4 seconds), the complete evaporation rate of DIO is prolonged (~90 minutes). The rapid evaporation of chloroform leaves a DIO swollen film in which the fullerene is soluble, but not the polymer. The extremely rapid evaporation of the $CHCl_3$ precludes resolution of the expected

interference fringes in the reflection data. Nonetheless, an inflection in the reflection can be observed at the anticipated point of $CHCl_3$ removal and the radical slowing of the evaporation rate. The absorbance data, recorded at nominally Brewster's angle, is insensitive to the film thickness interference and directly probes the polymer backbone order. There is a distinct change upon removal of the $CHCl_3$. Interestingly, over the next 90 minutes, while evaporation of the DIO is clearly occurring as seen in the evolution of the reflection data, there is little detectable change in the absorbance spectra. As the transition dipole moment along the backbone is only sensitive to a planarization of the backbone and aggregation, rather than a change in final crystallinity, invariant UV-vis absorbance does not preclude evolution of higher order, such as crystallinity. Similar invariant UV-vis spectra were reported during the processing of P3HT with the non-solvent octane dithiol.[66] In order to gain more quantitative insight into the time resolved absorbance spectra, three features, P1-P3, as labeled in Figure 59 were deconvoluted into three Gaussian peaks. The FWHM (σ) and the height (H) of the Gaussian peaks were plotted as a function of time in order to investigate if any changes had occurred during solvent evaporation as seen in Figure 61. What is noticeable about the deconvoluted peaks as a function of time is that they are relatively constant in their σ and height. This alludes to there being very little change in polymer conformation during solidification. In Figure 61 a) w/o DIO, peaks 1, the aggregate peak, show little change as the film solidifies. The evolution of Peak 2 shows a decrease in the height and σ during solidification due to the growth the Peak 3. Peak 3, the high energy peak, is the only peak that shows an increase in both its σ and height, however, this is likely caused by the fullerene rather than the polymer as it has been observed that fullerene aggregation is in the same wavelength region as peak

3, and the film is 1:2 weight ratio polymer to fullerene. When examining Figure 61 b) DIO, peaks 1 and 2 again show little change in σ or height. Peak 3 shows a similar trend in both the w/o DIO and DIO case in which the FWHM (σ3) slightly increases upon film solidification due to fullerene solidification. P(T3-TPD) processed with DIO and w/o DIO show little structural change upon solidification by in situ UV-vis absorbance.

It was found that when using an aggregated solution of P(T3-TPD):$PC_{71}BM$ there are no significant local order morphological changes that occur, other than increased aggregation during solidification, that were detected using in situ UV-vis absorbance. This further reinforces that an aggregated solution is being processed, and suggests that film morphology is predetermined when processing polymer aggregates and is less sensitive to processing method.

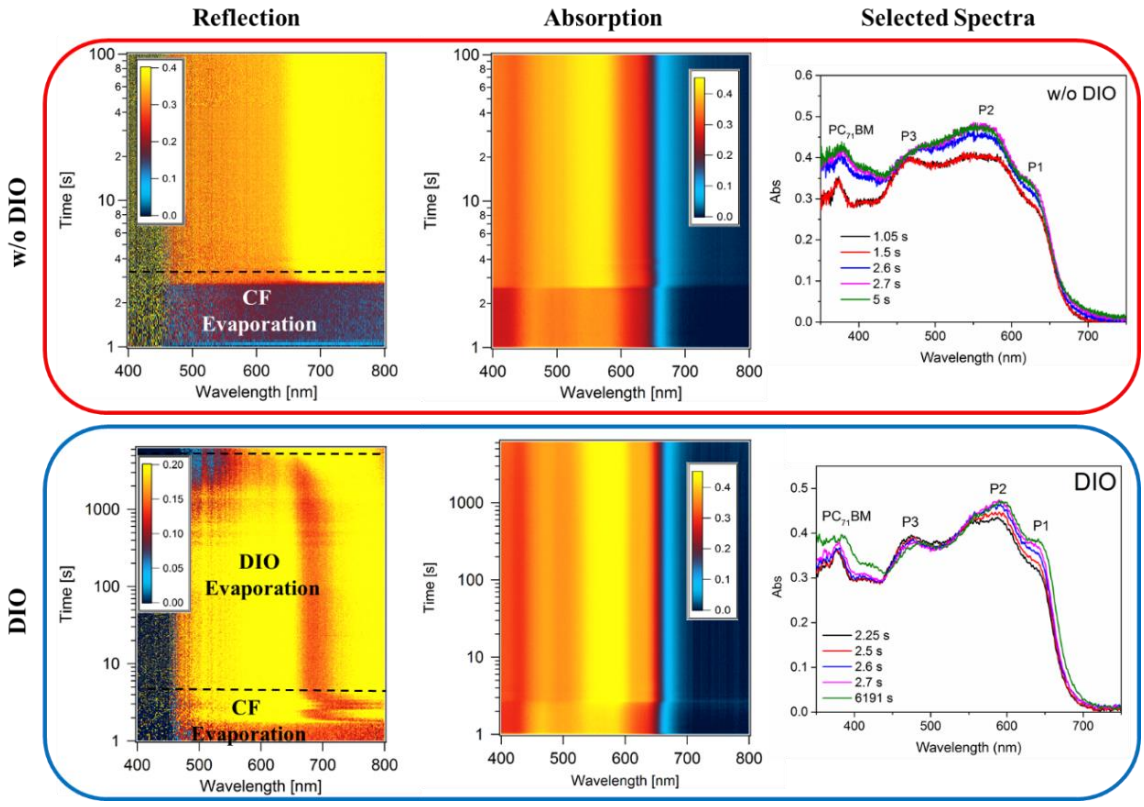

Figure 59. In situ reflection/absorbance UV-Vis measurements of blade coated pre-aggregated P(T3-TPD):$PC_{71}BM$ films cast with DIO and w/o DIO. Time resolved absorbance spectra were selected to show there is little change in local order during solidification.

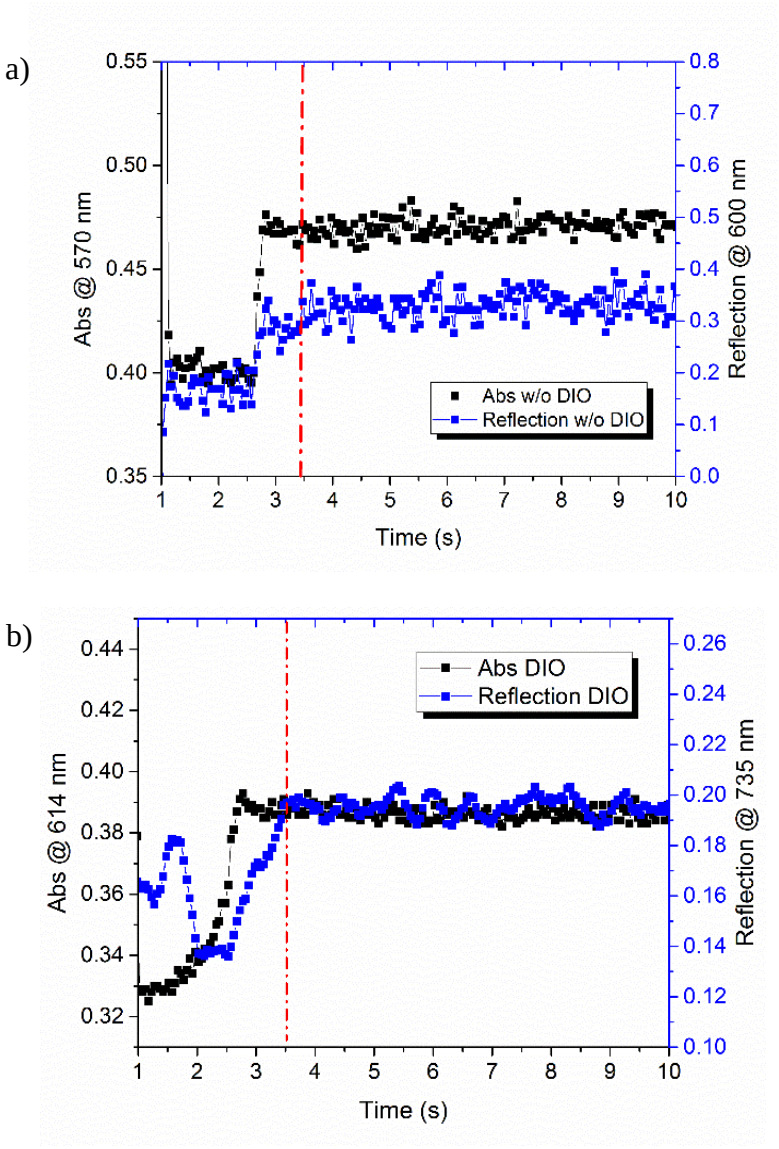

Figure 60. 1D line profiles taken at specific wavelengths indicated on the y-axis from Figure 59 of a) in situ absorbance/reflectance w/o DIO and b) in situ absorbance/reflectance DIO. The timing for solvent removal is determined by the evolution of the reflectance spectra. Dashed lines indicate transition from solution to dry film.

a)

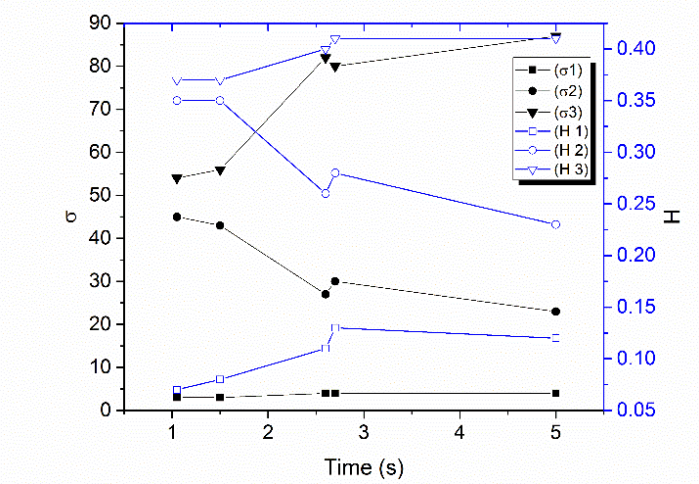

b)

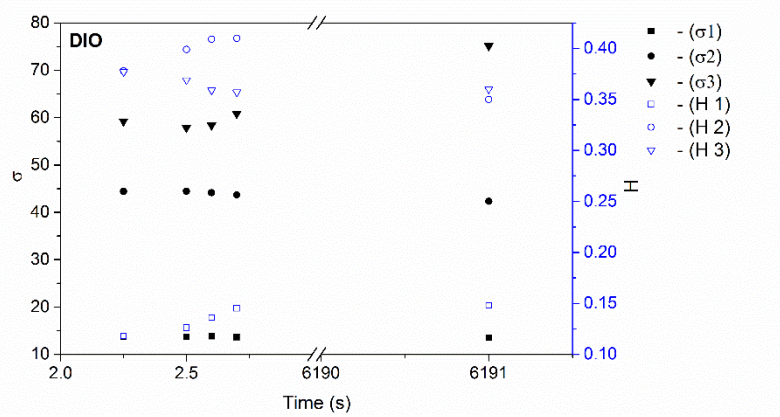

c)

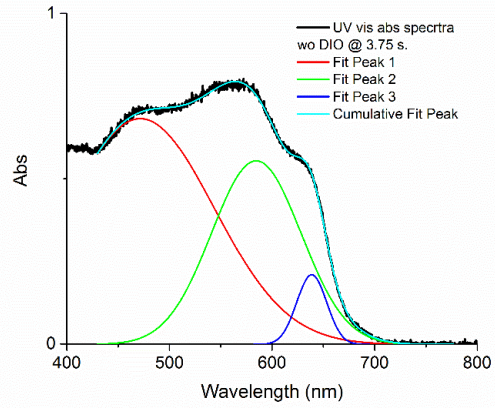

Figure 61. Deconvoluted peak parameters from in situ UV-vis sigma (σ), representing the FWHM, and height (H) representing the peak height as a function of time for P(T3-TPD):$PC_{71}BM$ a) w/o DIO and b) DIO. c) Example of how peaks were deconvoluted.

Combining the morphology and kinetic studies, a coherent picture of the processing of P(T3-TPD):$PC_{71}BM$ emerges. The robust behavior with respect to coating method: nominally identical film morphology and device performance is obtained with the same solution at the same temperature for both spin and blade coating, is directly attributable to the high level of aggregation in the solution. However, the overall low solids content enables adequate film quality for good devices, which is often not observed when processing from aggregated solutions.[148] While solution aggregates are critical for OPV[33] and OFET[167] performance, it is also clear that the presence of DIO in the solution significantly modifies the final film characteristics. The decrease in characteristic dimension for phase separation is consistent with the observation that DIO is a non-solvent for P(T3-TPD). It thus will lower the processing solution solvent quality, increasing the enthalpy drive to aggregation, increasing the nucleation density. An interesting question arises as to the origin of the beneficial effect of DIO on order and phase purity. Changes in nucleation density do not directly relate to subsequent changes in crystal growth and quality. Based on the in situ UV-vis absorbance and reflectance, the dominant effect of DIO on aggregation occurs during the early stages of deposition, consistent with the deposition of aggregates. However, it is possible that simply by extending the time over which the film is swollen with DIO (90 min) provides an opportunity for increased crystallization. Additionally, the selective solvent nature of DIO can plasticize any mixed amorphous phases of P(T3-TPD) and PCBM by extracting the high T_g fullerene.[66, 168]

4.4.Conclusion.

Using P(T3-TPD):$PC_{71}BM$, we have shown that processing via spin coating or blade coating yield similar electrical, and morphological, characteristics when processed from an aggregated solution. This is quite contrary to other polymer:fullerene systems which show drastic differences in film morphology and solar cell performance when processed via spin coating or blade coating. We have investigated the impact that DIO has on BHJ thin film morphology development. Using AFM, GIWAXS, and GISAXS, we show that DIO enhances the crystallinity of the polymer and reduces the domain size in the BHJ film. The decreased domain size increases the polymer:fullerene surface area which enhances the short circuit current density, and improves OPV performance. Combining static thin film measurements with in situ UV vis absorbance and reflectance spectroscopy reveal that DIO serves to increase the nucleation density which in turn reduces the average domain size and enhances polymer crystallinity. The lack of solution re-optimization, and simple transfer from spin coating to blade coating, without impacting the BHJ morphology, by using aggregated solutions, is advantageous for the scale up of organic electronic devices via roll-to-roll processing.

CHAPTER 5. MORPHOLOGICAL EVOLUTION OF POLYMER:FULLERENE BLENDS BLADE COATED FROM A SINGLE SOLVENT OR CO-SOLVENTS

5.1. Introduction.

Conjugated polymers containing the diketopyrrolopyrrole (DPP) moiety have been shown to yield high performance OPVs, and transistors, with power conversion efficiencies (PCE) beyond 8% [169, 170], and demonstrated hole mobility's of 11 cm^2 v^{-1} s^{-1}.[171] One particular advantage of DPP based materials for OPV applications is their ability to be solution processed into 'thick films' of ca. 300 nm, allowing for increased light absorption, without losses in fill factor, leading to enhanced PCE. Thick film solar cells have been demonstrated in numerous reports with the polymer DT-PDPP2T-TT.[44, 169, 172] The ability of DT-PDPP2T-TT to form an interconnected network of fibers, coupled with high charge carrier mobility, leads to reduced bimolecular recombination, allowing for thick active layer films. The high charge carrier mobility, semi-crystallinity, tunable band gap, and synthetic simplicity of DPP based materials make them excellent candidates for scale up and manufacturing of electronic devices.[173]

Here we report the morphological evolution of a DT-PDPP2T-TT:$PC_{71}BM$ bulk heterojunction (BHJ) films cast from one of two solvent systems, either chloroform (CF), or chloroform with 8% *ortho*-dichlorobenzene (CF:DCB) added by volume. We find that processing from a co-solvent mixture dramatically improves OPV device performance through a significant reduction in the characteristic length scale and enhanced polymer crystallinity. Further, in situ X-ray scattering: both grazing incidence diffraction (GIXD) and small angle scattering (GISAXS), combined with white light reflectometry of blade-

coated BHJ films, reveals the mechanism in which co-solvent processing yields optimum phase separated morphology relative to single solvent processing. We show the addition of DCB acts analogous to a plasticizer, in which it suppresses the $T_{g.}$ As DCB is removed, the polymer crystallizes leading to reduced domain sizes and enhanced polymer crystallinity relative to single solvent processing.

5.2. Experimental.

***Materials*.** DT-PDPP2T-TT, with a reported M_w of 75 kDa and a PDI of 2.5, was purchased from 1-Material. $PC_{71}BM$ was purchased from American Dye Source.

Organic solar cell fabrication. Patterned indium tin oxide (ITO) was sonicated in a solution of Millipore water and sodium dodecyl sulfate (SDS), followed by rinsing with Millipore water. Substrates were then sonicated in acetone, then isopropanol for 5 minutes in each cleaning solution. The ITO was blown dry with Ar gas, then UV ozone cleaned for 10 minutes. Clean substrates were transferred to a spin coater where PEDOT:PSS (Al 4083) was filtered through a 0.45 μm nylon filter onto the substrate. PEDOT:PSS solution was spin coated at 5000 rpm for 50 seconds, followed by drying on a hotplate in ambient air at 120 ºC for 10 minutes to produce a 25 nm thick film. The active layer, composed of DT-PDPP2T-TT:$PC_{71}BM$ with a weight ratio of 1:3, was blade coated onto the substrates in air with a substrate to blade gap of 300 μm for CF and 400 μm from CF:DCB, 92%:8% by volume, at a speed of 20 mm s^{-1} to yield optimum film thicknesses of 80 to 150 nm measured using a Bruker DetakXT profilometer. Devices were placed in a thermal evaporator at a pressure of 10^{-5} mbar for 30 minutes prior to sequential deposition of 1 nm of LiF followed by 80 nm of Al, which were used as the top electrodes. The active area of

the devices, defined by the overlap of the top and bottom electrode, are 0.08 cm^2. Film thicknesses were optimized to achieve the highest PCE. Devices were tested in an Ar filled glove box using a Newport ABB solar simulator coupled with a Keithley SMU for measuring device efficiency under standard AM 1.5 conditions calibrated to 100 mW cm^{-2}. A Newport EQE/IPCE setup with a white light source and a monochromator was used to collect EQE.

AFM. AFM was collected using a Bruker atomic force microscope (Dimension icon) with a Bruker SCANASYST-AIR probe in standard tapping mode.

In situ GIXD. In situ hard X-ray scattering measurements were performed at the Advanced Light Source beam line 7-3-3, with a beam energy of 10 keV. For GIXD measurements a 2D image detector (Dectris Pilatus 2M) was located at a distance of ≈260 mm from the sample center. Slits were adjusted to produce a nominally 0.3 mm high beam which overfilled the nominally 2 cm wide substrate. In situ GISAXS was performed at the same beam line with the 2D image detector-to-sample distance 3850 mm. An evacuated flight tube was used to minimize air scatter. The X-ray beam was attenuated to eliminate sample damage. The detector was calibrated with a silver behenate standard. Both GIXD and GISAXS data was reduced with the Nika software package.[92] Simultaneous with both GIXD and GISAXS measurements, normal incidence spectral reflectometry was performed with a home-made, fiber spectrometer based system. Care was take to overlap the reflectometry probe beam (≈0.3 mm diameter) with the stripe illuminated by X-rays (≈0.8 mm wide). The reflectometry results were analyzed using a commercial ellipsometry code (JA Woollam WVASE32). X-ray data was recorded with a variable integration time

and period. For films cast from CF, the initial 120 s were recorded at ≈0.1 s integration and period, while the next minute was recorded with 9 s integration and 1.5 s period. The reflectometry was recorded at a constant ≈0.1 s integration and period for films cast from chloroform. For films cast from CF:DCB the initial 120 s were recorded at ≈0.1 s integration and period while the next 3.5 minutes was recorded with 1 s integration and 1 s period .Ex situ (static) scattering measurements were performed with 9 s integration.

For quantitation of GISAXS, we make the approximation that the enhanced signal at $q_z \sim 0$ (the Yoneda peak) is a good proxy for q_x and assume a 3D isotropic scattering pattern such that the total scattering invariant becomes: $\int dqIq^2$. We note that the ≈4 m flight path of the GISAXS measurement limits the low q range and a significant amount of low q scattering is missed in the in situ experiment. This can lead to a bias in relative phase purity based on an experimentally derived total scattering invariant. We emphasize this by adopting the notation integrated scattering invariant, $ISI \equiv \int_{q_{min}}^{q_{max}} dq\ I\ q^2$, where q_{min} and q_{max} are defined by the experimentally accessible range.

5.3. Polymer: Solution and thin film UV-vis.

Figure 62 a) shows the chemical structure of DT-PDPP2T-TT. Figure 62 b) shows the solution and thin film UV-vis absorbance spectra of neat DT-PDPP2T-TT dissolved, or cast, from CF or CF:DCB. The neat polymer dissolved in CF, or CF:DCB, show overlapping spectra, suggesting that polymer conformation is similar in both solutions, and the addition of DCB does not induce additional polymer aggregation. Likewise, Figure 62 b) shows neat DT-PDPP2T-TT thin films, blade coated from CF or CF:DCB, spectra are overlapping suggesting the addition of DCB as little effect on local polymer order in the

solid state. The UV-vis absorbance spectra of the blade coated BHJ thin films, with an optimized polymer:fullerene weight ratio of 1:3 and coated at 20 mm/s using a 300 μm substrate to blade gap for CF and a 400 μm substrate to blade gap for CF:DCB, is shown in Figure 62 c). Spectra were normalized to the $PC_{71}BM$ peak at 375 nm in order to evaluate the effect the CF:DCB mixture has on local polymer order at the low energy part of the spectrum relative to processing from CF. As demonstrated in Figure 62 c) both spectra overlay one another indicating polymer local order is similar in both BHJ films. The absence of additional low energy vibrionic features, typically seen in P3HT and attributed to enhanced order [66, 67, 157], signify the addition of DCB does not promote increased polymer aggregation in solution or solid state. Vezie et al.[174] recently studied the UV-vis absorption of a series of semiconducting polymers in the solution state. A subset was identified as exhibiting anomalously high oscillator strength, attributed to long persistence lengths for the isolated chain. Polymers with the closely related backbone configurations of DPP-2TT-T and DPP-3T were in the long persistence length class, suggesting that DPP-2T-TT invariance of the spectrum is a reflection of chain rigidity and not aggregation.

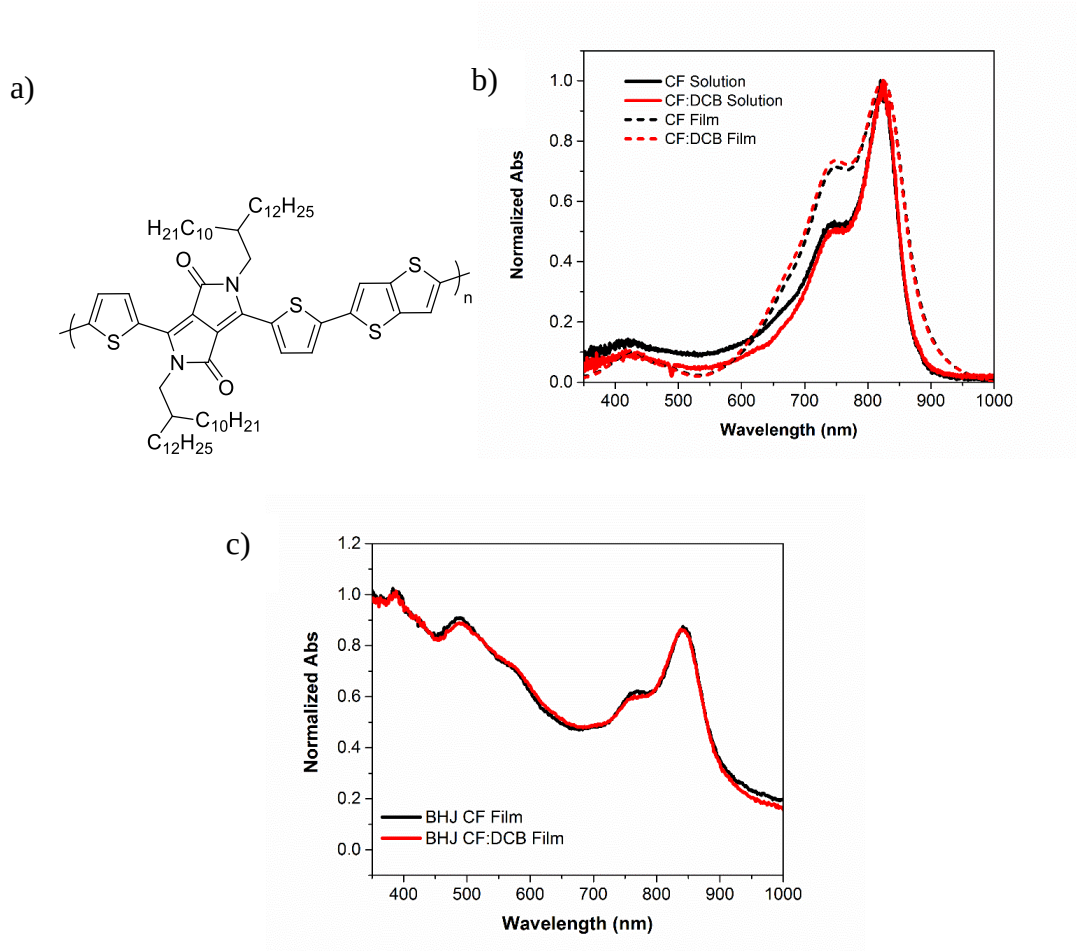

Figure 62. a) Chemical structure of DT-PDPP2T-TT, b) solution UV-vis absorbance of neat polymer in CF or CF:DCB, and thin film (dashed lines) processed from CF or CF:DCB. c) blade coated DT-PDPP2T-TT:$PC_{71}BM$ thin film UV-vis absorbance.

5.4. Solar Cell performance.

Conventional solar cells with the architecture of ITO/PEDOT:PSS/BHJ/LiF/Al were constructed in order to investigate the photovoltaic properties of DT-PDPP2T-TT:$PC_{71}BM$ thin films processed from either CF or CF:DCB. The active layer, made up of DT-PDPP2T-TT:$PC_{71}BM$ with a weight ratio of 1:3, was blade coated at room temperature in ambient conditions from a solution concentration of [12 mg/mL] in either CF or

CF:DCB. Optimized solar cells fabricated from the solvent mixture, CF:DCB, demonstrated average PCEs of 6%, while optimized devices fabricated from CF alone showed average PCEs of ~3%, which is in agreement with spun-coat device performance in the literature.[44, 172] Interestingly, a number of studies show an optimum performance of DT-PDPP2T-TT using film thicknesses > 200nm allowing for improved light harvesting, [44, 169, 172] whereas, in this study we find optimum film thickness to be < 200 nm, yet demonstrate similar OPV results, suggesting that DT-PDPP2T-TT:$PC_{71}BM$ based solar cells have a high tolerance for film thickness variability while maintaining high PCEs. Table 7 shows the optimized OPV performance of DT-PDPP2T-TT:$PC_{71}BM$ based solar cells. In order to compare OPV results, devices of a similar film thickness as the CF samples were fabricated from CF:DCB with an average film thickness of 80 nm.

Table 7. Optimized device performance of DT-PDPP2T-TT:$PC_{71}BM$ solar cells.

	J_{sc} (mA/cm^2)	***V_{oc}***	***FF%***	***PCE%***	***Film Thickness (nm)***
CF (Optimized)	7.0 ± 0.2	0.67 ± 0.01	63 ± 2.1	3.0 ± 0.2	85
CF:DCB	8.2 ± 0.3	0.68 ± 0.00	61 ± 2.4	3.4 ± 0.0	80
CF:DCB (Optimized)	14.2 ± 0.6	0.67 ± 0.01	63 ± 3.4	6.0 ± 0.2	150

Device architecture: Glass/ITO/PEDOT:PSS/BHJ/LiF (1 nm)/Al (80 nm). Statistics obtained from 10 devices.

Figure 63 a) shows the J-V plot of optimized DT-PDPP2T-TT:$PC_{71}BM$ devices, and devices of similar active layer film thickness, in which the BHJ film was cast from CF or CF:DCB. In both cases, films cast from the solvent mixture CF:DCB show improved short

circuit current density (J_{sc}) leading to enhanced power conversion efficiencies (PCE) over the CF devices, as shown in Table 7. Further, the 150 nm optimized film thickness for CF:DCB shows a doubling of J_{sc} and PCE compared to the 85 nm optimized CF devices, likely due to an almost doubling in film thickness. Increasing the film thickness of CF processed devices led to reduced OPV performance. Co-solvent processing allowed for thicker BHJ films, thereby improving J_{sc}, which suggests a film morphology consisting of an interpenetrating network of small domains, reduced recombination, and improved charge transport. Figure 63 b) shows the external quantum efficiency (EQE%) of devices fabricated from CF and CF:DCB. BHJ films of similar thickness cast from the mixed solvent system, CF:DCB, show enhanced current generation from 500 nm – 900 nm, and particularly at the low energy peak between 750 nm – 900 nm, while BHJ films cast from CF show increased current generation in the high energy side of the spectrum correlating to strong $PC_{71}BM$ absorption at 375 nm. The optimized CF:DCB 150 nm thick films show improved current generation from 370 nm to 770 nm. The question is, why does a small amount of DCB lead to enhanced OPV performance, and what is the mechanism in which it is operating?

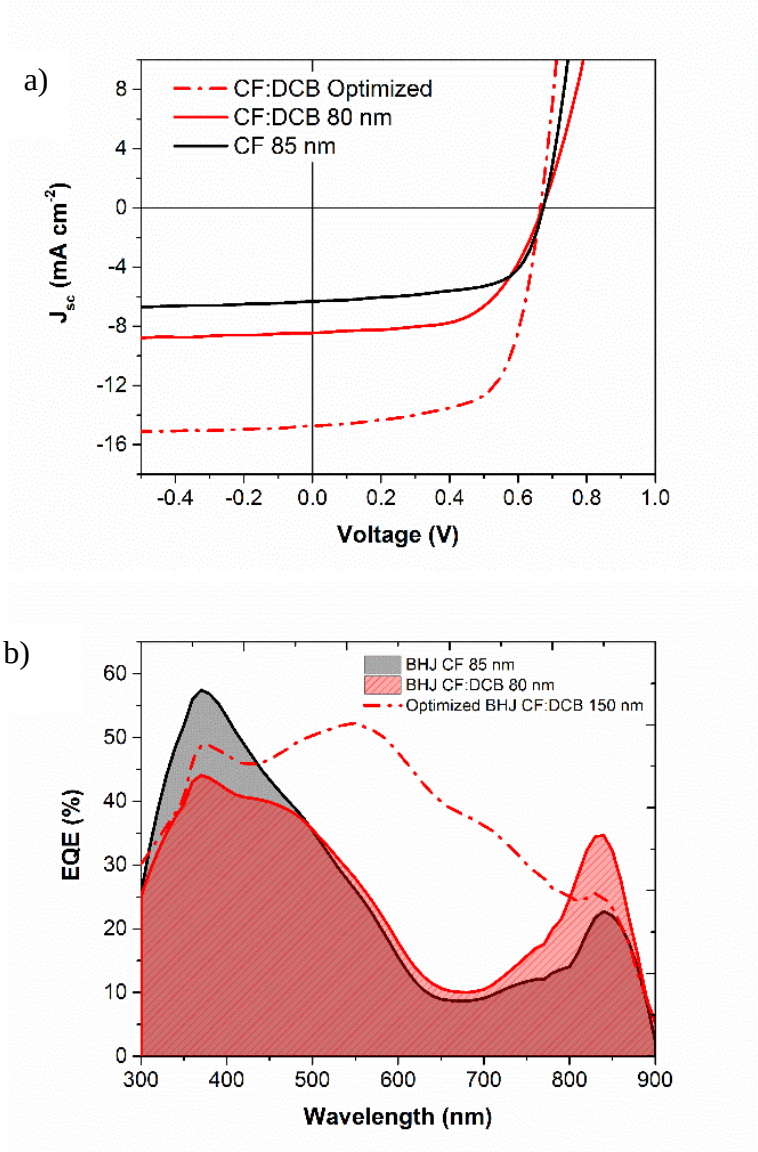

Figure 63. a) J-V curve of DT-PDPP2T-TT:$PC_{71}BM$ solar cells blade coated in ambient air from CF, or CF:DCB. Optimized film thickness for CF and a similar film thickness are shown for the BHJ cast from CF:DCB, and optimized (150 nm) film thickness is shown for CF:DCB. b) EQE of solar cells where the active layer was cast from CF or CF:DCB. Films cast from CF are optimized, and a film of similar thickness was cast from CF:DCB to compare. Optimized film thickness BHJ solar cells cast from CF:DCB are also shown.

5.5. Ex-Situ Thin Film Morphology.

In order to gain insight into the nature of how co-solvent processing leads to enhanced OPV performance we have investigated BHJ thin film morphology of DT-PDPP2T-TT:$PC_{71}BM$ in detail. Figure 64 shows the AFM height, AFM deformation, and low-angle annular dark-field transmission electron microscopy (LAADF TEM) images, of BHJ thin films blade coated from CF or CF:DCB. Examination of the AFM height and deformation images of BHJ films, cast from CF reveal large scale phase separation, with a polymer fiber network present in the deformation image. The LAADF TEM images show large scale features on the order of ca. 200 nm in diameter. These large features suggest L-L phase separation has occurred, leading to large domains of polymer and fullerene.[79, 175, 176] However, films cast from CF:DCB demonstrate markedly different topologies. Both the height and deformation images of BHJ films cast from CF:DCB show a fine fiber network which is reinforced by the TEM. The reduction in fiber size suggests smaller scale phase separation, and improved mixing between the polymer and fullerene. Janssen and co-workers found that polymer fiber width is controlled through polymer solubility for DPP based materials, in which reduced solubility led to decreased fiber width, while increased solubility shows enlarged fiber widths.[177] This behavior of reduced fiber size, caused by the addition of another solvent, is governed by nucleation and growth.

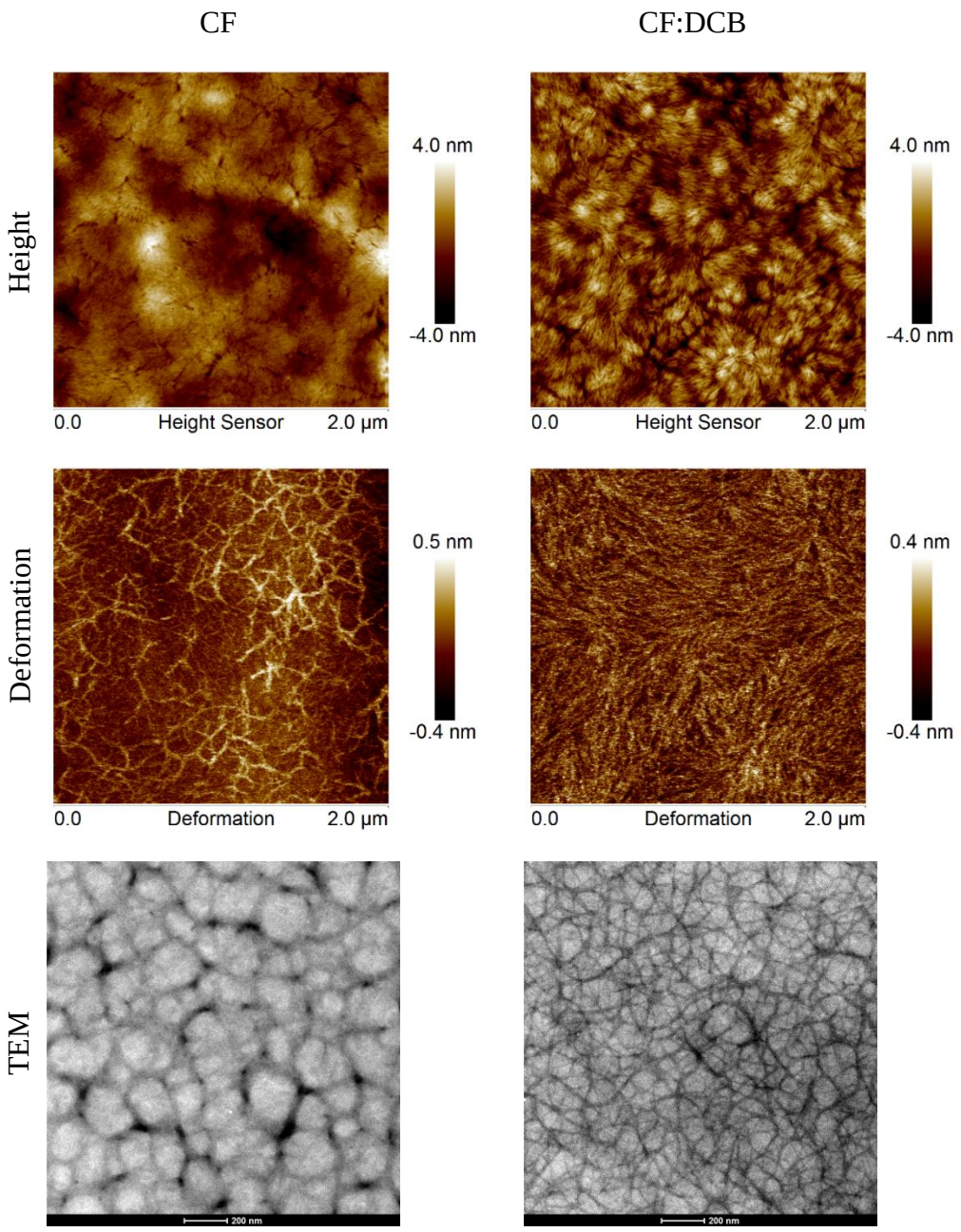

Figure 64. AFM height, deformation, and LAADF TEM of BHJ films cast from CF, or CF:DCB.

Figure 65 a) shows the TEM and GISAXS log q $[Å]^{-1}$ vs log I plot for DT-PDPP2T-TT:$PC_{71}BM$ BHJ films. GISAXS of BHJ films cast from CF could not be acquired due to the large scale phase separation present in the film, and the detector limit of 0.004 $Å^{-1}$ (157

nm). The broad 'Guinier knee', corresponding to a change in the gradient of the 1D line profile $\propto \exp(-R_g^2 q^2/3)$[163], found in the TEM and GISAX of the BHJ film processed from CF:DCB at ca. 0.01 q[Å]$^{-1}$, corresponds to a characteristic length scale ($=2\pi/q_{peak}$) of 62 nm. The overlapping TEM and GISAX line profiles for the BHJ processed from CF:DCB reinforce an average characteristic length scale of ~60 nm. When the BHJ is processed from CF, the TEM peak in Figure 65 a) is shifted to a lower q value, 0.003 q[Å]$^{-1}$, indicating a larger characteristic length scale of approximately 209 nm. Figure 65 b) shows the Kratky plot (Iq^2 v q [Å]$^{-1}$) of the TEM , and GISAXS of BHJ films processed using CF or CF:DCB. The integrated scattering intensity (ISI), which represents a relative average domain purity, determined using $ISI \equiv \int_{q_{min}}^{q_{max}} dq\ I\ q^2$ [45], was found to be 1 for BHJ processed from CF:DCB and 0.79 for CF. The increase in average domain purity, due to co-solvent or additives, has been shown to be an important morphological factor observed in high performance OPVs as it is thought to reduce bimolecular recombination.[41, 178, 179] The results from ex situ AFM, TEM, and GISAXS, confirm the addition of DCB significantly reduces domain size, increases phase purity, and increases polymer:fullerene surface area. While a reduction in domain size is detected when using co-solvent processing, AFM and TEM do not provide mechanistic information on the nature of how this BHJ is developed during film solidification.

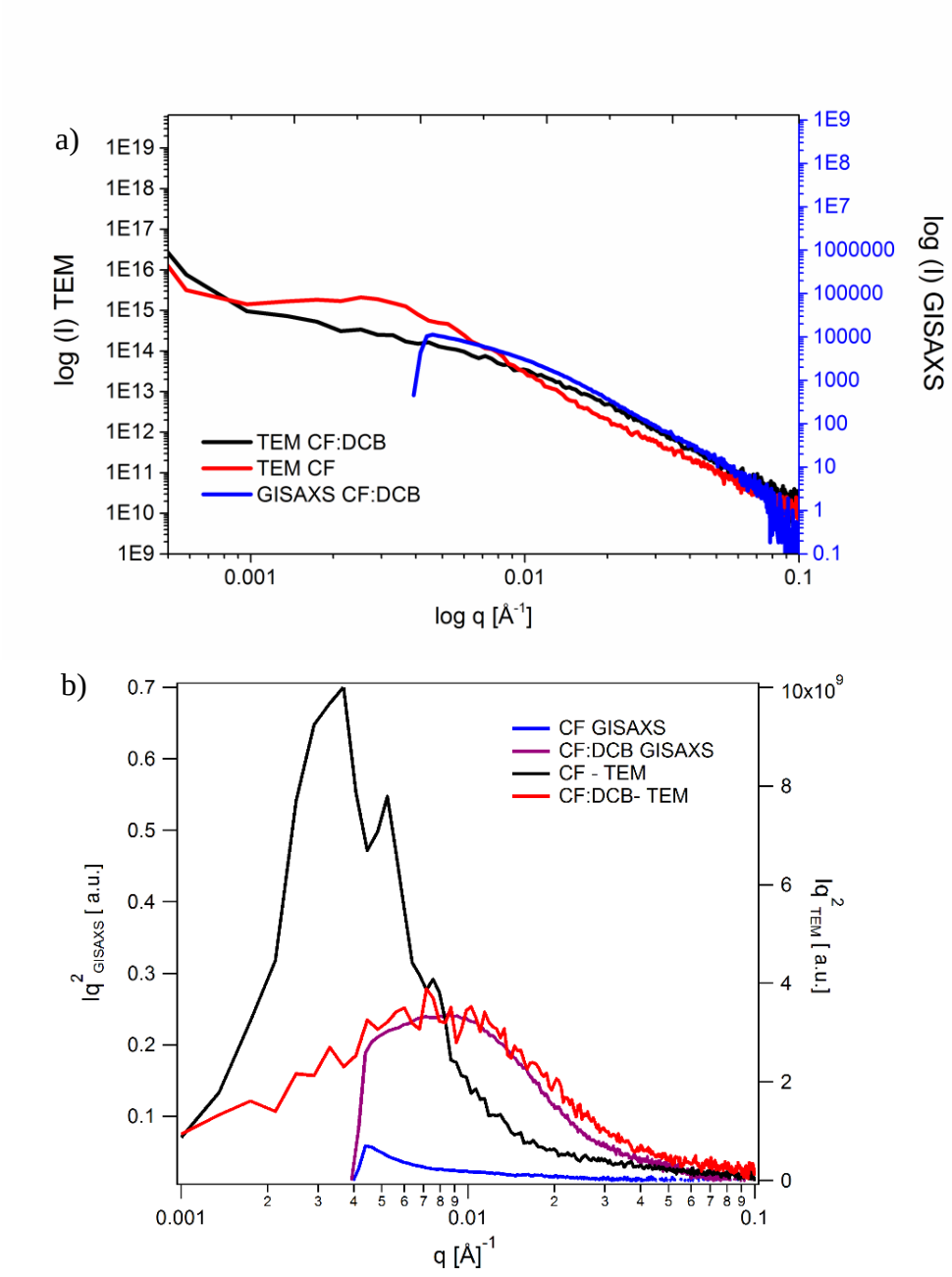

Figure 65. a) LAADF TEM, and GISAXS, 1D scattering profile of DT-PDPP2T-TT:$PC_{71}BM$ BHJ films blade coated from CF or CF:DCB, and b) Kratky plot of DT-PDPP2T-TT:$PC_{71}BM$ BHJ films LAADF TEM and GISAXS 1D line profiles used to determine the integrated scattering intensity.

5.6. Static GIWAXS.

Grazing incidence wide angle X-ray scattering (GIWAXS) was conducted in order to gain quantitative information on crystallinity, crystal orientation, and lamellar spacing. Figure 66 a) shows the film volume, and volume fraction, normalized intensity pole figure for the (100) peak, and b) the relative degree of crystallinity (rDoC), calculated using $\int_0^{\frac{\pi}{2}} I(\chi) \sin\chi \, d\chi$ [180], for the samples studied with poly CF:DCB representing neat polymer cast from CF:DCB and poly CF representing neat polymer cast from CF. Examination of Figure 66 a) demonstrates co-solvent processing influences rDoC. Neat polymer processed from CF or CF:DCB contain an isotropic crystal component with a slight increase in intensity at $\chi = 0^{o}$ and $\pm 90^{o}$, indicating that both face on and edge on crystal orientation is present. The orientation is preferentially edge-on for BHJ films when processed from CF or CF:DCB, demonstrated by the strong peak intensity centered around $\chi = 0^{o}$. The addition of DCB does not affect the crystal orientation in the BHJ samples, rather, it enhances polymer crystallinity as seen by the increase in intensity for BHJ CF:DCB from $\chi = -90^{o}$ to $90\ ^{o}$. The film volume, and volume fraction, normalized rDoC, Figure 66 b), shows both neat polymer, and BHJ, have enhanced polymer crystallinity when processed using CF:DCB over CF. Others have found that improved polymer crystallinity with DPP based materials leads to enhanced charge carrier mobility [181, 182], which explains why thicker co-solvent processed films are able to be produced without sacrificing FF or leading to increased recombination. Further, the use of co-solvent processing showed reduced lamellar stacking distance in the q_z direction in the neat polymer and BHJ films, and increased crystal coherence length (CCL) from 117 Å to 159 Å for the BHJ films, as demonstrated in Table 8. The reduced lamellar stacking distance coupled with increased

CCL, shown in Table 8, signifies improved polymer order in the film. CCL, lamellar stacking, and π-π stacking, distances were determined from 1D line cuts taken from 2D GIXD images shown in Figure 67.

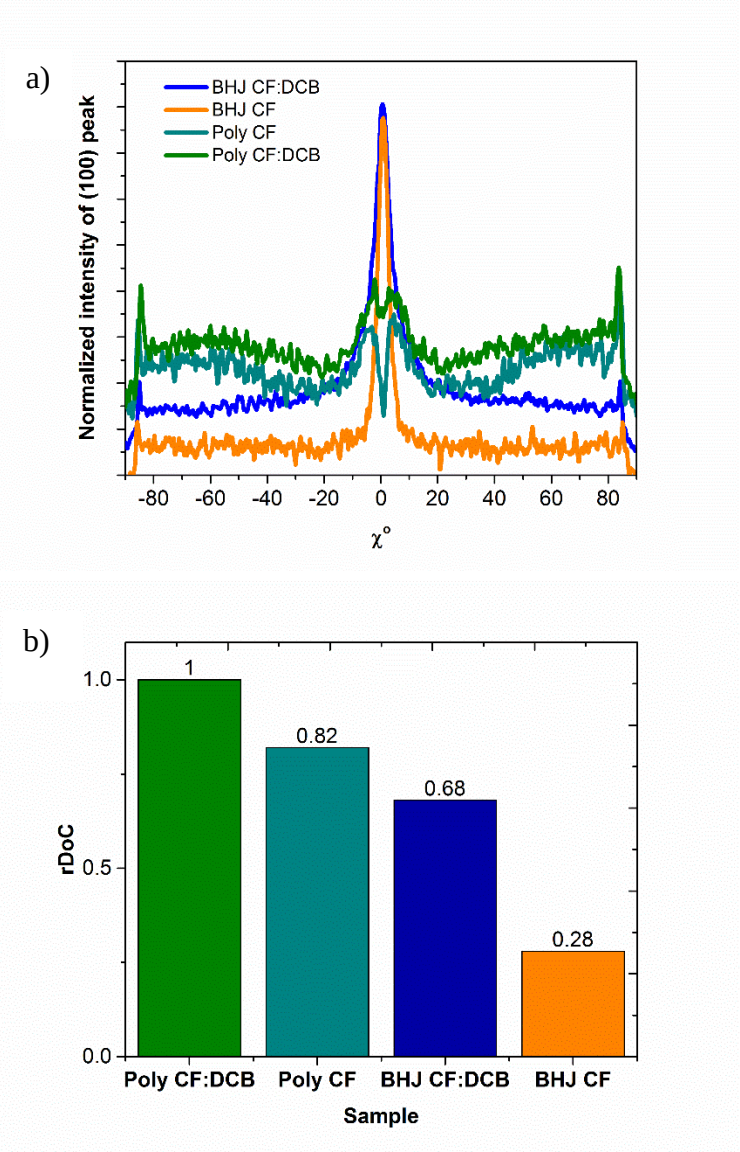

Figure 66. a) Film volume, and polymer fraction, normalized pole figure of neat DT-PDPP2T-TT, and DT-PDPP2T-TT:$PC_{71}BM$, cast from CF, or CF:DCB. b) Relative degree of crystallinity (rDoC) from the integrated pole figure.

Table 8. Lamellar and π-π stacking distance of neat DT-PDPP2T-TT and DT-PDPP2T-TT:$PC_{71}BM$ films blade coated from CF or CF:DCB.

GIWAXS	***(100) Spacing (Å)***		***(010) π-π (Å)***		***(100) CCL (Å)***	
	Vertical	Horizontal	Vertical	Horizontal	Vertical	Horizontal
Polymer CF	20.8	21.2	3.7	4.8	125.1	152.1
Polymer CF:DCB	20.3	21.1	3.8	NA	127.8	135.1
BHJ CF	25.5	N/A	3.3	3.3	117.2	N/A
BHJ CF:DCB	20.6	21.6	3.3	3.3	159.2	189.2

Lamellar, and π-π spacing, calculated using 2π/q, and crystal coherence length (CCL), CCL = 2π/FWHM, for neat polymer films and BHJ films processed from CF or CF:DCB. All calculations were performed on 1D line cuts shown in Figure 67.

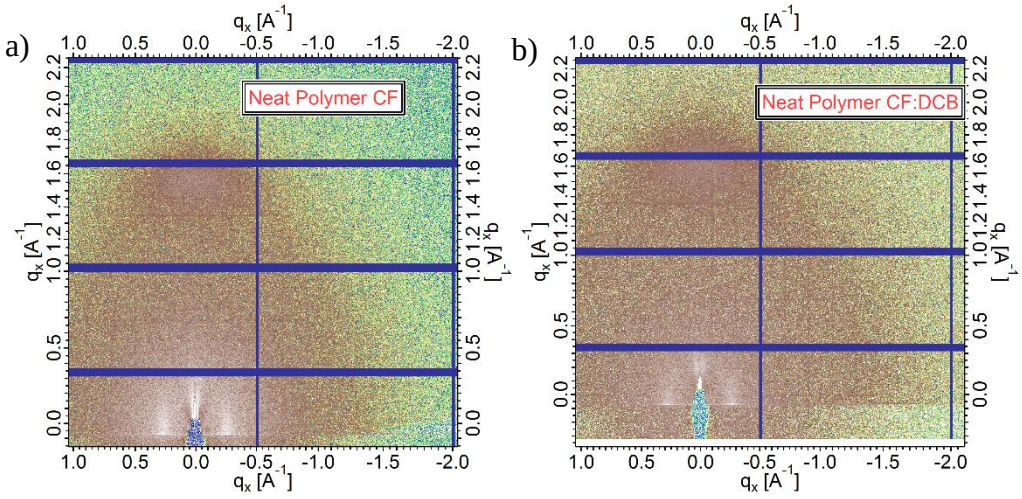

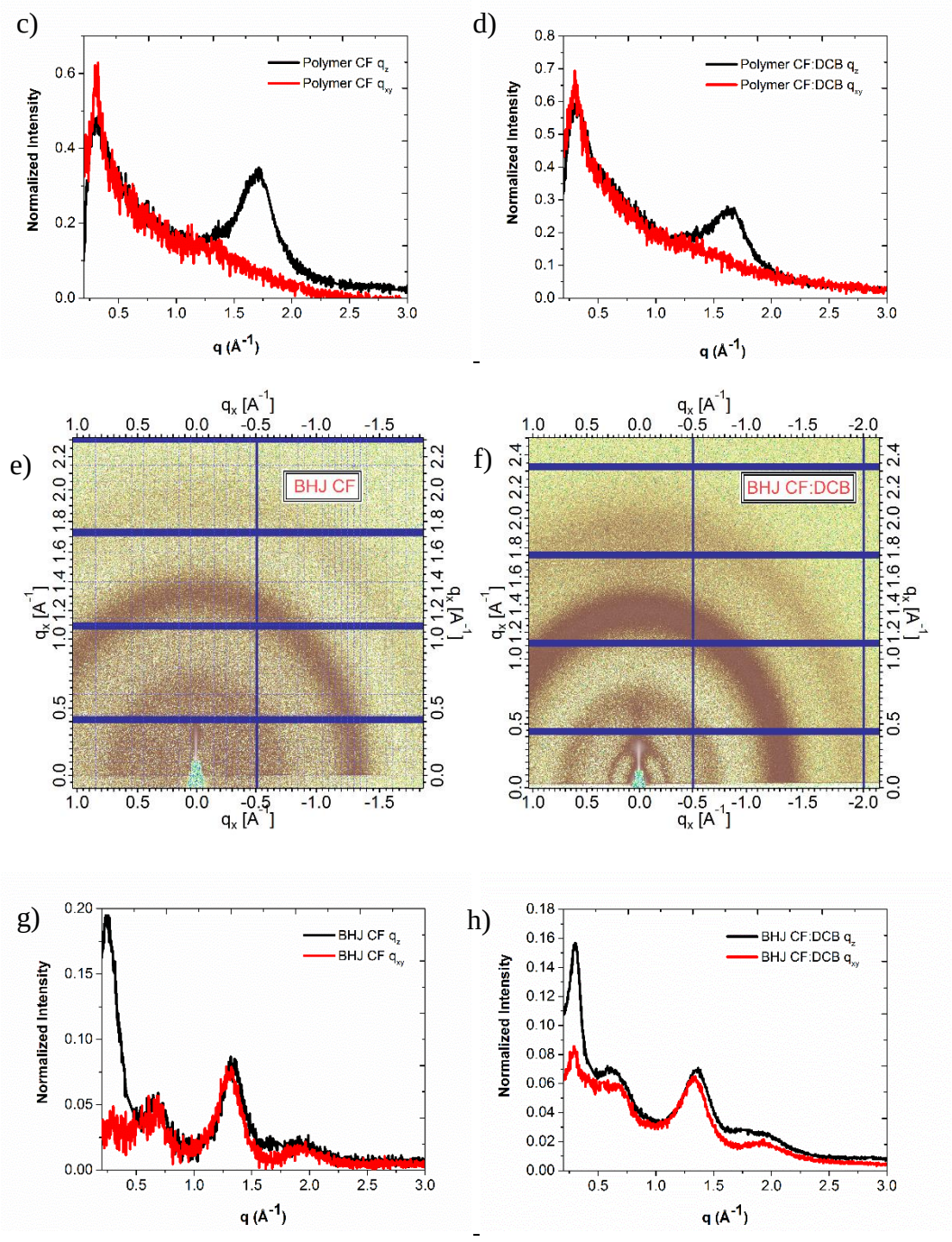

Figure 67. 2D GIWAXS images of a-b) neat polymer cast from a) CF or b) CF:DCB and their corresponding 1D line plots, c-d) in the vertical (q_z) and horizontal (q_{xy}) direction. Figures e-f) are 2d GIWAXS images of the BHJ cast from e) CF or f) CF:DCB, and their corresponding 1D line cuts in the q_z and q_{xy} direction in figures g-h).

5.7. In Situ Morphology Evolution.

5.7.1. BHJ Cast from CF.

In situ GIWAXS, GISAXS, and reflectometry was performed in order gain insight into the kinetics of blade coating DT-PDPP2T-TT:$PC_{71}BM$ from CF or CF:DCB. Figure 68 shows the volume normalized integrated (100) peak scattering intensity, and film thickness, as a function of time during solidification, with the blade passage set to 1 second, of the BHJ cast from CF. Film thickness for the BHJ film cast from CF or CF:DCB was determined from fringes shown in the 2D reflection images found in Figure 69. From Figure 68, there are two stages that can be observed during solidification. During stage I solvent is evaporating leading to increases in solute concentration as the film is thinning. The red sigmoidal line represents a fit, as a guide to the eye, to the integrated scattering intensity. Rapid removal of solvent leads to aggregation prior to polymer crystallization. As polymer crystallizes at the air-liquid and/or liquid-substrate interface this further increases phase separation of polymer from fullerene. In this case, we rationalize that phase separation is dominated by liquid-liquid (L-L) phase transition, similar to results found by van Franeker et al.[79] with PDPP5T:$PC_{71}BM$ spin coated from CF. Evolution of integrated (100) peak scattering intensity begins at a nominal film thickness of ca. 3000 nm corresponding to concentration of ~20 mg/mL. Early crystallization present in the wet film suggests L-L phase separation, whereas, in nucleation and growth, evolution occurs at super saturation.[66] The characteristic length scale of BHJ films processed from CF is larger than the detection limit of GISAXS as previously noted, therefore, real-time domain formation could not be accessed for this blend, however, this serves as indirect evidence for L-L de-mixing.

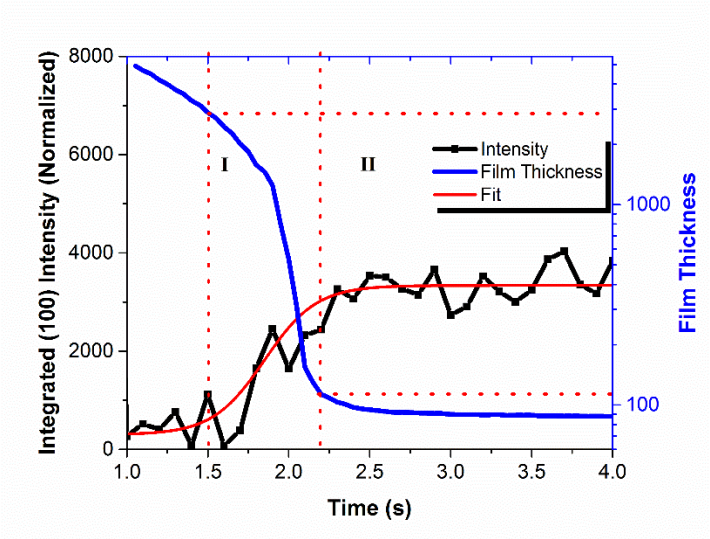

Figure 68. In situ GIXD. Integrated (100) intensity and film thickness as a function of time, with the blade passage set to 1 second. The red sigmoidal fit serves as a guide for the eye.

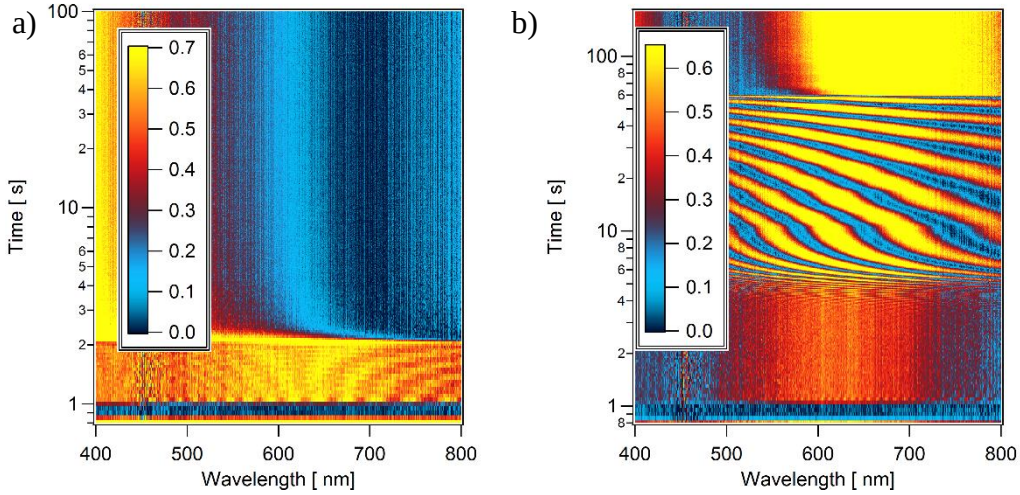

Figure 69. a-b) 2D In situ reflection spectra, taken normal to the substrate, of BHJ films cast from a) CF, or b)CF:DCB. Reflection spectra a-b) were used to determine film thickness as a function of time during solvent evaporation. Blade passage was set to 1 s.

5.7.2. BHJ Cast from CF:DCB.

Figure 70 a) shows the volume normalized integrated (100) peak scattering intensity, and film thickness, as a function of time during solidification, with the blade

passage set to 1 second, of the BHJ cast from CF:DCB. The sigmoidal fit to the integrated scattering intensity serves as a guide to the eye. There were three stages identified during solidification of the BHJ film when cast from co-solvents. In stage I, CF rapidly evaporates, leading to a significant thinning of the wet film thickness, and a sharp increase in concentration to ~74 mg/mL. From stage I to stage II there was no observed increase in polymer crystallinity, which is consistent with results found by Liu et. al.[80] Stage II is dominated by evaporation of the DCB, wherein, a large crystallization event occurs toward final DCB removal at a concentration of approximately ~246 mg/mL. Stage III signifies the final solid state thin film morphology. Figure 70 b) demonstrates the integrated scattering invariant (ISI), obtained through in situ GISAXS shown in Figure 71, and film thickness as a function of time. It is clear from Figure 70 b) that a single transition occurs indicated by the large increase in ISI intensity during the removal of DCB. This demonstrates that phases, and phase purity, evolve during the removal of DCB. The red line shows a fit to a three phase model system, in which one phase is composed of crystalline polymer, the second phase is amorphous polymer with additive, and the third phase is acceptor in additive, as described in previous reports.[66, 78] Since DCB serves as a solvent for both the polymer and fullerene, this three phase model describes the evolution of the ISI fairly well. From Figure 70 a) and 71 b) polymer crystallinity and phase purity occur simultaneously, indicating that nucleation and growth co-evolve upon evaporation of DCB at super-saturation. Evolution of the dominant low q peak (0.007 q [$Å^{-1}$]) observed in the in situ GISAXS, Figure 71, corresponding to a domain size of 90 nm, toward the end of DCB evaporation at super saturation is suggestive of nucleation and growth

mechanism.[148] In the case of CF:DCB the degree of crystallinity predicated from the 3 phase model is 78%.

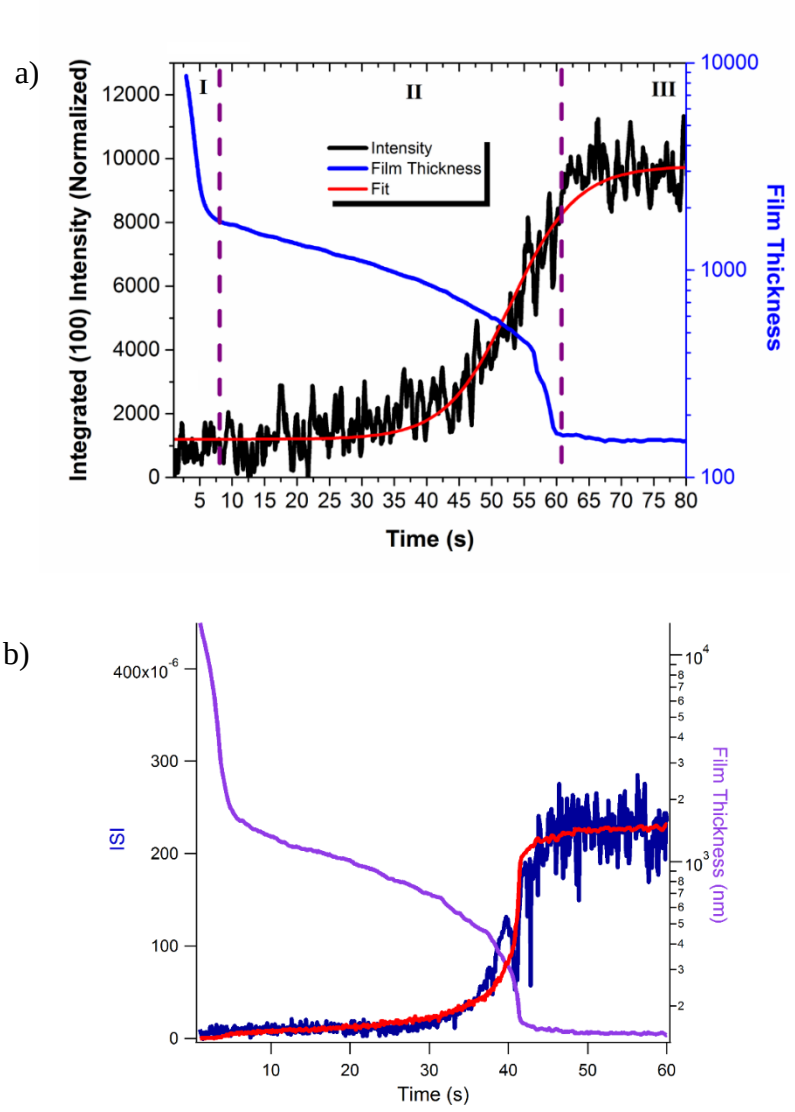

Figure 70. a) Normalized integrated pole figure of (100) peak, and film thickness, as a function of time of DT-PDPP2T-TT:$PC_{71}BM$ coated from CF:DCB, and b) ISI, and film thickness, as a function of time with a three phase model fit (red line).

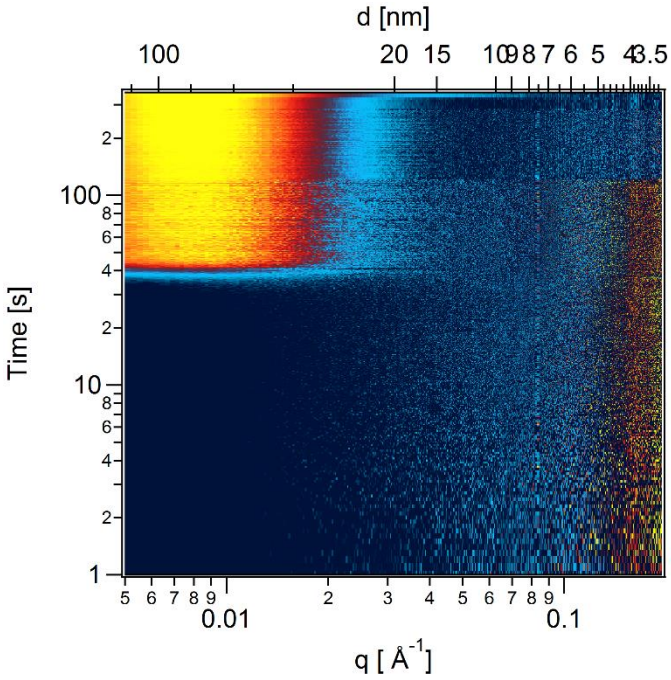

Figure 71. 2D in situ GISAXS of DT-PDPP2T-TT:$PC_{71}BM$, blade coated from CF:DCB, used to determine ISI as a function of time.

Others have investigated the role of solvent additives, and co-solvent processing, on DPP-thiophene based polymer materials. Janssen and co-workers studied phase separation using in situ UV-vis absorption, reflection, and light scattering, of diketopyrrolopyrrole–quinquethiophene:$PC_{71}BM$ (PDPP5T:$PC_{71}BM$) cast using spin coating from CF or a mixture of CF:DCB or CF:DIO.[79] Their results indicate phase separation of the BHJ blend processed from CF is dominated by L-L phase transition, leading to large scale phase separation of polymer and fullerene. The addition of DCB, or DIO, aggregates the polymer in solution preventing L-L phase separation from occurring, leading to a solid-liquid (S-L) transition, and a reduction in domain size.

Liu et al studied diketopyrrolopyrrole and quaterthiophene (pDPP), using in situ GIXD and GISAXS, blended with $PC_{71}BM$, which as drop cast from a mixture of

CF:DCB.[80] Liu et al. describes four stages that occur during film solidification of pDPP:$PC_{71}BM$ from drop casting. Where in stage I and stage II are dominated by CF evaporation leading to polymer crystallization and polymer fibril formation restricting large scale phase separation from occurring. A second event transpires during removal of the DCB in which there is further crystallization of pDPP forcing out $PC_{71}BM$ and creating a phase separated morphology. Liu et al. also studied diketopyrrolopyrrole quaterthiophene (DPPBT):$PC_{71}BM$ slot die coated from CF with varying amounts of DCB added.[81] Their results suggest that the polymer aggregates and orders locally as CF evaporates. Following CF evaporation, polymer aggregates form a fibrillar network in which the remaining polymer and fullerene are deposited to form the final BHJ morphology.

Our results are largely in agreement with those presented by Liu et al.[80] and van Franeker et al.[79] When DT-PDPP2T-TT:$PC_{71}BM$ is blade coated from chloroform the morphology evolution is dominated by L-L de-mixing. The large scale phase separation observed in our TEM results, the low relative degree of crystallinity, and the early onset of polymer crystallization in the wet film seen in the in situ GIXD, Figure 68, signifies that this BHJ morphology is formed from spinodal decomposition. The rapid evaporation of chloroform leads to polymer and fullerene de-mixing in solution, followed by verification of fullerene, and polymer crystallization.

When DT-PDPP2T-TT:$PC_{71}BM$ is blade coated from CF:DCB we find that DCB serves to reduce domain size, reduce polymer fiber aggregates, and enhance neat, and BHJ, polymer crystallinity, indicating DCB acts in a similar manner as a plasticizer. The rapid evaporation of CF sharply increases concentration, leading to an increase in polymer aggregate formation. However, there is no observed crystallization during removal of CF,

even as the concentration approaches ~74 mg/mL. This indicates that DCB serves to plasticize the polymer:fullerene blend, suppressing the T_g, and preventing crystallization from occurring, even at high concentrations. As the remaining DCB evaporates, the polymer aggregates and these aggregates serve as nucleation sites for crystallization. Upon removal of DCB the T_g increases leading to enhanced polymer crystallization. The polymer fiber network observed in the TEM, and AFM, occurs through a nucleation and growth mechanism, which has been reported for a similar DPP based polymer by Janssen and co-works.[183]

5.8. Conclusion.

The results presented here show enhanced photovoltaic performance when the BHJ is blade coated from mixed solvents instead of a single solvent. Using a combination of static, and in situ, thin film measurements we provide a mechanistic understanding as to why co-solvent processing leads to a more optimal BHJ phase separated morphology compared to single solvent processing. Our results show processing DT-PDPP2T-TT:$PC_{71}BM$ from chloroform leads to large scale phase separated domains of ~200 nm due to spinodal decomposition. When the polymer:fullerene blend is processed from a mixture of CF:DCB there is a significant reduction in domain size to ~60 nm and an increase in polymer crystallinity. The addition of DCB acts analogous to a plasticizer, which increases nucleation density, and crystallization upon evaporation, leading to enhanced polymer crystallinity, increased phase purity, and reduced domain size relative to a single solvent. This improved BHJ morphology allows for increased interfacial area between polymer and fullerene while maintaining an interconnected network for charges to be extracted.

CHAPTER 6. OUTLOOK AND PERSPECTIVES OF ORGANIC PHOTOVOLTAICS AND ORGANIC ELECTRONICS

6.1. Current Energy Technologies Comparison.

While the majority of this dissertation describes experimental techniques, conjugated materials processing, and measurement science related to thin film characterization, it is useful to provide broader context of the OPV field in order to understand how this technology relates to the PV field as a whole. Figure 72 shows the National Renewable Energy Laboratory (NREL) PV efficiency chart as a function of year.[184] A wide range of PV technologies are included in this chart, in which OPV are found in the emerging PV section (orange). Single junction OPVs, such as those examined in this dissertation, orange filled circle in Figure 72, have come a long way from a certified power conversion efficiency of < 4% in 2001 to multiple cases of 11% in 2016. While OPV technology does not match its Si counterpart in terms of efficiency performance, it is important to note that Si based technologies are significantly more mature, and Si power conversion efficiencies have largely plateaued since 1996, whereas OPV efficiencies have steadily increased since 2001. This section seeks to provide an overview of OPV technology and a comparison to Si technology, in terms of common economic variables and future outlook.

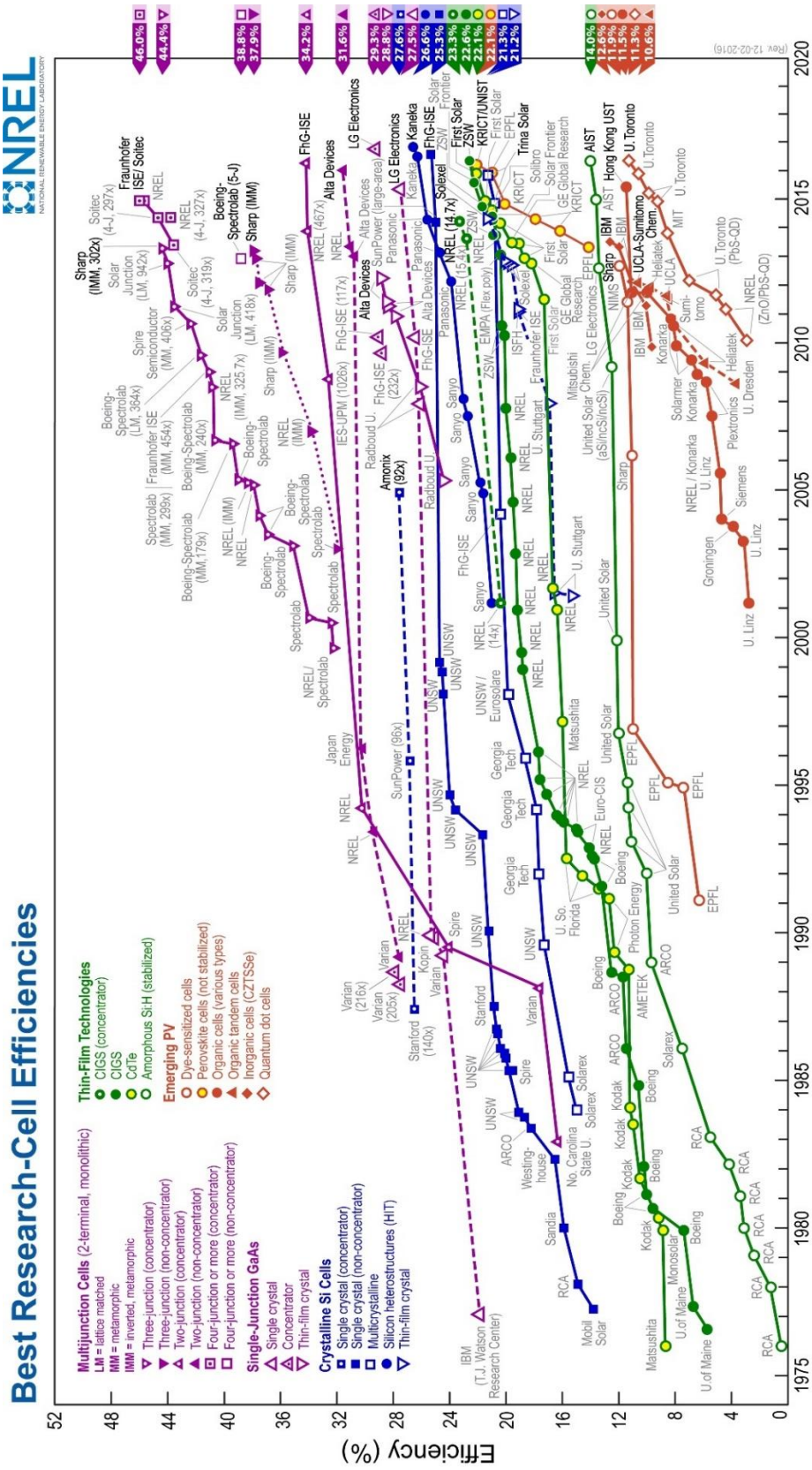

Figure 72. NREL solar cell efficiency table. Reproduced from NREL.[184]

6.2. Evaluating Solar Technologies.

To date crystalline Si based PV technology has dominated the market place, so it is useful to compare OPV technology to this market leader to provide a frame of reference. When comparing two different energy producing technologies, a valuable metric commonly used is the levelized cost of electricity (LCOE). LCOE can be calculated by Equation 6-1:[185]

$$\text{Equation 6-1: LCOE} = \frac{\sum lifetime\ cost}{\sum energy\ produced\ over\ lifetime} = \frac{\sum_{t=0}^{T} C_t/(1+r)^t}{\sum_{t=0}^{T} E_t/(1+r)^t}$$

Where C_t is the net cost of the project, r is the discount rate, t is time, E_t energy produced, and T is the lifetime of the project. While LCOE is an important metric used to compare energy technologies, it can be quite complex to determine values because many assumptions have to be made. Since LCOE accounts for the lifetime of the energy producing technology, which can be ca. 25 years for Si PV, it is difficult to accurately forecast factors such as weather, panel degradation, and maintenance. Therefore, all LCOE values contain assumptions based on forecasted projections. Further, LCOE can be highly subject to public policy, such as investment tax credits, which directly impact both the cost and penetration of the technology in the market place.[46] Nonetheless, LCOE is a useful metric that allows for direct comparison of energy producing technologies if care is taken in its determination.

Mulligan et al. reported the first commercial scale LCOE estimates for OPVs.[186] Their results shows that LCOE values of OPV, with a PCE of 2% and a lifetime of 3 years,

are equivalent to those of conventional rooftop Si based solar. Figure 73 shows key results from this study, in which LCOE ($/kWh) of commercial scale manufactured OPVs is calculated based on the efficiency (%) and lifetime (years) of the device. What is apparent from Figure 73 is efficiency and lifetime have a drastic impact on LCOE at low values, however, as efficiency and lifetime increase the change in LCOE values lessens. LCOE effectively plateaus at 5% efficiency and 5 years, which signals LCOE is not greatly affected by increasing either parameter. Past 5% efficiency and 5 years, the authors determine, using sensitivity analysis, that module balance of system (BOS) costs (installation labor, disposal, and shipping), and interest rate, have a greater impact on LCOE then system lifetime or PCE. Policies that address module systems cost and interest rates can greatly promote the advancement of this technology through reduction of BOS.

		Efficiency (%)					
		1	2	3	4	5	10
Lifetime (Yrs)	1	0.95	0.51	0.37	0.29	0.25	0.16
	2	0.59	0.33	0.24	0.20	0.18	0.12
	3	0.47	0.27	0.20	0.17	0.15	0.11
	4	0.41	0.24	0.18	0.16	0.14	0.11
	5	0.37	0.22	0.17	0.15	0.13	0.10
	10	0.30	0.19	0.15	0.13	0.12	0.09

Figure 73. LCOE ($/kWh) of OPVs as a function of efficiency and lifetime given a solar insulation of 1700 kWh/m^2 yr, a 10% discount rate, and a degradation coefficient of 0.8. Reproduced from Mulligan et al.[186] Copyright 2015, Elsevier.

Further, Mulligan et al.[186] have compared LCOE values between different energy producing technologies, shown in Figure 74, where the boundaries of the shaded region

correspond to 2, 3, 5 and 10, years from top to bottom. Interestingly, OPV technology at an efficiency of 2% and a 3-year lifetime is found to be cost competitive with rooftop PV. Additionally, OPVs with 10% power conversion efficiency are cost competitive with the fossil fuel technologies coal and natural gas. This work demonstrates the potential of manufacturing scale OPV as a contender for low cost energy producing technology. However, achieving reproducible solution processed large scale OPV devices, like those found in commercial applications, is very difficult. Laboratory scale OPV devices fabricated via spin coating have certified efficiencies >10%, but as this technology is scaled to larger areas, PCE values rapidly fall off due to increased resistances, increased exciton recombination, and film uniformity issues.[187]

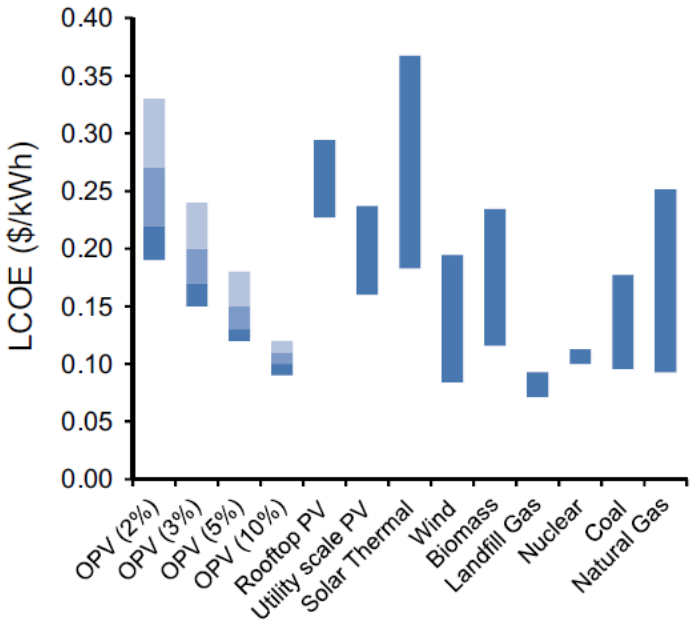

Figure 74. Comparison of LCOE ranges amongst varying energy producing technologies. Rooftop and utility scale PV is Si based. Percentage values in parenthesis next to OPV indicate the device efficiencies. Reproduced from Mulligan et al.[186] Copyright 2015, Elsevier.

Gambhir et al.[188] have also investigated the LCOE of OPV, finding a median LCOE of \$0.28/watt peak (W_p), which compares to projected LCOE values of established Si technologies which range from \$0.35 – 0.60/W_p by 2020. Figure 75 demonstrates the LCOE of OPV for ground and rooftop based systems with 5 and 10 year lifetimes, based on power conversion efficiencies of 3.5 – 7%, discount rates from 7 – 15%, and plant lifetimes of 10 - 20 years. Other factors influencing LCOE values are discussed in the article. The red lines in Figure 75 outline the established LCOE range for ground and roof top mounted PV. The range for established LCOE for ground is \$0.115 – 0.142/kWh while OPV, with a 10 year lifetime, was found to be \$0.123 – 0.139/kWh. Likewise, for roof top mounted PV the established LCOE range is \$0.144 – 0.170/kWh while OPV, with a 10-year lifetime, was found to be \$0.152 – 0.169/kWh. The effect that device lifetime has on LCOE is striking; when examining the ground and rooftop OPV with a 5 year lifetime, these LCOE values are significantly higher than the established range, indicating the sensitivity of lifetime to LCOE values, which is in contrast to Mulligan et al.[186] Interestingly, Gambhir et al. found four factors that significantly impact LCOE, which are; plant manufacturing scale, materials cost, geometric fill factor, and efficiency. Decreasing the cost in both plant manufacturing scale and materials cost can be addressed through policy intervention and economies of scale. However, geometric fill factor and efficiency must be improved through scientific advancement of materials, device architectures, and optimization, which can be indirectly influenced by policies that support the advancement and funding of this technology. Lastly, the analysis presented by Gambhir et al.[188] finds OPV to be cost competitive with Si based PV if the lifetime is 10 years, whereas Mulligan et al.[186] shows OPV LCOE, with a 3-year lifetime, to be cost competitive with Si PV. These

differences highlighted here demonstrate the difficulty of accurately determining LCOE values due to the complex assumptions that are made, and the lack of large scale OPV production data.

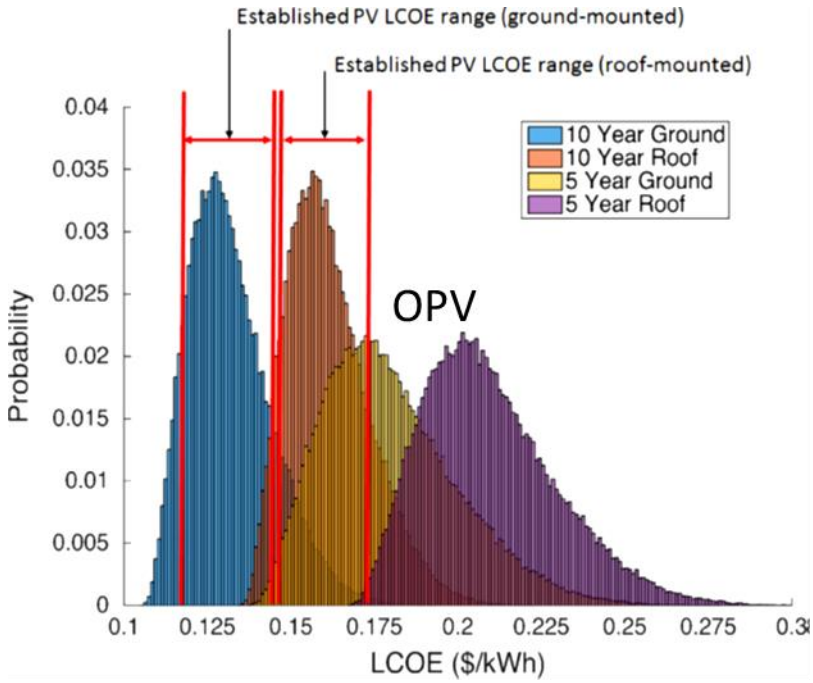

Figure 75. LCOE of roof and ground mounted OPV systems with a 5 year and 10 year lifetime, and the established LCOE range for PV systems. Adapted from Gambhir et al.[188] Copyright 2016, Elsevier.

When comparing, PV technologies it is also advantageous to examine the energy payback time (EPBT), defined by Equation 6-2, which is the time required for a renewable energy system to generate an equivalent amount of energy as it took to produce that system:[189]

$$\text{Equation 6-2: EPBT} = \frac{E_{input}}{E_{saved}}$$

Like LCOE, EPBT is complex to accurately calculate, particularly for OPV since both energy input (E_{input}), and energy saved (E_{saved}), are derived from many variables which

must be estimated. It is challenging to determine EPBT for OPV since large scale production data is not available for this technology as of today, therefore, many variables have to be estimated based on current, and projected, values of laboratory devices.

Darling et al.[190] performed a detailed life cycle analysis (LCA) in order to determine EPBT for OPV and its competitors. Table 9 show the EPBT of several PV technologies. What is evident from Table 9 is that OPV has a relatively good EPBT of 0.79 – 2.02 years, even with low efficiencies ranging from 2% - 4% compared to the market leader, monocrystalline Si (c-Si) solar cells, which demonstrate significantly higher efficiencies and EPBT. This establishes that solar cell efficiencies are not the most important metric to be considered when evaluating PV technology, rather, a holistic examination is needed to value and compare different PV technologies.

Table 9. Comparison of PV technologies and their respective EPBT based on solar cell efficiency ranges. Reproduced from Darling et al.[190] with permission from the Royal Society of Chemistry.

PV technology	EPBT (years)	Efficiency range
c-Si	4.12–2.38	11.5%–14%
p-Si	2–1.9	13%–13.2%
Ribbon-Si	1.4	11.5%
a-Si	1.13	7%
CIGS	2.26–2.2	8.9%–11%
CdTe	1.61–0.63	8%–13%
OPV	2.02–0.79	2%–4%

Figure 76 shows the EPBT for crystalline Si (c-Si), amorphous Si (a-Si), ribbon-Si, cadmium telluride (CdTe), and OPV, solar cells, with the current power conversion

efficiencies, mid-term (5 - 10 years) projected power conversion efficiencies, and the long term (>10 years) projected power conversion efficiencies in parenthesis. Figure 76 shows all solar technologies EPBT are forecasted to improve as power conversion efficiencies increase. OPV in particular shows the lowest EPBT values, where a 1% solar cell efficiency yields a EPBT of <6 months, and efficiencies of >10%, which have already been achieved on a laboratory scale[140], have an EPBT as short as 12 days. The dramatically low EPBT values seen in OPV is largely credited to the low manufacturing cost relative to Si based solar cells which require a high thermal budget, and large capital investment in equipment.

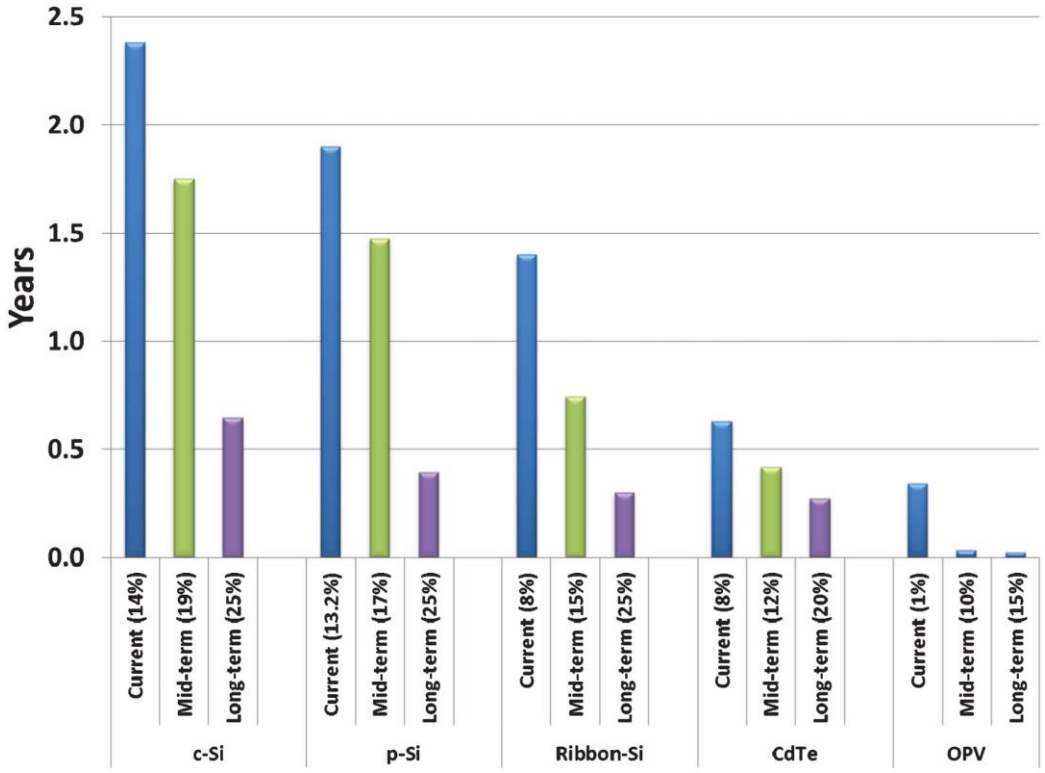

Figure 76. EPBT for c-Si, p-Si, ribbon-Si, CdTe, and OPV, solar cells, based on current efficiencies, mid-term (5 -10 years) projected efficiencies, and long term (>10 years) projected efficiencies. Results shown for EPBT are based on rooftop mounted solar with an insolation of 1700 kWh/m^2 per year. Reproduced from Darling et al.[190] with permission from the Royal Society of Chemistry.

To improve LCOE, and EPBT, two levers can be manipulated which are cost and power conversion efficiency. There are many scientific and engineering strategies employed that improve PCE, which have been discussed throughout this dissertation, here I will focus on manufacturing cost optimization as a route to decrease LCOE and EPBT.

One of the most highly cited arguments for advancement of OPV technology is its low manufacturing cost, however, few reports exist on the actual cost of large scale OPV production. Machui et al.[191] performed a detailed cost analysis of ITO free roll-to-roll manufactured tandem OPVs finding that active layer materials, barrier foils, and electrodes are the main share of the overall cost of the device. They examine the current status (kW production regime), an upscaling production (MW production regime), and an industrial production (GW production regime), for tandem OPV solar cells with a top cell composed of a novel polymer denoted as MH301, and a bottom cell composed of a novel polymer denoted as MH306, both of which are blended with PCBM. Table 10 shows a cost breakdown of the upscaling scenario of a tandem OPV. From Table 10, it is clear the costliest components of the device are the barrier foil, the Ag used for the electrode, and the acceptor PCBM. The authors indicate that replacement of the Ag back electrode with Al would lead to a 77% cost reduction. The total cost per square meter at the 100 MW production regime was found to be $\$13.4/m^2$ (a conversion rate of 1.05:1 euro to U.S. dollar was used).

Table 10. Cost analysis of OPV tandem solar cell based on an upscaling scenario. Active layer donor costs were estimated based on expert opinion. Reproduced from Machui et al.[191] with permission from the Royal Society of Chemistry.

Material	Supplier	Type	Used amount	Unit	Cost	Unit	Cost [€ per m^2]
Barrier foil			1.00	m^2	1.00	m^2	1.00
Ag	Pchem	PFI-722	0.26	g m^{-2}	2.00	€ per g	0.53
PEDOT:PSS	Heraeus	Clevios FET DK	1.67	mL m^{-2}	0.33	€ per mL	0.54
	Sigma-Aldrich	Isopropanol	3.33	mL m^{-2}	0.03	€ per mL	0.09
ZnO	DTU	ZnO	1.00	mL m^{-2}	0.01	€ per mL	0.01
Active layer 1 donor		MH301 based calculation	0.033	g m^{-2}	20.00	€ per g	0.66
Active layer 1 acceptor		PCBM based calculation	0.066	g m^{-2}	20.00	€ per g	1.32
Active layer 1 solvent	Sigma-Aldrich	Chlorobenzene	4.59	mL m^{-2}	0.02	€ per mL	0.11
PEDOT	Heraeus	PEDOT AI 4083	1.60	mL m^{-2}	0.20	€ per mL	0.32
	Sigma-Aldrich	Isopropanol	3.33	mL m^{-2}	0.03	€ per mL	0.09
ZnO	DTU	ZnO	1.00	mL m^{-2}	0.01	€ per mL	0.01
Active layer 2 donor		MH6 based calculation	0.033	g m^{-2}	20.00	€ per g	0.66
Active layer 2 acceptor		PCBM based calculation	0.050	g m^{-2}	20.00	€ per g	1.00
Active layer 2 solvent	Sigma-Aldrich	Chloroform	4.59	mL m^{-2}	0.02	€ per mL	0.11
PEDOT:PSS	Heraeus	Clevios AI 4083	1.67	mL m^{-2}	0.20	€ per mL	0.33
	Sigma-Aldrich	Isopropanol	3.33	mL m^{-2}	0.03	€ per mL	0.09
PEDOT:PSS	Heraeus	Clevios F010	3.33	mL m^{-2}	0.14	€ per mL	0.46
	Sigma-Aldrich	Isopropanol	1.67	mL m^{-2}	0.03	€ per mL	0.04
Ag	Dupont	5025	3.11	g m^{-2}	1.33	€ per g	4.13
Adhesive	DELO	DELO-KATIOBOND LP655	3.00	g m^{-2}	0.10	€ per g	0.30
Barrier foil			1.00	m^2	1.00	m^2	1.00
							12.81

Through scale up from the 100 MW regime to the 100 GW regime (industrial production) the price per square meter falls to \$7.11/m^2. Table 11 shows the cost analysis for industrial production of tandem OPV devices. It should be noted that the Ag back electrode found in the upscaling scenario was replaced with a significantly cheaper carbon back electrode. Like the upscaling scenario, the acceptor PCBM and barrier foil, are some of the costliest components in the industrial scenario.

Table 11. Cost analysis of OPV tandem solar cell based on an industrial scenario. Active layer donor costs were estimated based on expert opinion. Reproduced from Machui et al.[191] with permission from the Royal Society of Chemistry.

Material	Supplier	Type	Used amount	Unit	Cost	Unit	Cost [€ per m^2]
Barrier foil			1.00	m^2	1.00	m^2	1.00
Carbon			0.26	g m^{-2}	0.14	€ per g	0.04
PEDOT:PSS	Heraeus	Clevios FET DK	1.67	mL m^{-2}	0.33	€ per mL	0.54
	Sigma-Aldrich	Isopropanol	3.33	mL m^{-2}	0.03	€ per mL	0.09
ZnO	DTU	ZnO	1.00	mL m^{-2}	0.01	€ per mL	0.01
Active layer 1 donor		MH301 based calculation	0.033	g m^{-2}	10.00	€ per g	0.33
Active layer 1 acceptor		PCBM based calculation	0.066	g m^{-2}	10.00	€ per g	0.66
Active layer 1 solvent	Sigma-Aldrich	Chlorobenzene	4.59	mL m^{-2}	0.02	€ per mL	0.11
PEDOT	Heraeus	PEDOT AI 4083	1.60	mL m^{-2}	0.20	€ per mL	0.32
	Sigma-Aldrich	Isopropanol	3.33	mL m^{-2}	0.03	€ per mL	0.09
ZnO	DTU	ZnO	1.00	mL m^{-2}	0.01	€ per mL	0.01
Active layer 2 donor		MH306 based calculation	0.033	g m^{-2}	10.00	€ per g	0.33
Active layer 2 acceptor		PCBM based calculation	0.050	g m^{-2}	10.00	€ per g	0.50
Active layer 2 solvent	Sigma-Aldrich	Chloroform	4.59	mL m^{-2}	0.02	€ per mL	0.11
PEDOT:PSS	Heraeus	Clevios AI 4083	1.67	mL m^{-2}	0.20	€ per mL	0.33
	Sigma-Aldrich	Isopropanol	3.33	mL m^{-2}	0.03	€ per mL	0.09
PEDOT:PSS	Heraeus	Clevios F010	3.33	mL m^{-2}	0.14	€ per mL	0.46
	Sigma-Aldrich	Isopropanol	1.67	mL m^{-2}	0.03	€ per mL	0.04
Carbon			3.11	g m^{-2}	0.14	€ per g	0.42
Adhesive	DELO	DELO-KATIOBOND LP655	3.00	g m^{-2}	0.10	€ per g	0.30
Barrier foil			1.00	m^2	1.00	m^2	1.00
							6.79

Figure 77 illustrates the cost per m^2 of various components that make up the tandem OPV based on current status, upscaling scenario, and industrial scenario. In the current status, the active layer donor makes up the highest cost component, however, it is forecasted that polymeric, and discrete molecule, donor materials will significantly drop in price through economies of scale and optimized synthesis. In the upscaling scenario, Ag electrodes and the active layer acceptor pose the highest costs on production. Scientific focus on replacing Ag electrodes with cheaper alternatives is necessary to ensure low manufacturing cost of this technology. Likewise, replacement of costly PCBM will be needed to drive costs down. Recently in the literature, there has been a surge in non-fullerene acceptors to replace PCBM that yield high performance OPVs [192, 193], which have the potential to be manufactured at reduced costs relative to PCBM. Replacement of

fullerene with non-fullerene alternatives will lead to significant cost reductions. It is forecasted that industrial production of OPV solar cells will lead to expected module costs of \$0.05-0.06/W_p which is significantly cheaper than \$0.50/W_p for current c-Si modules.[194]

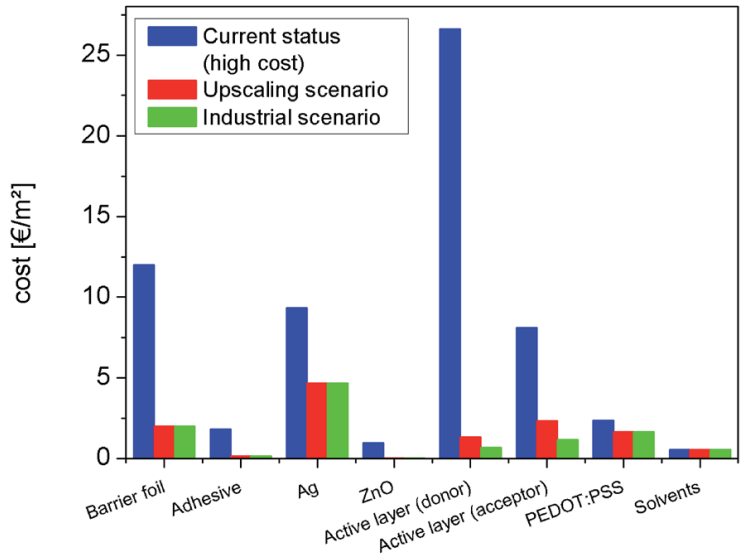

Figure 77. Cost per m^2 reduction for each component of a tandem OPV based on three scenarios; current status, upscaling, and industrial, production. Reproduced from Machui et al.[191] with permission from the Royal Society of Chemistry.

6.3. Future and Challenges of OPVs and Organic Electronics.

The future of organic electronics, and OPVs, is bright. As demonstrated by NREL's solar efficiency chart (Figure 72), certified OPV efficiencies have been steadily rising as new materials, and improved processing techniques yield an enhanced morphologies leading to high performance devices. However, many challenges still face OPVs, and organic electronics in general, which must be addressed to become a commercially viable technology. This section seeks to provide a discussion of advancements needed the OPV

field, beginning from materials design through scale up of polymeric materials used in OPV and manufacturing of devices, that will push this technology from the academic setting into the marketplace.

6.3.1. Materials Design Challenges.

To date there are no concrete design rules that yield high performance OPV materials, rather, it is a trial and error process based on previous work, and some well-studied materials. Figure 78 show the complexity of designing new materials in this field. Xiao et al.[195] sketched a rough relationship of all the variables that go into designing, processing, and measuring, OPV materials that yield high performance devices. The initial stages begin with designing and synthesizing donor-acceptor co-polymers with appropriate energy levels, side chains, and M_w. This initial stage is quite challenging as many structurally dissimilar polymers lead to high performance OPV devices. This is illustrated in Figure 79, which is a small compilation OPV donor polymer materials with demonstrated PCEs beyond 6%.[196] These polymers are then solution processed with fullerene to yield a BHJ morphology, which is sensitive to many factors such as deposition methods, temperature, and additives. This morphology then dictates physical processes, and ultimately device performance. Chapters 3, 4, and 5, dealt with how processing conditions and ink formulation impact morphology and device efficiency. Lessons learned from each of these independent studies helps to guide future work. In each of those chapters, there are some overlapping similarities, which include, increased polymer order and average domain size reduction. In all cases, achieving these morphologies leads to improved devices even though these morphological traits were achieved in various ways. The key challenge that organic electronic materials design faces is the lack of structure-

property relationships. Numerous high performance polymers exist with a wide range of chemical structures, physical characteristics, and processing methods, that yield high performance OPV devices, yet, quantitative correlation between structure and function that serve as a feedback mechanism to synthetic chemists, allowing them to create the next generation of advanced OPV materials, has not been determined.

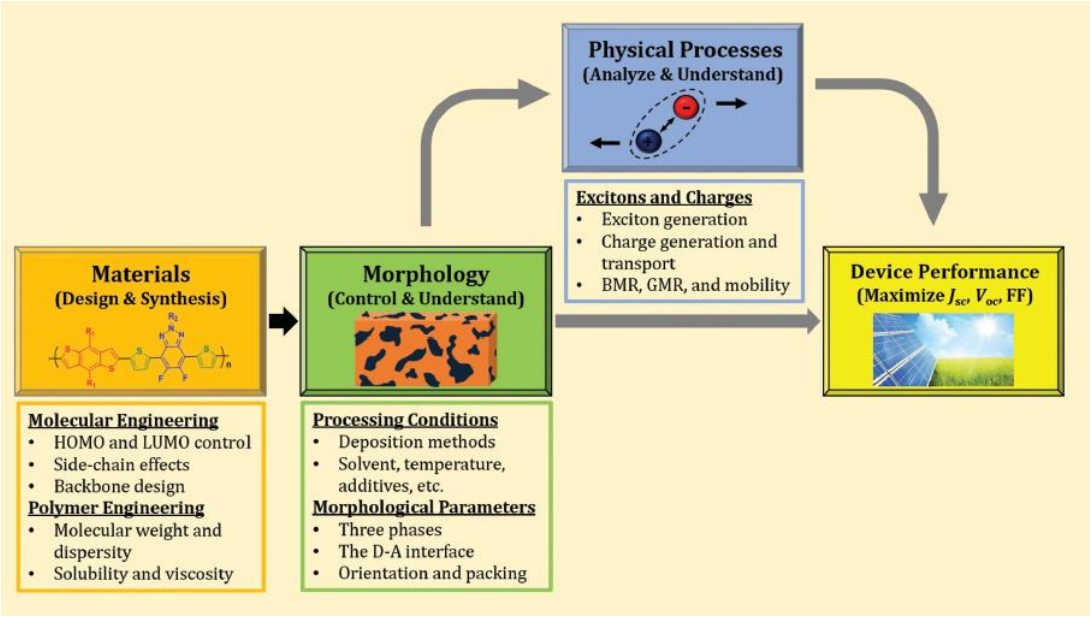

Figure 78. Relationship and variables that go into materials design, morphology, physical processes, and device performance, for OPVs. Reproduced from Xiao et al.[195] Copyright 2016, Wiley-VCH.

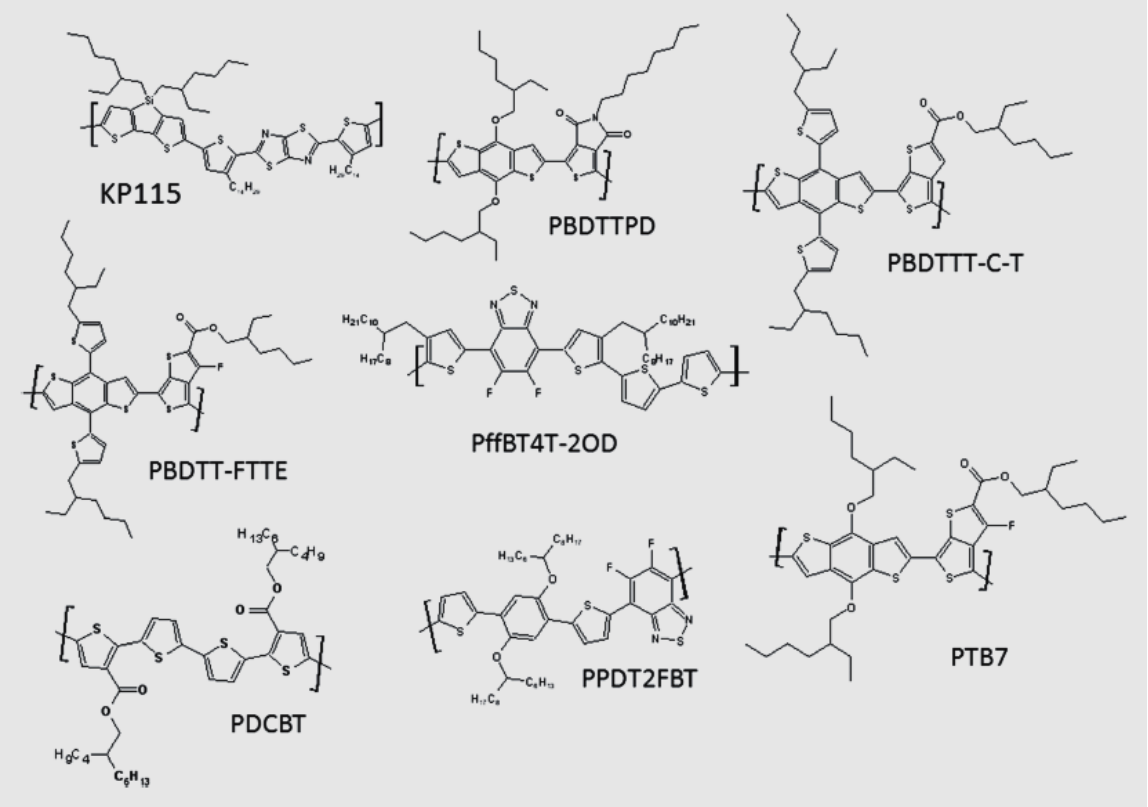

Figure 79. Chemical structures of high performance OPV donor polymer materials. Adapted from Scharber et al.[196] Copyright 2016, Wiley-VCH.

6.3.2. Scale up Challenges.

While the economics of scale up have been shown to be favorable for OPVs, the technical challenges that face scale up of this technology from small lab scale devices, to large commercially available panels, are complex. This is highlighted in a review of printed energy technologies by Hosel et al.[141] Table 12 show an overview of published OPV devices fabricated on small to large scale roll-to-roll equipment that would be seen in a production scenario. It is evident from Table 12 that scale up of this technology leads to reduced device efficiencies. The highest performance device found using large scale production equipment was found to be 2.9% with an active area of 1.1 cm^2, and requiring

4 evaporations. While small scale laboratory devices are achieving efficiencies beyond 10%,[140] the simple transfer to large scale production modules is not trivial and numerous factors contribute to decreased performance.

Table 12. Overview of OPV devices fabricated using different roll-to-roll methods on small to large scale equipment. Table reproduced from Hösel et al.[141] Copyright 2015, Wiley-VCH.

Structure	Conductive Substrate	Layer processed	Method	Evap.	A_{active} [cm^2]	PCE [%]	Notes	Ref
Small-scale R2R systems with small footprint or narrow web width (experimental machines)								
normal C	ITO	HTL, AL	G	1×	0.68	0.3	3.7–8.7 m min^{-1}	Ref. [75]
normal C	ITO	HTL, AL	G	1×	0.5	1	3.7 m min^{-1}	Ref. [76]
inverted C	ITO	AL, ETL	SD	2×	1	2.4	1 m min^{-1}, external drying	Ref. [77]
normal C	ITO	HTL, AL	SD	1×	0.25	1.74	1–4 m min^{-1}, 13 m air dryer	Ref. [78]
normal C	ITO	HTL, AL	SD	2×	0.25	3.2	1–2 m min^{-1}	Ref. [79]
inverted M	ITO	ETL, AL, HTL, BEL	SD, SP	–	120	1.7	$<$2 m min^{-1}, flatbed SP	Ref. [80]
inverted M	Ag	BEL, ETL, AL, HTL, FEL	SD, SP	–	120	0.3	0.2–0.9 m min^{-1}, flatbed SP	Ref. [81]
inverted M	ITO	ETL, AL, HTL, BEL	SD, SP	–	360	1.69	$\leqq$2 m min^{-1}, flatbed SP	Ref. [30]
inverted C	Zn	Glue, AL, HTL	G, F	–	0.09	1.3	18–30 m min^{-1}, paper substrate	Ref. [82]
normal M	ITO	HTL, AL	G	2×	6	1.6		Ref. [83]
Large-scale R2R systems with large footprint, large web width and high speed capabilities (close to industrial machinery)								
inverted C	Cr, Al, Cr	AL, HTL	SD	4×	1.1	2.9	1 m min^{-1}, aerosol jet tested	Ref. [84]
normal M	ITO	HTL, AL	SD	2×	21	0.7	10 m min^{-1}, manuel patterning	Ref. [85]
inverted M	ITO	ETL, AL, HTL, BEL	SD, SP	–	n.a.	3	full R2R	Ref. [4]
inverted M	ITO	ETL, AL, HTL, BEL	SD, SP	–	35.5	2.75	$<$2 m min^{-1}, full R2R	Ref. [86]
inverted M	Ag grid/PEDOT:PSS	FEL, ETL, AL, HTL, BEL	F, SP, SD	–	66	1.6	2–10 m min^{-1}, full R2R, inline	Ref. [87]
inverted M	Ag grid/PEDOT:PSS	FEL, ETL, AL, IL, HTL, BEL	F, SP, SD	–	52.2	1.76	$<$20 m min^{-1}, full R2R, tandem	Ref. [88]
inverted M	Ag grid/PEDOT:PSS	FEL, ETL, AL, HTL, BEL	F, SP, SD	–	14 7000	2	$<$20 m min^{-1}, full R2R, 21 000 cells	Ref. [5]
inverted M	Ag grid/PEDOT:PSS	FEL, ETL, AL, HTL, BEL	F, SP, SD	–	57	1.82	$<$20 m min^{-1}, full R2R	Ref. [89]
inverted M	PEDOT:PSS	FEL, ETL, AL, HTL, BEL	SP, SD	–	30	1.85	4–10 m min^{-1}, full R2R, silver free	Ref. [90]
inverted C	Ag grid/PEDOT:PSS	FEL, ETL, AL, HTL, BEL	F, IJ, IP, SD, SP	–	6	$<$1.9	0.5–25 m min^{-1}, full R2R	Ref. [91]
normal M	ITO	HTL, AL	G	2×	15	1.86	8 m min^{-1}	Ref. [39]

C = cell, M = module, HTL = hole transport layer, ETL = electron transport layer, AL = active layer, FEl = front electrode, BEL = back electrode, IL = intermediate layer, DB = doctor blading, G = gravure printing, SD = slot–die coating, IJ = inkjet printing, SP = screen printing, F = flexo printing, IP = imprinting

The challenge here is to move away from small scale device fabrication to commercial scale device fabrication methods which was partly the subject of Chapter 3, 4, and 5. One step forward in scale up of organic electronics is the use of roll-to-roll coating techniques, described in previous chapters. P3HT, P(T3-TPD), and DT-PDPP2T-TT, OPV devices, fabricated using blade coating in air, demonstrated similar performance to devices spun coat in an inert glovebox. Further, results found in Chapter 4 demonstrates that the use of aggregated polymer solutions predetermines the solid-state morphology, thus reducing the

optimization process required when transferring from spin coating to blade coating, making it simpler to move to roll-to-roll deposition techniques. During deposition of the active layer, the use of in situ absorbance and reflection monitoring, as described in Chapters 3,4, and 5, provide a useful real time measurement technique to determine when thin film solidification is complete. Incorporating optical probes throughout the manufacturing process would allow for accurate real time feedback on the drying dynamics and polymer aggregation within the BHJ film. This information aids in quality control and optimization of the roll-to-roll coaters to reduce fabrication time. Furthermore, the use of in situ optical probes provides insights into polymer alignment induced by the shear force of the coating technique. While polymer alignment is typically not a factor for OPV technology, it has been shown to impact OFET performance.[167] One production rate limiting step, particularly for OFETs, is polymer alignment. If optimal polymer alignment is achieved at low coating speeds, then effectively the coating speed that induces polymer alignment will be the rate limiting step for production. For OPVs, one production rate limiting step will be drying of the active layer. The use of high boiling point solvent additives, such as DIO, drastically increases the drying time of the active layer. In Chapter 4 when the polymer:fullerene (P(T3-TPD):$PC_{71}BM$) blend is processed from chloroform the drying time was <4 seconds, but when the solvent additive DIO was used the drying time increased to ca. two hours. To overcome this production rate limiting step dryers should be put in place that increase the evaporation rate of the solvent additive without affecting the morphology, or material systems will need to be developed that achieve optimal OPV performance without the use of high boiling point solvent additives.

Moving from laboratory scale device to manufacturing scale devices includes many factors that influence efficiency losses, some of which include increased series resistance and film thickness variation.[197] As of today, Lucera et al.[197] have demonstrated the highest reported large area roll-to-roll processed OPV devices with efficiencies of 5.3% on glass/ITO substrates, and 4.4% on flexible PET substrates, with an active area of 10.4 mm^2. These laboratory grade large area devices provide an excellent demonstration that the scale up of this technology to high throughput manufacturing process is viable. While challenges still face scale up of OPVs, such as increased production of conjugated materials from small batch reactions to multi-pound batch synthesis, reducing resistance losses as active area increases, and tight control of film uniformity, they can be met through a combination of academic research, industrial research, and policy geared toward the advancement of this technology.

In conclusion, OPVs show great promise as a cost effective renewable energy generation source. While this technology is still in the research phase, slowly more and more recognition of the technology is being generated as power conversion efficiencies rise, new materials are developed, and device lifetimes improve. There are still numerous trials that face this field, however, with the dedication of research groups across the globe, and the need for increased renewable energy generation, this technology offers a low cost energy generation solution.

Appendix

A1. Blade coater.

Blade coater schematic:

The following schematic (below) and list of parts is of the blade coater used for this work. Special thanks to Dean DeLongchamp, Lee Richter, Sebastian Engmann, and Jon Downing, for aid in construction of this blade coater.

Blade Coater Schematic

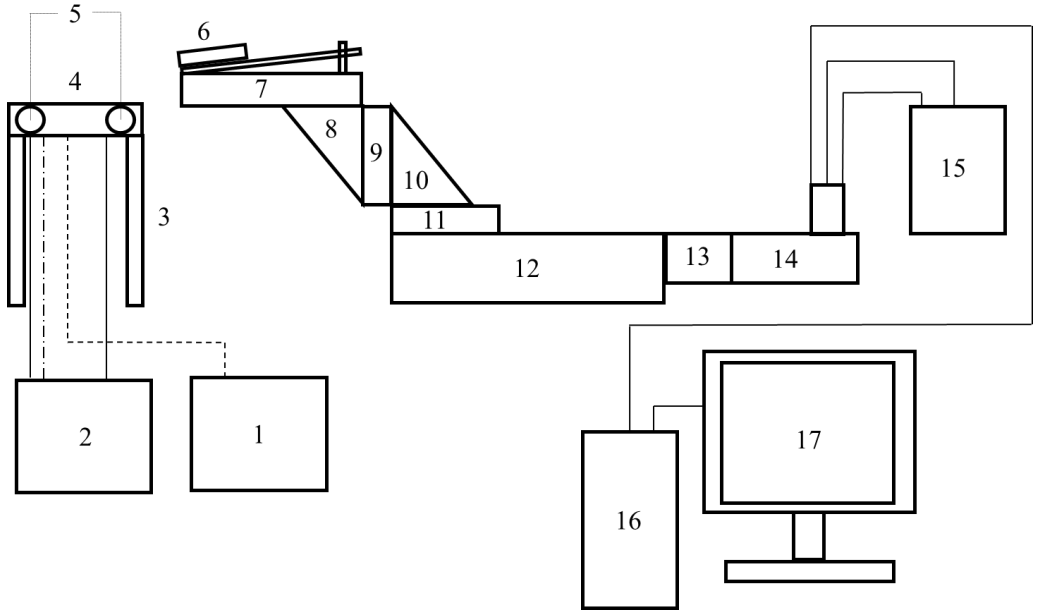

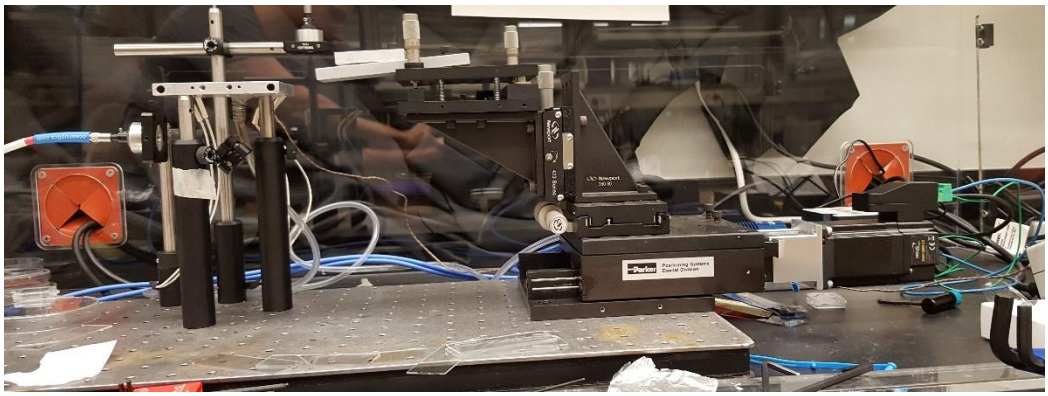

Side view of blade coater

Parts List:

1. Vacuum pump.
2. Bench top temperature controller (Omega csi32k-c24)
3. Optical posts
4. Custom aluminum stage

a)

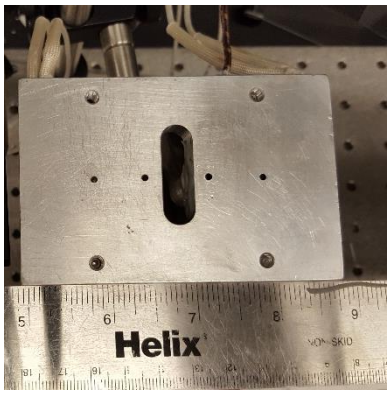

b)

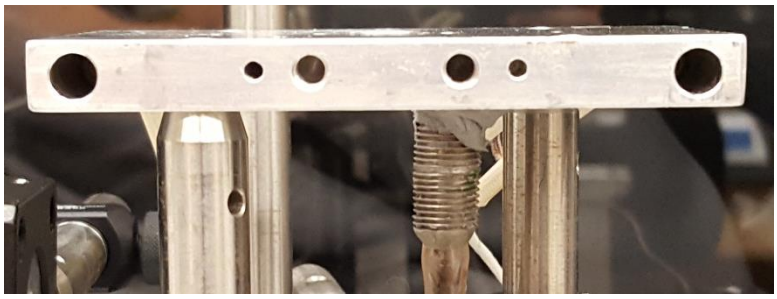

a) Top view, b) side view of aluminum stage.

5. Heating elements: Omega 1/4" Diameter Hi-Density Cartridge Heaters
6. Custom blade holder

a)

b)

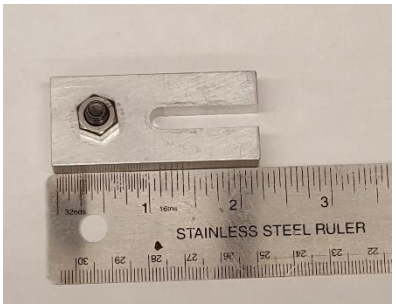

a) Top down view of blade holder, b) top down view of glass holder that goes on top of the blade holder.

7. Newport 2 Axis Tilt & Rotation Platform, ±4° Tilt & Rotate, SM-13
8. Newport Angle Bracket, 90°, Slotted Faces. Model: 360-90

9. Newport High-Performance Low-Profile Ball Bearing Linear Stage, 1.81 in.,1/4-20
10. Newport Angle Bracket, 90°, Slotted Faces. Model: 360-90
11. Newport High-Performance Low-Profile Ball Bearing Linear Stage, 1.81 in.,1/4-20
12. Stage: Parker/Daedel 4" travel stage
13. Custom connector from stage to motor

a) b)

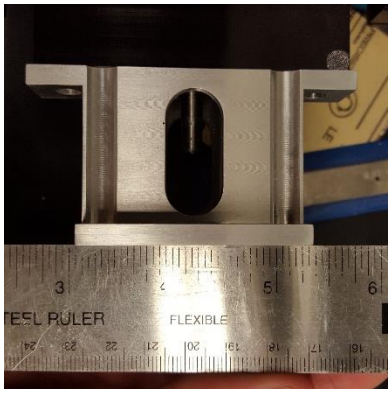

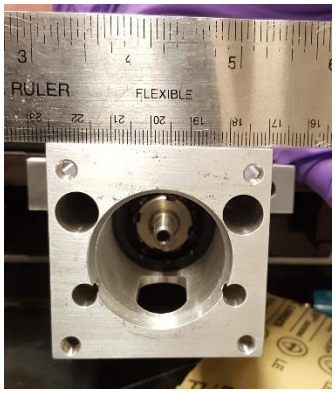

c)

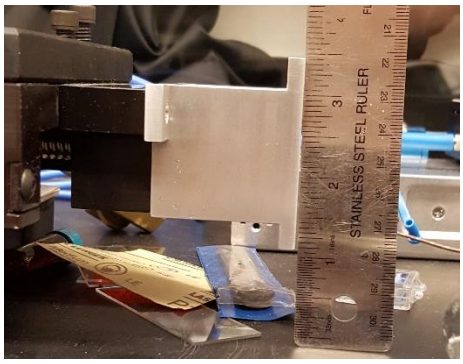

a) Top down view, b) front view, and c) side view of stage to motor connector.

14. Arcus NEMA 23 USB Stepper, model: DMX-UMD-23
15. 24 V Power supply (Mean Well HRP-300-24)
16. Computer
17. Monitor

Parts are held together using black oxide Newport screws.

The coater is controlled through a user interface on the computer with DriveMax software.

A2. Low Donor Content Organic Solar Cells via Side Chain Substitution.

A2.1. Introduction.

Conjugated polymers have shown great promise in organic electronic devices such as, photovoltaics and organic field effect transistors. While the large length scale connectivity of semiconducting polymers imparts a plethora of avenues for charge to be transported throughout a solid-state organic polymer film, certain drawbacks when using polymer films can be mitigated by instead using discrete conjugated molecules for organic electronics.[198] For a given polymer structure and synthetic method, batch-to-batch variations in molecular weight, polydispersity, and solubility decrease the ability to optimize processing conditions to consistently make devices, such as solar cells, with dependable performance. Reproducibility is essential for scalability and reliability of this technology.

In this work, we have synthesized two donor-acceptor conjugated multi-heterocyclic molecules with the same conjugated backbone and different side chains on the central atom. With cyclopentadithiophene (CPDT) flanked by two fluorene benzothiadiazole bithiophene groups and thiophenes as the alternating donor-acceptor backbone, the central carbon atom on the CPDT either has a close branching 2-ethylhexyl chain (CL-B for close-branch) or a far branching 5-ethylnonane chain (FAR-B for far-branch). Similar discrete molecules containing a Si central atom[77, 199, 200], or a Ge central atom [201], have been reported achieving photovoltaic power conversion efficiencies (PCE) >5%. Control of morphology through side chain adjustment has been well studied in the literature, but particularly with polymer systems. [202, 203] Because we have made discrete

molecules rather than polymers, it is easy to exclusively compare the effect of these side chains on the molecules since there are no confounding variables such as the inherent dispersity of a polymer.[204]

We examined a class of small molecules in the literature comprised of a similar core with flanking mono-flouro BTD coupled to thiophenes, where so far a Si and Ge variation has been published. We chose to complete the study with the C analogue, and additionally vary the side chains of the molecule to understand the effect of the branch point on morphology and ultimately organic photovoltaic performance. The C-C bond length is the shortest, so the effect of the sidechains should be greater than in DTS or DTG; subsequently, DTC should have the lowest amount of pi-pi stacking and highest solubility. Bazan and co-workers have published the Si analog in 2012 which achieves 7.0% PCE.[199] As cast devices achieve 2% PCE, but thermal annealing improves PCE to 5.6%, while using 0.4%v of 1,8-diiodooctane (DIO) brings PCE up to 7%. The DTG analog has been reported by Heeger and co-workers in 2014, with PCEs also ca. 7.0% when 0.4%v of the solvent additive DIO is used.[201]

We have made p-CDT(FBTTh$_2$)$_2$, in attempt to elucidate what small effect changing this heteroatom to C would have on device performance. We hypothesize a change in solid-state packing, morphology, and photovoltaic performance relative to the Si and Ge analogues given the difference in size of the heteroatom and bond lengths to it. We have completed a control for effectiveness of DTS and DTG compared to DTC. Using the smaller carbon relative to silicon or germanium brings the solubilizing side chains closer to the conjugated backbone and thus reduces pi-pi stacking efficiency, and hinders charge transport. Furthermore, we have investigated the effect of modulating the side chain on the

dithieno- heteroatom, which also effects the tendency to crystallize and subsequently the photovoltaic properties.

Through optimization of p-CDT($PTTh_2$)$_2$:$PC_{71}BM$ solar cells, we have found that the peak power conversion efficiency lies at a low donor:acceptor ratio of 1:9. Typically, organic photovoltaic systems with low donor concentrations use discrete conjugated donor molecules rather than polymers. Most low donor content studies feature a vacuum evaporated active layer.[205-208] with few reports of solution processing [209] making these bulk-heterojunction (BHJ) morphologies not well understood. In this work, we have solution processed 2EH-CDT($FBTTh_2$)$_2$ and 5EN-CDT($FBTTh_2$)$_2$ comparing the results of a single atom change to literature of the Si and Ge analogs, and have studied the impact of the branch point on the solubilizing side chain. Our results show that a close branch point yields an improved morphology with PCE of >3% at a low donor content relative to $PC_{71}BM$.

A2.2. Results and Discussion.

Two discrete molecules were synthesized, 2EH-CDT($FBTTh_2$)$_2$ and 5EN-CDT($FBTTh_2$)$_2$, which we call CL-B for close branch point, and FAR-B for far branch point, with the chemical structures found in Figure 80.

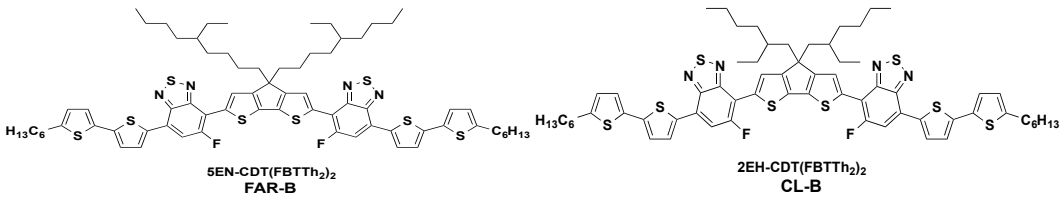

Figure 80. Chemical structures of 2EH-CDT($FBTTh_2$)$_2$ (CL-B) and 5EN-CDT($FBTTh_2$)$_2$ (FAR-B).

Figure 81 depicts the solution UV-vis absorbance, and the spin coated thin film UV-vis absorbance, of neat CL-B and FAR-B. For both CL-B and FAR-B, the solution spectra show no difference indicating that both small molecules have similar optical properties. However, in the film spectra, Figure 81, we find an onset of absorption at lower energy for FAR-B than CL-B. This indicates there is a solid state structural difference between the two molecules in which there is increased local order in FAR-B films relative to CL-B films. FAR-B shows a λ_{max} shift of 10 nm, going from 635 nm for CL-B to 645 for FAR-B. The observed bathohromic shift reinforces enhanced order in FAR-B over CL-B in the solid state, and thus improved electronic communication between intermolecular stacks.[210, 211] The low energy shoulder present at ca. 700 nm in both CL-B and FAR-B indicate π-π stacking.[212, 213] The HOMO/LUMO levels, estimated from cyclicvoltamitry (CV), and the onset of film absorption, of CL-B are -5.32/-3.60 eV, and FAR-B are -5.20/-3.59 eV. The UV-vis absorbance of the bulk-heterojunction films made using optimized solar cell parameters are similar, as shown in Figure 82.

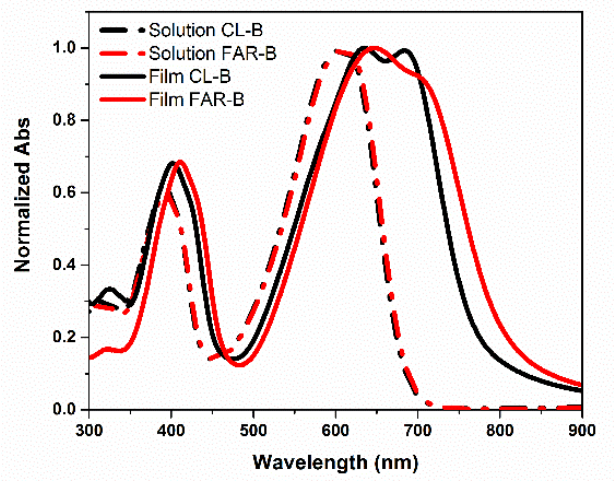

Figure 81. Solution and thin film UV-vis absorbance of neat CL-B and FAR-B.

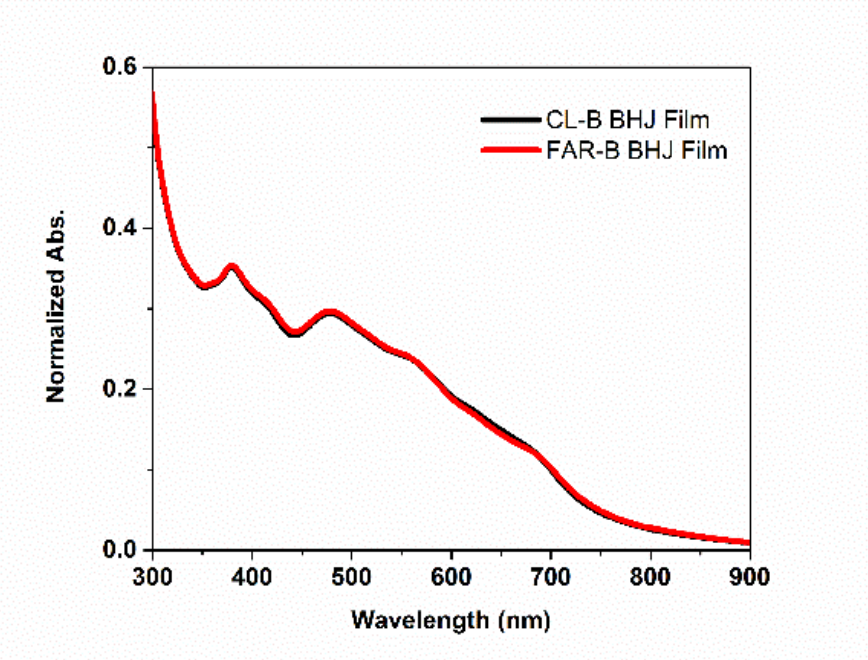

Figure 82. BHJ thin film UV-vis absorption of CL-B and FAR-B with a D:A ratio of 1:9.

Using CL-B or FAR-B, conventional bulk-heterojunction (BHJ) solar cells were fabricated with the architecture of ITO/PEDOT:PSS/Discrete molecule:$PC_{71}BM$/Ca/Al. Figures 83 a) and 81 b) show the short circuit current (J_{sc}), open circuit voltage (V_{oc}), and fill factor (FF) as a function of the donor:acceptor (D:A) ratio by weight percent for FAR-B and CL-B respectively. For solar cells made using FAR-B, the lowest donor:acceptor that achieved any photovoltaic performance was 5:5, and devices made using high percentages of FAR-B relative to $PC_{71}BM$ did not form films. What is evident from both Figure 83 a) and 81 b) is that at low donor concentrations J_{sc} and FF reach their maxima. The V_{oc} remains fairly constant among most donor:acceptor ratios. This is further reinforced when examining Figure 83 c), which is the power conversion efficiency (PCE%) of devices made from CL-B and FAR-B as a function of D:A ratio. What is demonstrated in Figure 83 c) is that a donor:acceptor ratio of 1:9 results in the highest performing devices.

Table 13 shows the solar cell characteristics of devices made with a donor:acceptor ratio of 1:9, averaged over 6 devices. CL-B demonstrated an average PCE of 3.2% while FAR-B showed a PCE of 1.5% at a low D:A ratio of 1:9 A complete table of varying small molecule to fullerene ratio can be found in Table 14. From Table 13 we see that CL-B outperforms FAR-B in J_{sc}, V_{oc}, FF, and PCE%. The increased V_{oc} observed in devices made using CL-B is expected since it has a lower calculated HOMO level than FAR-B. Figure 83 d) shows the J-V curve of devices made with a donor:acceptor ratio of 1:9, and the inset is the external quantum efficiency (EQE). By examining the EQE of Figure 83 d) it is clear that the additional current generated when using CL-B is in the high-energy wavelength region of 300-600 nm. This correlates with the high energy peak seen in the UV-vis absorption of both molecules in Figure 81. This is quite interesting as there are few systems that show improved solar cell performance at such low donor concentrations. Further, it is important to note that processing of CL-B and FAR-B in the same manner as described by Bazan and co-workers yielded very low OPV performance. The solvent additive 1,8-diiodooctante (DIO) decreased device performance, as did thermal annealing, Table 15, which is why this system had to undergo re-optimization.

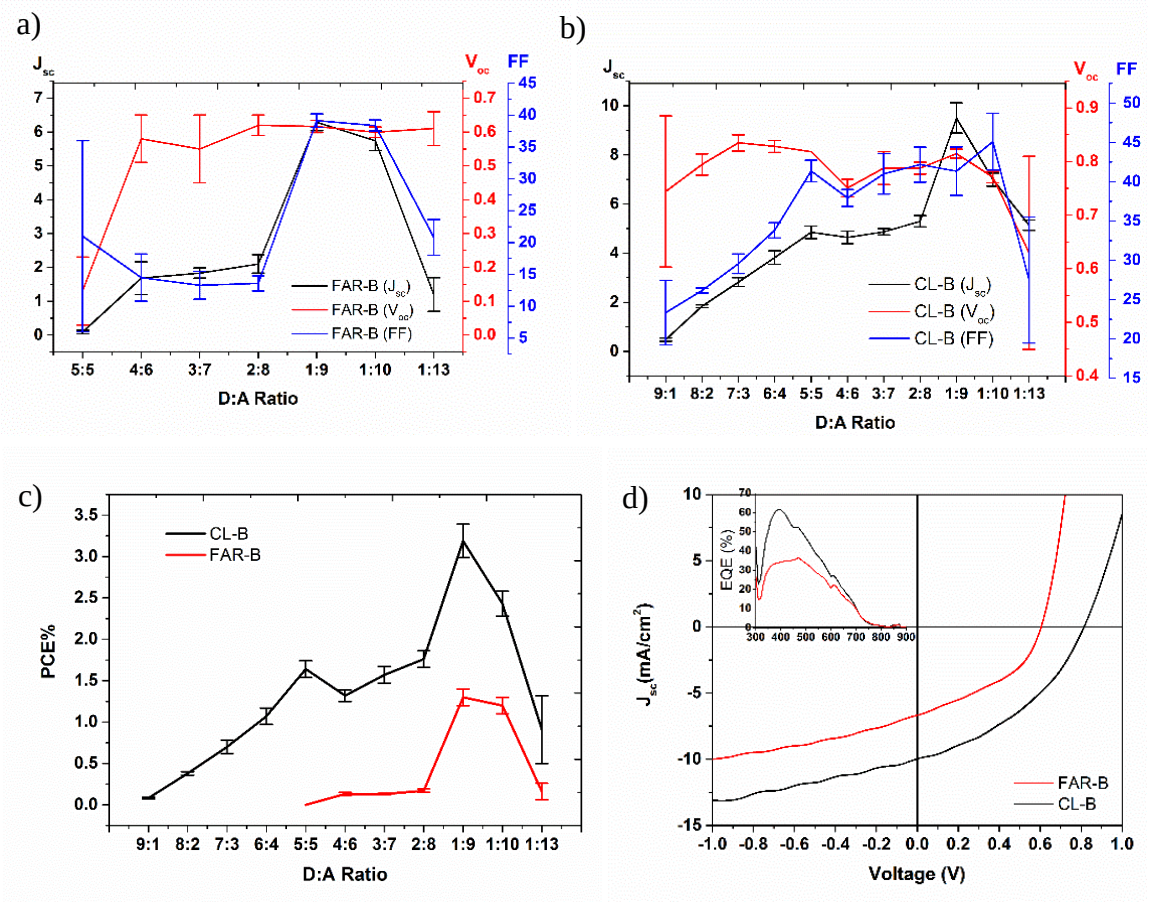

Figure 83. a) and b) show the J_{sc}, V_{oc}, and FF as a function of the D:A ratio for discrete molecules a) FAR-B, and b) CL-B. Figure c) shows the PCE as a function of D:A ratio for both FAR-B and CL-B, and d) shows the J-V curve of optimized FAR-B and CL-B, with a D:A ratio of 1:9, and the inset showing the EQE.

Table 13. Solar cell characteristics of optimized devices composed of CL-B, or FAR-B, blended with $PC_{71}BM$. Statistics were obtained over 6 devices.

	J_{sc} (mA cm^{-2})	***V_{oc} (V)***	***FF***	***PCE%***
CL-B	9.5 ± 0.6	0.81 ±0.01	41.4 ± 3.1	3.2 ± 0.2
FAR-B	6.3 ± 0.3	0.62 ± 0.02	39.1 ± 1.1	1.5 ± 0.1

Table 14. Solar cell characteristics of CL-B and FAR-B with a varying D:A ratio. All values are an average of 6 devices.

	FAR-B:$PC_{71}BM$				***CL-B:$PC_{71}BM$***			
D:A Ratio	J_{sc}	V_{oc}	FF	PCE%	J_{sc}	V_{oc}	FF	PCE%
5:5	-	-	-	-	4.85	0.82	41.37	1.64
4:6	1.68	0.58	14.54	0.13	4.64	0.75	37.93	1.32
3:7	1.83	0.55	13.26	0.13	4.87	0.79	41.01	1.57
2:8	2.10	0.62	13.59	0.17	5.30	0.79	42.17	1.76
1:9	6.29	0.62	39.14	1.52	9.50	0.81	41.35	3.19
1:10	5.00	0.60	38.16	1.15	7.00	0.77	45.10	2.43
1:13	1.23	0.61	20.78	0.16	5.14	0.63	27.50	0.91

Table 15. CL-B:$PC_{71}BM$ with a D:A ratio of 1:9 cast with 0.5% DIO added by volume, 1% DIO added by volume, and annealing at 150 ºC for 10 minutes in a glovebox.

CL-B:$PC_{71}BM$ (1:9)	***J_{sc}***	***V_{oc}***	***FF***	***PCE%***
Annealing at 150 ºC for 10 min	2.88	0.61	24.73	0.43
0.5% DIO	1.68	0.60	31.97	0.32
1% DIO	0.51	0.29	31.72	0.05

In order to better understand the nature of these low donor content solar cells the active layer morphology was explored. Grazing-incidence wide-angle x-ray scattering (GIWAXS) was collected for the neat films, and the BHJ films. Figure 84 shows 2D GIWAXS images of neat CL-B and FAR-B films respectively. Their corresponding film thickness normalized 1D line cuts in the q_z and q_{xy} directions are shown in Figure 85. By examining the 2D images, and 1D line cuts, of neat films in Figure 84 it is clear that the FAR-B shows more order than the CL-B. The strong (100) lamellar stacking peak, and corresponding (010) π-π stacking peak in the q_{xy} direction present in the 2D image of FAR-B, reinforce that FAR-B shows a greater extent of order and packing in the solid state. Furthermore, when examining the film thickness normalized 1D line cut of CL-B and FAR-B in the q_z direction shown in Figure 85, FAR-B shows greater integrated peak intensity of the (100) lamellar peak than CL-B, indicating a higher degree of crystallinity [214, 215] that is preferentially edge-on. Further, the enhanced (010) peak, corresponding to π-π stacking, of FAR-B relative to CL-B suggests improved π-π stacking in FAR-B films. The lamellar spacing for CL-B and FAR-B were found to be 16.2 Å and 16.6 Å in the q_z direction respectively. The mean size of crystallites, found using Scherrer's relation [215], was calculated to be 7.7 nm for CL-B, and 16.9 nm for FAR-B. Using the crystal size and spacing parameters, Table 16, the number of lamellar stacks for CL-B was estimated to be ~ 4, while FAR-B showed ~ 10 stacks. The increased crystallinity and order of neat FAR-B compared to CL-B explains the earlier onset of absorption seen the neat film UV-vis spectra shown in Figure 81. Furthermore, the different chains reinforce that small chemical structure changes lead to diverse solid state packing morphologies. Figure 84 also shows the 2D GIWAXS images of optimized CL-B, and FAR-B, BHJ films. Their corresponding

1D line cuts in the q_z and q_{xy} direction are shown in Figure 85. Since the optimized donor:acceptor ratio is 1:9, the 2D images, and line cuts, closely resemble those of pure $PC_{71}BM$. The reflections present at ~0.2, 0.6, 1.38, and 1.9 q ($Å^{-1}$) correspond to $PC_{71}BM$. (Figure 85 c) and d) No distinction features were observed in the BHJ blend belonging to CL-B or FAR-B, indicating that the discrete molecule is dispersed in the amorphous $PC_{71}BM$ matrix.

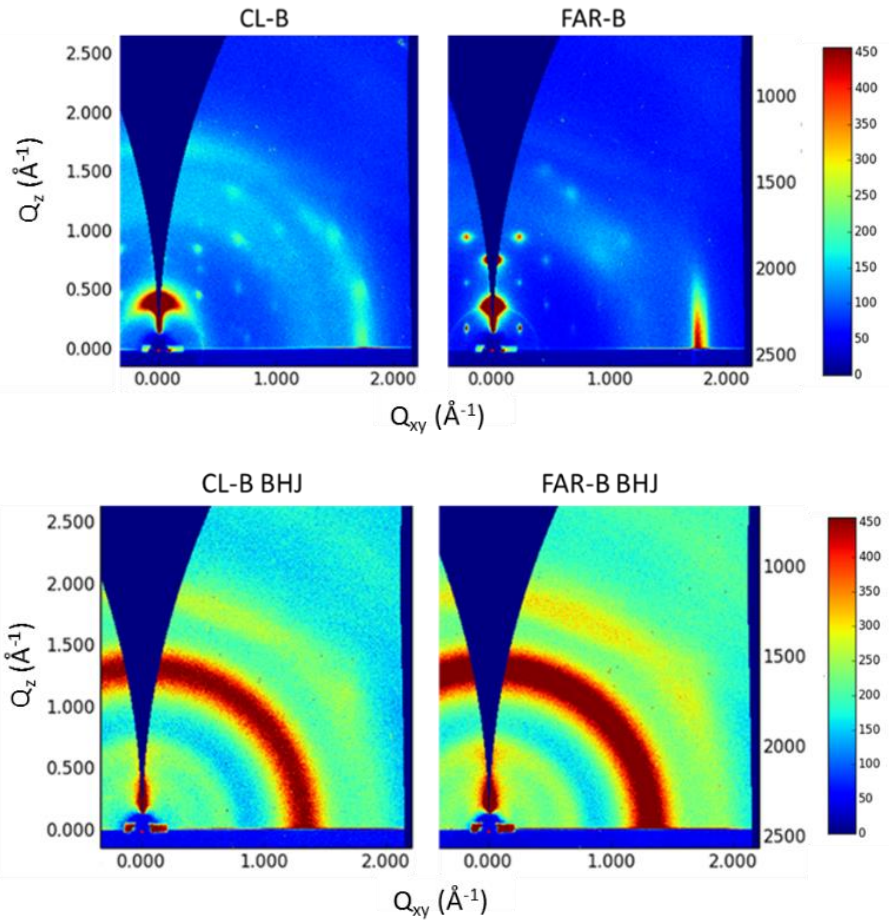

Figure 84. 2D GIWAXS images of neat CL-B and FAR-B, and BHJ CL-B and FAR-B.

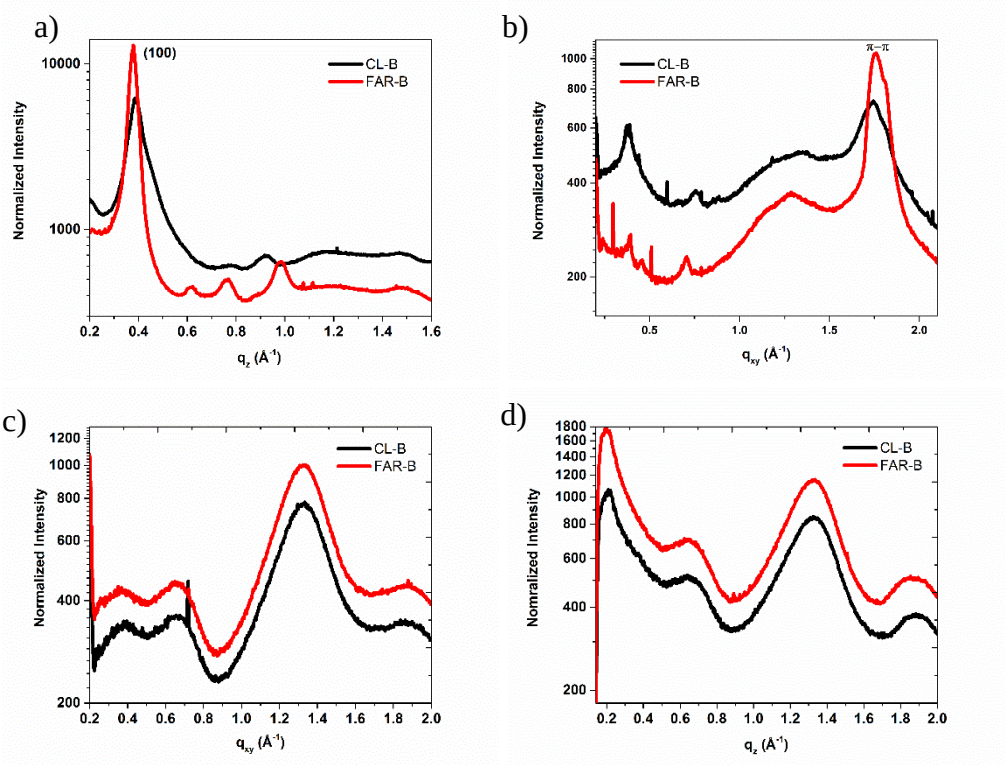

Figure 85. 1D GIWAXS line cuts in the a) q_{xy} and b) q_z direction for neat CL-B and FAR-B films. Figures c) and d) are 1D GIWAXS line cuts in the q_{xy} and q_z direction for BHJ CL-B and FAR-B films with a D:A ratio of 1:9.

Table 16. GIWAXS parameters of CL-B and FAR-B films.

	q_{xy}			q_z		
	(100) Lamellar stacking (Å)	(010) π-π stacking (Å)	(010) CCL (π-π peak nm)	(100) Lamellar stacking (Å)	(010) π-π stacking (Å)	(100) CCL(Lamellar peak nm)
CL-B	16.8	3.6	1.8	16.2	N/A	7.7
FAR-B	16.0	3.6	3.9	16.6	N/A	16.9

Lamellar and π-π stacking distances were determined using 2π/q, and crystal coherence length (CCL) was determined using 2π/FWHM.

Atomic force microscopy (AFM) images were collected in order to examine the surface morphology of the BHJ films. Figure 86 shows the AFM height images of optimized BHJ films (D:A ratio 1:9) comprised of a-b) CL-B:$PC_{71}BM$ or c-d) FAR-B:$PC_{71}BM$, taken at 5 μm by 5 μm and 1 μm by 1 μm length scales. Films cast using CL-B, shown in Figure 86 a) and 4 b), show no large features, signifying that CL-B is well dispersed in the amorphous $PC_{71}BM$ matrix. Films cast using FAR-B, Figures 86 c) and 4 d), show small indents in the film topography. Interestingly, similar AFM height images are shown in BHJ mixture of p-DTS$(FBTTh_2)_2$:$PC_{71}BM$ blend films, and p-DTG$(FBTTh_2)_2$:$PC_{71}BM$ blend films.[201] in which the indents were classified as holes with an average diameter of 150 nm. Here, we find an average hole diameter of 80 nm. All films show smooth surfaces with RMS values below 1 nm indicating that differences observed in device performance are not likely due to interface resistance caused by a rough surface.

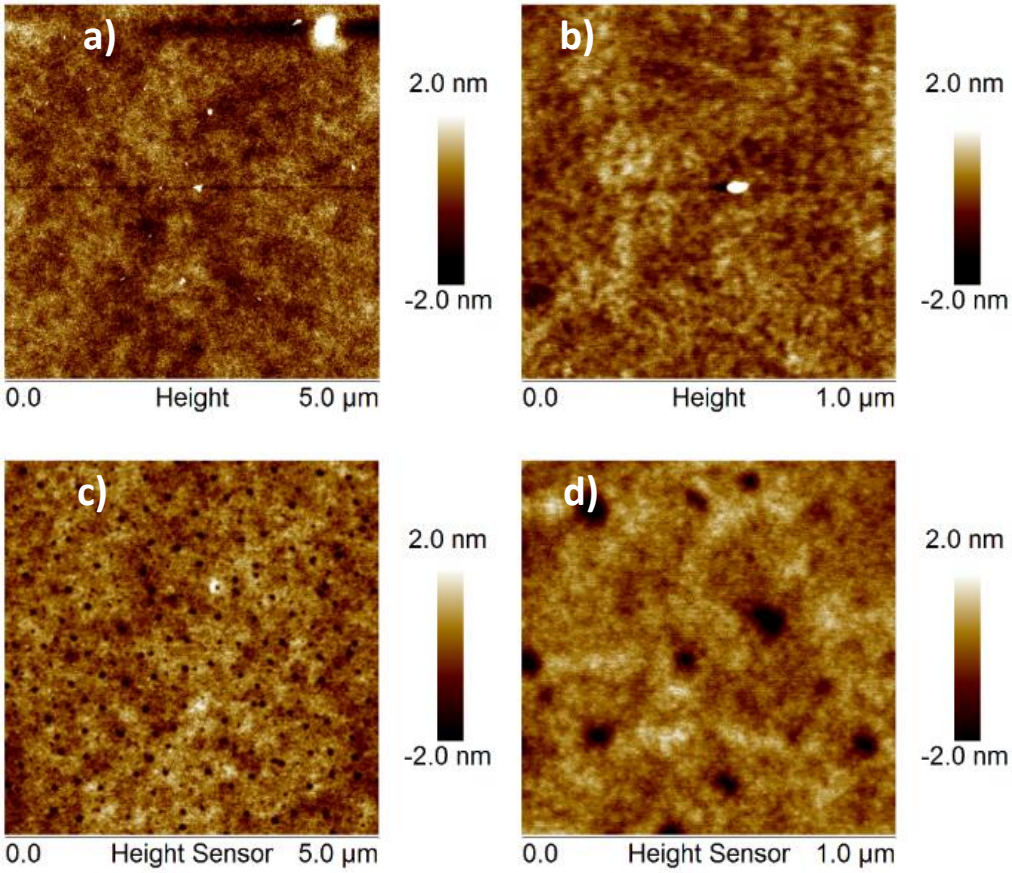

Figure 86. AFM height images of a-b) BHJ CL-B, and c-d) BHJ FAR-B, taken at 5 µm by 5 µm and 1 µm by 1 µm.

A2.3. Conclusion.

Here we have synthesized two novel discrete conjugated molecules for organic photovoltaic application. We have investigated the structure property relationship between two commonly used side chains, one exhibiting a branching point close to the backbone of the discrete molecule, and the other exhibiting a branching point far from the backbone. Through morphological studies we find that the CL-B side chain increases structural disorder in the system allowing for improved mixing between the small molecule and the fullerene. The FAR-B side chain allows for improved packing of the small molecule, which

in turn leads to unfavorable phase separation of the small molecule and fullerene, and thus, decreased solar cell performance. Increased concentration of the donor component, like that found in polymer:fullerene systems, leads to unfavorably large domain sizes due to the tendency for discrete conjugated molecules to crystallize to a higher degree than their entropically hindered polymeric counterparts. On the other hand, if the donor content is below 1:9, photovoltaic performance worsens with rapid decrease in fill factor and J_{sc}. With too little donor, hole transport suffers; conversely, with too much donor, the dielectric constant and electron mobility both decrease, which is unfavorable.[208] In the case of low donor content solar cells such as the system presented here, the donor material is present mainly to ensure efficient dissociation of excitons rather than to absorb a significant amount of light. Solution processable low donor content photovoltaics may be advantageous for the commercialization of organic solar cells as new non-fullerene acceptors replace costly $PC_{71}BM$.

Acknowledgments.

Jungho Lee, Ian Pelse, and Changduk Yang .

References

1. H. Letheby, *Journal of the Chemical Society*, 1862, **15**, 161-163.
2. A. Dall'Olio, G. Dascola, V. Vacara and V. Bocchi, *CR Acad. Sci. Paris*, 1968, **267**, 433-435.
3. R. McNeill, R. Siudak, J. Wardlaw and D. Weiss, *Australian Journal of Chemistry*, 1963, **16**, 1056-1075.
4. B. A. Bolto, R. McNeill and D. Weiss, *Australian Journal of Chemistry*, 1963, **16**, 1090-1103.
5. R. De Surville, M. Jozefowicz, L. Yu, J. Pepichon and R. Buvet, *Electrochimica Acta*, 1968, **13**, 1451-1458.
6. K. Müllen, J. R. Reynolds and T. Masuda, *Conjugated Polymers: A Practical Guide to Synthesis*, Royal Society of Chemistry, 2014.
7. J. J. Eisch, *Organometallics*, 2012, **31**, 4917-4932.
8. D. Berets and D. Smith, *Transactions of the Faraday Society*, 1968, **64**, 823-828.
9. T. Ito, H. Shirakawa and S. Ikeda, *Journal of polymer science: polymer chemistry edition*, 1974, **12**, 11-20.
10. C. K. Chiang, C. Fincher Jr, Y. W. Park, A. J. Heeger, H. Shirakawa, E. J. Louis, S. C. Gau and A. G. MacDiarmid, *Physical Review Letters*, 1977, **39**, 1098.
11. A. Suzuki, *Angewandte Chemie International Edition*, 2011, **50**, 6722-6737.
12. U. Salzner, J. Lagowski, P. Pickup and R. Poirier, *Synthetic Metals*, 1998, **96**, 177-189.
13. J. Chien, *New York*, 1984, 483.
14. J.-M. Nunzi, *Comptes Rendus Physique*, 2002, **3**, 523-542.
15. Z. Wu, W. Wang, Y. Cao, J. He, Q. Luo, W. A. Bhutto, S. Li and J. Kang, *Journal of Materials Chemistry A*, 2014, **2**, 14571-14576.
16. C. A. Thomas, K. Zong, K. A. Abboud, P. J. Steel and J. R. Reynolds, *Journal of the American Chemical Society*, 2004, **126**, 16440-16450.
17. R. Tautz, E. Da Como, T. Limmer, J. Feldmann, H.-J. Egelhaaf, E. Von Hauff, V. Lemaur, D. Beljonne, S. Yilmaz and I. Dumsch, *Nature communications*, 2012, **3**, 970.
18. B. C. Thompson and J. M. Fréchet, *Angewandte chemie international edition*, 2008, **47**, 58-77.
19. L. Koster, S. E. Shaheen and J. C. Hummelen, *Advanced Energy Materials*, 2012, **2**, 1246-1253.
20. B. Kippelen and J.-L. Brédas, *Energy & Environmental Science*, 2009, **2**, 251-261.
21. J.-L. Brédas, J. E. Norton, J. Cornil and V. Coropceanu, *Accounts of chemical research*, 2009, **42**, 1691-1699.
22. B. Qi and J. Wang, *Physical Chemistry Chemical Physics*, 2013, **15**, 8972-8982.
23. C. W. Tang, *Applied Physics Letters*, 1986, **48**, 183-185.
24. M. Dogru and T. Bein, *Chemical Communications*, 2014, **50**, 5531-5546.
25. D. E. Markov, E. Amsterdam, P. W. Blom, A. B. Sieval and J. C. Hummelen, *The Journal of Physical Chemistry A*, 2005, **109**, 5266-5274.
26. G. Yu, J. Gao, J. C. Hummelen, F. Wudl and A. J. Heeger, *Science*, 1995, **270**, 1789.

27. J. Halls, C. Walsh, N. Greenham, E. Marseglia, R. Friend, S. Moratti and A. Holmes, 1995.
28. A. Zen, M. Saphiannikova, D. Neher, J. Grenzer, S. Grigorian, U. Pietsch, U. Asawapirom, S. Janietz, U. Scherf and I. Lieberwirth, *Macromolecules*, 2006, **39**, 2162-2171.
29. P. Schilinsky, U. Asawapirom, U. Scherf, M. Biele and C. J. Brabec, *Chemistry of Materials*, 2005, **17**, 2175-2180.
30. A. M. Ballantyne, L. Chen, J. Dane, T. Hammant, F. M. Braun, M. Heeney, W. Duffy, I. McCulloch, D. D. Bradley and J. Nelson, *Advanced Functional Materials*, 2008, **18**, 2373-2380.
31. T. Y. Chu, J. Lu, S. Beaupré, Y. Zhang, J. R. Pouliot, J. Zhou, A. Najari, M. Leclerc and Y. Tao, *Advanced Functional Materials*, 2012, **22**, 2345-2351.
32. W. Li, L. Yang, J. R. Tumbleston, L. Yan, H. Ade and W. You, *Advanced Materials*, 2014, **26**, 4456-4462.
33. J. A. Bartelt, J. D. Douglas, W. R. Mateker, A. E. Labban, C. J. Tassone, M. F. Toney, J. M. Fréchet, P. M. Beaujuge and M. D. McGehee, *Advanced Energy Materials*, 2014, **4**.
34. P. M. Beaujuge and J. M. Fréchet, *Journal of the American Chemical Society*, 2011, **133**, 20009-20029.
35. C. Liu, K. Wang, X. Hu, Y. Yang, C.-H. Hsu, W. Zhang, S. Xiao, X. Gong and Y. Cao, *ACS applied materials & interfaces*, 2013, **5**, 12163-12167.
36. A. T. Yiu, P. M. Beaujuge, O. P. Lee, C. H. Woo, M. F. Toney and J. M. Fréchet, *Journal of the American Chemical Society*, 2012, **134**, 2180-2185.
37. Y. Liang, D. Feng, Y. Wu, S.-T. Tsai, G. Li, C. Ray and L. Yu, *Journal of the American Chemical Society*, 2009, **131**, 7792-7799.
38. J. M. Szarko, J. Guo, Y. Liang, B. Lee, B. S. Rolczynski, J. Strzalka, T. Xu, S. Loser, T. J. Marks and L. Yu, *Advanced Materials*, 2010, **22**, 5468-5472.
39. C. m. Cabanetos, A. El Labban, J. A. Bartelt, J. D. Douglas, W. R. Mateker, J. M. Fréchet, M. D. McGehee and P. M. Beaujuge, *Journal of the American Chemical Society*, 2013, **135**, 4656-4659.
40. J. Mei and Z. Bao, *Chemistry of Materials*, 2013, **26**, 604-615.
41. Y. Liu, J. Zhao, Z. Li, C. Mu, W. Ma, H. Hu, K. Jiang, H. Lin, H. Ade and H. Yan, *Nature communications*, 2014, **5**.
42. H. W. Ro, J. M. Downing, S. Engmann, A. A. Herzing, D. M. DeLongchamp, L. J. Richter, S. Mukherjee, H. Ade, M. Abdelsamie and L. K. Jagadamma, *Energy & Environmental Science*, 2016.
43. A. Pivrikas, H. Neugebauer and N. S. Sariciftci, *Solar Energy*, 2011, **85**, 1226-1237.
44. H.-C. Liao, C.-C. Ho, C.-Y. Chang, M.-H. Jao, S. B. Darling and W.-F. Su, *Materials today*, 2013, **16**, 326-336.
45. S. Engmann, H. W. Ro, A. Herzing, L. Richter, P. B. Geraghty and D. J. Jones, *Journal of Materials Chemistry A*, 2016.
46. K. A. Mazzio and C. K. Luscombe, *Chemical Society Reviews*, 2015, **44**, 78-90.
47. M. Campoy-Quiles, T. Ferenczi, T. Agostinelli, P. G. Etchegoin, Y. Kim, T. D. Anthopoulos, P. N. Stavrinou, D. D. Bradley and J. Nelson, *Nature materials*, 2008, **7**, 158-164.

48. F. Padinger, R. S. Rittberger and N. S. Sariciftci, *Advanced Functional Materials*, 2003, **13**, 85-88.
49. W. Ma, C. Yang, X. Gong, K. Lee and A. J. Heeger, *Advanced Functional Materials*, 2005, **15**, 1617-1622.
50. M. Morana, P. Koers, C. Waldauf, M. Koppe, D. Muehlbacher, P. Denk, M. Scharber, D. Waller and C. Brabec, *Advanced Functional Materials*, 2007, **17**, 3274-3283.
51. S. Zhang, L. Ye, H. Zhang and J. Hou, *Materials Today*, 2016.
52. W. Ma, G. Yang, K. Jiang, J. H. Carpenter, Y. Wu, X. Meng, T. McAfee, J. Zhao, C. Zhu and C. Wang, *Advanced Energy Materials*, 2015, **5**.
53. F. C. Krebs, *Solar energy materials and solar cells*, 2009, **93**, 394-412.
54. K. Norrman, A. Ghanbari-Siahkali and N. Larsen, *Annual Reports Section" C"(Physical Chemistry)*, 2005, **101**, 174-201.
55. Y. Yuan, G. Giri, A. L. Ayzner, A. P. Zoombelt, S. C. Mannsfeld, J. Chen, D. Nordlund, M. F. Toney, J. Huang and Z. Bao, *Nature communications*, 2014, **5**.
56. R. Søndergaard, M. Hösel, D. Angmo, T. T. Larsen-Olsen and F. C. Krebs, *Materials today*, 2012, **15**, 36-49.
57. L. Shaw, P. Hayoz, Y. Diao, J. A. Reinspach, J. W. To, M. F. Toney, R. T. Weitz and Z. Bao, *ACS applied materials & interfaces*, 2016, **8**, 9285-9296.
58. K. X. Steirer, J. J. Berry, M. O. Reese, M. F. van Hest, A. Miedaner, M. W. Liberatore, R. Collins and D. S. Ginley, *Thin Solid Films*, 2009, **517**, 2781-2786.
59. C. Girotto, B. P. Rand, J. Genoe and P. Heremans, *Solar energy materials and solar cells*, 2009, **93**, 454-458.
60. K. X. Steirer, M. O. Reese, B. L. Rupert, N. Kopidakis, D. C. Olson, R. T. Collins and D. S. Ginley, *Solar Energy Materials and Solar Cells*, 2009, **93**, 447-453.
61. J. G. Tait, B. J. Worfolk, S. A. Maloney, T. C. Hauger, A. L. Elias, J. M. Buriak and K. D. Harris, *Solar Energy Materials and Solar Cells*, 2013, **110**, 98-106.
62. A. Teichler, J. Perelaer and U. S. Schubert, *Journal of Materials Chemistry C*, 2013, **1**, 1910-1925.
63. C. N. Hoth, S. A. Choulis, P. Schilinsky and C. J. Brabec, *Advanced Materials*, 2007, **19**, 3973-3978.
64. M. Sanyal, B. Schmidt-Hansberg, M. F. Klein, A. Colsmann, C. Munuera, A. Vorobiev, U. Lemmer, W. Schabel, H. Dosch and E. Barrena, *Advanced Energy Materials*, 2011, **1**, 363-367.
65. B. Schmidt-Hansberg, M. Sanyal, M. F. Klein, M. Pfaff, N. Schnabel, S. Jaiser, A. Vorobiev, E. Müller, A. Colsmann and P. Scharfer, *Acs Nano*, 2011, **5**, 8579-8590.
66. L. J. Richter, D. M. DeLongchamp, F. A. Bokel, S. Engmann, K. W. Chou, A. Amassian, E. Schaible and A. Hexemer, *Advanced Energy Materials*, 2015, **5**.
67. N. Shin, L. J. Richter, A. A. Herzing, R. J. Kline and D. M. DeLongchamp, *Advanced Energy Materials*, 2013, **3**, 938-948.
68. L. H. Rossander, N. K. Zawacka, H. F. Dam, F. C. Krebs and J. W. Andreasen, *AIP Advances*, 2014, **4**, 087105.
69. M. Abdelsamie, K. Zhao, M. R. Niazi, K. W. Chou and A. Amassian, *Journal of Materials Chemistry C*, 2014, **2**, 3373-3381.

70. S. Pröller, F. Liu, C. Zhu, C. Wang, T. P. Russell, A. Hexemer, P. Müller-Buschbaum and E. M. Herzig, *Advanced Energy Materials*, 2016, **6**.
71. N. S. Güldal, T. Kassar, M. Berlinghof, T. Ameri, A. Osvet, R. Pacios, G. L. Destri, T. Unruh and C. J. Brabec, *Journal of Materials Chemistry C*, 2016, **4**, 2178-2186.
72. T. Agostinelli, S. Lilliu, J. G. Labram, M. Campoy-Quiles, M. Hampton, E. Pires, J. Rawle, O. Bikondoa, D. D. Bradley and T. D. Anthopoulos, *Advanced Functional Materials*, 2011, **21**, 1701-1708.
73. A. P. Böttiger, M. Jørgensen, A. Menzel, F. C. Krebs and J. W. Andreasen, *Journal of Materials Chemistry*, 2012, **22**, 22501-22509.
74. N. K. Zawacka, T. R. Andersen, J. W. Andreasen, L. H. Rossander, H. F. Dam, M. Jørgensen and F. C. Krebs, *Journal of Materials Chemistry A*, 2014, **2**, 18644-18654.
75. X. Gu, J. Reinspach, B. J. Worfolk, Y. Diao, Y. Zhou, H. Yan, K. Gu, S. Mannsfeld, M. F. Toney and Z. Bao, *ACS applied materials & interfaces*, 2016, **8**, 1687-1694.
76. R. Zhang, H. Yang, K. Zhou, J. Zhang, X. Yu, J. Liu and Y. Han, *Macromolecules*, 2016, **49**, 6987-6996.
77. L. A. Perez, K. W. Chou, J. A. Love, T. S. Van Der Poll, D. M. Smilgies, T. Q. Nguyen, E. J. Kramer, A. Amassian and G. C. Bazan, *Advanced Materials*, 2013, **25**, 6380-6384.
78. S. Engmann, F. A. Bokel, A. A. Herzing, H. W. Ro, C. Girotto, B. Caputo, C. V. Hoven, E. Schaible, A. Hexemer and D. M. DeLongchamp, *Journal of Materials Chemistry A*, 2015, **3**, 8764-8771.
79. J. J. van Franeker, M. Turbiez, W. Li, M. M. Wienk and R. A. Janssen, *Nature communications*, 2015, **6**.
80. F. Liu, Y. Gu, C. Wang, W. Zhao, D. Chen, A. L. Briseno and T. P. Russell, *Advanced Materials*, 2012, **24**, 3947-3951.
81. F. Liu, S. Ferdous, E. Schaible, A. Hexemer, M. Church, X. Ding, C. Wang and T. P. Russell, *Advanced Materials*, 2015, **27**, 886-891.
82. F. Buss, B. Schmidt-Hansberg, M. Sanyal, C. Munuera, P. Scharfer, W. Schabel and E. Barrena, *Macromolecules*, 2016, **49**, 4867-4874.
83. T. Kassar, N. S. Güldal, M. Berlinghof, T. Ameri, A. Kratzer, B. C. Schroeder, G. L. Destri, A. Hirsch, M. Heeney and I. McCulloch, *Advanced Energy Materials*, 2016, **6**.
84. C. M. Stafford, K. E. Roskov, T. H. Epps III and M. J. Fasolka, *Review of scientific instruments*, 2006, **77**, 023908.
85. I. B. Martini, I. M. Craig, W. C. Molenkamp, H. Miyata, S. H. Tolbert and B. J. Schwartz, *Nature nanotechnology*, 2007, **2**, 647-652.
86. R. Verduzco, I. Botiz, D. L. Pickel, S. M. Kilbey, K. Hong, E. Dimasi and S. B. Darling, *Macromolecules*, 2011, **44**, 530-539.
87. W.-R. Wu, U.-S. Jeng, C.-J. Su, K.-H. Wei, M.-S. Su, M.-Y. Chiu, C.-Y. Chen, W.-B. Su, C.-H. Su and A.-C. Su, *Acs Nano*, 2011, **5**, 6233-6243.
88. E. Verploegen, C. E. Miller, K. Schmidt, Z. Bao and M. F. Toney, *Chemistry of Materials*, 2012, **24**, 3923-3931.
89. P. Müller-Buschbaum, *Advanced Materials*, 2014, **26**, 7692-7709.

90. J. Rivnay, S. C. Mannsfeld, C. E. Miller, A. Salleo and M. F. Toney, *Chemical reviews*, 2012, **112**, 5488-5519.
91. S. Mannsfeld, *Journal*, 2009.
92. J. Ilavsky, *Journal of Applied Crystallography*, 2012, **45**, 324-328.
93. B. W. Boudouris, V. Ho, L. H. Jimison, M. F. Toney, A. Salleo and R. A. Segalman, *Macromolecules*, 2011, **44**, 6653-6658.
94. J. L. Baker, L. H. Jimison, S. Mannsfeld, S. Volkman, S. Yin, V. Subramanian, A. Salleo, A. P. Alivisatos and M. F. Toney, *Langmuir*, 2010, **26**, 9146-9151.
95. A. Tuteja, M. E. Mackay, C. J. Hawker, B. Van Horn and D. L. Ho, *Journal of Polymer Science Part B: Polymer Physics*, 2006, **44**, 1930-1947.
96. J. R. Tumbleston, B. A. Collins, L. Yang, A. C. Stuart, E. Gann, W. Ma, W. You and H. Ade, *Nature Photonics*, 2014, **8**, 385-391.
97. Z. He, C. Zhong, S. Su, M. Xu, H. Wu and Y. Cao, *Nature Photonics*, 2012, **6**, 591-595.
98. J. Rostalski and D. Meissner, *Solar energy materials and solar cells*, 2000, **61**, 87-95.
99. K. Emery, http://rredc.nrel.gov/solar/spectra/am1.5/, (accessed 12/21, 2016).
100. P. Murgatroyd, *Journal of Physics D: Applied Physics*, 1970, **3**, 151.
101. H. Zhou, Y. Zhang, J. Seifter, S. D. Collins, C. Luo, G. C. Bazan, T. Q. Nguyen and A. J. Heeger, *Advanced Materials*, 2013, **25**, 1646-1652.
102. *International Energy Outlook 2013*, U.S. Energy Information Administration (EIA)

2013.
103. A. K. K. Kyaw, D. H. Wang, D. Wynands, J. Zhang, T.-Q. Nguyen, G. C. Bazan and A. J. Heeger, *Nano letters*, 2013, **13**, 3796-3801.
104. K. Sun, Z. Xiao, S. Lu, W. Zajaczkowski, W. Pisula, E. Hanssen, J. M. White, R. M. Williamson, J. Subbiah and J. Ouyang, *Nature communications*, 2015, **6**.
105. Z. He, C. Zhong, X. Huang, W. Y. Wong, H. Wu, L. Chen, S. Su and Y. Cao, *Advanced Materials*, 2011, **23**, 4636-4643.
106. W. Nie, R. C. Coffin, J. Liu, Y. Li, E. D. Peterson, C. M. MacNeill, R. E. Noftle and D. L. Carroll, *Applied Physics Letters*, 2012, **100**, 083301.
107. J.-W. Kang, Y.-J. Kang, S. Jung, M. Song, D.-G. Kim, C. S. Kim and S. H. Kim, *Solar Energy Materials and Solar Cells*, 2012, **103**, 76-79.
108. J.-S. Yu, I. Kim, J.-S. Kim, J. Jo, T. T. Larsen-Olsen, R. R. Søndergaard, M. Hösel, D. Angmo, M. Jørgensen and F. C. Krebs, *Nanoscale*, 2012, **4**, 6032-6040.
109. S. H. Eom, H. Park, S. Mujawar, S. C. Yoon, S.-S. Kim, S.-I. Na, S.-J. Kang, D. Khim, D.-Y. Kim and S.-H. Lee, *Organic Electronics*, 2010, **11**, 1516-1522.
110. C. N. Hoth, P. Schilinsky, S. A. Choulis and C. J. Brabec, *Nano letters*, 2008, **8**, 2806-2813.
111. P. Schilinsky, C. Waldauf and C. J. Brabec, *Advanced Functional Materials*, 2006, **16**, 1669-1672.
112. J.-H. Chang, Y.-H. Chen, H.-W. Lin, Y.-T. Lin, H.-F. Meng and E.-C. Chen, *Organic Electronics*, 2012, **13**, 705-709.
113. S.-L. Lim, E.-C. Chen, C.-Y. Chen, K.-H. Ong, Z.-K. Chen and H.-F. Meng, *Solar Energy Materials and Solar Cells*, 2012, **107**, 292-297.

114. R. Mens, F. Demir, G. Van Assche, B. Van Mele, D. Vanderzande and P. Adriaensens, *Journal of Polymer Science Part A: Polymer Chemistry*, 2012, **50**, 1037-1041.
115. Y.-H. Chang, S.-R. Tseng, C.-Y. Chen, H.-F. Meng, E.-C. Chen, S.-F. Horng and C.-S. Hsu, *Organic Electronics*, 2009, **10**, 741-746.
116. Y.-R. Hong, P.-K. Chen, J.-C. Wang, M.-K. Lee, S.-F. Horng and H.-F. Meng, *Solar Energy Materials and Solar Cells*, 2014, **120**, 197-203.
117. C.-M. Liu, Y.-W. Su, J.-M. Jiang, H.-C. Chen, S.-W. Lin, C.-J. Su, U. S. Jeng and K.-H. Wei, *Journal of Materials Chemistry A*, 2014, **2**, 20760-20769.
118. C.-Y. Chen, H.-W. Chang, Y.-F. Chang, B.-J. Chang, Y.-S. Lin, P.-S. Jian, H.-C. Yeh, H.-T. Chien, E.-C. Chen and Y.-C. Chao, *Journal of Applied Physics*, 2011, **110**, 094501.
119. K. W. Chou, B. Yan, R. Li, E. Q. Li, K. Zhao, D. H. Anjum, S. Alvarez, R. Gassaway, A. Biocca and S. T. Thoroddsen, *Advanced Materials*, 2013, **25**, 1923-1929.
120. M. T. Dang, G. Wantz, H. Bejbouji, M. Urien, O. J. Dautel, L. Vignau and L. Hirsch, *Solar Energy Materials and Solar Cells*, 2011, **95**, 3408-3418.
121. F. Machui, S. Langner, X. Zhu, S. Abbott and C. J. Brabec, *Solar Energy Materials and Solar Cells*, 2012, **100**, 138-146.
122. D. T. Duong, B. Walker, J. Lin, C. Kim, J. Love, B. Purushothaman, J. E. Anthony and T. Q. Nguyen, *Journal of Polymer Science Part B: Polymer Physics*, 2012, **50**, 1405-1413.
123. S. K. Hau, H.-L. Yip, N. S. Baek, J. Zou, K. O'Malley and A. K.-Y. Jen, *Applied Physics Letters*, 2008, **92**, 253301.
124. E. J. Luber and J. M. Buriak, *ACS nano*, 2013, **7**, 4708-4714.
125. S.-H. Jin, B. V. K. Naidu, H.-S. Jeon, S.-M. Park, J.-S. Park, S. C. Kim, J. W. Lee and Y.-S. Gal, *Solar Energy Materials and Solar Cells*, 2007, **91**, 1187-1193.
126. K. Kawano, J. Sakai, M. Yahiro and C. Adachi, *Solar Energy Materials and Solar Cells*, 2009, **93**, 514-518.
127. M. Yusli, T. W. Yun and K. Sulaiman, *Materials Letters*, 2009, **63**, 2691-2694.
128. Y. Yao, J. Hou, Z. Xu, G. Li and Y. Yang, *Advanced Functional Materials*, 2008, **18**, 1783-1789.
129. G. Li, V. Shrotriya, J. Huang, Y. Yao, T. Moriarty, K. Emery and Y. Yang, *Nature materials*, 2005, **4**, 864-868.
130. A. Zhang, C. Du, H. Bai, Y. Wang, J. Wang and L. Li, *ACS applied materials & interfaces*, 2014, **6**, 8921-8927.
131. M. Srinivasarao, D. Collings, A. Philips and S. Patel, *Science*, 2001, **292**, 79-83.
132. T.-F. Guo, T.-C. Wen, G. L. v. Pakhomov, X.-G. Chin, S.-H. Liou, P.-H. Yeh and C.-H. Yang, *Thin Solid Films*, 2008, **516**, 3138-3142.
133. Y. Zhao, Z. Xie, Y. Qu, Y. Geng and L. Wang, *Applied Physics Letters*, 2007, **90**, 043504.
134. T. Wang, A. D. Dunbar, P. A. Staniec, A. J. Pearson, P. E. Hopkinson, J. E. MacDonald, S. Lilliu, C. Pizzey, N. J. Terrill and A. M. Donald, *Soft Matter*, 2010, **6**, 4128-4134.
135. S. T. Turner, P. Pingel, R. Steyrleuthner, E. J. Crossland, S. Ludwigs and D. Neher, *Advanced Functional Materials*, 2011, **21**, 4640-4652.

136. F. C. Spano, *Chemical physics*, 2006, **325**, 22-35.
137. N. F. Mott and R. W. Gurney, 1940.
138. B. Schmidt-Hansberg, M. F. Klein, K. Peters, F. Buss, J. Pfeifer, S. Walheim, A. Colsmann, U. Lemmer, P. Scharfer and W. Schabel, *Journal of Applied Physics*, 2009, **106**, 124501.
139. Z. He, B. Xiao, F. Liu, H. Wu, Y. Yang, S. Xiao, C. Wang, T. P. Russell and Y. Cao, *Nature Photonics*, 2015, **9**, 174-179.
140. J. Zhao, Y. Li, G. Yang, K. Jiang, H. Lin, H. Ade, W. Ma and H. Yan, *Nature Energy*, 2016, **1**, 15027.
141. M. Hösel, H. F. Dam and F. C. Krebs, *Energy Technology*, 2015, **3**, 293-304.
142. X. Gu, Y. Zhou, K. Gu, T. Kurosawa, Y. Guo, Y. Li, H. Lin, B. C. Schroeder, H. Yan and F. Molina-Lopez, *Advanced Energy Materials*, 2017.
143. Y. Sun, G. C. Welch, W. L. Leong, C. J. Takacs, G. C. Bazan and A. J. Heeger, *Nature materials*, 2012, **11**, 44-48.
144. Y.-J. Hwang, T. Earmme, B. A. Courtright, F. N. Eberle and S. A. Jenekhe, *Journal of the American Chemical Society*, 2015, **137**, 4424-4434.
145. J. K. Lee, W. L. Ma, C. J. Brabec, J. Yuen, J. S. Moon, J. Y. Kim, K. Lee, G. C. Bazan and A. J. Heeger, *Journal of the American Chemical Society*, 2008, **130**, 3619-3623.
146. W. Zhao, L. Ye, S. Zhang, M. Sun and J. Hou, *Journal of Materials Chemistry A*, 2015, **3**, 12723-12729.
147. R. G. Brandt, F. Zhang, T. R. Andersen, D. Angmo, M. Shi, L. Gurevich, F. C. Krebs, J. W. Andreasen and D. Yu, *RSC Advances*, 2016, **6**, 41542-41550.
148. H. W. Ro, J. M. Downing, S. Engmann, A. A. Herzing, D. M. DeLongchamp, L. J. Richter, S. Mukherjee, H. Ade, M. Abdelsamie and L. K. Jagadamma, *Energy & Environmental Science*, 2016, **9**, 2835-2846.
149. P.-T. Tsai, C.-Y. Tsai, C.-M. Wang, Y.-F. Chang, H.-F. Meng, Z.-K. Chen, H.-W. Lin, H.-W. Zan, S.-F. Horng and Y.-C. Lai, *Organic Electronics*, 2014, **15**, 893-903.
150. M. Guérette, A. Najari, J. Maltais, J. R. Pouliot, S. Dufresne, M. Simoneau, S. Besner, P. Charest and M. Leclerc, *Advanced Energy Materials*, 2016.
151. K. Xiong, L. Hou, M. Wu, Y. Huo, W. Mo, Y. Yuan, S. Sun, W. Xu and E. Wang, *Solar Energy Materials and Solar Cells*, 2015, **132**, 252-259.
152. J. J. van Franeker, S. Kouijzer, X. Lou, M. Turbiez, M. M. Wienk and R. A. Janssen, *Advanced Energy Materials*, 2015, **5**.
153. K. Zhao, H. Hu, E. Spada, L. Jagadamma, B. Yan, M. Abdelsamie, Y. Yang, L. Yu, R. Munir and R. Li, *Journal of Materials Chemistry A*, 2016, **4**, 16036-16046.
154. X. Guo, N. Zhou, S. J. Lou, J. Smith, D. B. Tice, J. W. Hennek, R. P. Ortiz, J. T. L. Navarrete, S. Li and J. Strzalka, *Nature Photonics*, 2013, **7**, 825-833.
155. N. Zhou, X. Guo, R. P. Ortiz, T. Harschneck, E. F. Manley, S. J. Lou, P. E. Hartnett, X. Yu, N. E. Horwitz and P. M. Burrezo, *Journal of the American Chemical Society*, 2015, **137**, 12565-12579.
156. N. Zhou, A. S. Dudnik, T. I. Li, E. F. Manley, T. J. Aldrich, P. Guo, H.-C. Liao, Z. Chen, L. X. Chen and R. P. Chang, *Journal of the American Chemical Society*, 2016, **138**, 1240-1251.

157. J. L. Hernandez, E. Reichmanis and J. R. Reynolds, *Organic Electronics*, 2015, **25**, 57-65.
158. J. T. Rogers, K. Schmidt, M. F. Toney, G. C. Bazan and E. J. Kramer, *Journal of the American Chemical Society*, 2012, **134**, 2884-2887.
159. T. Ameri, P. Khoram, T. Heumüller, D. Baran, F. Machui, A. Troeger, V. Sgobba, D. M. Guldi, M. Halik and S. Rathgeber, *Journal of Materials Chemistry A*, 2014, **2**, 19461-19472.
160. H. F. Mark, *Encyclopedia of polymer science and technology, concise*, John Wiley & Sons, 2013.
161. T.-Q. Nguyen, V. Doan and B. J. Schwartz, *The Journal of chemical physics*, 1999, **110**, 4068-4078.
162. A. C. Stuart, J. R. Tumbleston, H. Zhou, W. Li, S. Liu, H. Ade and W. You, *Journal of the American Chemical Society*, 2013, **135**, 1806-1815.
163. J. C. Rivière and S. Myhra, *Handbook of surface and interface analysis: methods for problem-solving*, CRC press, 2009.
164. L. Ye, Y. Xiong, H. Yao, A. Gadisa, H. Zhang, S. Li, M. Ghasemi, N. Balar, A. Hunt and B. T. O'Connor, *Chemistry of Materials*, 2016, **28**, 7451-7458.
165. I. Osaka, M. Saito, T. Koganezawa and K. Takimiya, *Advanced Materials*, 2014, **26**, 331-338.
166. C. Lu, H.-C. Chen, W.-T. Chuang, Y.-H. Hsu, W.-C. Chen and P.-T. Chou, *Chemistry of Materials*, 2015, **27**, 6837-6847.
167. P.-H. Chu, N. Kleinhenz, N. Persson, M. McBride, J. L. Hernandez, B. Fu, G. Zhang and E. Reichmanis, *Chemistry of Materials*, 2016, **28**, 9099-9109.
168. D. Leman, M. A. Kelly, S. Ness, S. Engmann, A. Herzing, C. Snyder, H. W. Ro, R. J. Kline, D. M. DeLongchamp and L. J. Richter, *Macromolecules*, 2015, **48**, 383-392.
169. H. Choi, S. J. Ko, T. Kim, P. O. Morin, B. Walker, B. H. Lee, M. Leclerc, J. Y. Kim and A. J. Heeger, *Advanced Materials*, 2015, **27**, 3318-3324.
170. R. S. Ashraf, I. Meager, M. Nikolka, M. Kirkus, M. Planells, B. C. Schroeder, S. Holliday, M. Hurhangee, C. B. Nielsen and H. Sirringhaus, *Journal of the American Chemical Society*, 2015, **137**, 1314-1321.
171. J. Y. Back, H. Yu, I. Song, I. Kang, H. Ahn, T. J. Shin, S.-K. Kwon, J. H. Oh and Y.-H. Kim, *Chemistry of Materials*, 2015, **27**, 1732-1739.
172. Y. J. Kim, W. Jang, S. Ahn, C. E. Park and D. H. Wang, *Organic Electronics*, 2016, **34**, 42-49.
173. W. Li, K. H. Hendriks, M. M. Wienk and R. A. Janssen, *Accounts of chemical research*, 2015, **49**, 78-85.
174. M. S. Vezie, S. Few, I. Meager, G. Pieridou, B. Dörling, R. S. Ashraf, A. R. Goñi, H. Bronstein, I. McCulloch and S. C. Hayes, *Nature materials*, 2016.
175. C. Wang, C. J. Mueller, E. Gann, A. C. Liu, M. Thelakkat and C. R. McNeill, *Journal of Materials Chemistry A*, 2016, **4**, 3477-3486.
176. S. Kouijzer, J. J. Michels, M. van den Berg, V. S. Gevaerts, M. Turbiez, M. M. Wienk and R. A. Janssen, *Journal of the American Chemical Society*, 2013, **135**, 12057-12067.
177. W. Li, K. H. Hendriks, A. Furlan, W. C. Roelofs, M. M. Wienk and R. A. Janssen, *Journal of the American Chemical Society*, 2013, **135**, 18942-18948.

178. W. Ma, J. R. Tumbleston, M. Wang, E. Gann, F. Huang and H. Ade, *Advanced Energy Materials*, 2013, **3**, 864-872.
179. S. Mukherjee, C. M. Proctor, J. R. Tumbleston, G. C. Bazan, T. Q. Nguyen and H. Ade, *Advanced Materials*, 2015, **27**, 1105-1111.
180. W. Chen, M. P. Nikiforov and S. B. Darling, *Energy & Environmental Science*, 2012, **5**, 8045-8074.
181. J. S. Lee, S. K. Son, S. Song, H. Kim, D. R. Lee, K. Kim, M. J. Ko, D. H. Choi, B. Kim and J. H. Cho, *Chemistry of Materials*, 2012, **24**, 1316-1323.
182. Z. Yi, S. Wang and Y. Liu, *Advanced Materials*, 2015, **27**, 3589-3606.
183. J. J. van Franeker, G. H. Heintges, C. Schaefer, G. Portale, W. Li, M. M. Wienk, P. van der Schoot and R. A. Janssen, *Journal of the American Chemical Society*, 2015, **137**, 11783-11794.
184. NREL, *Journal*, 2016.
185. K. Branker, M. Pathak and J. M. Pearce, *Renewable and Sustainable Energy Reviews*, 2011, **15**, 4470-4482.
186. C. J. Mulligan, C. Bilen, X. Zhou, W. J. Belcher and P. C. Dastoor, *Solar Energy Materials and Solar Cells*, 2015, **133**, 26-31.
187. W. I. Jeong, J. Lee, S. Y. Park, J. W. Kang and J. J. Kim, *Advanced Functional Materials*, 2011, **21**, 343-347.
188. A. Gambhir, P. Sandwell and J. Nelson, *Solar Energy Materials and Solar Cells*, 2016.
189. V. Fthenakis and H. C. Kim, *Solar Energy*, 2011, **85**, 1609-1628.
190. S. B. Darling and F. You, *Rsc Advances*, 2013, **3**, 17633-17648.
191. F. Machui, M. Hösel, N. Li, G. D. Spyropoulos, T. Ameri, R. R. Søndergaard, M. Jørgensen, A. Scheel, D. Gaiser and K. Kreul, *Energy & Environmental Science*, 2014, **7**, 2792-2802.
192. Y. Lin and X. Zhan, *Materials Horizons*, 2014, **1**, 470-488.
193. S. Holliday, R. S. Ashraf, A. Wadsworth, D. Baran, S. A. Yousaf, C. B. Nielsen, C.-H. Tan, S. D. Dimitrov, Z. Shang and N. Gasparini, *Nature communications*, 2016, **7**.
194. A. Louwen, W. Van Sark, R. Schropp and A. Faaij, *Solar Energy Materials and Solar Cells*, 2016, **147**, 295-314.
195. S. Xiao, Q. Zhang and W. You, *Advanced Materials*, 2016.
196. M. C. Scharber, *Advanced Materials*, 2016.
197. L. Lucera, F. Machui, P. Kubis, H. Schmidt, J. Adams, S. Strohm, T. Ahmad, K. Forberich, H.-J. Egelhaaf and C. Brabec, *Energy & Environmental Science*, 2016, **9**, 89-94.
198. A. L. B. Gap, *Journal of Physical Chemistry C*, 2008, **112**, 11545-11551.
199. T. S. Van Der Poll, J. A. Love, T. Q. Nguyen and G. C. Bazan, *Advanced Materials*, 2012, **24**, 3646-3649.
200. J. A. Love, C. M. Proctor, J. Liu, C. J. Takacs, A. Sharenko, T. S. van der Poll, A. J. Heeger, G. C. Bazan and T. Q. Nguyen, *Advanced Functional Materials*, 2013, **23**, 5019-5026.
201. Y. Sun, J. Seifter, L. Huo, Y. Yang, B. B. Hsu, H. Zhou, X. Sun, S. Xiao, L. Jiang and A. J. Heeger, *Advanced Energy Materials*, 2015, **5**.

202. J. Mei, D. H. Kim, A. L. Ayzner, M. F. Toney and Z. Bao, *Journal of the American Chemical Society*, 2011, **133**, 20130-20133.
203. C. Lee, H. Kang, W. Lee, T. Kim, K. H. Kim, H. Y. Woo, C. Wang and B. J. Kim, *Advanced Materials*, 2015, **27**, 2466-2471.
204. J. Mei, H. C. Wu, Y. Diao, A. Appleton, H. Wang, Y. Zhou, W. Y. Lee, T. Kurosawa, W. C. Chen and Z. Bao, *Advanced Functional Materials*, 2015, **25**, 3455-3462.
205. M. Zhang, H. Wang and C. W. Tang, *Organic electronics*, 2012, **13**, 249-251.
206. G. Chen, H. Sasabe, Z. Wang, X. F. Wang, Z. Hong, Y. Yang and J. Kido, *Advanced Materials*, 2012, **24**, 2768-2773.
207. X. Xiao, J. D. Zimmerman, B. E. Lassiter, K. J. Bergemann and S. R. Forrest, *Applied Physics Letters*, 2013, **102**, 073302.
208. M. Zhang, H. Wang, H. Tian, Y. Geng and C. Tang, *Advanced Materials*, 2011, **23**, 4960-4964.
209. D. M. Stoltzfus, C.-Q. Ma, R. C. Nagiri, A. J. Clulow, P. Bäuerle, P. L. Burn, I. R. Gentle and P. Meredith, *Applied Physics Letters*, 2016, **109**, 103302.
210. B. Walker, A. B. Tamayo, X. D. Dang, P. Zalar, J. H. Seo, A. Garcia, M. Tantiwiwat and T. Q. Nguyen, *Advanced Functional Materials*, 2009, **19**, 3063-3069.
211. L. Li, L. Xiao, H. Qin, K. Gao, J. Peng, Y. Cao, F. Liu, T. P. Russell and X. Peng, *ACS applied materials & interfaces*, 2015, **7**, 21495-21502.
212. M.-C. Yuan, M.-Y. Chiu, S.-P. Liu, C.-M. Chen and K.-H. Wei, *Macromolecules*, 2010, **43**, 6936-6938.
213. Y. Chen, Y. Yan, Z. Du, X. Bao, Q. Liu, V. Roy, M. Sun, R. Yang and C. S. Lee, *Journal of Materials Chemistry C*, 2014, **2**, 3921-3927.
214. M. E. Farahat, C.-S. Tsao, Y.-C. Huang, S. H. Chang, W. Budiawan, C.-G. Wu and C.-W. Chu, *Journal of Materials Chemistry A*, 2016, **4**, 7341-7351.
215. A. Sharenko, M. Kuik, M. F. Toney and T. Q. Nguyen, *Advanced Functional Materials*, 2014, **24**, 3543-3550.

VITA

Jeff Hernandez was born in Caracas, Venezuela where he stayed for three years. His family moved to Clearwater, Florida when he was three. Jeff attended Dunedin High School where he graduated with his H.S. Diploma in 2006. He enrolled in St. Petersburg College in 2006 where he earned his A.A. degree, then transferred to the University of South Florida where he finished his B.A. in Chemistry in 2011. In 2012 Jeff enrolled in the Chemistry graduate program at Georgia Tech to pursue his Ph.D. under John R. Reynolds. While he studied at Georgia Tech, he developed collaborations with the National Institute of Standards and Technology (NIST) and was a guest researcher at NIST for four months during his graduate program. Jeff graduated in the Spring semester of 2017 and has started an industrial career as a Research Scientist at Solvay Specialty Polymers.